Thermal performance analysis of a PCM combined solar chimney system for natural ventilation and heating/cooling

Li, Yongcai

Award date:
2013

Awarding institution:
Coventry University

Thermal Performance Analysis of A PCM Combined Solar Chimney System for Natural Ventilation and Heating/Cooling

By

Yongcai Li

For the degree of Doctor of Philosophy

September, 2013

The work contained within this document has been submitted by the student in partial fulfilment of the requirement of their course and award

ABSTRACT

Solar chimney is an important passive design strategy to maximize solar gain to enhance buoyancy effect for achieving adequate air flow rate and a desired level of thermal comfort inside a building. Therefore, solar chimney has the potential advantages over mechanical ventilation systems in terms of energy requirement, economic and environmental benefits. The main aim of this project is to study the technical feasibility of a solar chimney incorporating latent heat storage (LHS) system for domestic heating and cooling applications.

The research work carried out and reported in this thesis includes: the development of a detailed theoretical model to calculate the phase change material (PCM) mass for solar chimney under specific climatic condition, the development of a CFD model to optimise the channel depth and the inlet and outlet sizes for the solar chimney geometry, experimental and numerical investigations of the thermal performance of the proposed system using a prototype set-up, a parametric study on the proposed system to identify significant parameters that affect the system performance was carried out by using the verified numerical model.

The numerical and experimental study showed that the numerical model has the ability to calculate the PCM mass for the proposed system for the given weather conditions. The optimum PCM should be selected on the basis of its melting temperature, rather than its other properties such as latent heat.

The experimental work on the thermal performance of the proposed system has been carried out. The results indicated that the LHS based solar chimney is technically viable. The outlet air temperature and the air flow rate varied within a small range during phase change transition period which are important for a solar air heating system. A numerical model was developed to reproduce the experimental conditions in terms of closed mode and open mode. The model results were in a close agreement with the experimental results particularly the simulated results for the discharging process.

With the verified model, a comprehensive parametric analysis intended to optimise the

thermal performance of proposed the system was performed. The results analysed are quantified in terms of charging/discharging time of the PCM, temperature difference between outlet air and inlet air of the solar chimney, and mass flow rate of the chimney, which are the most important quantities of the proposed system.

ACKNOWLEDGEMENTS

I would like to express my sincere gratitude to Dr. Shuli Liu, my director, for her direction, supervision, and sharing of expertise which guided me through my research period. I am also very grateful to my second supervisor Pro. John Davies and to my third supervisor Pro. Mark Gaterell for their valuable suggestions. I would also like to thank Dr. Abdullahi Ahmed, for providing his supports and thoughtful advices to my research work.

I am sincerely and heartily acknowledge my colleagues, xxx and Muriel Iten for the assistance and advice relating to my research that they gave me. In the same way, I appreciate all the help and support from my friends Yougui Lin and Yi Xu, who helped and encouraged me throughout my study.

My special thanks to all the technicians of the John Lang Building at Coventry University, Ian Breakwell, Terry Teeling, Kieran Teeling, and Steve Hutton. I owe sincere and earnest thankfulness to Mr. Ian Breakwell, who has provided me plenty of help in my experimental work. I am very sure my project would have not been finished without his helps. His helps in encouraging me to get used to the British life and to write formal English during the course of my study would also be appreciated.

Finally, I would like to express my deepest gratitude to all my family members: my mother, my brother and sister, who constantly provided their emotional support to me during my research years. Yaqin Zhang, my wife, deserves special thanks for her caring of our family during these years. Your encouragement and support without regrets get me through those difficult times. Nobody knows how much I owe them.

TABLE OF CONTENTS

NOMENCLATURE

A	area, m^2
C_d	discharge coefficient
c_{sp}	average specific heat between T_i and T_m, $kj.kg^{-1}.K^{-1}$
c_{lp}	average specific heat between T_m and T_f, $kj.kg^{-1}.K^{-1}$
c_p	specific heat at constant pressure, $kj.kg^{-1}.K^{-1}$
f	melt fraction
H	sum of sensible and latent heat, kJ
H_c	height of a solar chimney, m
$h(T)$	sensible heat of the PCM, kJ
H	total volumetric enthalpy, $kJ.m^{-3}$
h	specific enthalpy, $kJ.m^{-3}$
k	thermal conductivity, $W.m^{-1}.K^{-1}$
L	latent heat of fusion, $kJ.kg^{-1}$
m	mass of heat storage material, kg
Δp	stack pressure, Pa
Q	total quantity of heat stored, kJ
q_s	applied heat flux, W/m^2
q_{p-g}	heat flow rate transferred from absorber plate to glazing, W/m^2
q_{g-sky}	heat flow rate transferred from glazing to ambient, W/m^2
q_{p-l}	heat transfer rate transferred from absorber plate to PCM, W/m^2
q_{air-g}	heat transfer rate convected from air inside channel to glazing, W/m^2
q_{l-p}	heat transfer transferred from PCM to absorber surface, W/m^2
t	time, s
T	temperature, ℃
T_1	the lower limit of the melting temperature range, ℃
T_2	the higher limit of the melting temperature range, ℃
T_m	melting temperature, ℃
T_i	initial temperature of solid PCM, ℃
T_f	final temperature, ℃
T_o	outlet air temperature, ℃
T_a	ambient temperature, ℃

T_{air}	mean air temperature inside cavity, ℃
V	volume, m^3
x	Cartesian coordinate

Greek Symbols

Δ	difference
α	thermal diffusivity of PCM, $m^2.s^{-1}$
ρ	density, $kg.m^{-3}$
δ	thickness, m
α_g	glazing absorptance
g	gravitational acceleration, m/s^2
τ_g	transmittance of glazing
γ	mean temperature approximation coefficient
α_p	absorptivity of absorber plate
β	volumetric thermal expansion coefficient, 1/K

Subscripts

eff	effective
g	glazing cover
l	liquid
m	phase change material
p	absorber plate
s	solid

Acronyms

LHS	latent heat storage
PCM	phase change material
SHS	sensible le heat storage
TCE	Thermal conductivity enhancer

LIST OF FIGURES

LIST OF TABLES

1. INTRODUCTION

1.1 ENERGY AND ENVIRONMENTAL CONCERNS

Nowadays people spend almost 90% of their time on working and living in buildings, therefore it's very important to maintain the indoor environment in good quality. Building ventilation provides the fresh air into a building under specified weather. Heating and cooling of the building keeps the indoor temperature in required level for occupants. As shown in Figure 1-1, each building is an integrated dynamic system separately and needs large amounts of energy to maintain the building working properly.

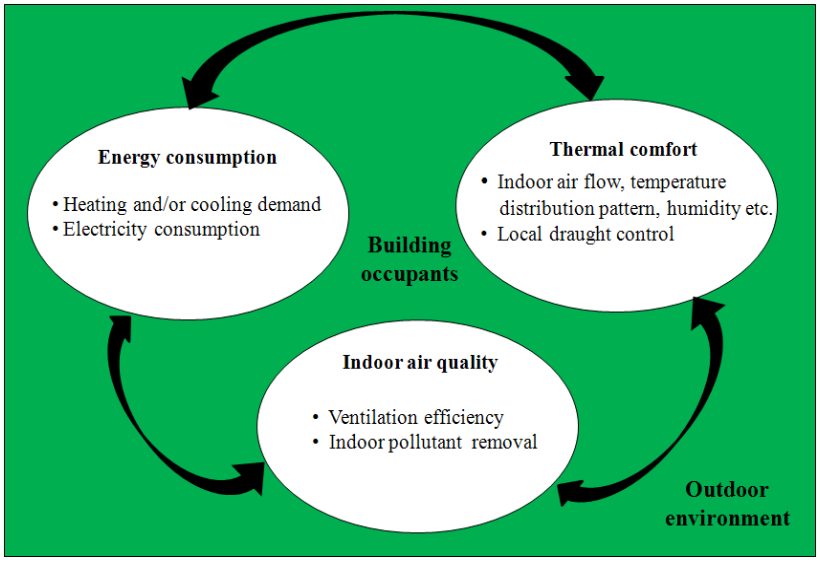

Figure 1- 1 Relationships between the occupants, building energy and indoor environment

The energy consumption in the building sector is an important factor in the total energy consumption. Generally, building sector consumes more than 35.3%～40% of final demand (IEA, 2007; Arkar, 2007), and the figure is 40%-50% in the UK (CIBSE, 2003). The energy consumption in building sector produced over 75.8 million tons of CO_2 in 2007, which accounts for 14% of the UK's total CO_2 emissions (National Statistics, 2008). With energy demand rising and greenhouse effect strengthening, the buildings, energy and the

environment are key issues for the building professions worldwide (Lam et al., 2006). The UK government set out the challenging goal in the Energy White Paper to reduce 60% of emissions of greenhouse gases by around 2050 (DTI Energy White Paper, 2003). Its main strategies to reduce CO_2 emissions were the increase in the use of renewable energy sources and improvements in energy efficiency. The renewable energy is a reliable alternative to fossil fuels in domestic sector application as they are clean and abundant. Amongst the renewable energies are in the forms of wind power, geothermal power and solar energy, etc. Solar energy is the largest potential renewable energy. The amount of the cost-free solar energy from the sun reaching the earth surface is so huge that it is almost twice as much as can ever be obtained from all of the Earth's non-renewable resources (http://gcep.stanford.edu/research/exergycharts.html). Researchers have known how to utilize of solar chimneys to supply ventilation into buildings and the cooling or heating of buildings. Passive solar heating and cooling technologies convert solar energy into the usable heat, cause air-movement for heating or cooling, or store heat for future use.

1.2 SOLAR CHIMNEY- A PASSIVE STRATEGY

The availability of abundant solar energy has been an impetus for solar energy application research. One of the solar energy application technologies is solar chimney, being a simple and practical idea of a passive heating, cooling and natural ventilation design.

1.2.1 Working Mechanism and Components of the Solar Chimney

The solar chimney is an air channel, which utilises solar energy to improve the natural ventilation of buildings (Zhai et.al, 2011). Solar energy received by the solar chimney causes a temperature rise as well as a density drop in the air inside the solar chimney to drive an adequate air flow rate. The air flows up from inlet to outlet due to the density difference of air between the inlet and outlet. This air stream will have the effect of ventilation heating and cooling of buildings. Two main operation modes of the solar chimney are illustrated in Figure 1-2. As described in Figure 1-2 (a), when the solar chimney is used for passive heating operation, the indoor air is introduced into the air cavity, and is heated up by the absorber surface. The heated air flows into the room to reduce the heating load. When the cooling load is required and the ambient air temperature is lower than the room air temperature, the solar chimney can operate in the mode for natural ventilation and passive cooling. In this project,

phase change material (PCM) is used to replace the mass wall that can enhance the thermal storage capacity of the solar chimney.

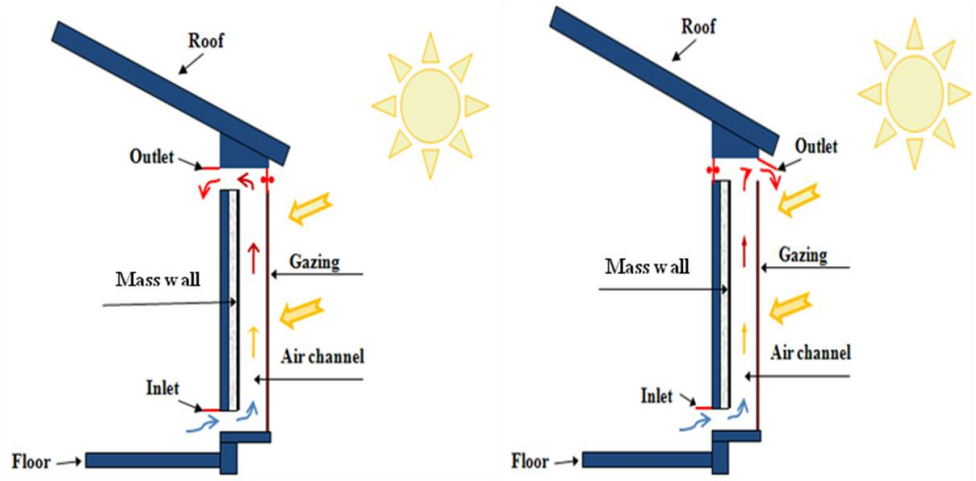

Figure 1- 2 Two operation modes of the solar chimney: (a) passive heating mode; (b) natural ventilation and cooling mode

1.2.2 Thermal Storage

For heating and cooling of buildings using solar energy, the energy needs to be collected, stored and distributed properly. In a passive system all the three functions are done by natural means and generally, no electrical or mechanical power and electronic controls are used (Morrison, 1978). A well-known difficulty in effectively utilising the solar energy is that solar energy is often unpredictable and intermittent (Sukhatme, 1996). Another barrier in utilising solar energy is that the domestic dwellings are not occupied during the day time therefore there is a mismatch between peak solar radiation and demand. Though solar chimney has the potential to reduce energy demand on building services whilst simultaneously reducing CO_2 emissions, its thermal performance is limited by the low thermal storage capacity of the mass wall. PCM as the thermal storage medium is an effective way of enhancing the overall thermal performance of the solar chimney, as the PCMs offer higher energy density due to their high latent heat of fusion, while the phase change transition occurs at relatively constant temperature (isothermal), namely melting or solidification temperature. This makes such materials an excellent choice for the solar chimney, incorporating PCM to store excess energy

during the periods when solar energy is plentiful and releasing it during the off-sunshine periods. By this means two main problems of the conventional solar chimneys are tackled.

(1) Conventional solar chimneys are not able to work during the night-time, due to the low heat storage capacity of conventional solar energy storage materials (concrete, metal etc).
(2) Owing to the temperature fluctuation of the solar absorber, the outlet air temperature changes with absorber temperature, variations that can reduce thermal comfort.

Although there have been plenty of studies carried out on the performances of solar chimneys or PCMs respectively, only a few comprehensive experimental or computational studies have been undertaken for solar chimneys integrated with PCMs so far (Stritih and Medved, 1994; Stritih, and Novak,1996; Amori and Mohammed, 2012). Therefore, this study will address this shortfall in data and will provide a significant contribution to knowledge in the area of incorporating PCMs with solar chimney. This new data will provide a design method of such a solar chimney.

1.3 AIMS AND OBJECTIVES

In light of the above background, the project aims to develop a novel solar chimney combined with suitable PCMs to ventilate a building with heating and cooling capacity.
A solar chimney containing PCM allows it to work during low or no solar radiation periods. In order to utilize solar energy efficiently, the melting time and freezing time of the PCM unit are two of the essential parameters in designing of the solar energy system, as they must correspond to the total amount of daily insolation and the heating or cooling time respectively. To be specific, the proposed system should be designed in such a way that within a certain time, complete melting or solidification of the PCM is achieved. In that way, the system achieves its maximum efficiency.
The aim of the current work will be accomplished by successfully completing the following objectives:

1) Development of a detailed theoretical model to calculate the quantity of PCM and PCM unit geometry for the solar chimney under specific climatic conditions.

2) Development of an experimental testing rig as a stand-alone component to validate the theoretical model developed in objective 1) and to study experimentally the performances of the PCM unit with and without different thermal conductivity enhancers (TCEs) experimentally to evaluate the melting and solidification times.

3) Development of a Computational Fluid Dynamics (CFD) model to optimise the solar chimney geometry. (Including the depth of air channel, the inlet and outlet sizes).

4) Experimental and numerical investigations of the thermal performance of the novel solar chimney using a prototype set-up under specific operating conditions (different flux intensities).

5) Thermal performance analysis of the novel solar chimney using the numerical model which is built and validated based on the experimental data obtained from objective 4).

1.4 RESEARCH METHODOLOGY

In order to accomplish the above objectives, the proposed research methodologies are given below:

1) Selection of the suitable PCM including category, the amount for specific climate conditions. There are a large number of possible phase change materials that may be used as operation materials to store latent heat. Depending on the applications, the PCMs at first will be selected based on their melting temperature, and then the density, latent heat and specific heat. Once the PCMs have been selected primarily according to the requirements mentioned above, the amount of the candidate PCM will be determined by using a theoretical approach (Matlab). The optimal mass of PCM should correspond to the largest availability of solar energy in a year.

2) Development of a small scale experimental apparatus for three main objectives: to validate the numerical model presented in 1). To explore the properties and behaviour of melting and freezing processes of the PCM selected and to evaluate the performance of the system with different TCEs.

3) Design and assessment of the proposed solar chimney combined with PCM. A CFD model shall be developed to optimise the solar energy system geometry. A full scale solar chimney with the optimal geometry shall be set up and experiments shall be carried out under different operating conditions in the laboratory to generate performance data.

4) Development of a Matlab model which is validated by using the performance data obtained in 3) to evaluate the thermal performance of the proposed system.

1.5 THE SYSTEM WILL BE NOVEL IN THE FOLLOWING ASPECTS:

1) Inclusion of PCMs in solar chimney can store a large amount of solar energy to achieve the purpose of 'time-shifting'.
2) The proposed system is able to work all year around.
3) Nearly stable air mass flow rate and air supply temperature could be provided by the proposed system to improve the thermal comfort.
4) It will give a reduction in the electrical consumption and so reduce the CO_2 emission.

1.6 THE STRUCTURE OF RESEARCH PROGRAM

The overall structure of the research program is shown in Figure 1-3 below. It provides the inter-relationship of various components of the current research and is described previously.

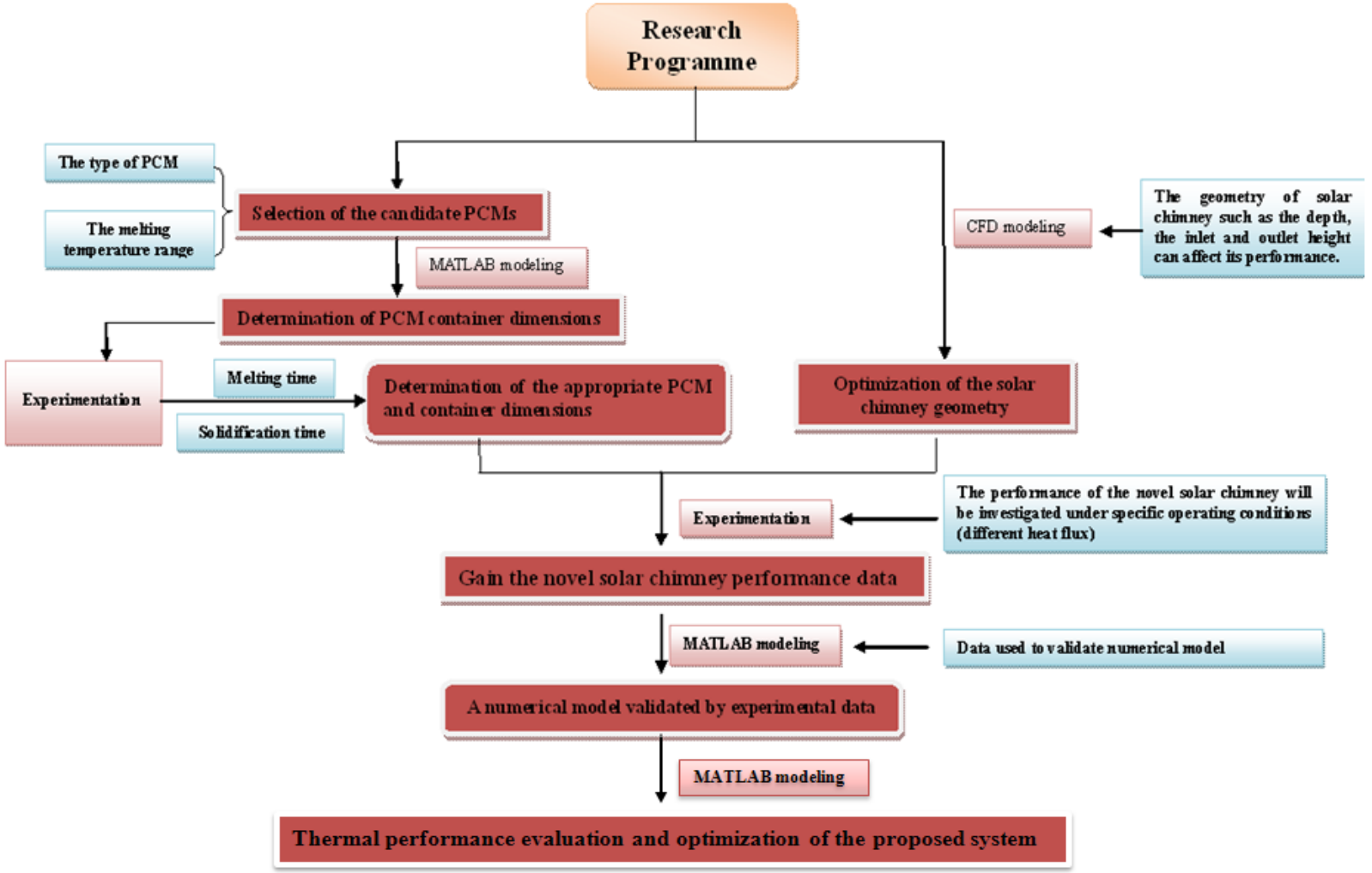

Figure 1- 3 Flow-chart of the research structure

1.7 OUTLINE OF THE THESIS

The thesis consists of eight chapters. Chapter 1 presents a general introduction and background of the research area, which highlights the significance of the research. The aim, objectives as well as the research methodology of the research are listed. Finally the structure of the research program is introduced.

In Chapter 2, a comprehensive literature review of the previous research on PCM and latent thermal storage is presented. The application and thermal performance of latent thermal storage for domestic ventilation heating and cooling are discussed. The classification of the PCMs available, advantages and disadvantages, the potential of PCMs used for spacing heating and cooling applications is highlighted.

The knowledge obtained for Chapter 2 is used to formulate selection criteria of PCMs for the proposed system in Chapter 3. A comprehensive mathematical model is developed to calculate the amount of the PCM for the system. Appropriate assumptions, boundary and initial conditions are made to the model. An experimental testing rig as a stand-alone component is developed to validate the mathematical model and to study the performances of PCM unit without and with different TCEs experimentally to evaluate the melting time and solidification time.

In Chapter 4, the optimization of the proposed system is carried out. This chapter analyses the influences of the inlet and outlet sizes and the air channel depth. The CFD modeling is aimed at finding optimum design solutions for maximizing the natural ventilation rate and the increment in outlet air temperature. Once the optimum physical parameters is identified by the simulations, they will be used to a full-scale laboratory testing rig to study the thermal performance of the proposed system under different operating conditions.

Chapter 5 describes the physical configurations of the full-scale testing rig, test procedures and the measurement devices. The method of the data collection and the treatment of the data are presented in detail. Two mathematical models based on the configuration of laboratory experimental rig are developed to predict the thermal performance and air flow rate of the experimental rig. One model is built for charging period. In this period the inlet and outlet are closed to maximize the solar gains. Another model is used for discharging period. The inlet

and outlet are opened during this period the end conditions of the first model is the initial conditions of this model.

Chapter 6 presents the data gained from the experiments and numerical simulations, and a comprehensive analysis of the results are carried out. A comparison is made between the experimental and numerical results. Any differences between the two sets of data are identified and the reasons for causing the differences are analyzed. The comparison shows that the numerical models are accurate enough to predict the thermal performances of the proposed system for difference conditions.

In Chapter 7 a further comparative numerical study of the system is carried out by using the verified numerical model to indentify the parameters which may greatly affect the performance of the proposed system. These parameters investigated include: the inlet air temperature, the latent heat of fusion, sensible heat, the melting temperature range, thermal conductivity, etc. An economic analysis of the system based on a theoretical case study is also performed in this chapter.

Finally, Chapter 8 summarizes the key findings and conclusions of the current research and highlights its limitations. It also gives the recommendations for the further research to take the work forward.

2. LITERATURE REVIEW ON LATENT HEAT STORAGE

2.1 THERMAL STORAGE

2.1.1 Sensible Heat Storage

The significance of a thermal storage unit in the solar applications is identified in Dincer et al's research (Dincer et al, 1996). A comparative study of two solar collectors which one incorporating thermal energy storage and one without any thermal storage was carried out by using numerical simulation. The results indicated that the solar collector with the thermal storage was more efficient than that without any storage. The authors thus highlighted that the use of thermal energy storage is particularly essential for solar power systems due to the time-dependent characteristic of the solar energy availability. Inclusion of a thermal storage unit in solar energy applications provides a valuable solution for overcoming the mismatch issue between the supply and demand of energy (Ghoneim, 1989). Consequently provide the potential capability of saving energy by reducing the wastage of energy, which in turn cuts down the environment impact related to energy use. From this point of view, the development of thermal energy storage unit is as important as developing new sources of energy.

Thermal energy storage generally possesses the following benefits: a) reduction in the energy consumption; b) increase in the operation flexibility; c) reduction in the maintenance costs; d) enhancement of the efficiency and effectiveness of the operating systems and e) decrease in the greenhouse gases (e.g. CO_2 and CFCs).

The two most common methods to store thermal energy are sensible heat storage (SHS) and latent heat storage (LHS) (Hasnain, 1998). SHS is that thermal energy stored in liquid or solid materials, the only process those materials experience is the change of temperature within one phase, and there is no change in phase involved. One of the most attractive advantages of SHS is that charging and discharging operations can be expected to be completely reversible for an unlimited number of cycles. The amount of energy stored is

dependent on the mass of the material, the specific heat capacity and the rise in its temperature (Lane, 1983).

The thermal energy storage for heating and cooling of building/space is mainly based on sensible heat storage materials. SHS utilizes the heat capacity and the change in temperature of the material during the process of charging or discharging – temperature of the storage material rises when energy is absorbed and drops when energy is extracted. The quantity of heat stored (Q) can be calculated with the following equation:

$$Q = \int_{T_1}^{T_2} m \cdot C_p \cdot dT \quad (2.1)$$

$$Q = m \cdot \overline{C_p} \cdot (T_2 - T_1) \quad (2.2)$$

Q = Quantity of sensible heat stored, kJ;

T_1 = Initial temperature, K;

T_2 = Final temperature, K;

m = Mass of heat storage material, Kg;

C_p =Specific heat, kJ/kg K;

$\overline{C_p}$ = Averaged specific heat between T_1 and T_2, kJ /kg K;

SHS may be classified on the basis of the heat storage medium as a) liquid medium storage such as water or oil, and b) solid medium storage such as rocks and concrete. Solid sensible storage medium is abundant, inexpensive, and easy to handle. However, the low specific heat and significant void volume in this heat storage media results in huge volume requirements. A major barrier of the SHS is that the thermal storage process does not occur isothermally.

2.1.2 Latent Heat Storage

LHS is one of the most promising thermal storage methods in which the heat stored and released involves a phase transmission (Liu et al., 2013). The materials used to store energy as latent heat are called phase change materials (PCMs). The PCM offers several advantages, and the most remarkable features are its high storage capacity in comparison to the

conventional SHS, resulting in reduction of the thermal storage unit size (Ghoneim, 1991). Esen et al. (Esen et al.,1996) illustrated that if sodium sulphate decahydrate ($Na_2SO_4\ 10H_2O$) is used as a thermal storage medium instead of conventional water based storage medium, the volume of the storage tank could be reduced by approximately 50%. The studies were conducted by Ghoneim (Ghoneim, 1989) and Morrison and Abdel-Khalik (Morrison and Abdel-Khalik, 1978) indicated that to store the same amount of heat from one unit collector area, rock requires mass seven times more than Paraffin 116 Wax (P116-Wax), five times that of medicinal paraffin. Another major advantage of LHS is its isothermal phase change characteristic. The heat is charged and discharged in PCMs at a nearly constant temperature (phase change temperature) corresponding to the phase transition. The isothermal characteristic of heat storage offers the following advantages: a) maintaining thermal comfort; b) reduction in heat loss due to lower storage temperatures; and c) increase in solar panel efficiency (Lane, 1986). This makes them ideal for space heating applications where the thermal comfort can be achieved as a result of a reduction in temperature swings (Pasupathy et al., 2008).

The thermal storage capacity of the LHS depends on the amount and latent heat of fusion of PCM. The storage capacity of the LHS system can be calculated from following equations (Lane, 1983).

$$\boldsymbol{Q = m \cdot f \cdot L + \int_{T_i}^{T_m} m \cdot c_p \cdot dT + \int_{T_m}^{T_f} m \cdot c_p \cdot dT} \quad (2.3)$$

$$\boldsymbol{Q = m \cdot [f \cdot L + c_{sp} \cdot (T_m - T_i) + c_{lp} \cdot (T_f - T_m)]} \quad (2.4)$$

Where

Q = Total quantity of heat stored in PCM (kJ);

m = Mass of PCM (kg);

f = Melt fraction;

L = Heat of fusion per unit mass (kJ/kg);

T_m = Melting temperature (K);

T_i = Initial temperature (K);

T_f = Final temperature (K);

c_{sp} = Average specific heat between T_i and T_m (kJ/kg K);

c_{lp} = Average specific heat between T_m and T_f (kJ/kg K);

c_p = Specific heat capacity (kJ/kg K).

It is important to highlight that for a LHS unit thermal energy is predominantly stored as latent heat during the charging period. However, some sensible heat due to small temperature changes will inevitably be stored in PCM. Though such energy storage can be ignored compared to the latent heat of phase transformation, sensible heat will provide significant additional heat and should be considered in any applications, if the PCM has a high phase change temperature or a large rise above the phase change temperature of PCMs.

LHS units are more expensive than the SHS as the PCM itself can be expensive (Ghoneim and Klein, 1989), whilst SHS medium itself can be abundant and low-cost. Moreover many PCMs have poor thermal conductivities and therefore require heat exchangers to enhance the heat transfer rate between the PCMs and the heat transfer fluid. Special containers will be required due to the change in the volume and the corrosive of the PCMs, which would increase the whole system cost. Though the cost of a LHS system is higher than a SHS system, LHS has the following advantages compared with SHS (Hawes et al., 1989):

1) LHS can store larger amount of energy per unit mass;
2) It is adaptable to conventional structural mass while SHS requires a larger mass to store the same amount of energy;
3) It stores energy within a small temperature swing, thus large temperature variation is avoided;
4) It achieves more efficient energy management.

Generally, any latent heat energy storage system should possess at least the following three basic components (Lane, 1983):

1) A suitable PCM, its phase change temperature in the desired temperature range, which can store/release latent heat in the thermal comfort temperature range.

2) A suitable heat exchange area is required for transferring the heat effectively from heat source to PCM and then from PCM to the required point of use.

3) A suitable container for holding the PCM, the container can be the form of microencapsulation, macro- encapsulation or incorporation in a building material.

The heat exchange plays an important role in the design of the LHS, as it strongly influences the temperature gradients for charging and discharging processes. Therefore, the development of a LHS unit involves two essentially diverse aspects:

1) Selection of heat storage materials (PCMs);
2) Design of heat exchangers for enhancing heat transfer (Abhat, 1983).

Thus the development of a LHS system for practical engineering applications, the knowledge of phase change materials and heat exchangers is required. A flow chart which indicates the different stages of the development of LHS is shown in Figure 2-1

Figure 2- 1 Different stages involved in the development of a LHS (Abhat, 1981)

2.2 PHASE CHANGE MATERIALS

The heat stored or released during the phase change process of material is called latent heat, also named 'phase change enthalpy' or 'heat of fusion'. Materials used in the LHS unit as working medium are called 'phase change materials (PCMs)'. Generally, PCMs are divided into four main types: solid ↔gas, liquid ↔gas, solid ↔ solid and solid ↔ liquid PCMs.

2.2.1 Solid ↔ Gas and Liquid ↔ Gas PCMs

A major advantage of solid ↔gas and liquid ↔ gas PCMs is that they have a higher latent heat of phase transformation in comparison to the other two types of PCMs. However, these two types of PCMs are generally not employable for energy storage owing to the large variation in volume during phase transition, in spite of their outstanding advantages. The volume expansion for gas state can be 1000 times of the original solid/liquid state (Salyer, 1997). The large fluctuation in volume reflects on the container for PCMs large, expensive and impractical (Abhat, 1981).

2.2.2 Solid ↔ Solid PCMs

Solid ↔ solid PCMs absorb or release heat as they are transformed from one crystalline form to another. The major advantages of solid ↔ solid PCMs incarnates in longer life span than other types of PCMs, smaller volume changes, no leakage, and less erosion to the device (Wang et al., 2000). The solid ↔ solid PCMs have less stringent container requirements and greater design flexibility. However the lower latent heats and higher phase transformation temperatures limit their applications. Currently only limited number of available materials have suitable phase transformation temperatures and fusion heats for applied thermal energy storage (Hasnain, 1998).

2.2.3 Solid ↔ Liquid PCMs

Solid ↔ liquid PCMs store heat when they change phase from solid to liquid and release heat during their reversible processes from liquid to solid, during phase change the materials themselves remains at a near constant temperature which calls phase change temperature. It can be said that phase transformations of solid ↔ liquid PCMs have high latent heat and small volume changes, currently appear to be the greatest practicable materials. Therefore they attract the most researchers' attentions as well as widely used in LHS.There are a large number of organic, inorganic and eutectic materials, which can be identified as solid ↔liquid PCMs from the view of melting temperature and fusion heat (Sharma et al., 2009). The melting temperature and phase change enthalpy of existing PCMs are shown in Figure 2-2 (Zhou, et al., 2012). From the point of phase change temperature, it can be seen that for LHS in building applications, the potential PCMs are paraffin, fatty acids, salt hydrates and eutectic mixtures.

Figure 2- 2 Melting temperature and phase change enthalpy of existing PCMs (Zhou et al., 2012)

2.3 CLASSIFICATION OF SOLID ↔LIQUID PCMS

An extensive study by Lane GA. (Lane, 1983) researched about 20000 substances, seeking potential PCMs. Majority of them was rejected for improper melting point, melting with decomposition. The most suitable three categories of PCMs will be discussed in detail below.The classification of PCMs is shown in Figure 2-3.

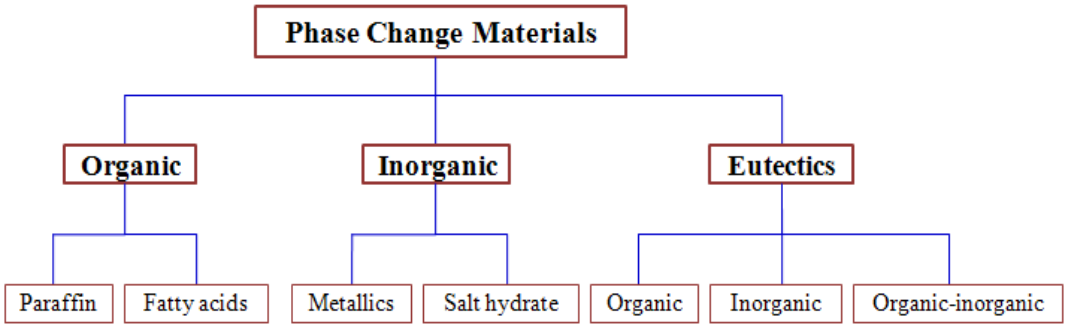

Figure 2- 3 Classification of phase change materials

2.3.1. Organic PCMs

Organic PCMs produced primarily from natural fats, oils or petrochemical products, including paraffin and non-paraffin organics. Organic materials feature congruent melting, meaning melt and freeze repeatedly without phase segregation and consequent degradation of their heat of fusion, self nucleation meaning they crystallize with little or no super-cooling

and usually non-corrosiveness (Sharma et al., 2009).

PARAFFINS

Paraffins are mineral oil products, and consist of mixture of mostly straight chain alkanes which have the general formula (C_nH_{2n+2}). The paraffins are a family of saturated hydrocarbons with similar properties. The crystallization of the (CH_3)-chain can store or release latent heat. Both the melting point and latent heat of fusion rise with chain length increasing. The paraffins are in the series from $C_{14}H_{30}$ to $C_{40}H_{82}$ having the responding melting temperature in the range of 6 to 80 degrees, which is adaptive for thermal energy storage. Paraffin possesses a lot of desirable characteristics utilised as LHS (Garg et al., 1985a). Figure 2-4 shows some of advantages of paraffins, such as: a large number of paraffins can be used for LHS at a relative low cost with high latent heat of fusion; they can be supplied in a wide range of melting temperatures with low volume change at melting, low density, high wetting ability; usually they undergo rapid phase transformation with self-nucleating and negligible supercooling at low supersaturation; besides they are non-corrosive, non-toxic, chemically stable and compatible with encapsulation materials. All of these properties indicate that the paraffins have an indefinitely long freezing-melting cycle life. However apart from these advantages of the paraffins, they also have inevitable drawbacks (as shown in Figure 2-5), and all these undesirable effects can be partly eliminated by slightly modifying the wax and the storage unit.

NON-PARAFFIN ORGANIC PCMS

The non-paraffin organic PCMs are the largest category of candidate materials for phase change materials. Lane et al (Lane, 1983; Lane, 1989) and Abhat (Abhat, 1983) have conducted an extensive survey of organic materials and identified a number of esters, fatty acids, alcohol's and glycol's suitable for energy storage. The non-paraffins PCMs are further sub-grouped into fatty acids (characterized by $CH_3\ (CH_2)\ –COOH$) and other non-paraffin organic. Although the non-paraffin organic is different from the paraffins that having very similar properties, each of non-paraffin organic has its own properties. Some common features of non-paraffin organic are presented in Figures 2-4 and 2-5. For example, fatty acids have high heat of fusion values comparing to that of paraffin's. Fatty acids also show reproducible melting and freezing behaviors and freeze with no super cooling (Herrick, 1978).

Though these advantages, the fatty acids are generally not preferred as heat storage materials due to their high cost, which are 2~2.5 times higher than paraffin (Abhat, 1981).

2.3.2 Inorganic PCMs

The inorganic PCMs can be further classified into slat hydrate and metallics. The metallics are seldom used for the thermal energy storage applications as they are rare and expensive. Slat hydrate is the oldest and most common inorganic PCMs, and can be considered as the alloys of inorganic salt and water, characterized by $AB\,nH_2O$, where AB is an inorganic compound, form an important class of heat storage substances due to their high volumetric latent storage density. Therefore, salt hydrates have been extensively used for latent heat storage. The major problem to utilise salt hydrates is that most of them melt incongruently leading that the solid phase settles down at the bottom of the container due to the higher density. This will result in the thermal characteristics deteriorating with each charge–discharge cycle. Another serious problem is their poor nucleating characteristic resulting in super-cooling of the liquid salt hydrate prior to freezing. This will deteriorates thermal performance of inorganic salt hydrate.

2.3.3 Eutectics

A eutectic is a minimum melting composition of two or more components, each of which melts and freezes congruently, forms a mixture of the component crystals during crystallization (Lane, 1989), which means they have fixed phase change temperatures. The components of the eutectic can be either inorganic or organic PCM. Hence, eutectic PCMs are normally classified into three subgroups: inorganic-inorganic eutectic, organic-organic eutectic, and organic-inorganic eutectic.

Eutectics nearly always melt and freeze without segregation because they freeze to an intimate mixture of crystals, leaving little opportunity for the components to separate. On melting, both components liquefy simultaneously, again with separation unlikely.

2.3.4 Summary of PCMs

The summaries of the advantages and disadvantages of organic, inorganic and eutectic

materials are shown in Figures 2-4 and 2-5, respectively. It can be seen that no single material can has all the optimal characteristics required for a PCM, as each of them has their advantages and disadvantages, which must be balanced out. Commendably understanding of the PCM thermal behaviors such as the heat transfer processes and the available techniques to deal with the issues associated with each PCM are essential in order to optimise the application of PCM. Therefore, the synthetically consideration of the PCMs' chemical, physical and thermal characteristic and the reactions with their encapsulations are very important to maximize the benefit of LHS.

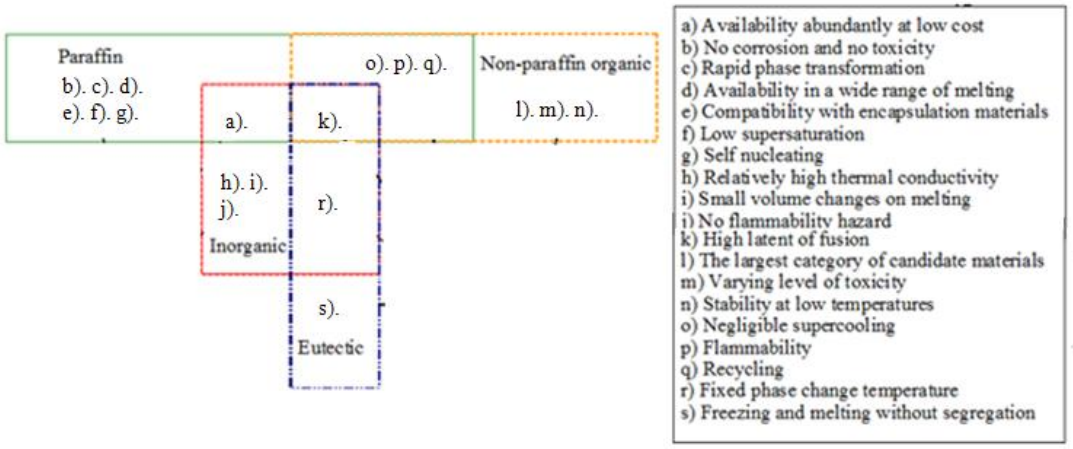

Figure 2- 4 Advantages of various materials used as PCMs

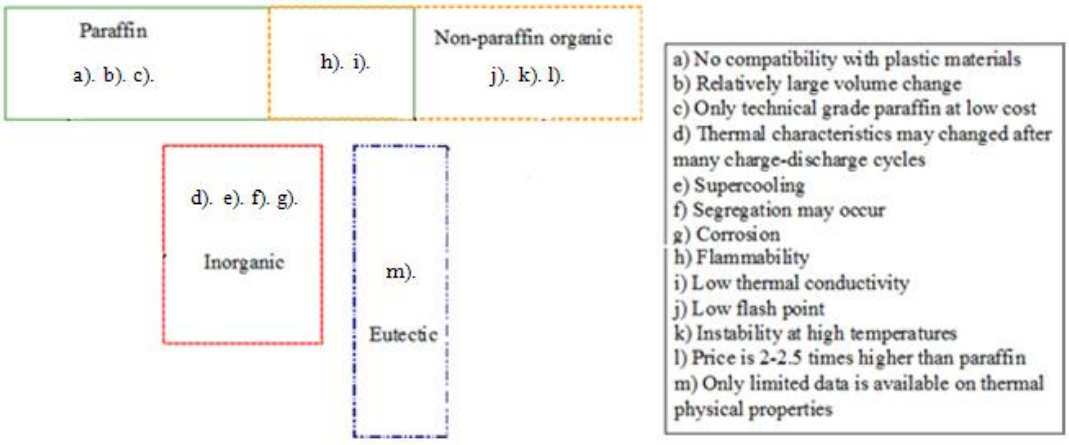

Figure 2- 5 Disadvantages of different kinds of PCMs

Table 2-1 presents some materials (organic, inorganic, and eutectics) that have been studied as PCMs for thermal energy storage. It can be seen that the organic PCMs have been mostly

researched for their feasibility as energy storage medium rather than inorganic and eutectic PCMs. About 70% of studies in Table 2-1 were carried out by using organic PCMs, and then followed by inorganic PCMs (21%) and eutectic PCMs (9%). This is due to that organic PCMs possess most of desired advantages among others, and meanwhile their main disadvantage of low thermal conductivity can be addressed easily by employing thermal conductivity enhancers (TCEs).

Table 2- 1 Groups of solid-liquid phase change materials

Type	Compound	Melting point (℃)	Heat of fusion (kJ/kg)	Reference
Organic	Paraffin wax	32.1	251	(Esen and Durmus,1998; Lv et al., 2006)
	Capric acid	32	152.7	(Sharma et al., 2005a; Dincer and Rosen, 2002; Tuncbilek et al., 2005)
	Lauric acid	41-43	211.6	(Sari and Kaygusuz, 2002; Sari, 2003a; Farid et al., 2004)
	Polyglycol E600	22	127.2	(Hawes et al., 1993)
	Butyl stearate	19	140	(Sari, 2005)
	Myristic acid	52.2	182.6	(Sharma et al., 2005b; Baran and Sari, 2003)
	Palmitic acid	57.8-61.8	185.4	(Sari,2003b; Feldman et al., 1986)
	1-Dodecanol	26	200	(Sari, 2005)
	Vinyl stearate	27-29	122	(Ghoneim, 1989)
	Medicinal acid	40-44	146	(Zalba et al., 2004)
	Paraffin $C_{16} - C_{18}$	20-22	152	(Naumann and Emons, 1989)
Inorganic	$Na_2SO_4 \cdot 10H_2O$	32,39	180,251	(Ghoneim, 1989; Naumann and Emons, 1989)
	$Mg(NO_3)_2 \cdot 6H_2O$	25.8	125.9	(Wada et al., 1984)
	$CaCl_2 \cdot 6H_2O$	29,29.9	190.8,187	(Zivkovic and Fujii,2001; Lane, 1980)
Eutectic	$48\%CaCl_2 + 4.3\%NaCl +$	26.8	188	(Abhat, 1983)
	$47\% Ca(NO_3)_2 \cdot 4H_2O$ $+53\% Mg(NO_3)_2 4H_2O$	30	136	(Abhat, 1983)
	60% $Na(CH_3COO) \cdot 3H_2O +$ $40\%CO(NH_2)_2$	30	200.5	(Li et al., 1993)

2.4 HEAT TRANSFER MECHANISMS

During the charging and discharging processes, the heat transfer mechanisms are conduction and convection. When PCMs are used to store thermal energy, pure conduction is treated as the mechanism leading the heat transfer in the PCM during the phase transformation processes (Ho and Chu, 1996; Costa et al., 1998; Khodadadi and Zhang, 2001). However, some researchers persist that natural convection plays a major role in the phase change process especially in the melt region. Hasan (Hasan, 1994) concluded that the convection heat transfer plays an important role in the melting process, and a simplified model by only considering the conduction heat transfer does not describe the melting process properly. Lacroix and Duong (Lacroix and Duong, 1998) reported the similar findings that natural convection is the main heat transfer process during the melting process. Velraj et al (Velraj et al, 1999) obtained the same conclusion in their research and reported that during the melting process natural convection occurs in the melt layer which results in the increase in heat transfer rate in comparison to the solidification process. Buddhi et al (Buddhi et al, 1988) proposed an explanation for this phenomenon that the densities' differences between the solid and liquid phases induce the buoyancy, which causes the convective motions in the liquid phase. However, Zhang and Yi (Zhang and Yi, 1999) believed that with the solid PCM melting into liquid, the PCM volume kept increasing, which result in the convection becoming the predominant heat transfer mechanism rather than conduction.

Contrary to melting process, during solidification process natural convection is believed that it exists only in the beginning, as the time elapses natural convection diminishes (Lamberg, 2004). Stritih (Stritih, 2004) indicated that the analytical result (conduction based) of solidification process showed a good agreement with experimental result. They concluded that solidification process can be modelled only by conduction. Similar conclusion was made by Ettouney et al. they found that though natural convection exists in the liquid PCM at earlier stage, it becomes negligible rapidly as the solidification progresses and the process becomes conduction dominated as the liquid volume of PCM becomes smaller and smaller (Ettouney et al., 2005; Ettouney et al., 2004). Many studies have proved that in all configurations of LHS, the PCM solidifies from heat transfer surface during solidification process and the solidified layers remain parallel to it.

2.5 NUMERICAL SOLUTIONS FOR PHASE CHANGE PROBLEMS

The heat transfer during the phase change process started to be numerically solved by using either the effective heat capacity method or the enthalpy method since 1970s, and these two methods have been extensively used by researches (Comini et al., 1974; Sparrow et al., 1977; Voller and Cross, 1981; Date, 1991; Yao and Chait, 1993; Yener and Kakac, 2008;). Both of the two methods allow using the same governing equations for the two phases and avoid solving the melting front position.

2.5.1 Enthalpy-Based Methods

The existence of the nonlinear liquid – solid interface and the unknown location of the moving boundary are the two main challenges in simulating the phase change problems (Kim and Kaviani, 1990). In the enthalpy models, the enthalpy is used as a dependent variable value along with temperature. By introducing an enthalpy method, the phase-change problem becomes much simpler since the governing equations are the same for the two phases. The interface conditions are automatically achieved and a mushy region between the two phases is created. This mushy region avoids sharp discontinuities that may create some numerical instability. Hence, the enthalpy methods are most attractive and commonly used to handle phase change problems. Hunter (Hunter and Kuttler, 1989) confirmed that the enthalpy method is most suitable for typical applications, the reason for that is this method does not require explicit treatment of the conditions on the phase change boundary.

Enthalpy-based method can be illustrated by considering a one-dimensional heat conduction controlled phase transformation. For a phase change process, energy conservation can be expressed in terms of total volumetric enthalpy and temperature. This relationship between enthalpy and temperature is usually assumed to be a step function for isothermal phase change problems. Figure 2-6 shows the enthalpy–temperature curves for isothermal phase change.

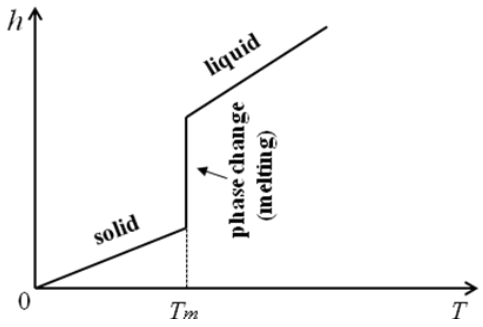

Figure 2- 6 Relationships between enthalpy and temperature for isothermal phase change

For isothermal phase change, the temperature and the total volumetric enthalpy can be expressed as follows (Sharma et al., 2009):

$$\frac{\partial H}{\partial t} = \nabla[k(\nabla T)] \tag{2.5}$$

Where the total volumetric enthalpy H is the sum of sensible and latent heat, and can be expressed in terms of temperature of the PCM as follows:

$$H(T) = h(T) + \rho_l f(T) f \tag{2.6}$$

The first term on the right side of equation 2.6 accounts for the sensible heat of the PCM while the second term accounts for the latent heat of the PCM.
And where

$$h(T) = \int_{T_m}^{T} \rho c \, dT \tag{2.7}$$

To be able to calculate the total enthalpy, the liquid fraction f is given as follows:

$$f = \begin{cases} 0 & T < T_m \quad solid \\ ]0,1[& T = T_m \quad mushy \\ 1 & T = T_m \quad liquid \end{cases} \tag{2.8}$$

Integrating the equations 2.6 and 2.7, an alternate form of equation 2.5 for one-dimensional heat transfer in the PCM was obtained:

$$\frac{\partial h(T)}{\partial t} = \frac{\partial}{\partial x}\left(\alpha \frac{\partial h(T)}{\partial x}\right) - \rho_l \, k \frac{\partial f}{\partial t} \tag{2.9}$$

Where α is the thermal diffusivity.

2.5.2 Effective Heat Capacity Method

The effective heat capacity method is also a common method used in modelling phase change problems except for the enthalpy method. The effective heat capacity method was first proposed in by Tihonov and Samarskii (Tihonov and Samarskii, 1953) and Albasiny (Albasiny, 1956). In the effective heat capacity method, the latent heat is approximated by a large effective heat capacity over the phase change temperature interval, (T_2-T_1) (Peippo et al., 1991). The effective heat capacity of the PCM (c_{eff}) is directly proportional to the energy stored and released during the phase change process but inversely proportional to the interval of the melting or solidification temperature range. During the phase change process the heat capacity of the PCM is

$$c_{eff} = h_f/(T_2 - T_1) + c_s \tag{2.10}$$

Where T_1 is the temperature when PCM begins melting or solidification, and T_2 is the temperature when the PCM is totally melted or solidified. The following is a definition of the effective heat capacity for each phase change period.

$$c_{eff} = \begin{cases} c_s & T < T_1 \quad \text{solid} \\ h_f/(T_2 - T_1) + c_s & T_1 \le T \le T_2 \quad \text{mushy} \\ c_l & T > T_2 \quad \text{liquid} \end{cases} \tag{2.11}$$

In terms of the definition of the effective heat capacity, the energy equation for one dimension can be written as follows:

$$\rho c_{eff} \frac{\partial T}{\partial t} = k \frac{\partial^2 T}{\partial x^2} \quad (2.12)$$

2.6 PHASE CHANGE MATERIAL SELECTION CRITERIA

In order to determine a suitable PCM for LHS, a list of selection criteria was compiled. The main criteria that govern the selection of PCM are (Lane, 1983; Abhat, 1983):

Thermophysical properties

i) Melting temperature in the desired operating temperature range (temperature range of application).
ii) High latent heat of fusion per unit mass to store a given amount of energy with a smaller mass.
iii) High specific heat capacity to provide additional significant sensible heat storage.
iv) High thermal conductivity of both solid and liquid phases, so that the temperature gradients for charging and discharging are small.
v) Small volume changes during phase transition, so that a simple container and heat exchanger geometry can be used.
vi) Congruent melting of the phase change material for a constant storage capacity of the material with each freezing/melting cycle.

Kinetic properties

i) High nucleation rate to avoid super cooling of the liquid phase.
ii) High rate of crystal growth, so that the system can meet demand of heat recovery from the storage system.
iii) Chemical properties.
iv) Complete reversible freezing/melting cycle.
v) No degradation after a large number of freezing/melting cycles.
vi) No corrosiveness to the construction materials.
vii) Non-toxic, non-flammable and non-explosive material for safety.

Economic properties

Available in large quantities at low cost

No single material can have all the optimal characteristics required for a PCM, as each of them has their advantages and disadvantages, which must be balanced out. The understanding of PCM behavior such as the heat exchange processes especially the melting and solidification processes and the techniques available to deal with problems associated with the various PCMs, are required in order to select the correct PCM.

2.7 ENCAPSULATION OF PCM

Efficient and reliable thermal storage systems are an important requirement for many applications due to the non-coincidence of heat demand and supply or availability. Once the proper PCM has been selected based primarily on the temperature range of application, the next most important factors to consider are (Garg et al., 1985a):

(i). The geometry of the PCM container and the container should meet the requirements of strength, flexibility, corrosion resistance and thermal stability for a given amount of PCM.
(ii). Protecting the PCM from harmful interaction with the environment.
(iii).Providing sufficient surface for heat transfer.

Each of these factors has a direct influence on the heat transfer characteristics in the PCM and ultimately affects the melting time and performance of the PCM storage unit. In order to ensure long-term thermal performance of LHS, the size and shape of the container must correspond to the melting time of the PCM and the daily isolation at a given location. Advantages of different geometries of PCM encapsulation with different materials and their compatibility was discussed by Lane (Lane, 1986). In general, encapsulation results in the following three advantages: a) the physical and chemical stability of the latent heat material is improved, b) the rate of heat transfer is increased and c) a self-supporting structure for the PCM is provided. There are two principal methods of encapsulation: macroencapsulation and microencapsulation.

2.7.1 Macroencapsulation

The technology with PCMs encapsulated in a container, for example, tubes, spheres or panels, is called macroencapsulation in which a significant quantity of PCM is encapsulated in a discrete unit. With macro-encapsulated PCMs, the leakage problem can be avoided and the function of the construction structure can be little affected. Macro-encapsulation is the most common form of PCM encapsulation and is the most suited to domestic applications (Regin et al., 2008). The shape of macro-capsules can be rectangular panels, spheres or cylinders. The rectangular and cylindrical containers are commonly employed as PCM containers (Agyenim et al., 2010). Figure 2-7 presents the schematics of the basic modes of cylindrical and rectangular PCM containers.

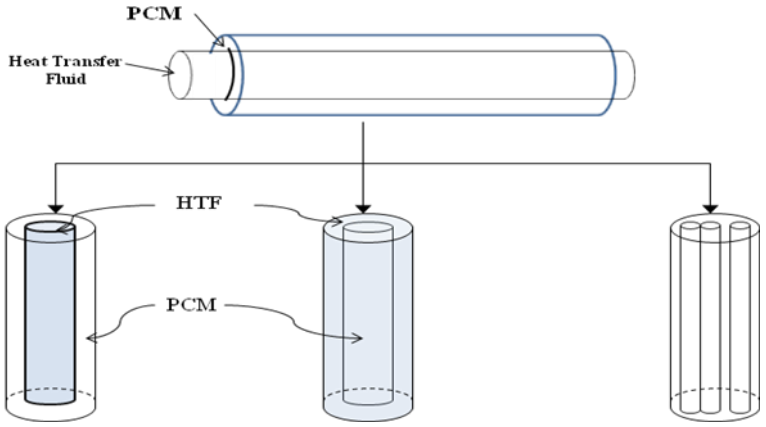

(a)Pipe model (b) Cylinder model (c) Shell and tube model

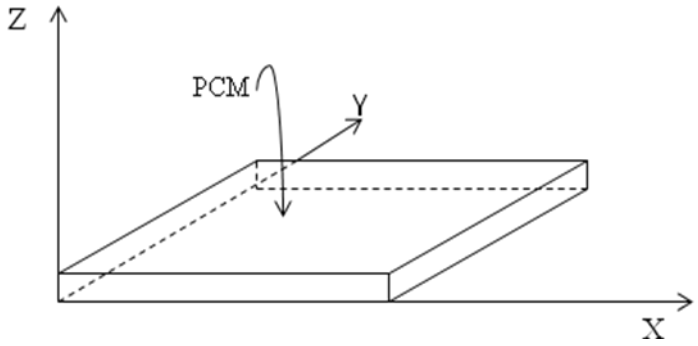

(d) Rectangular or slab container

Figure 2- 7 Schematics of the basic modes of cylindrical and rectangular PCM containers

2.7.2 Microencapsulation

Microencapsulation refers to techniques in which a large number of small PCM particles are contained within a sealed, continuous matrix, such as small, spherical or rod-shaped particles. There are many advantages of microencapsulated PCMs: a) increasing heat transfer area, b) reducing PCMs interaction with the outside environment, c) controlling the changes in the PCM volume as phase change occurs (Stark, 1990). Many previous experiments with large volume containment or macro-encapsulation failed due to the poor conductivity of the PCM. When it was time to release the heat from the liquid phase, the PCM solidified around the heat transfer area, and prevented effective heat transfer. However for microencapsulation, the dimensions are so small that this effect does not occur. Some studies have been carried out on microencapsulated PCMs combined with different shell materials (Hawlader, et al., 2003; Alkan et al., 2009; Cabeza et al., 2007). Presently the cost of the microencapsulation is high compared to other storage methods. However, many researchers still believe that the development of microencapsulated PCMs could be a milestone for space heating and cooling technologies (Mulligan et al., 1996).

2.7.3. Incorporation PCMs into Building Materials

Incorporation of PCMs into the building materials can meet the demand for thermal comfort and energy conservation purpose (Soaresa et al., 2013). Particularly the use of PCMs in thermally lightweight construction has been seen as a way of introducing thermal mass without the weight or bulk normally associated with conventional thermal storage mediums, such as concrete or brick (Ip and Gates, 2001). The PCM integrated building wall is most commonly studied and concerned due to its relatively more effective heat exchange area and more convenient implementation.

The three major traditional methods of incorporating PCMs in the conventional construction materials were direct incorporation and immersion (Hawes et al., 1993).

i) Direct incorporation. It is the simplest method in which liquid or powdered PCMs are directly added to building materials such as gypsum, concrete or plaster during production. No extra equipment is needed in this method but leakage and incompatibility with construction materials are the biggest problems.

ii) Immersion. It is technologies in which the building structure components, such as gypsum, brick or concrete, are dipped into melted PCMs and then absorb PCMs into their internal pores with the help of capillary elevation. While some researchers pointed out this method may have a leakage problem which is not good for long-term use. Direct incorporation and immersion have different operation processes, but they both incorporate PCMs directly in conventional construction materials.

Encapsulation: comprises the inclusion of PCM in a high molecular weight polyrneric film (capsule) which is mixed with other components of building materials. With encapsulated PCMs, the leakage problem can be avoided and the function of the construction structure can be less affected. It has the disadvantages of poor thermal conductivity and the solidification tendency at the edges.

A major advantage with incorporating PCMs in building materials is that they would become part of the building, which has cost implication and space constraints are not an issue as with bulk storage (Dincer and Dost, 1996). Furthermore, the thermal storage capacity of the incorporated PCM building materials has been investigated by Kaassinen (Kaassinen, 1992), who found that in comparison with untreated building materials, the thermal storage capacity of treated building materials increased by a factor of 15 in gypsum wallboard, 5 in timber, 32 in porous wallboard, 9 in wood particle board, 8 in cellular concrete and 3 in brick. However, this is still very small in comparison to the storage capacity offered by macro-encapsulation, and this can be a major drawback if the design load is high. Furthermore once incorporated within the structure or fabric of the building, PCMs become difficult or impossible to remove, unless the PCM decomposes or the building is rebuilt.

2.7.4. Compatibility of PCM with the encapsulation material

The compatibility of PCM with the encapsulated material is of great significance, since this affects the life of the storage system. Generally, salt hydrates are compatible with plastics whereas organic materials are compatible with metals but can cause some plastics to become soft, which allows the PCM to migrate through them during phase change process. Stainless steel is compatible with many PCMs in both groups. Venkatasetty (Venkatasetty, 1975) conducted a few studies on the compatibility of PCMs from the view point of corrosion to containment. Heine and Abhat (Heine and Abhat, 1978) carried out a detailed investigation on the compatibility of candidate PCMs with the metals. The results indicated that organic

materials are compatible with the metals. Stainless steel was found to be compatible with all PCMs tested. Ghoneim et al (Ghoneim, 1989) found that a potential problem with incorporating PCM into some cementious products is that some organic PCMs react with the products of hydration. When PCM is introduced to concrete it can reduce its compressive strength dramatically, unless extra cement is added to provide a stronger mix, which has cost implications (Salyer and Sircar, 1997).

2.8 THERMAL CONDUCTIVITY ENHANCERs (TCEs)

Although the solid-liquid PCMs offer much higher energy density, the low conductivity of the PCMs limits the potential applications of LHS systems in practical applications. All the conventional PCMs—both organic and inorganic possess very low thermal conductivity ranging from 0.1 - 0.6 W/m K (Jegadheeswaran and Pohekar, 2009). Thus, the surface heat flux decreases due to the increasing thermal resistance of the growing layer of molten or solidified PCM during the phase change process. The problem arises especially in solidification process where the sole heat transfer mechnism is conduction. PCM solidifies on the heat transfer surface and acts as a self-insulator because of low thermal conductivity. Therefore effective heat transfer enhancement methods for the liquid- solid phase change are the key issue, and various methods for PCM thermal conductivity enhancement have been proposed and studied by a number of researchers.

Heat transfer enhancement methods in LHS can be summarized to the following categories:

i) Using microencapsulated PCM (Sari et al., 2009).
ii) Dispersion of high conductivity particles or lessing rings (Jegadheeswaran and Pohekar, 2010).
iii) Using PCM graphite or concrete composite material (Sari and Karaipekli, 2007).
iv) Using extended surfaces such as finned structures or heat pipes (Robak et al., 2011; Shabgard et al., 2010; Lacroix and Benmadda, 1997; Lacroix and Benmadda, 1998; Huang et al., 2004; Shatikian et al., 2005; Akhilesh et al., 2005).

Figure 2-8 shows the pictures and drawings of some of the common heat transfer enhancement techniques mentioned above.

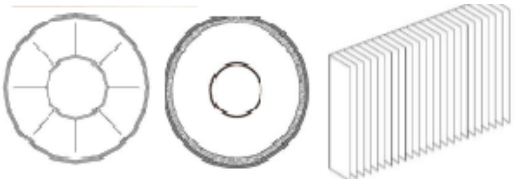

(a) Finned structures: longitudinal or axial fins, circular fins and straight fin

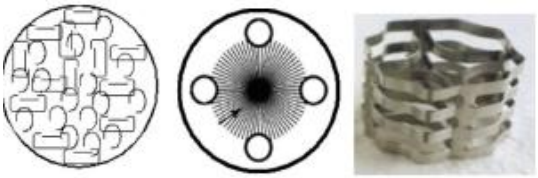

(b) metal rings, carbon brushes and metal matrix

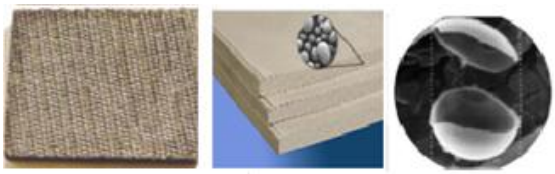

(c) PCM – graphite, gypsum wall – PCM and microencapsulation

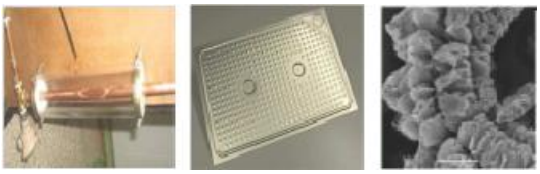

(d) heat pipes, compact flat panel and graphite flakes

Figure 2- 8 A summary of various TCEs techniques

It has proven that the phase change rate (melting/solidification) can be considerably increased by using these thermal conductivity enhancement methods summarised. In general, however, adding TCEs into PCMs may result in loss of storage capacity of LHS system. The loss in storage capacity limits the mass/ volume fraction of TCEs. Therefore it is important to estimate the optimum mass/volume fraction of TCEs, while employing such additives.

2.9 BUILDING APPLICATIONS

The incorporation of PCMs for thermal storage in buildings is one of the first applications studied (Belén et al., 2003). The first application of PCMs is used for heating and cooling in

buildings (Telkes, 1975; Lane, 1986). In the literature, the PCM-building material components are mainly to enhance the thermal energy storage capacity of standard gypsum wallboard and concrete blocks, with particular interest in peak load shifting and solar energy utilization.

2.9.1 PCM Wallboards

The PCM wallboards are believed to be a cheap and effective alternative solution of the conventional building walls, in which the PCM is imbedded into the concrete or gypsum board and other building structures. The thermal characteristics of PCM wallboard are very close to those of PCMs alone (Athienitis et al., 1997). Figure 2-9 shows a schematic program of a lightweight wall equipped with micro-capsulated PCM. Scalat et al. (Scalat et al., 1996) conducted an investigation on a full scale room with PCM wallboard. The results were compared with those obtained from a similar room lined with ordinary wallboard and showed that the PCM wallboard could maintain room temperature within the thermal comfort zone for longer time after the heating or cooling system was turned off. A full-scale experimental investigation on a new PCM wallboard material was carried out by Kuznik et al. (Kuznik et al., 2008). The purpose of this new wall was to enhance the thermal storage capacity of light weight building internal partition wall. Their experiment indicated that the PCM wallboard can reduce the room air temperature fluctuations and enhance the natural convection mixing of the air to avoid uncomfortable thermal stratifications.

Figure 2- 9 Schematic view of a lightweight wall with microencapsulated PCM (Scalat et al., 1996)

2.9.2 Under-Floors and Ceilings for Heating and Cooling

Floor and ceiling are also the two important parts of a building, which are utilised for heating and cooling of buildings. Floor heating systems are better than conventional radiators due to the fact that they may provide a more comfortable indoor environment, and they save living and working space since it is integrated into the building envelope. Thermal mass can be integrated with a floor heating system for off-peak thermal energy storage. As PCM can provide large latent heat storage capacity over a narrow melting temperature range, thus it can improve the thermal comfort level in buildings. Figure 2-10 describes a schematic view of an under-floor electric heating system with shape-stabilized PCM plates (Lin et al., 2004). This system can charge heat by using cheap nighttime electricity and discharge the heat stored at daytime. The study indicated that this heating system can work well in ordinary buildings and really has good application feasibility.

Pasupathy and Velraj (Pasupathy and Velraj, 2008) studied the thermal performance of a PCM integrated roof system. In the roof system, a stainless steel panel with PCM was placed between the roof top slab and the bottom concrete slab, which forms the roof of the room. The integrated PCM stores heat from the sun and releases it to the ambient air and to the air inside the room during the charging processes (sunshine hours and night hours). This cycle continues every day. They suggested and recommended a double layer PCM to be incorporated in the roof to narrow indoor air temperature swing and to better suit for all seasons.

Figure 2- 10 Schematic of under-floor electric heating system with shape-stabilized PCM plates (Lin et al., 2004)

Kondo and Iwamoto (Kondo and Iwamoto, 2002) examined the effects of a rock wool PCM ceiling board with micro-capsulated PCM for an office building. The outline of this ceiling board system is shown in Figure 2-11. They found that the reduced use of maximum-charge electricity during the peak shaving time and the use of cheaper-rate nighttime electricity results in lower energy costs, and they also suggested the ceiling board needed improvement because of the flammability.

Figure 2- 11 Outline of the ceiling board system (Kondo and Iwamoto, 2002)

2.9.3 PCM Shutter

In this concept of PCM shutter, the PCM shutter is placed on the outside of window. During daytime they are opened to the outside the exterior side is exposed to solar radiation, the room temperature is hence reduced. At night the shutter is closed, and heat from the PCM radiates into the rooms. Mehling (Mehling, 2004) firstly presented his project report at 8th Expert Meeting and Work Shop on the ‘‘Innovative PCM Technologies’’ and suggested to use of the PCM shutter with windows. The photograph of PCM shutter is shown in Figure 2-12. His investigation showed that the maximum shading temperature could be delayed by 3h and room temperature was reduced by 2 ℃ with the application of this PCM shutter.

Figure 2- 12 PCM shutter (Mehling, 2004)

2.9.4 PCM Solar Walls

Experimental and numerical investigations have been carried out to study the effect of PCM solar walls (Swet, 1980; Ghoneim et al., 1991). For a given amount of solar energy, as mentioned previously, the PCMs require less space than massive walls and are much lighter in weight, which make them much convenient in solar wall application.

In order to gain an understanding of how a latent heat storage unit can help to improve thermal performance of an ordinary solar wall, Bourdeau (Bourdeau, 1980) carried out a comparison between masonry wall and a PCM wall. The calcium chloride hexahydrate (melting temperature 29. 8 ℃) used as a phase change material. He found that an 8.1 cm PCM wall had slightly better thermal performance than that for a 40-cm thick masonry wall. Chandra et al (Chandra et al., 1985) investigated the reliability of the PCM solar wall by using experimental and numerical methods. They also concluded that PCM solar wall with smaller thickness was more desirable in comparison to an ordinary masonry wall for providing efficient thermal energy storage. Knowler (Knowler, 1983) used commercial grade paraffin wax with metallic TCEs for enhancing the overall conductivity and efficiency of the Trombe wall. Stritih and Novak (Stritih and Novak, 1996) developed a numerical model of a PCM solar wall for building heating. In their study, a black paraffin wax (melting temperature 25–30.8 ℃) was used to store solar energy, and then the stored heat was used to heat the air for the ventilation. The efficiency of the absorption was evaluated to be 79%. The result of the simulation showed that the melting temperature of the PCM has an important influence on the outlet air temperature. They concluded that the optimum thickness of the

PCM wall is 50 mm and the melting temperature is a few degrees higher than the room temperature for the heating season given.

Gracia et al (Gracia et al., 2013) experimentally tested the thermal performance of a double skin façade (DSF) with PCM. The PCM used in this study was salt hydrate SP-22 from Rubitherm. This PCM (melting temperature 22 ◦C) allows the system to store large quantities of solar energy during winter periods, and to be used as a cold storage system during summer periods. The configuration of the DSF is illustrated in Figure 2-13. The experimental results indicated that the use of the PCM DSF significantly improved the thermal performance of the whole building under free floating conditions and reduced significantly the electrical consumption of the HVAC systems. Moreover, they also concluded that the phase change temperature of the SP-22 is very low (20 ◦C) during the solidification process, thus the use of this PCM did not show any thermal benefits in this system and only in some operational modes, a part of the stored latent heat is injected to the indoor environment.

Figure 2- 13 Experimental set-up: reference and ventilated facade cubicles (Gracia et al., 2013)

The studies mentioned above have shown that buildings might benefit from using PCMs to solar walls for heating. Its energy saving potential and the potential contribution to improved thermal comfort has been indicated by using either numerical simulation or experimental work. There are, however, still some problems for wide application of this kind of solar wall. At present there are only a few demonstration systems in use and limited experimental data collected from testing in a real situation, particularly there is a real lack of research for cooling performance in this area.

2.10 CONCLUSIONS

Two common thermal storage methods of sensible heat storage and latent heat storage used for heating and cooling of buildings have been discussed in this chapter. The latent heat storage was highlighted here, as it possesses a number of advantages over sensible heat storage. The most valuable of merits of latent heat storage are its high energy storage density, which can reduce the size of the thermal storage unit and the isothermal nature in which the energy is stored and released at a nearly constant temperature. These special characteristics make the latent heat storage ideal for space heating and cooling applications.

The review revealed that PCMs can be summarized as follows: solid - gas, liquid - gas, solid - solid and solid - liquid PCMs. The majority of research involved latent heat storage focused on solid to liquid PCMs, as they have the greatest practicable potential for spacing heating and cooling applications. To gain a clear insight of heat transfer characteristics in PCMs is very important to design any latent heat storage unit. Heat conduction and natural convection are believed to be two main mechanisms that control the heat transfer process during melting and solidification processes. The two most common kinds of solid to liquid PCMs are inorganic and organic PCMs. However, the research suggested that organic PCMs are better than inorganic PCMs, though their thermal conductivities are lower than those of inorganic PCMs.

Containment is required for all categories of solid to liquid PCMs in order to operate. Two common types of containerisation were identified, macro-encapsulation and microencapsulation. It was found that macro-encapsulation offer the greatest scope, as macro-encapsulation could contain a significant amount of PCM and address the self-insulating problem through careful design of the container. Though microencapsulation is preferable to incorporate into building materials, it was found that the PCM weight is quite low in these applications, and the cost is high.

The application of PCMs in buildings, e.g., solar wall, wallboards, shutters, and under floor and ceiling heating systems has been subject of considerable interest. Potential application of solar wall has been explored. Most of the studies on solar wall however are still in their initial stages. The existing performance data of such a system is very limited, particularly in cooling applications.

The present work attempts to address the above problems by collecting comprehensive performance data from a full scale system and developing suitable models. The models can then be used to analyse the characteristics and thermal performance of such a system.

3. DESIGN AND DEVELOPMENT OF A PHASE CHANGE THERMAL STORAGE SYSTEM

3.1 INTRODUCTION

Chapter two summarised the potential materials that can be used as PCMs for thermal energy storage applications, and highlighted the potential of the latent heat heating and cooling systems for energy savings in buildings. The selection of a suitable PCM is one of the key aspects that may affect significantly the thermal performance of the system. It is necessary thus to conduct a comprehensive study on the selection of the potential PCMs based on the purpose of application.

In this Chapter, a selection criterion of the PCMs for the proposed system is developed, a detailed mathematical model for calculating the quantity of the candidate PCM is presented. The quantity of PCM under this study is determined for the maximum solar radiation of a specific location. Experimental validation of the model is carried out by using a simple small scale experimental rig, besides that, the experimental rig is also used to explore the charging and discharging characteristics of the PCM selected and to evaluate the thermal performance of the thermal storage system with different TCEs.

3.2 PHASE CHANGE MATERIAL SELECTION

Selection of a suitable PCM is critical in designing a space LHS system. Some of required properties of candidate PCM for solar chimney application will be discussed below.

1) The influence of surface temperature on mass flow rate through a solar chimney is an important parameter as the rate of mass flow increases with the surface temperature rises (Bouchair, 1989). Hence, one of the most important criteria is to select PCM with a suitable melting temperature. For given climate condition, if the melting temperature is too high, the quantity of solar radiation energy stored by PCM is little. If the melting

temperature is too low, it is not able to create enough temperature gradient to drive the indoor air under cooling operation mode or keep the indoor air temperature at a comfortable level at night time under heating mode.

2) A high latent heat of fusion is essential to the candidate PCM, which means less quantity of the PCM is required to store a given amount of energy.

3) Thermal conductivity is another important parameter, with a high thermal conductivity the heat transfer coefficient is enhanced during charging and discharging. As a result, the problem of the PCM being a self-insulator is reduced greatly.

4) Thermal stability and no degradation over long term melting-freezing cycle is important as this ensures the whole system works efficiently over the working life. Maintenance and the performance of the system would be a problem, if the PCM intends to degrade over time.

5) A small volume change during phase change is desirable so a simple container and heat exchanger geometry can be used, and the PCM container would suffer less of a strain.

6) The PCM should show little or no super-cooling, as PCM does not discharge the stored heat at its melting temperature with supercooling.

The suitable PCMs will be determined by using these six selection criteria above, as previously mentioned, PCMs are classified into three kinds: solid-solid PCM, solid-gas or liquid-gas PCMs and solid-liquid PCMs. Solid-solid PCMs and solid-gas PCMs are firstly eliminated from consideration due to their own limitations. Solid –solid PCMs have certain attractive features such as: no or very small change in volume during phase transition, encapsulation is easy to design due to no potential leakage problems and they have high latent heats. Unfortunately, only very limited work on solid – solid transitions exists and there are only a number of such materials and most of them have very high phase transition temperatures, which are in the range of 43 ℃- 578 ℃ (Garg,1985). Solid – solid PCMs are thus not suitable for building applications. For solid-gas or liquid-gas, they are ruled out from the candidate PCMs just because of the complications in designing encapsulation due to the large change in volume and leakage problems.

Therefore, solid-liquid PCMs are the only potential option for the proposed system. Organic, inorganic and eutectics are three main kinds of PCMs, eutectics are eliminated firstly, as only limited data is available on thermo-physical properties of the eutectics, and the selected PCMs with any uncertain thermo-physical properties would significantly increase risk in the performance deterioration of the proposed system. Hence, the use of eutectics to a LHS is very new and a big challenge. It is clear that the potential PCMs selected would be from inorganic or organic PCMs. Inorganic PCMs and organic PCMs are selected herein for further consideration. Organic PCMs can basically be divided into paraffin and fatty acids (non-paraffin organics). Although fatty acids have high latent heat of fusion values comparable to those of paraffins, and have high thermal stability with no supercooling, these fatty acids are generally not preferred as heat storage materials, as they are more expensive than paraffins, and corrosion is their big disadvantage (Abhat, 1983). Paraffins and salt hydrates are of the representative organic PCMs and inorganic PCMs respectively considered herein as candidate PCMs. Extensive research has been carried out integrating these two kinds of PCMs with solar energy storage applications and published data of their thermophysical properties and performances are also available. Both paraffins and salt hydrates have high latent heat of fusion, for instance, sodium sulphate decahydrate ($Na_2SO_4 \cdot 10H_2O$) and calcium chloride hexahydrate ($CaCl_2\ 6H_2O$) the two most common forms of salt hydrate have a latent heat of fusion at 251.2 kJ/kg and 190.8 kJ/kg respectively (Lane,1986). The latent heat of fusion of paraffin wax can be as high as 269 kJ/ kg (Sharma et al., 2009).

Generally, salt hydrates have higher thermal conductivities (around 0.5 W/m K) than organic PCMs (only 0.2 W/m K), which are almost double of the paraffin's (Sharma et al., 2009). The poor thermal conductivity is a major problem with paraffin wax, which prolongs its charging and discharging processes. However, effective techniques to deal with this problem have been proposed and hence paraffins as thermal energy storage medium are not a problem.

The reliability and long term chemical stability of the PCMs are the most important issues for the practical applications of LHS, and therefore there should be no or little changes in melting temperature and latent heat of fusion after undergoing a great number of charging and discharging cycles. Shukla et al.(Shukla et al., 2008) carried out the thermal cycling tests to check the stability of some organic and inorganic PCMs. The experimental results indicated

that organic PCMs have better thermal stabilities than inorganic PCMs. This can be attributed to salt hydrates suffer from supercooling and phase segregation. Although supercooling can be considerably reduced by existing techniques, it must be noted that the more additives or additional techniques that are introduced to a LHS would decrease its thermal storage capacity and increase its cost. Hence the use of salt hydrates may still be unsuitable even the additives applied to inorganic PCMs (Abhat, 1983). Another major problem with salt hydrates is highly corrosive to metallic materials with salt hydrates the selection of the container materials would be severely restricted. Stainless steel is the only metal that would be compatible with salt hydrates. Paraffin wax is compatible with most metallic containers concerned.

The PCM that is selected for the proposed system is paraffin wax, and the most important factor that affects the selection is the reliability and long-term stability. The long term chemical stability is not in question for paraffin wax and in fact it is one of its major advantages. The melting temperature of PCM is also another important factor that would affect the PCM selection. Heating energy is the biggest slice of Britain's household energy use, and the energy use for heating increased by 17% in the past 40 years (Great Britain's housing energy fact file). Thus, the PCM selection emphasizes energy supply on heating, whilst taking into account the cooling energy. Generally speaking, PCMs with melting temperature between 20 ℃ and 65 ℃ are used / recommended for solar energy storage for cooling and heating in buildings (Regin et al., 2008; Feldman and Shapiro, et al., 1989; Tyagi and Buddhi, 2007). Stritih and Medved (Stritih and Medved, 1994) presented a solar heat storage wall with black paraffin wax, which is quite similar to the heating mode of the proposed system. In their study the paraffin wax with the melting temperature of 52 ℃ was used as the PCM, the stored heat in PCM was used for heating the air for the ventilation of the house. They found that due to the too high melting temperature of paraffin (52 ℃), resulting in the considerable heat lost to the air and the stored heat was insufficient for heating of air throughout the day. As a result, the proposed system is less practical value. And then in Stritih and Novak's another research, they found that the optimal melting temperature of PCM should be a few degrees higher than the room temperature, and the temperature range of 25 ℃ - 30 ℃ was chosen as the optimal melting temperature for their study (Stritih and Novak, 1996). To the best of author's knowledge, there are very few studies that carried out on incorporation of PCM with solar chimneys. Hence, there is no a selection criterion identified for solar chimney application in literature. A criterion was proposed here to assist

in selecting the PCMs for the proposed system: When the solar chimney operates in the passive heating mode, the outdoor air or indoor air flows into the chimney, and is heated up by the absorbed solar energy in PCM then returns to the room. The supply of warm air into the room contributes to maintain the thermal comfort for occupants. CIBSE recommends the figure of 21℃ as the average of all the upper winter operative temperature ranges (CBISE, 2008). Consequently the melting temperature of the potential PCMs should be above 21℃. The minimum melting temperature was determined here is 25℃ which is the same as Stritih and Novak's. Meanwhile, the melting temperature should not too high as well. This is because that higher melting temperature results in insufficient stored heat for heating of air. The maximum melting temperature of 45 ℃ is chosen herein. Therefore, the optimal melting temperature range of PCM for the proposed system is 25 ℃ - 45 ℃.

The phase change materials used in this study are paraffin RT 25 and paraffin RT 42, which are commercial organic PCM from Rubitherm GmbH Company. The commercial paraffin RT25 and RT 42 do not have a "sharp" melting temperature, and the relevant thermophysical properties of the paraffin RT 25 and RT 42 are listed in Table 3-1.

Table 3- 1 Thermo-physical properties of RT25 and RT 42 (http://www.rubitherm.de/english/index.htm)

Thermophaysical properties	Paraffin RT 25	Paraffin RT 42
Melting temperature [℃]	22-26	38-43
Thermal conductivity (k) [W/m ·℃]	Solid: 0.19	Solid: 0. 2
	Liquid:0.18	Liquid:0.2
Heat of fusion [kJ/kg]	148	174
Density (ρ) [kg/m^3]	Solid: 880	Solid: 880
	Liquid: 760	Liquid: 760
Specific heat (kJ/kg K)	Solid: 2.9	Solid: 1.8
	Liquid: 2.11	Liquid: 2.4

3.3 PCM CONTAINER MATERIALS

Successful utilization of liquid-solid PCM depends on developing the containment for any thermal energy storage applications. In some cases where the PCM cost is low, the cost of the containment can be one of the most expensive components of a LHS system. Some

prerequisites for PCM container selection are discussed below.

1) The compatibility of PCM with the container material
2) The physical strength of the container material
3) The cost of container construction

The compatibility of PCM with the container material is of great significance since it affects the design life of the storage system. Lane (Lane, 1980) found that in his study the organic PCMs can cause degradation, embrittlement and softening in some plastics, this may cause leakage problems during PCM's liquid phase. However, organic materials are compatible with metals.

The physical strength of the container material is another factor that may affect the design life of the storage system. Physical support must be provided by the container during the PCM is in liquid phase, due to the liquid PCM is incapable of supporting itself. It has also been mentioned previously, the liquid-solid PCMs generally exhibit a change in volume during their phase transitions. High strength of material can keep the container shape stable over years. The container must also be able to prevent the PCM leaking from the container, so the PCM containers should be carefully designed.

The type of the PCM selected would have direct influence on the choice of container material. Plastics are eliminated from the candidate materials as organic PCMs cause some plastics to soften, but any metal would be compatible with organic PCMs. The metals under consideration must possess high thermal conductivities and should be cheap and easy to be manufactured to reduce the overall cost of the LHS system. Three metallic materials of aluminium, copper and stainless steel are considered herein as candidates. Copper is ruled out firstly, due to its extremely expensive compared to the other two metals. For a sheet of 1000 ×1000×1.5 mm, the price of the copper is £860, whilst stainless steel and aluminium are just £90 and £26 (http://www.metals4u.co.uk/). Aluminium has a better "strength to weight" ratio means that it is not as strong as stainless steel and copper, and is generally more corrosion resistant than all other metals, except the stainless steels. Aluminium is fairly soft, whereas stainless steel is stronger than aluminium if weight is not a consideration. During the phase change transition, container surface would be thicker to handle the same pressure if it was made of aluminium, so in this case it would be cheaper by using stainless steel. Stainless steel

is easy to weld, however welding aluminium is very difficult. Aluminium is thus eliminated from the candidate metals, and stainless steel is selected for the current study.

3.4 PCM CONTAINER CONFIGURATION

The melting time of the encapsulated PCM is one of crucial parameters to size and shape the container, as it must match to the total daily radiation (Saldivar, 2005). As discussed in Chapter two, rectangular geometry is one of most common encapsulation methods as it is possible to achieve more surface area per unit volume of PCM container with low PCM thickness for reducing the solidification time (Raj and Velraj, 2010). Zivkovic and Fujii (Zivkovic and Fujii, 2001) numerically investigated the thermal performances of rectangular and cylindrical containers. The melting time for the two containers was compared, and their results showed that a rectangular container requires as half of the melting time as that of a cylindrical one of the same volume and heat transfer area. Although the charging/ discharging times depend on the specific conditions of the system application, in this study, faster rate of charging and discharging processes of the system is required. For this reason the rectangular geometry is chosen for the current research.

3.5 NUMERICAL AND EXPERIMENTAL ANALYSIS OF THE CANDIDATE PCMS

The proposed system containing PCM allows it to operate during the night and cloudy days, when there is low or no solar radiation. However, the performance of the solar chimney varies significantly with the solar energy stored in PCM. Once the candidate PCMs has been selected, the next most important factor should be the determination of the PCM container dimensions under the specific weather conditions.

The volume of PCM container should allow storing total amount of daily solar energy to achieve the maximum efficiency. Hence, the time taken for the whole PCM to melt is one of the crucial factors for design of a thermal storage system. To be specific, the container containing PCM should be designed in such a way that at the end of the day, complete melting of the PCM is achieved. In that way, the maximum efficiency of the LHS unit is achieved. Besides, the discharging rate of the heat stored in PCM is another important aspect of the system's efficiency. Therefore any passive energy storage system should ensure that the PCM is given the opportunity to discharge adequately before the next charge cycle. A

numerical model is developed to determine the thickness of PCM container and is validated with a small scale experimental rig designed for this purpose. Prior to testing the performance of the solar chimney containing PCM, the small scale experimental rig is used for two purposes: 1) to validate numerical results and 2) to investigate the melting and freezing characteristics of PCMs selected.

3.5.1 Determination of PCM Container Dimensions

In this project a mathematical model is developed to provide a tool to determine the container dimensions under London-like weather conditions. London–like weather conditions will be the basis for investigation of the thermal performance of the proposed system in this project. The total energy stored in a LHS unit is a complex function of the PCM and weather data (the volume of the PCM, the physical properties of the PCM, specially the melting temperature of the PCM and the solar irradiance data).

Melting temperature of the PCM in the simulation

Application of the actual melting temperature of the PCM to numerical modelling is essential, since any calculations on the thermal storage capacity of the PCM rely on the melting temperature of the PCM, as the melting temperature is the parameter to identify the energy that is sensible heat or latent heat. If the assumed melting point is wrong then the energy stored in PCM may overestimated or underestimated. The thermophysical properties of PCMs selected from the manufacturer's data are employed to the numerical study, and experimentation is further used to establish the actual thermophysical characteristics of the PCMs.

The source of heat

Regarding the solar radiation data, a long term historic daily mean data is used as the basis for calculating the maximum amount of the PCM instead of measuring the actual solar radiation. This is because a long historic solar irradiation data can obtain a far more realistic result. A long term solar radiation data for London area is used for this current research (see Appendix 1). The solar radiation data of each month over south vertical surface for London area is presented in Figure 3-1.

Figure 3- 1 Long term daily profile of solar radiation incident on south vertical surface (CBISE, 2008)

The storage capacity of the LHS is defined as the maximum solar energy that can be stored in the unit. It can be seen from Figure 3-1 that the maximum solar radiation occurs on 4th Oct, which is selected to calculate the amounts of the PCMs to utilization of solar energy adequately.

3.5.1.1 Description of the closed mode of the proposed system

There are two different operation modes are considered: 1) Closed mode. Generally, the residential building is not occupied, and the indoor temperature is high enough to maintain the indoor thermal comfort when the solar energy available, the chimney is closed there is no air flow in the air channel so as to maximize the store of the solar energy. 2) Open mode. When heating is required, the chimney is open and then air flow occurs. Hence, the PCM should melt within the time of the chimney closes.

When the chimney is operated in closed mode, the vents are closed, so the chimney consists of four components presented in Figure 3-2: 1) the glazing which allows the solar radiation to pass through glazing and prevents the convective heat transfer during discharging process; 2) a closed air channel in where the air treated as a insulation layer; 3) the encapsulated PCM (paraffin wax) in a rectangular container made of stainless steel; 4) thermal insulator which minimizes the effect of lateral heat transfer from the sides.

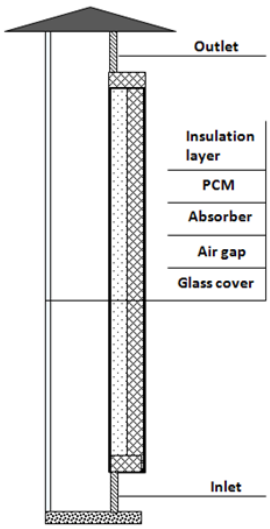

Figure 3- 2 Schematic diagram of the proposed system in closed mode

Numerical simulation is carried out to calculate the amount of the PCM for the proposed system based on the solar radiation data of a representative day, which is the maximum solar energy of the year. As mentioned above, there is no air flow occurs in the air channel during this period, and, hence, the numerical simulation result is independent of the chimney configuration. It just relies on the solar radiation data, the thermophysical properties of the PCM and the assumptions made to the numerical simulation.

Assumptions made for the theoretical model

- Mean hourly solar radiation is employed.
- The reflectance and absorption of the radiant energy by the glazing, as well as its thermal capacity can be neglected.
- Heat transfer is assumed to be in the horizontal direction only.
- The PCM behaves ideally, i. e., such phenomena as property degradation and super-cooling are not accounted for.
- The PCM is homogeneous isotropic.
- Lateral and back sides of the rectangular container are well insulated.
- Heat transfer within the PCM is one – dimensional conduction controlled (the effects of natural convection within the melt zone can be ignored).

Analysis of heat transfer for each component

Energy balance equations are developed for each major component of the chimney in closed mode and are given as follows in details.

The glass

Energy transfer through the glass can be written as follows:

$$\frac{dT_g}{\Delta t}\rho_g C_g \delta_g A_g = \alpha_g q_s A_g + q_{p-g} A_g - q_{g-sky} A_g \quad (3.1)$$

Neglecting the absorption of radiant energy by the glass, as well as its thermal capacity, the left hand of the equation and the first term of the right hand above are equal to zero.

$$\frac{dT_g}{\Delta t}\rho_g C_g \delta_g A_g = 0 \quad (3.2)$$

$$\alpha_g q_g A_g = 0 \quad (3.3)$$

The equation 3.1 can be rewritten as follow:

$$q_{p-g} A_g - q_{g-sky} A_g = 0 \quad (3.4)$$

Where

$$q_{p-g} = U_{p-g}\,(T_p - T_g) \quad (3.5)$$

$$U_{p-g} = h_{r,p-g} + h_{c,p-g} \quad (3.6)$$

The radiative heat transfer coefficient between absorber plate and glass cover is (Ong, 2003):

$$h_{r,p-g} = \sigma\left(T_p^2 + T_g^2\right)(T_p + T_g)/(\xi_p^{-1} + \xi_g^{-1} - 1) \quad (3.7)$$

$$h_{c,p-g} = Nu\lambda_{air}/\delta_{air} \quad (3.8)$$

Where

$h_{r,p-g}$ – Radiative heat transfer coefficient between absorber and glass cover, $W/m^2 \cdot K$

$h_{c,p-g}$ – Convective heat transfer coefficient between absorber plate and glass cover, *W/*

$m^2 \cdot K$

ζ_p, ζ_g – Emittances of absorber plate and glass cover

λ_{air} – Thermal conductivity of air between glass cover and absorber, W/m $\cdot K$

δ_{air} , δ_g – Thicknesses of the air layer between glazing and absorber and glass cover, m

T_p, T_g – Temperatures of absorber plate and glass cover, *K*

t – Time, *s*

σ – Stefan–Boltzmann constant, $W/m^2 \cdot K^4$

ρ_g – Density of glass cover, kg/m^3

C_g – Specific heat of glass cover, *J/kg K*

α_g – Absorptivity of glass cover

q_s , q_{p-g} , q_{g-air} – Applied heat flux, heat flow rate transferred from absorber plate to glass cover, and heat flow rate transferred from glass cover to ambient, W/m^2

The Nusselt number is given by the following relation (Khoukhi and Maruyama, 2005)

$$Nu = [0.06 - 0.017(\theta/90)]Gr^{1/3} \quad (3.9)$$

θ represents the solar collector tilt angle in degrees.

The Prandtl number, Pr is included in the above equation and assumed to be independent of temperature and taken equal to 0.7 (Khoukhi and Maruyama, 2005).

The Grashoff number is given as:

$$Gr = g\beta(T_p - T_g)\delta_{air}^3/\upsilon^2 \quad (3.10)$$

where g is gravitational acceleration, m/s^2; β is volumetric thermal expansion coefficient (equal to approximately *1/T*, for ideal air, where *T* is absolute temperature), *1/K*.

$$q_{g-sky} = U_{g-sky}\,(T_g - T_a) \quad (3.11)$$

$$U_{g-sky} = h_{r,g-sky} + h_{c,g-sky} \quad (3.12)$$

The radiative heat transfer coefficient from the glass surface to the sky considering the ambient temperature is given as below (Ong, 2003):

$$h_{r,g-sky} = \sigma \xi_g (T_g + T_{sky})(T_g^2 + T_{sky}^2)(T_g - T_{sky})/(T_g - T_a) \quad (3.13)$$

$$h_{c,g-sky} = 5.7 + 3.8v \quad (3.14)$$

$$T_{sky} = 0.0552 T_a^{1.5} \quad (3.15)$$

where U_{p-g} includes the effects of radiative and convective heat losses, which can be calculated from equations 3.6 – 3.9 are described in (Khoukhi and Maruyama, 2005). The total heat transfer coefficient U_{g-sky} is calculated from equations 3.12 – 3.15 which are obtained from references (Ong, 2003). υ represents the kinematic viscosity, m^2/s.

The absorber plate

The absorber plate is made of a thin metal material with high thermal conductivity, and the heat balance for absorber plate is given as below.

$$\frac{dT_p}{\Delta t} \rho_p C_p \delta_p A = \tau_g \alpha_p q_s A - q_{p-g} A - q_{p-l} A \quad (3.16)$$

$$q_{p-l} = U_{p-l} (T_p - T_l) \quad (3.17)$$

$$U_{p-l} = 1/(\frac{1}{k_p} + \frac{\Delta \delta}{2k_l}) \quad (3.18)$$

Where

τ_g – Transmittance of glass cover, it is set to be 1

α_w – Absorptivity of absorber plate

q_{p-l} – Heat transfer rate transferred from absorber plate to PCM, W/m^2

U_{p-l} – Total heat transfer coefficient between absorber plate and PCM, $W/m^2 K$

k_p , k_l – Thermal conductivities of absorber plate and PCM, W/m ·*K*

δ_p, $\triangle\delta$ – Thicknesses of the absorber plate and each layer of PCM, m

Phase change material (PCM)

Effective heat capacity method

The PCM selected does not melt over a single temperature, but rather over a temperature range of $\Delta T_m = (T_2 - T_1)$. Since melting or freezing process of a PCM involves phase change, the thermal state of the PCM is affected not only by the sensible process but also by the latent process. In the effective heat capacity method, the latent heat is approximated by a large heat in sensible form over the phase change temperature interval, $(T_2 - T_1)$. Figure 3-3 shows the relation between the temperature of the PCM and its stored heat during melting or freezing processes.

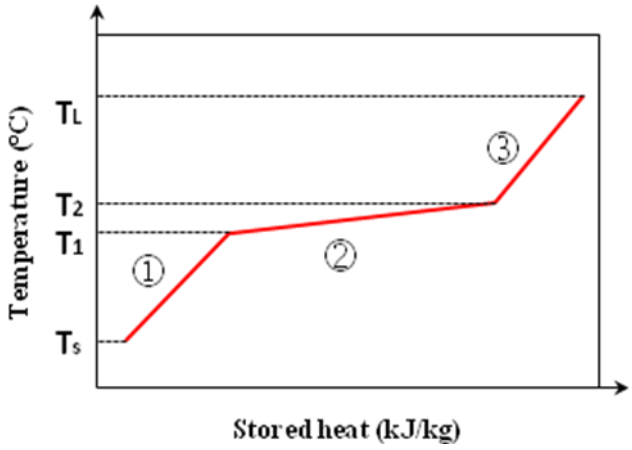

Figure 3- 3 Relationship of the temperature and the stored heat

It can be seen from Figure3-3 that any melting process involves a temperature rise in the solid zone (region 1), a slight increase in mushy temperature (region 2), and a rise in temperature in the liquid zone (region 3). T_1 is defined as the lower limit of the melting temperature range, and T_2 is the higher limit of the melting temperature range. During the phase change, the heat capacity of the PCM is given as follows:

$$C_{eff} = \frac{L}{T_2 - T_1} + C \qquad (3.19)$$

The phase change process of the PCM can be transformed into ‘‘single-phase’’ by using three equations (i.e. solid state, liquid state and mushy state). The following is a definition of the

effective heat capacity for each phase change period.

$$c_{eff} = \begin{cases} c_s & T < T_1 \quad solid \\ \frac{L}{T_2 - T_1} + c_s & T_1 \leq T \leq T_2 \quad mushy \\ c_l & T > T_2 \quad liquid \end{cases} \tag{3.20}$$

where

c_s – Specific heat of solid PCM, J/kg ·K

c_l – Specific heat of liquid PCM, J/kg ·K

In terms of the definition of the effective heat capacity, the heat transfer equation for one dimension can be written as follows:

$$\rho c_{eff} \frac{\partial T}{\partial t} = k \frac{\partial^2 T}{\partial x^2} \tag{3.21}$$

Thermal analysis and calculation method

The PCM is encapsulated by a metallic container, and the absorber plate serves as heat exchanger, good thermal contact between the PCM and the container is assumed, for simplicity, in the present analysis, the change of density with phase change is neglected, and the density of the liquid is used throughout.

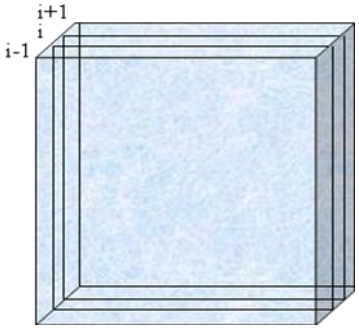

Figure 3- 4 Schematic diagram of the PCM container and the control volume

Finite-difference method is applied in this numerical simulation. As shown in Figure 3-4, the PCM container is divided to n cells along the thickness of the container, each step is selected at $\Delta\delta$=1 mm. There hence are $n=\delta/1$ cells in the numerical simulation, where δ is the

thickness of the container. The number of cells changes with the thickness of the PCM. The initial thickness of the container is 1 mm if the PCM temperature exceeds 43 ℃, the thickness increases at the interval of 1 mm until the PCM reduces to 43 ℃, and this thickness is the desirable one for the PCM. The heat balance equation for cell, *i* is given as follows:

$$\frac{dT_{l,i}}{\Delta t}\rho_l C_{eff}\,\Delta\delta = q_{i-1} - q_{i+1} \tag{3.22}$$

The initial conditions and boundary conditions are given as follows:

Initial conditions

For the melting process, the PCM is initially solid and its temperature is assumed at a value below the melting temperature, T_1 (assumed at 20 ℃). This situation can be expressed as follows

$$T_l = T_1\,, \qquad t = 0 \tag{3.23}$$

Boundary conditions

$$-k_l\frac{\partial T_l}{\partial x} = q_{p-l}\,, \qquad x = 0 \tag{3.24}$$

$$\frac{\partial T_l}{\partial x} = 0, \qquad x = L, t > 0 \tag{3.25}$$

The computer program is made in 'Matlab' for calculation of the optimum thickness of PCM container. Only the container dimensions for PCM RT 42 is simulated in the present study, in order to reduce the simulation time and experimental validation time and cost. However, the charging and discharging characteristics of RT 25 will be tested using experimentation to assist in selecting the optimal PCM within the melting temperature range selected. The thermophysical properties of the RT 42 are given in Table 3-1.

3.5.1.2 Numerical simulation result

The relationship of the container thickness and the PCM temperature is presented in Figure 3-5. It is obvious that the temperature of the PCM varies with the thickness increasing. When

the thickness is 1 mm the temperature is as high as 135 ℃, with the thickness increasing the temperature decreases quickly till 40 mm, at where the PCM temperature decreases to the higher limit of the melting temperature range of 43 ℃, once the thickness outstrips 40 mm the temperature drops under 43 ℃. That is, 40 mm is the optimum thickness for RT 42 under the given conditions. Once the container thickness is larger than 40 mm the PCM inside container cannot melt completely.

An experiment will be carried out to validate the simulation result using a small scale experimental rig.

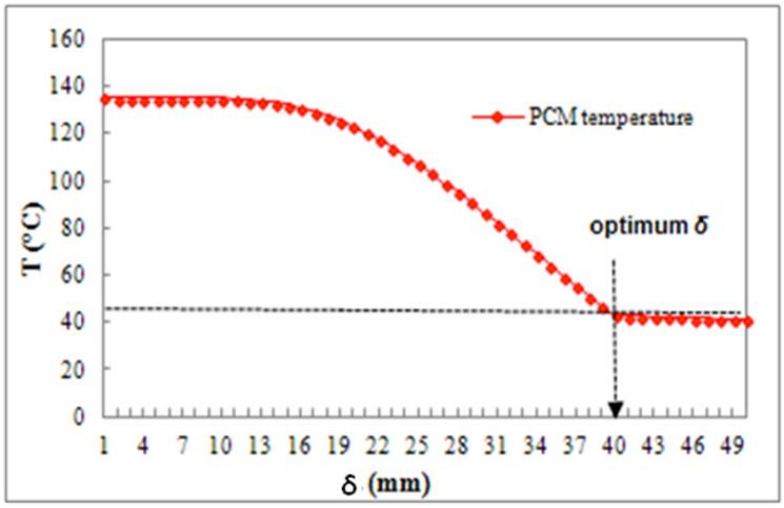

Figure 3- 5 Variation of PCM temperature with container thickness

3.5.2 Experimental Study

3.5.2.1 Experimental apparatus

A simplified small scale of the latent heat storage system is design to validate the theoretical model. In order to determine the optimal PCM for the proposed system, the candidate PCMs under identical conditions are also studied by using the designed system. Consequently, it is possible to evaluate the melting and freezing characteristics of other PCMs with melting temperatures within 25 ℃ and 45 ℃. Figure 3-6 shows the schematic diagram of the experimental apparatus, which consists of three major parts: 1) PCM container, 2) solar simulator, and 3) data acquisition system.

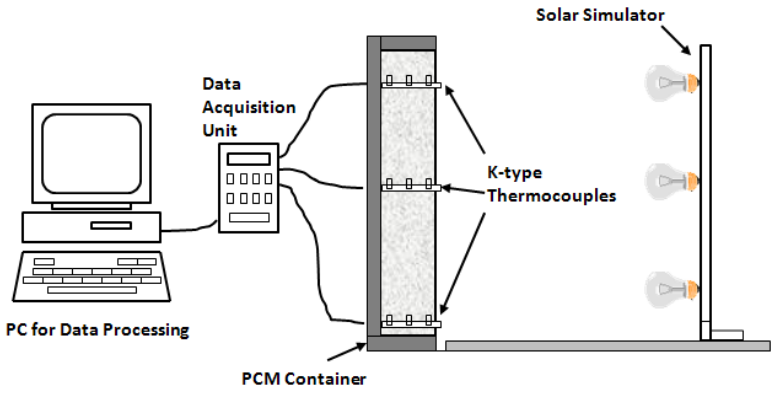

Figure 3- 6 Schematic diagram of the small scale of experimental rig

PCM container unit

In this study, the rectangular shape is chosen to encapsulate the PCMs. As already mentioned, when the chimney is operated in closed mode, the simulation results have no reference to the dimensions of chimney. In the experimental rig, a rectangular container is made of stainless steel with dimensions of 400 mm length × 400 mm width × 40 mm thickness, the value of thickness is chosen according to the numerical result for paraffin RT 42. One face with dimensions of 400 mm × 400 mm was painted black as the heat absorber. With the dimensions of 400 mm length × 400 mm width, the heat loses to air from absorber plate during charging process can be ignored, due to low convective heat transfer coefficients of the air and relatively short containers (from 200 to 400 mm) (Zivkovic and Fujii, 2001). Furthermore, the whole charging process is relatively short (within 6 hours). Hence, the glass cover is not employed to the small scale experimental rig. 30 mm thick polystyrene foam with thermal conductivity of 0.036 W/m K is applied as the thermal insulation material in this study, provided insulation on the top, bottom and side areas of the system. In this manner, the effect of lateral heat transfer from the sides can be negligible.

Solar simulator and data acquisition system

A solar simulator is designed as the heat source to reproduce solar radiation in this experiment. In previous researches, the charging process of LHS units has been performed experimentally by imposing a constant thermal current to the surface using thermoelectric devices or by exposing the unit to solar irradiation directly. Exposing the LHS systems to outdoor condition is the simplest way, and it is cheap and straightforward. However, the

variation of weather conditions (such as solar intensity, ambient temperature and wind velocity) makes this method time-consuming and unrepeatable. Such problems can be avoided if the assessment of the performance of a LHS system is tested under laboratory conditions. Solar simulators offer significant advantages over outdoor exposure, also is able to reproduce any location's solar conditions. Solar simulator is superior to thermoelectric devices in solar energy storage applications. This is because that using an artificial lighting can more accurately reproduce solar radiation than other heat sources. The indoor solar simulator should be close to an ideal representation of the sun (Garg et al., 1985b). Intensity level on the irradiated surface and radiation spectral distribution are the parameters that guide the design of a simulator. The design of any solar simulator is based on the correct choice of the type and number of lamps as well as the distance from the irradiated surface.

Selection of light source

Several kinds of lamps have been used as light sources in solar simulators, such as xenon arc or mercury xenon arc lamps, metal halide lamps, high pressure sodium vapour lamps, mercury vapour lamps and Quartz Tungsten Halogen Lamps (QTH). Xenon arc or mercury xenon arc lamps provide the closest spectral match to solar spectra available from any artificial source. However, even if the lamp current is constant the light output of the xenon lamps varies with electrode erosion, gas adsorption, and arc lamps have sharp peaks. In this study a continuous irradiation is required, to achieve the continuous irradiation within the economic restraints, Quartz Tungsten Halogen Lamps (QTH) is recommended to construct the solar simulator, since it is known that the radiation produced by halogen lamps has a spectral distribution is similar to solar radiation in the wavelength range of 0.20–2.7 mm, which contain 97% of the energy linearization in solar radiation (Kenny and Davidson, 1994). Meanwhile, it is relatively cheap and its flux is smooth, continuous to simulate a constant short period of time assuming an average level of radiation (Meng et al., 2011). As is illustrated in Figure 3-7 the tungsten-halogen lamps generate a continuous spectrum of light that ranges from the central ultraviolet through the visible and into the infrared wavelength regions, which match to solar spectra.

Figure 3- 7 Spectral distribution of the sun and tungsten-halogen lamp
(http://zeisscampus.magnet.fsu.edu/articles/lightsources/tungstenhalogen.html)

Flux uniformity

In order to obtain the required flux uniformity, it is necessary to screen the intensity of a QTH lamp. At the same time the impact of the lamp position and the number of the lamp on surface flux uniformity should be assessed.

The flux intensity of one lamp is firstly measured. Once the radiation from one lamp was obtained, and then just simply adds the output of the lamps based on the measured intensity of one lamp until the number and the position of lamps to achieve the required irradiance level and uniformity of radiation on the test plane.

The intensity of the irradiation is supplied according to solar irradiation data of a representative day (4^{th} Oct) in London area. Although the sunshine time of 4^{th} Oct is 11 hrs, it shortens to 6 hours in the experimental testing due to the limitation of working time in lab and preventing the lamps burnout from long time working.

The hourly profile of solar radiation intensity of 4^{th} Oct incident on south vertical surface is shown in Figure3-8, it can be seen that the most of whole day's solar radiation centralizes between 9: 00 am and 3: 00 pm. This is consistent with Montgomery and Livingston' conclusion that maximum solar radiation availability occurred between the hours of nine o'clock to three o'clock in the afternoon (Montgomery and Livingston, 1986), and the variations of the solar radiation intensities are relatively small during this period. Therefore, it is possible to employ a 6 h constant heat flux to the experiment for the numerical validation. That is, if the value of the PCM container thickness is correctly calculate by the numerical model, the PCM inside the designed container should fully melt at the end of 6 h.

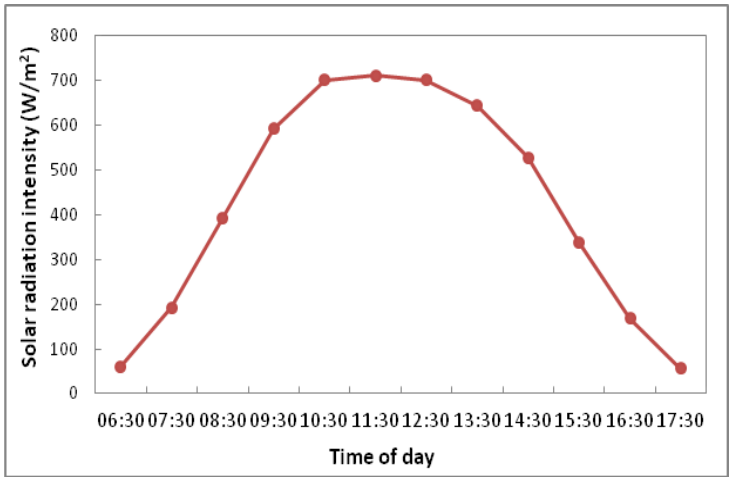

Figure 3- 8 Hourly profile of solar radiation intensity of 4th Oct incident on south vertical surface

According to solar irradiation data of 4th October, the mean irradiation intensity of 817 W/ m^2 over 6 hrs is obtained. For this reason, the 800 W / m^2 of solar radiation is selected for the experimental test. At the distance of 50 cm, the required output intensity level of 800 W/ m^2 can be achieved, which is the same as that applied to numerical model.

Eight 120-W halogen lamps are used to design this multiple-lamp solar simulator system, the lamps specifications are described in Table 3-2:

Table 3- 2 Properties of the selected light source

Lamp	Tungsten halogen
Voltage	240 V
Wattage	120 W
Life	2000 Hrs
Dimmable	Yes
Diameter	120 mm
Length	133 mm

These lamps are installed in a staggered form in an area of 500 by 500 mm. This kind of solar simulator in staggered arrangement creates adequate uniformity of irradiance and has been employed in many researches (Garg et al., 1985b; Kenny and Davidson, 1994; Meng et al., 2011; Bilgen and Richard, 2002). The arrangement of the eight lamps and the distribution of the radiation over the heat absorber surface are shown in Figure 3-9. It can be seen that the radiation scatters evenly on the most part of the absorber surface.

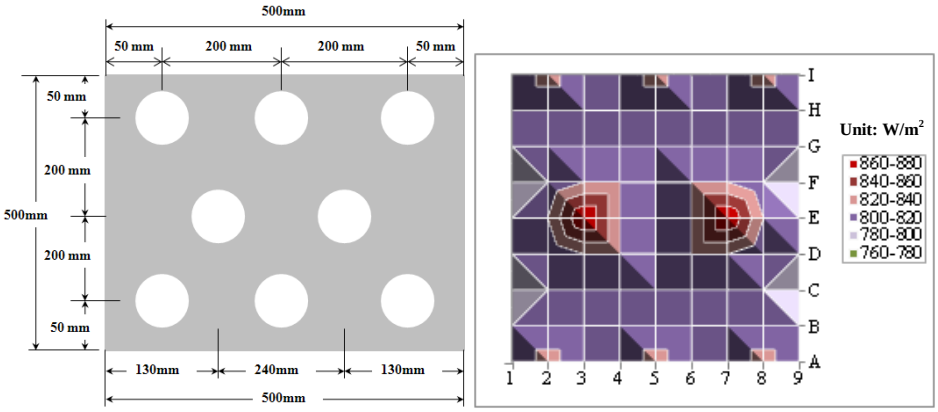

Figure 3- 9 Schematic diagram of the arrangement of the 8 halogen lamps and radiation distribution with 800 W/m^2

3.5.2.2 Measurement conditions

The experimental system should experience conditions similar to those existing in a real environment. The reproduction of the actual transient environmental conditions is a complex task, and it is out of the scope of this study. Furthermore, in a real passive heating operating condition, the PCM container prevents contacting from the ambient environment. This is possible to consider running the experimental testing under constant environmental conditions in laboratory. The PCM charging process is carried out by supplying constant heat flux by solar simulator during daytime. For the discharging process, the unit is cooled down by natural convection without special cooling apparatus during night. All conditions (such as radiation flux, air temperature) are kept constant for the duration of each process (discharging or charging).

3.5.3 Experimental Study on RT 42

The experimental study with RT 42 has three main objectives: to validate the numerical model presented by considering the impact of the assumptions made for the physical phenomenon simplification. To explore the properties and behaviour of melting and freezing processes of the PCMs selected and evaluate the performance of the system with different thermal conductivity enhancers (TCEs).

For melting process, all experiments are carried out under the same constant heat flux from the same initial temperature. Once all thermocouple readings reach steady state condition,

indicating the charging process finished. For freezing process, all of the liquid PCM begin to solidify at the same temperature by natural convection without any special cooling apparatus. Ten calibrated K-type thermocouples with accuracy of ± 0.3 ℃ are used to measure the temperature field at the pre-selected locations inside PCM. One is used to record the ambient air temperature. The other nine are inserted into the PCM at three different heights along the centre-line of the container. These locations are 30, 200, and 330 mm away from the bottom of the container. Then every three thermocouples as a set are distributed at 5 mm, 20 mm and 35 mm away from the absorber plate at each height, respectively, as shown in Figure 3-10. Each thermocouple set is encased in a thin plastic tube, and the total volume of the three sets is too small to affect the heat transfer process during charging and discharging processes. All of the thermocouples are connected to the data acquisition, and the collected date is then transferred to a PC for analysis. All temperature variations are automatically recorded at an interval of 10 s.

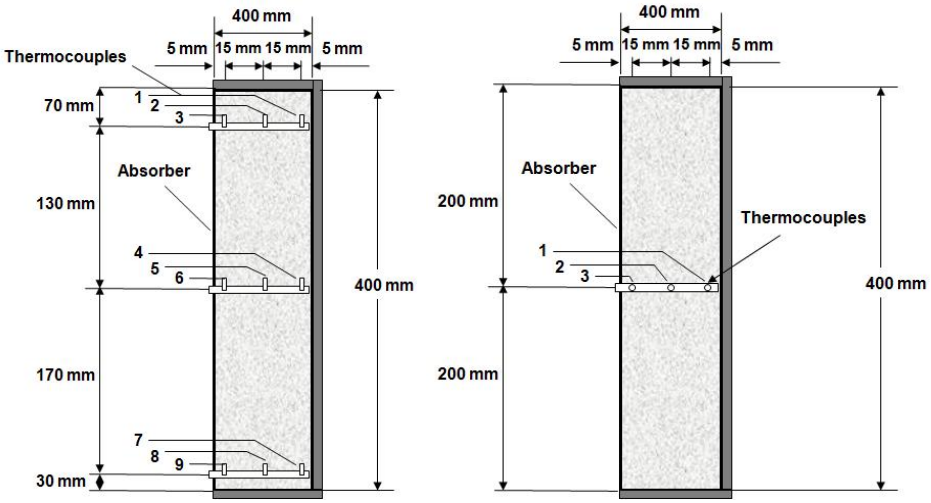

Figure 3- 10 Dimensions of PCM container and locations of the thermocouples: (a) lateral section; (b) cross section

3.5.3.1 Melting test of RT 42

The melting of the RT 42 is carried out first to validate the numerical model. In order to further confirm the melting time of the pure PCM, the charging test of pure PCM is carried out twice to ensure that the experimental results can be comparative to the numerical result. A rectangular metallic container with the optimum thickness of PCM container that calculated

by numerical model is manufactured to contain the PCM.

The testing starts at the temperature of the PCM equal to the room temperature 20 ℃, and then, the solar simulator is turned on to heat up the absorber plate. Figure 3-11 displays the temperature variations of nine thermocouples inside paraffin RT 42 with time for the 1st test and 2nd test. The melting temperature range is evaluated from the temperature curves as 38-42 ℃ in Figure 3-11. This temperature range is agreed with that determined by supplier, there is however a discrepancy of 1 ℃ between them. During the initial period of charging, the energy is absorbed and stored by the PCM in the form of sensible heat. This heat is used to raise the temperature of the PCM gradually to its melting point. During the melting process, the temperature of points T_1, T_2 and T_3 at the upper region of PCM container are found to be higher than those in the lower region, consequently accelerating the melting process. It is due to the reason that natural convection of the liquid PCM at upper region is developed, which leads to the ascending of the hot liquid and the descending of the cold liquid.

Because of the low thermal conductivity of the PCM, the temperature of the points near the absorber rise very quickly. After the temperature of the PCM reaches its melting point the melting process starts. The heat absorbed by the PCM stored as latent heat, and the heat transfer mode of convection occurred afterwards the combined conduction and convection will determine the melting process during this period. The convective heat transfer is the mechanism that causes the different trends of the temperature variations at the different locations. For instance, the temperature of the lowest thermocouples of T_7, T_8 and T_9 almost increase linearly with time during the whole process, which is quite different from other 6 thermocouples.

T_7 is the last point at which the melting starts, the temperature of T_7 climbs quickly at the beginning then reaches to a temperature plateau, about 38 ℃, indicating the phase change occurs afterwards. When its temperature reaches around 42 ℃, there is abrupt transition occurred to T_7 where the natural convection takes place. This means that the PCM surrounding T_7 fully melts. The whole melting process lasts for about 5 hrs 45 min for the sample. It can be seen clearly that the temperature variation curves for the 2nd test are approximately the same as those for 1st test, and the melting time for 2nd test is 5 hrs 45 min, which is exactly consistent with that for 1st test. Hence it is reasonable to validate the theoretical result by the experimental result. The actual melting temperature range of 38 -

42 ℃, no large difference compared with that of theoretical numerical.

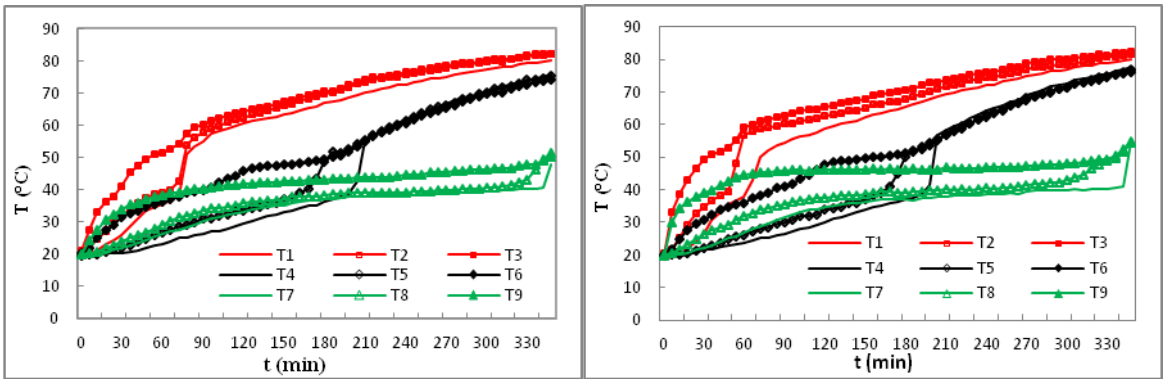

(a) (b)

Figure 3- 11 Temperature variation with time of RT 42 during melting process: (a) 1st test and (b) 2nd test

Regarding the assessment of the mathematical model, a modified model in which the depth of PCM container is 400 mm is developed to re-produce the experimental conditions. The energy supply is the same as that has been applied to the experimental testing. Experimental temperature profiles of a typical point (T_7) for 1st and 2nd tests are selected to compare with the numerical data. Good agreement between the numerical and experimental values is found. As can be observed in the following curves of Figure 3-12, the error between them is only 4.4 %. The difference could be due to differences between the actual material properties and the theoretical values assumed and the natural convection that exists in liquid PCM while ignore in numerical model. The experimental results prove that it would be possible to use the numerical model as a tool to determine the dimensions of PCM container for other locations, if the weather conditions for other locations are known.

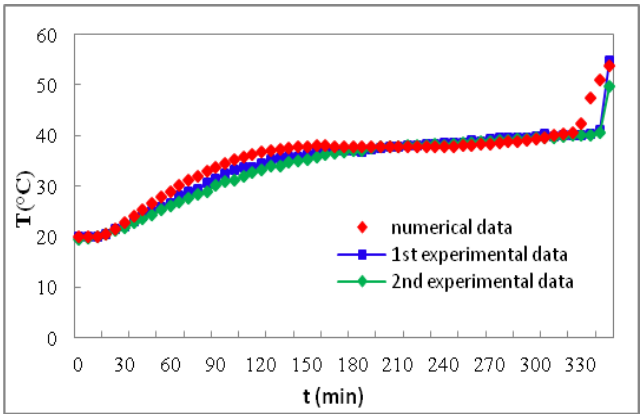

Figure 3- 12 Comparison the temperature profiles of numerical data and experimental data

3.5.3.2 Freezing test of RT42

The discharging rate of the heat stored in PCM is also an important aspect of determination of the optimal PCM for the proposed system that must be considered. It needs to ensure that the PCM discharges adequately until next charge cycle. The variable that would affect the discharging rate of the proposed system is the room air temperature. The room temperature hence used in the experiment has to be comparable to that expected in a real building. For this study, the warm air introduced to the occupied zone and release heat to occupied zone, and then cooled air flows back into air channel through inlet. The air temperature at inlet of solar chimney is expected to be 1 - 2 ℃ lower than 21 ℃, which is the value recommended by CIBBSE.

For practical purposes, melting test and freezing test are conducted in sequence, that is, after a heating test a subsequent freezing test is carried out immediately. The temperature variations of the surrounding air and the temperature profiles of points T_4, T_5, T_6, T_7, T_8 and T_9 are presented in Figure 3-13. The dotted lines represent the solidification temperature range of 38- 44 ℃ in Figure 3-13. It can be seen that the surrounding air temperature maintained nearly constant varied between 19 ℃ and 20.3 ℃ during the whole freezing test. The temperature variations inside PCM show a typical solidification process. At the very beginning period of the solidification, the temperature of the PCM is very steep. During this period, the temperature of the PCM is high, and the heat dissipates from the PCM is mainly its sensible heat. Natural convection controls the heat transfer process within the PCM. As the large initial temperature difference and the smaller thermal resistance, the heat transfer rate between the air and the PCM is large. These factors explain the rapid temperature drop during this period. When thermocouple T_9 reaches the solidification temperature of 44 ℃, afterwards which the trend becomes gentler. The solidification process begins, meaning the PCM near the absorber surface of the container starts to freeze and discharge its latent heat not the sensible heat, consequently, the frozen layer of PCM acts as a thermal insulator and results in a large thermal resistance. This reduces the heat transfer rate and causes large temperature gradient within PCM. When the temperature of point T_4 reaches around 38 ℃, indicates that the phase of the PCM inside container changes into solid completely. The heat extracted from the PCM is again mainly the sensible heat of the solid PCM. Therefore, though the

temperature difference between the air and the PCM is becoming smaller, the temperature curves drop more quickly compared with the phase change controlled period.

As can be seen from Figure 3-11 and Figure 3-13, a melting or freezing process can be identified to comprise of three stages: stage I where sensible heat exchange is dominant (b) stage II where latent heat exchange is dominant and (c) stage III where sensible heat dominates the heat exchange again.

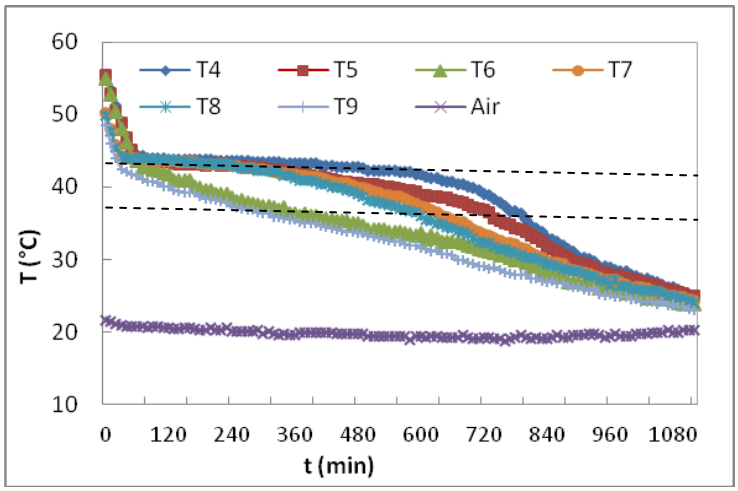

Figure 3- 13 Temperature variations with time during freezing process

The total phase change process lasted for 12 hrs 30 min including the initial sensible heat discharging time. For the representative day of 4th Oct the sunshine duration is 11 hrs, that is, the rest time of 13 hrs is heating time which is almost equal to the freezing time. However, there still is a large amount of sensible heat stored in PCM. Even for the worst condition of 4th Dec the heating time of that day is as long as 16 hrs, if the PCM completely melted under the solar irradiance condition of 4th Dec. The temperatures of the thermocouples inside PCM for 13 hrs and 16 hrs are showed in Table 3-3.

Table 3- 3 Temperatures of thermocouples inside RT42

Time	Temperature of thermocouples						
(h)	T_4	T_5	T_6	T_7	T_8	T_9	Air
13	36.6	34.4	29.9	32.1	30.8	27.9	19.1
16	28.9	27.9	26.0	27.2	26.6	25.1	19.8

It can be seen clearly that sensible heat stored in the stage III could not discharge adequately before next charge cycle. Despite a PCM stores energy primarily as latent heat, sensible heat

can form up to 50% of the total heat stored (Wang et al., 1999). Consequently the sensible heat of the PCM is one of the most important parameters that influence the performance of the LHS unit. Besides, the problem of the PCM being a self insulating material during solidification results in large temperature gradient within PCM, which decreases the surface temperature. Hence it is necessary to utilize effective techniques to accelerate the sensible heat discharging and minimize the temperature gradient.

3.5.4 Thermal Conductivity Enhancements (TCE)

Organic PCMs suffer from a very low thermal conductivity, which drastically affects the performance of the LHS unit. The heat transfer rate inside PCMs has not been up to the expected level and the large-scale utilization of LHS units in practical applications remains unsuccessful. Therefore, it is necessary to address the above-mentioned drawback of organic PCMs. Some effective techniques used for enhancing the thermal conductivity of the PCMs have been enumerated in Chapter two.

According to the TCE techniques summarized, the insertion of metal finned structures is the best method among others for the proposed system as the fins are able to improve the thermal contact with the PCM furthest away from the heat exchanger surface and they are fixed, non-moving structures that can maintain high performance after long charging–discharging cycle. The high cost in microencapsulation limits their use accepted for large scale applications. Dispersing high conductivity materials into PCMs is less practical, since the substances dispersed in PCMs usually sink to the bottom or float to the top of the container due to their different densities from PCMs. As previously mentioned, when integrating PCM with construction materials like concrete, gypsum board, brick and so on, it can lead to leakage problems during phase change transition. This leakage problem may accompany with PCM-construction materials over the lifetime of building. On another hand, in order to maintain the construction material strength, incorporation enough PCM with the building materials sometimes is permitted. With regard to heat pipe, it is commonly used in solar thermal water heating applications. In this application, heat pipes embedded in PCMs and distilled water is used as the heat transfer fluid rather than air to release heat to or absorb heat from PCM when it going through the PCM. In current study, the stainless steel used to manufacture the finned structure, as the metal is available in laboratory, thought aluminium or copper maybe a better choice for TCEs.

It is important to highlight that introducing TCEs into PCMs can enhance the heat transfer whilst influence the heat storage capacity of the LHS. The heat storage capacity decreases with the increase in the volume of the TCEs. For this reason, the balance between TCEs and heat storage capacity needs to be considered. Generally, the small percentage (usually < 7 %) of heat storage loss is reasonable (Zhao, et al., 2010). In order to minimize the influence of adding TCEs on the heat storage capacity of LHS system, the volume percentages of these three TCEs are within 5 % of the volume of PCM container.

Four different finned TCEs are constructed by using stainless steel: vertical fin (VF), horizontal fin (HF), honeycomb structure (HCS) and square cell structure (SCS). As is shown in Figure 3-14 (a and b), VF or HF consists of seven rectangular fins, and each fin has the following dimensions: 400 mm length, 40 mm height and 1 mm thickness, and each two fins are spaced by 50 mm so that cut the whole PCM into smaller layers. The SCS is manufactured based on the rectangular fins, i.e., seven rectangular fins are evenly inserted into other seven same fins to divide the whole PCM into more and smaller PCM chambers. Each square cell has the same volume of 1.0×10^{-4} m^3 (Figure 3-14 (d)). Whilst each honeycomb volume of the HCS is approximately 1.68×10^{-4} m^3 which is a little larger than that of square cell (Figure 3-14 (c)). The volume fractions of VF or HF, HCS and SCS are 1.8 %, 2.7 % and 3.6 %, respectively

(a) (b)

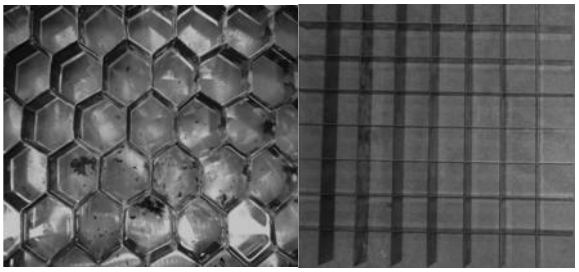

(*c*) (d)

Figure 3- 14 Four finned structures for heat-transfer enhancement (a) vertical fin, (b) horizontal fin, (c) honeycomb structure, and (d) square cell metal structure

3.5.5 Melting and Freezing Test of RT 42 with TCEs

Three main benefits of the introduction of TCEs to the proposed system can be achieved: To reduce the melting time, as the container dimensions designed based on the maximum irradiance, if the charging time is reduced, the PCM would be more chargeable in other months. To facilitate the stored heat discharge before next charge cycle and to reduce the temperature gradient inside PCM to increase the absorber surface temperature during discharging process. For the purpose of comparison of the performances of the TCEs inside PCM, all the experiments are performed under the identical conditions.

3.5.5.1 Horizontal fin (HF)

The heat transfer performance of the HF with paraffin RT 42 during charging process and discharging process are studied. Figure 3-15 presents the temperature variations inside paraffin RT 42 with time at different points. The melting temperature range of 38-42℃ is similar to the pure PCM charging test. It is seen that similar characteristics of temperature field for RT42 with HF are observed. However, the temperature stratifications between upper region of the PCM and lower region are lower than those of the pure PCM case. This is due to the presence of the TCE enhancing the conduction heat transfer at the initial melting period and suppressing the onset of natural convection, leading to a more uniform temperature distribution within the PCM. As expected, with the TCE, the melting requires shorter time than pure PCM does. The melting lasts for 5 hrs 5min that it is 40 min shorter than that of the

pure PCM.

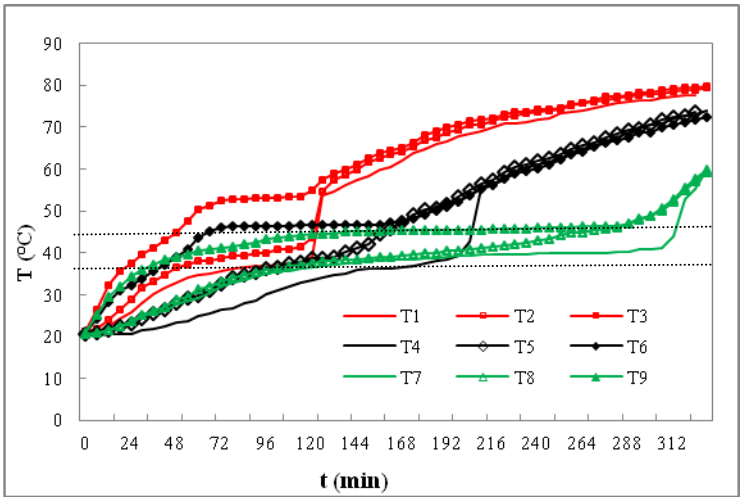

Figure 3- 15 Temperature variations with time during melting process of the PCM with HF

The temperature variation of the surrounding air and the temperature profiles of point T_4 ~T_8 and T_9 during the freezing process are presented in Figure 3-16. The air temperature varies between 19 ℃ and 20.4 ℃ during the whole freezing process. The whole freezing time is 11hr 15 min, which is 1 hr 15 min shorter than that of pure PCM.

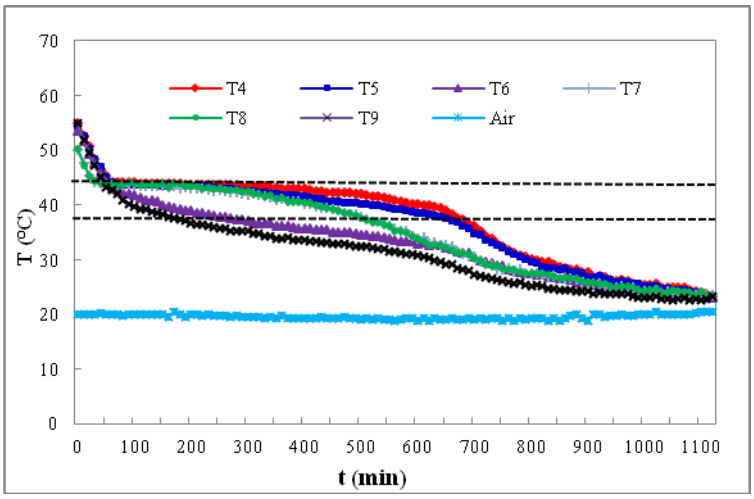

Figure 3- 16 Temperature variations with time during freezing process

The temperatures of the thermocouples inside PCM for 13 hrs and 16 hrs are shown in Table 3-4 as well. It can be seen that the temperatures of innermost thermocouples (T_4 and T_7) drop as much as 5.8 ℃ and 3.9 ℃ for 13 hrs respectively, and as much as 2.6 ℃ and 2 ℃ respectively for 16 hrs, in comparison to those of pure PCM freezing test. Whilst the

temperatures of outermost thermocouples (T_6 and T_9) only drop 2.1 and 2.1 ℃ for 13 hrs, and 1.3 and 1.5 ℃ for 16 hrs, respectively.

Table 3- 4 Temperatures of thermocouples inside RT42 for HF

Time (h)	Temperature of thermocouples						
	T_4	T_5	T_6	T_7	T_8	T_9	Air
13	30.8	30.5	27.8	28.2	27.9	25.8	19.4
16	26.3	26.1	24.7	25.2	25.2	23.6	20.1

3.5.5.2 Vertical fin (VF)

Figure 3-17 depicts the temperature profiles of PCM with VF during melting and freezing processes. It is seen from Figure 3-17(a) that the melting time lasts for 5 hrs 18 min, which is 13 min longer than that of the HF sample. This is attributed to the fact that for the RT42 with HF, the solid PCM sinks to the lower fin as the solid PCM has higher density than the liquid PCM. Hence, solid PCM is in contact with the lower fin throughout the melting process. As shown in Figure 3-17 (b), during freezing process the air temperature varies between 19.4 ℃ and 20.4 ℃. The whole freezing time lasts for 11hr 5 min, which is 10 min shorter than that of HF sample.

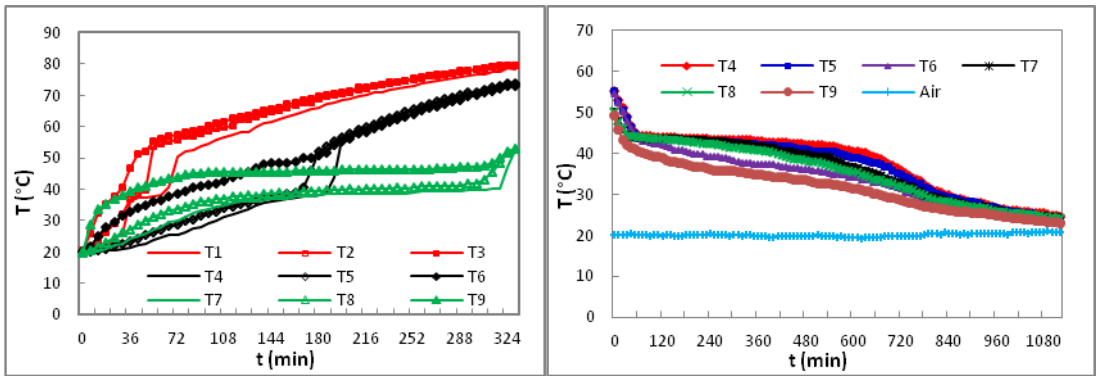

(a) **(b)**

Figure 3- 17 Temperature profiles in PCM: (a) melting process; and (b) freezing process

The temperatures of the thermocouples inside PCM with HCS for 13 hrs and 16 hrs are shown in Table 3-5. In comparison to those of HF sample, the temperatures of all thermocouples for VF sample are almost same.

Table 3- 5 Temperatures of thermocouples inside RT42 for VF

Time	Temperature of thermocouples						
(h)	T_4	T_5	T_6	T_7	T_8	T_9	Air
13	31.2	30.8	27.9	28.9	28.7	25.9	19.6
16	26.7	26.5	24.9	26.1	25.8	24.8	20.3

3.5.5.3 Honeycomb structure (HCS)

Figure 3-18 presents the temperature variations in paraffin RT 42 with HCS during melting and freezing processes. The melting time is estimated from Figure 3-18 (a), which is 4 hrs 55 min. The melting time of the PCM with HCS is just 10 min shorter than that of the HF sample. It can be seen from Figure 3-18(b) that the air temperature varies between 19 ℃ and 20.2 ℃ during the whole freezing process, and the whole freezing time lasts for 11hr, it is 1 hr 30 min shorter than that of pure PCM freezing test.

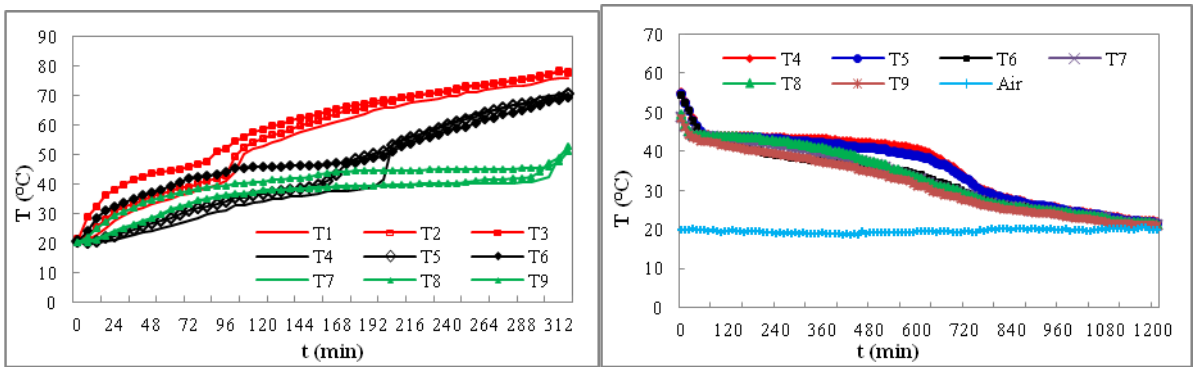

(a) **(b)**

Figure 3- 18 Temperature profiles in PCM: (a) melting process; and (b) freezing process

The temperatures at different points for HCS sample for 13 hrs and 16 hrs are presented in Table 3-6. The temperatures of all thermocouples dropped slightly compared to those of HF sample.

Table 3- 6 Temperatures of thermocouples inside RT42 for HCS

Time	Temperature of thermocouples						
(h)	T_4	T_5	T_6	T_7	T_8	T_9	Air
13	29.8	29.3	27.3	27.1	26.8	26.2	19.8
16	25.4	25.3	24.0	24.6	24.3	23.8	19.8

3.5.5.4 Square cell structure (SCS)

The temperature variation profiles of paraffin RT 42 with SCS at different points during charging and discharging processes are presented in Figure 3-19. The melting time for RT 42 with SCS evaluated from Figure 3-19a is 4 hrs 50 min, which is 15 min shorter than that of the HF sample, whilst it is nearly the same as that of honeycomb sample. This indicates that though introducing the TCEs to PCM can enhance heat conduction in the solid phase zone, the suppression of the natural convection becomes stronger when the volumes of TCEs increase. As a result, the discharging time is 11 hrs 30 min, which is 15 min longer than that of the HF sample (see Figure 3-19b). This may be attributed to the suppression of SCS on natural convection is stronger than HF, it hence prolongs the discharging time. Thus it can be understood that TCEs may have different heat transfer performance in different process (melting process and freezing process).

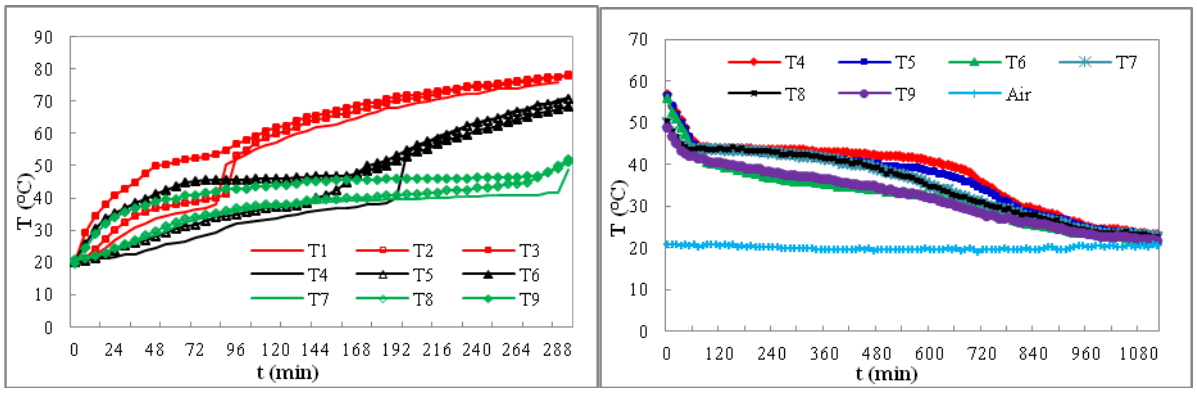

(a) (b)

Figure 3- 19 Temperature variation of square structure sample during charging and discharging processes

The temperatures at different points for 13 hrs and 16 hrs were presented in Table 3-7. In

comparison to those of HF sample, there is little difference between the corresponding thermocouples.

Table 3- 7 Temperatures of thermocouples inside RT42 for SCS

Time	Temperature of thermocouples						
(h)	T_4	T_5	T_6	T_7	T_8	T_9	Air
13	31.6	30.8	27.2	29.3	29.3	27.3	19.4
16	25.2	24.7	23.4	24.3	24.0	23.2	20.0

3.5.5.5 Heat transfer characteristics during freezing process

As the temperatures are different at different positions inside PCM, temperature gradients exist within PCM. Lower temperature gradient indicates a higher heat transfer performance and vice versa. Hence, the temperature differences between different thermocouple positions can be used to describe the heat transfer capacity for a given condition. Figure 3-20 shows the temperature differences of $\Delta T_{4\text{-}6}$ (T_4 -T_6) inside PCM during freezing process. It can be seen that at the initial 570 min, the temperature difference for PCM with SCS is slightly higher than that for pure PCM, and the maximum temperature difference is around 2.2 ℃, followed by sample with HCS (460 min, 2.0 ℃) and sample with HF (340 min, 1.3 ℃). In contrast, the temperature difference of $\Delta T_{4\text{-}6}$ for VF is lower than that for pure PCM. The reason for that can be due to though natural convection in freezing process is weaker compared with that in melting process, the natural convection influences heat transfer inside PCM during this period, and the HF, HCS and SCS reduce the convection heat transfer. This is the reason why the SCS takes longer time to solidify than other TCEs, whilst the VF takes shorter time than HF. After this period, the natural convection vanishes gradually, and conduction becomes stronger and replaces convection. When the PCM is completely solidified the temperature difference for pure PCM is larger than those for all of sample with TCEs, that is, the TCEs can reduce the temperature gradient inside PCM during late period of freezing. It should be noted that the temperature differences for PCM with VF and PCM with HF are nearly same during this period.

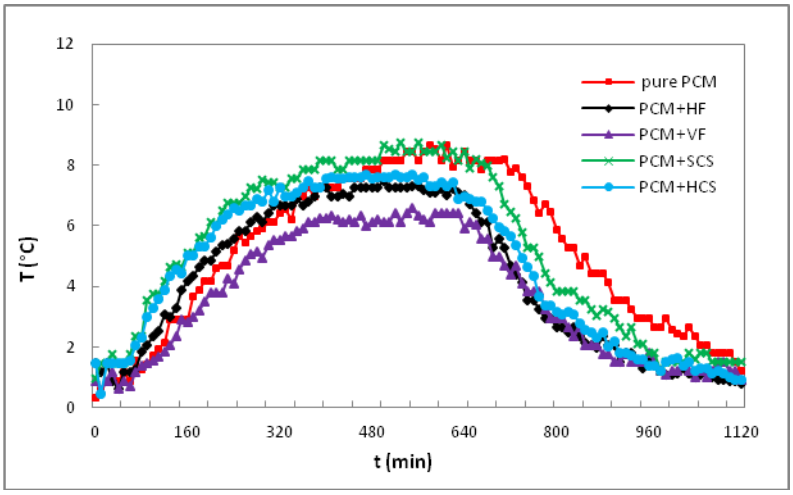

Figure 3- 20 Temperature differences of $\Delta T_{4\text{-}6}$ inside the PCM during freezing process

3.5.6 Experimental Study on RT 25

For this study it is not possible to manufacture a real container for RT 25 instead of using the current container for testing due to short of time availability. Nevertheless, the proposed experiment allows the characterization of the melting and solidification characteristics of RT 25. Moreover, one of benefits of using the current container is that the experimental results can be compared with those of RT 42 directly, so that it is convenient to scale other PCMs within the melting temperature range of 25-40 ℃.

3.5.6.1 Melting tests of RT 25 samples

The temperature variations of RT 25 with and without HF during melting process are presented in Figure 3-21. Similar to the melting processes of RT 42 samples, the melting of RT 25 samples start from top to bottom and from front to back at each level with clear temperature stratification. When the temperature of T_7 reaches 25 ℃, an abrupt rise occurs to it, which means the PCM inside container fully melts.

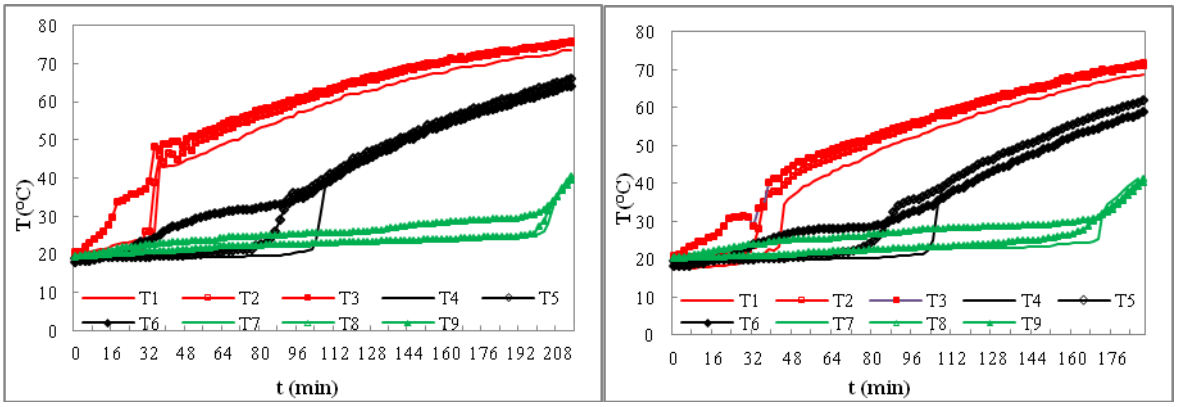

(a) Pure PCM sample (b) HF sample

Figure 3- 21 Temperature variations inside the container with time during charging process

Figure 3-22 shows the melting temperature curves of RT25 with/without four TCEs. The melting times are estimated from T_7 starting at 20 ℃ until rise to the melting temperature of 26 ℃. Same to RT42 samples, with an increase in volume fraction of TCE, the melting requires shorter times in all cases studied. The melting times for pure RT25, PCMs with VF, HF, HCS and SCS are 202 min, 178 min, 173 min, 162 min and 152 min, respectively.

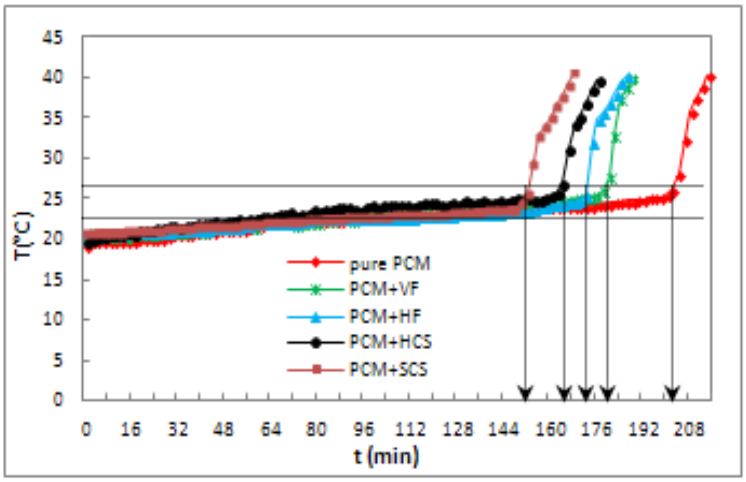

Figure 3- 22 Temperature curves of pure RT25 an RT25 with different TCEs

3.5.6.2 Freezing tests of RT 25 samples

Figure 3-23 shows the temperature variation of T_4 for RT 25 without and with TCEs during freezing process, the PCM releases its sensible and latent heat at a very low rate for a long period of time. The total solidification times for pure RT25, RT25 with VF, HF, HCS and

SCS are 2400 min, 1980 min, 1990 min, 1760 min and 1580 min, respectively. All the four TCEs can enhance the discharging process and the solidification times far outstrip the maximum heating time of 16 hrs, even though the sample were not encapsulated in the container with the optimal dimensions.

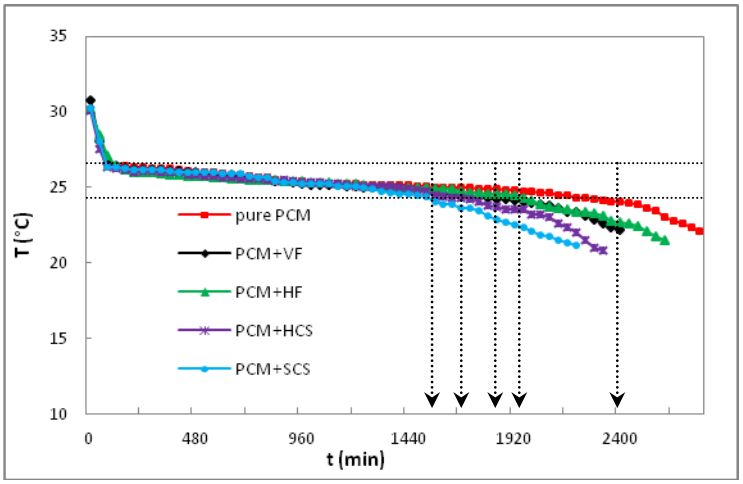

Figure 3- 23 Temperature variations of T_4 during the discharging process

3.6 DETERMINATION OF THE OPTIMUM PCM AND TCE

3.6.1. The Selected PCM

Comparing the solidification time of RT 42 with that of RT 25, it is certain that within the melting temperature range of 25 – 45 ℃, the solidification time of the PCM decreases with the melting temperature increases. This is due to the higher melting temperature results in higher absorber surface temperature, and, hence, higher heat transfer rate between air and PCM. We can conclude that for an air - based solar heating system, the melting temperature has a more significant influence on the system performance than its other properties such as latent heat. In this research, a 24 h charging-discharging cycle is required. From this point of view, the RT 42 is the optimum PCM for the proposed system, since it has a desirable discharging time among the PCMs within the melting temperature range selected.

3.6.2. The Optimum TCE

The experimental results confirmed that TCEs are capable of influence on both of melting and solidification processes by improving the thermal conductivity of PCM. However, the

experimental result of heat transfer enhancement of SCS on RT42 also shows that adding more TCE into PCM would not always give a satisfied improvement in heat transfer. As discussed previously, the heat transfer enhancement and the volume fraction of the TCE must be considered for any specific LHS application.

A new concept of measurement is presented herein, by introducing a value simply: $\varphi_{ef} / \varepsilon$, which can be regarded as a direct indication of the efficiency of a TCE for phase change process. Where φ_{ef} is the heat transfer enhancement of a TCE during melting or solidification process, and ε is the volume fraction of the corresponding TCEs. The heat transfer enhancements efficiency of the four TCEs are determined by comparing the melting times of the TCEs with PCM to that of pure paraffin. Therefore, the heat transfer enhancements of the four TCEs are 8%, 12 %, 14.5 % and 16 % during melting process. For freezing process, the heat transfer enhancements of the four TCEs are approximately 11%, 10 %, 12 % and 8 %, respectively.

Figure 3-24 shows the efficiencies of TCEs for RT 42 during the melting and solidification processes. It can be seen clearly that the HF has the highest efficiency amongst all the TCEs during melting process, and has the almost same efficiency as the VF during freezing process test. Moreover, straight finned structure takes advantages of the simplicity, ease to fabrication and low cost of manufacture that means a higher efficiency can be achieved at a low cost. Because of those reasons above, the HF has been selected as the optimum TCE for the proposed system.

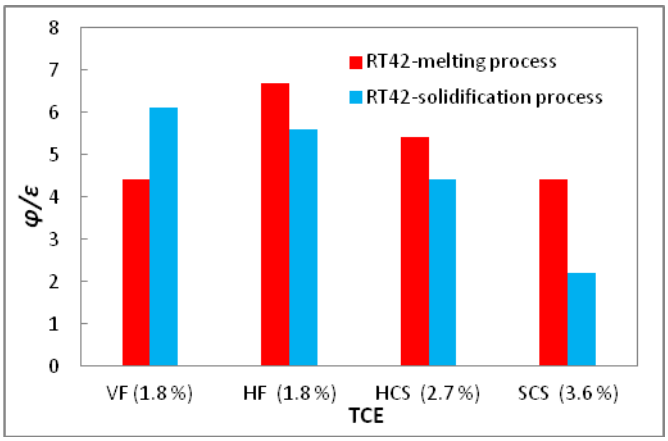

Figure 3- 24 Efficiency of difference TCEs during melting and solidification process

3.7 CONCLUSIONS

1) The melting time of the encapsulated PCM is a crucial parameter when designing the container, as it must match to the total amount of daily solar energy. In this section, a mathematical model for determination of the thickness of the PCM container for RT 42 has been presented. A long term historic maximum daily solar radiation of the year was used as the basis in this numerical study.

2) The model has been validated by using experimental data which was obtained from a small scale experimental test rig. The experimental results showed that it is in close agreement with the assumption melting time. The experimental result proved that it would be possible to use the numerical model as a tool to determine the dimensions of PCM container for the proposed system for other locations, if the weather conditions are known.

3) The melting and freezing characteristics of RT 42 and RT 25 have been studied by using the same experimental rig. The temperature variation curves of the PCMs during charging process and freezing process presented more details of the heat transfer characteristics of a PCM. A typical melting or freezing process of a PCM consists of three stages: (a) stage I where sensible heat is dominant and characterised by pure conductive heat transfer, (b) stage II where latent heat is dominant with convective and conductive combined heat transfer, and (c) stage III where latent heat dictates the heat exchange with conduction mode.

4) The discharging rate of the heat stored in PCM is also an important factor to determine the optimum PCM for the proposed system. In the heating mode, the encapsulated PCM was considered to be capable of being completely charged over a period of 6 hours and have the capacity to discharge heat over a period of up to 16 h. However, for pure PCM, there is a large amount of sensible heat still stored in PCM after 16 h discharging. Therefore the sensible heat exchange rate is one of the most important parameters that influence the sensible heat contribution to the melting/freezing of PCM. Effective techniques to accelerate the sensible heat discharging are necessary for the proposed system.

5) Four types of metal finned TCEs were manufactured to achieve three purposes: to reduce the melting time, to facilitate the heat stored discharge before next charge cycle and to reduce the temperature gradient inside PCM during discharging process. The volume percentages of these TCEs are within 5 % of the volume of PCM container to minimize the influence on the heat storage capacity. The volume percentages of HF, VF, HCS and SCS are 1.8 %, 1.8 %, 2.7 % and 3.6 %, respectively. The performances of the four TCEs with RT 42 and RT 25 have been investigated, the following are the main findings:

   i) Introduction of TCEs into the PCMs can enhance the heat transfer in the solid region of the PCM but they suppress the natural convection effect in the liquid zone, which results in the enhancement performance weakening with the increase in the volume percentage of the TCEs during melting process.

   ii) One of purposes of using TCEs is to minimize the problem of the PCM being a self insulating material during solidification process. However, the experimental results showed that the TCEs do not always have a positive effect on this problem, since the suppression of the TCEs on natural convection influences the heat transfer in liquid PCM zone during early solidification period. This phenomenon deteriorates as HCS or SCS are inserted into PCM.

   iii) HF has the highest efficiency amongst all the TCEs during melting process, and VF has the highest efficiency during freezing process. However, HF' efficiency during freezing is just a little lower than that of VF.

6) The freezing time of the PCM must correspond to the period of heating or cooling time to achieve the maximum efficiency. From the experimental results it can be concluded that the solidification times of the PCMs decrease with the melting temperature increase. Hence, the optimum PCM should be selected on the basis of its melting temperature, rather than its other properties such as latent heat. From this point of view, the RT 42 is the optimum PCM for the proposed system. Since it has a desirable discharging time among the PCMs within the melting temperature range selected.

7) For a LHS system of given volume, the use of metal TCEs to improve the heat transfer performance of PCM considerably increases the weight and decreases the volumetric heat

of fusion of the LHS system at the same time. A new quantity was introduced here to describe the relationship between the heat transfer enhancements of TCEs and the volumes occupied by them.

8) The efficiencies of the four TCEs have been evaluated for melting and solidification processes. the efficiencies of TCEs are given as below:

   Melting process: HF ＞ HCS ＞ SCS ＞ VF;

   Solidification process: VF＞ HF ＞HCS ＞ SCS.

   HF has the highest efficiency amongst all the TCEs during melting process, and has the almost same efficiency as the VF during freezing process test. Therefore, the HF is most effective TCE amongst all the enhancers for RT 42 test samples.

4. DESIGN AND DEVELOPMENT OF A RIG FOR THE INVESTIGATION OF A SOLAR CHIMNEY

4.1 INTRODUCTION

The current chapter is aimed at finding optimum design solutions for a solar chimney by consideration of different design parameters, such as the chimney aspect ratio (stack height/channel depth), inlet and outlet heights. Studies of optimum solar chimney design can be done using both experimental and computer modelling methods, which are based on Computational Fluid Dynamics (CFD). Experimentation is considered to give results that are easy to check. However, for an experiment which involves optimizing model designs, this method can become expensive and time-consuming. The computer simulation method however allows easy modification of the design with more precise results in less time, Due to the aforementioned factors the CFD modelling is chosen to optimise the solar chimney design herein.

CFD is a computer based tool design to solve a wide range of fluid mechanics problems to obtain a numerical description of the whole flow field. The physical properties of fluid flows are governed by three fundamental conservation laws: the conservation of mass, momentum (Newton's second law) and energy. CFD is the most widely used software to simulation of the solar-induced ventilation model due to its robustness, accuracy, and user friendliness, and masses of studies on solar chimneys have been conducted using CFD method, and showed that the existing CFD models predict velocity and temperature profiles along with other flow characteristics accurately (Khanal and Lei, 2011).

4.2 THEORETICAL ANALYSIS

To understand the working mechanism of solar chimney, simple mathematical methods for representing natural ventilation in solar chimney are useful for designers and engineers because the methods offer an easy mean of understanding the characteristics of airflow in

chimneys. Dimoudi (Dimoudi, 1997) provided a typical analytical model for buoyancy-driven flow in a solar chimney with high and low level openings.

For a solar chimney with a height of H_c is attached to a room of height H_r, the stack pressure Δp, is given by:

$$\Delta p = g H_c (\rho_a - \rho_i) + g H_r (\rho_a - \rho_r) \quad (4.1)$$

Where ρ_a , ρ_i and ρ_r are the densities of the external ambient air, the air in chimney and the air in the room. The density of dry air can be calculated using the ideal gas law, expressed as a function of temperature and pressure:

$$\rho = \frac{p}{RT} \quad (4.2)$$

Where p is absolute pressure, R is the specific gas constant for dry air (R=287.058 J/ kg K), and T is absolute temperature. The stack pressure may be written:

$$\Delta p = g \frac{p}{R} [H_c [\frac{1}{T_a} - \frac{1}{T_c}] + H_r [\frac{1}{T_a} - \frac{1}{T_r}]] \quad (4.3)$$

Where T_a , T_c and T_r are the absolute temperatures of the external ambient, the air in chimney and the air in room and p is assumed to be constant, p/R can be replaced by ρT :

$$\Delta p = 273 \rho_0 g [H_c [\frac{1}{T_a} - \frac{1}{T_c}] + H_r [\frac{1}{T_a} - \frac{1}{T_r}]] \quad (4.4)$$

Due to the main pressure losses are in the chimney not in the room, the chimney stack pressure, Δp, is balanced by the pressure losses through the chimney, Δp_{loss}, which are composed of the inlet and outlet pressure losses and the channel friction loss:

$$\Delta p_{loss} = \Delta p_i + \Delta p_o + \Delta p_c \quad (4.5)$$

Meanwhile, the pressure losses in orifices are usually expressed as functions of the velocity:

$$\Delta p = k \frac{\rho \cdot v^2}{2} \quad (4.6)$$

Where k is the velocity pressure loss coefficient which relates to the flow pattern and size and shape of the orifices，The friction pressure loss in fully developed flow in a straight chimney of length H_c is evaluated using the D'arcy-Weisbach relation:

$$\Delta p_c = \epsilon \frac{4H_c}{D_h} \frac{\rho \cdot v^2}{2} \tag{4.7}$$

Where ϵ is the coefficient of friction and D_h is the hydraulic diameter,

$$D_h = 4 \frac{W \cdot d}{2(W+d)} \tag{4.8}$$

W is the width of chimney and d is the depth of chimney. Thus, the total pressure loss in chimney is:

$$\Delta p_{loss} = k_{in} \frac{\rho \cdot v_i^2}{2} + k_{out} \frac{\rho \cdot v_o^2}{2} + \epsilon \frac{4H_c}{D_h} \frac{\rho \cdot v^2}{2} \tag{4.9}$$

where k_{in} and k_{out} are the velocity pressure loss coefficients at inlet and outlet. Using the mass flow rate, m, instead of the velocity, v, from the continuity equation, $m = \rho v A$, thus, equation (4-9) can be written as:

$$\Delta p_{loss} = k_i \frac{m^2}{2\rho A_i^2} + k_o \frac{m^2}{2\rho A_o^2} + \epsilon \frac{4H_c}{D_h} \frac{m^2}{2\rho A_c^2} \tag{4.10}$$

Combining (4-4) with (4-10), the mass flow rate in the chimney is obtained:

$$m = \sqrt{\frac{273\rho_0 g[H_c[\frac{1}{T_a} - \frac{1}{T_c}] + H_r[\frac{1}{T_a} - \frac{1}{T_r}]]}{k_i \frac{1}{2\rho A_i^2} + k_o \frac{1}{2\rho A_o^2} + \epsilon \frac{4H_c}{D_h} \frac{1}{2\rho A_c^2}}} \tag{4.11}$$

In the following analysis, the room effect will be not considered, i.e. it is assumed that H_r is small. It can be seen from equation 4.11 that for a given ambient air temperature (T_a), chimney air temperature (T_c) and room air temperature (T_r), the above equation could be written:

$$m = \sqrt[2]{\frac{M H_C}{\frac{k_i}{A_i^2} + \frac{k_O}{A_O^2} + \epsilon \frac{4H\ 1}{D_h A_C^2}}} \tag{4.12}$$

Where

$$M = 273\rho_0 g \left(\frac{1}{T_a} - \frac{1}{T_c}\right)(2\rho\ )$$

It can be seen from equation 4.12 that the mass flow rate is related to the chimney geometry. The effect of various chimney geometries on solar chimney ventilation performance in terms of mass flow rate is investigated under two different conditions:

1) If the friction loss in the chimney can be negligible compared to inlet and exit pressure losses and 2) the inlet and exit pressure losses can be negligible.

1) The friction loss inside the chimney is small compared to the pressure losses at exit and inlet, the channel friction loss can be neglected and the equation 4.12 can be written as:

$$m = \sqrt[2]{\frac{M H_C}{\frac{k_i}{A_i^2} + \frac{k_O}{A_O^2}}} = A_i A_o \sqrt{\frac{M}{k_i A_O^2 + k_o A_i^2}} \sqrt{H_c} \tag{4.13}$$

If the inlet area is small compared to the outlet area, the mass flow rate of the solar chimney is:

$$m = A_i \sqrt{\frac{M}{k_i}} \sqrt{H_c} \tag{4.14}$$

For unit height of inlet with chimney length, L_c, mass flow rate becomes:

$$m = W \sqrt{\frac{M}{k_i}} \sqrt{H_c} \tag{4.15}$$

If the inlet area, A_i is the same as the outlet area, A_o the mass flow rate can be expressed as follow:

$$m = A_i \sqrt{\frac{M}{k_i + k_o}} \sqrt{H_c} \tag{4.16}$$

For unit height of inlet with chimney length, L_c, equation 4.16 becomes:

$$m = Lc \sqrt{\frac{M}{k_i}} \sqrt{H_c} \tag{4.17}$$

Hence, under the condition of neglecting friction losses inside a chimney, the mass flow rate is direct proportion to the square root of the chimney height and proportional to the chimney length.

2) If the inlet and exit pressure losses can be neglected, and the equation 4.12 can be rearranged as follow:

$$m = \sqrt[2]{\frac{MH_c}{\epsilon \frac{4H_c}{D_h} \frac{1}{A_c^2}}} = \frac{A_{ch}}{2} \sqrt{MD_h} \sqrt{\epsilon^{-1}} \tag{4.18}$$

For a unit depth of chimney with chimney length,L_c, equation 4.18 is written as:

$$m = Lc \sqrt{\frac{M}{k_i + k_o}} \sqrt{H_c} \tag{4.19}$$

Thus, if neglect the inlet and outlet pressure losses, the mass flow rate is approximately proportional to the chimney length.

From the theoretical analysis above, it is seen that the configuration can affect the performance and the applicability of the solar chimney for natural ventilation and passive cooling and heating of buildings, so those parameters would be considered carefully when designing a solar chimney.

4.3 NUMERICAL SIMULATION

The theoretical analysis above indicated that the mass flow rate always increases with the width or height of chimney increases. That means that the higher the chimney height or the longer the chimney length, the larger mass flow rate. For this study it would not be possible to build a solar chimney attached to a real scale dwelling in laboratory for testing from the view of technology and economy. Even though the geometry of the system will be chosen only for experimental purposes, it reproduces neither a real size chimney for a real building nor a scale of it, as the air flow inside a solar chimney is generated by buoyancy forces created at the boundaries, there is difficulty in scale modelling the process (Dimoudi, 1997). The proposed geometry of the system for testing is still chosen under practical consideration. Within this proposed solar chimney the flow is driven by buoyancy effect and the height of the chimney generally would not exceed the height of one storey i.e. 3m. Therefore, in practical terms 2m is herein selected as the height of the proposed system, which is a typical figure has been employed in many studies (Dimoudi, 1997; Martlĭ-Herrero et al., 2007; Ong and Chow, 2003; Mathur et al., 2006a; Mathur et al., 2006b; Mathur et al., 2006c; Hirunlabh et al., 1999; Saifi et al., 2012; Bouchair, 1994; Gan, 1998; Khedari, 2000), and as the theoretical analysis indicates that the mass flow rate is proportional to the width of chimney, for practical applications, the use of a solar chimney for the promotion of natural ventilation would be based on modular dimensions used for building. Furthermore, the unit width of the channel, nominally 1 m, is sufficient that edge effects are largely eliminated at the centre (Ryan and Burek, 2010). This width is similar to the large-scale test rigs used by other investigators (La Pica et al., 1993; Nguyen et al., 2000; Chen et al., 2003). A channel width of 1m is therefore considered as a practical minimum for this type of chimney configuration. This allows the rough estimation of the performance of the proposed system in different width for a given chimney height.

Once the height and width of chimney are determined, the optimum inlet, outlet orifice size and chimney depth should exist. Therefore a two dimensional model is used to investigate the effects of the orifices size and chimney depth on the mass flow rate, that can save a considerable time compared with using three dimensional models.

4.3.1 Development of the Numerical Model

The CFD software package FLUENT is used to simulate the air flow and heat transfer through the two-dimensional solar chimney. CFD calculation always simulates a flow in a finite domain. Therefore, realistic boundary conditions must be defined to correctly reproduce the flow characteristics in solar chimney. Figure 4-1 presents the schematic diagram of the two-dimensional solar chimney with a horizontal inlet and two horizontal outlets.

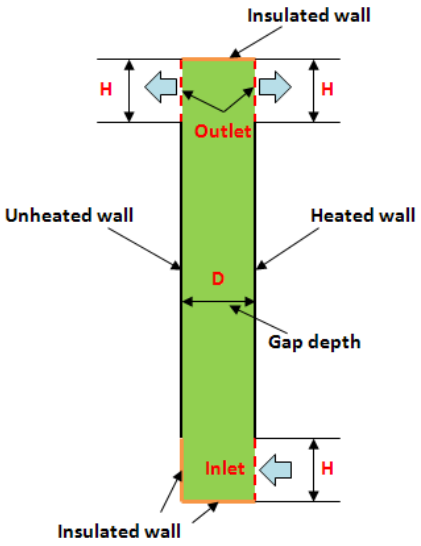

Figure 4- 1 Schematic diagram of the two-dimensional solar chimney

Simulation is carried out for the steady state incompressible air flow, and in order to increase the speed of convergence the Boussinesq approximation is used. This approximation allows the assumption that the density of the air remains constant for all solved equations, except the buoyancy term in the momentum equation. The following section outlines the boundary specifications and assumptions made to the numerical model.

Boundary Conditions

In the CFD simulation of the airflow in solar chimney, the air velocity profile and the turbulent characteristics of the air should be correctly simulated. Thus, the definitions of the boundary conditions, in particular those of the inlet, outlet and turbulence model have great potential influence on the outcome of the CFD simulation.

Inlet and outlet

The driving force of the solar chimney is the stack pressure difference caused by the temperature differences, and thus the change in density of the air within the vertical channel. For this reason the description of the inlet or outlet velocities and profiles should be correct. At the inlet section, it is obvious that there is a specific velocity profile which is well-known that the result of the pressure difference between inlet and outlet of the channel. At the outlet section, the stream-wise variations of velocity components and temperature are neglected. In addition, it is assumed that the fluid's pressure becomes equal to the ambient pressure. To ensure that the CFD calculates the airflow rate, both the inlet and outlet boundaries are described as pressure boundaries with pressure equal to atmospheric pressure at their respective heights. This allows the CFD programme to balance the pressure losses due to the fluid flow with the stack pressure created.

Walls

A solid wall boundary condition is one of the most common boundaries used in CFD, since fluid is not allowed to flow across the wall boundary surface therefore a no-slip condition is specified on the boundary for the velocity components. Because of applying the PCM to solar chimney, Isothermal wall condition is applied to the heated plate of chimney to represent the solidification temperature of the PCM: $T_p = T_m$. All other solid surfaces (solar chimney' sides and the outer surface of the heated plate) are adiabatic walls, so that there was no heat loss off the back of them: $\frac{\partial T}{\partial n} = 0$.

Turbulence models

Air flow in a solar chimney would likely be turbulent for buoyancy-driven flow (Gan, 1998). For the numerical simulation of the turbulent flow inside the solar chimney, it worth noting that the turbulence model should account for both the high and low Reynolds areas of the computational domain, since flow might be less turbulent in certain areas such as the lower part of a symmetrically heated cavity or adjacent to the unheated wall of an asymmetrically heated cavity (Gan, 1998). Therefore, the RNG k-e turbulence model is used for modeling of buoyancy-driven cavity flow as it is able to represent both strongly turbulent and less turbulent flow. In order to ensure the accuracy of the numerical results, the grid independence is checked by doubling the cell number along the cavity width and then along the cavity height. Little variation in the predicted flow rate is observed.

4.3.2 Model Validation

To evaluate the reliability and accuracy of the turbulence model and the inlet and outlet specifications for the simulation of solar chimney with vertical solar energy collector, the model has previously been validated by comparison of numerical results with the experimental results available in literature (Chen et al., 2003). The experiments were carried out using an experimental solar chimney model with uniform heat flux on one chimney wall. The dimensions of experimental solar chimney were 1.5 m high, 0.62 m wide and a variable chimney gap from 100 to 600 mm. The chimney was heated with a uniform heat flux on one wall varied from 200 to 600 W/m^2 while other walls were insulated. An air velocimeter probe was used to measure the air velocities in the cavity, and the air flow rate through the cavity was obtained from the air velocity measurements. The estimated uncertainty of the velocity measurements for the cavity depth up to 400 mm was around 15%, and 20% for chimney gaps larger than 400 mm. Numerical simulations are carried out by a two-dimensional model to represent air flow through the solar chimney (along the height and gap directions of the cavity). Figure 4-2 presents the comparison of air flow rates between simulation and experiment under the conditions of gap depth varies from 100 to 600 mm for a fixed heat flux of 400 W/m^2. The average difference between the predictions and measurements was 9.54 % and the maximum difference between experiment results and simulation results is 12.8%, all differences within the uncertainty in velocity measurements of the experiments. Therefore, this two-dimensional model can be considered to provide more realistic simulation of buoyancy-driven flow in a ventilation cavity.

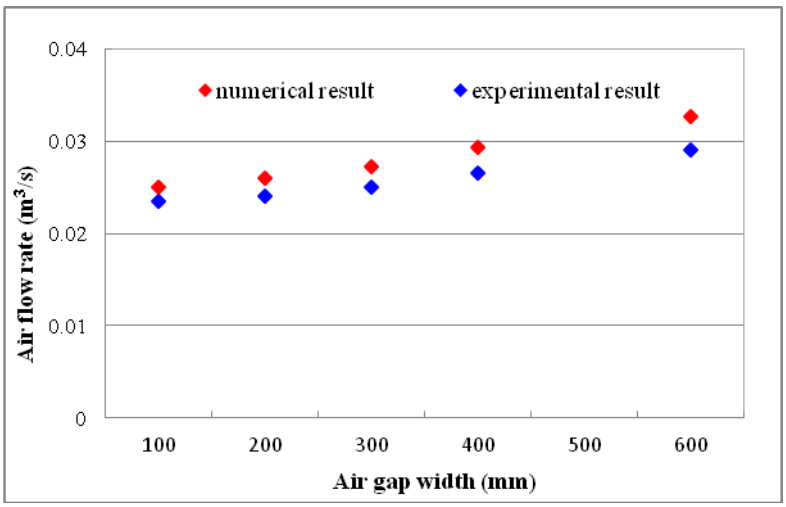

Figure 4- 2 Air flow rate comparison of simulation and experiment

4.3.3 Simulation Method

Numerical simulation is carried out for a vertical solar chimney of constant height of 2 m and one heated wall with constant temperature of 41 ℃ under the condition of inlet air temperature is fixed at 20 ℃. A number of different configurations of solar chimney have been simulated to find the optimum configuration for the solar chimney. The simulation results are here focused on the effects of air gap depth D, height of inlet and outlet H on airflow rate and outlet temperature T_{out} for cavities with a horizontal inlet and two horizontal outlets.

Parameters and simulation conditions

The ranges of simulation parameters and conditions are presented as follow:

(i). The depth of air gap varies from 0.1 m to 0.5 m, and heights of inlet and outlet vary from 0.1 and 0.5 m. The inlet height and outlet height are maintained as equal for all of the air gap depth.

(ii). The surface temperature of the single-sided heated wall $T_w = t_w+273$, t_w = 41 ℃ (representing the typical solidification temperature of the PCM), and the inlet air temperature is fixed at 20 ℃.

(iii). The horizontal inlet fixed on heated wall and one outlet fixed on heated wall, while the other outlet is on non-heated wall.

4.4. RESULT AND DISCUSSION

The proposed system is aimed to transfer the stored energy to the inside building for winter heating or facilitates room air movement for summer cooling depending on the operation of vent openings. The heating mode aims to maximize the heat transfer into the building, so the outlet air temperature and the airflow rate are therefore the two key parameters. This is because for heating mode, the outlet air supplies thermal comfort. The outlet air temperature indicates that how much the inlet air temperature is elevated by the heated surface. The air flow rate which is a direct measure of how much warm air is delivered into a living space.

Whereas, the cooling mode aims to maximize the mass flow rate induced. In this application the degree of heating of the air is not the key variable.

4.4.1 Outlet Fixed on Unheated Wall

4.4.1.1 Air flow patterns

In summer cooling mode, air enters the air channel from the bottom inlet opened to the living room, and the air is heated up by the heated wall and flows upwards due to the buoyancy effect. The heated air flows out to the ambient through the top outlet fixed on the unheated wall (the glass cover) and the cool outdoor air flows into the room through open windows or vents in other exterior walls. Figures 4-3, 4-4 and 4-5 show the predicted air flow patterns near the inlet and outlet of the solar chimney with different cavity depths for different inlet heights. It is seen that the air flows into the horizontal inlet and then air detaches from the bottom wall and turns from horizontal to vertical direction along the unheated wall (left wall), forming a recirculation zone in the corner between the bottom wall and unheated wall. The air flows toward the heated wall and another recirculation is developed above the inlet and near the heated wall, this is attributed to the separation of the incoming air through inlet in that zone. The air flow is very asymmetrical as the air in the cavity is heat up by the heated wall only. The distribution of the air velocity along the air gap depth for vertical solar chimney is non-uniform. Air velocity near heated wall is much higher than those in the middle and near the opposite wall. From the flow display of simulation results, it could be clearly recognized that reverse flow near the outlet of vertical solar chimney.

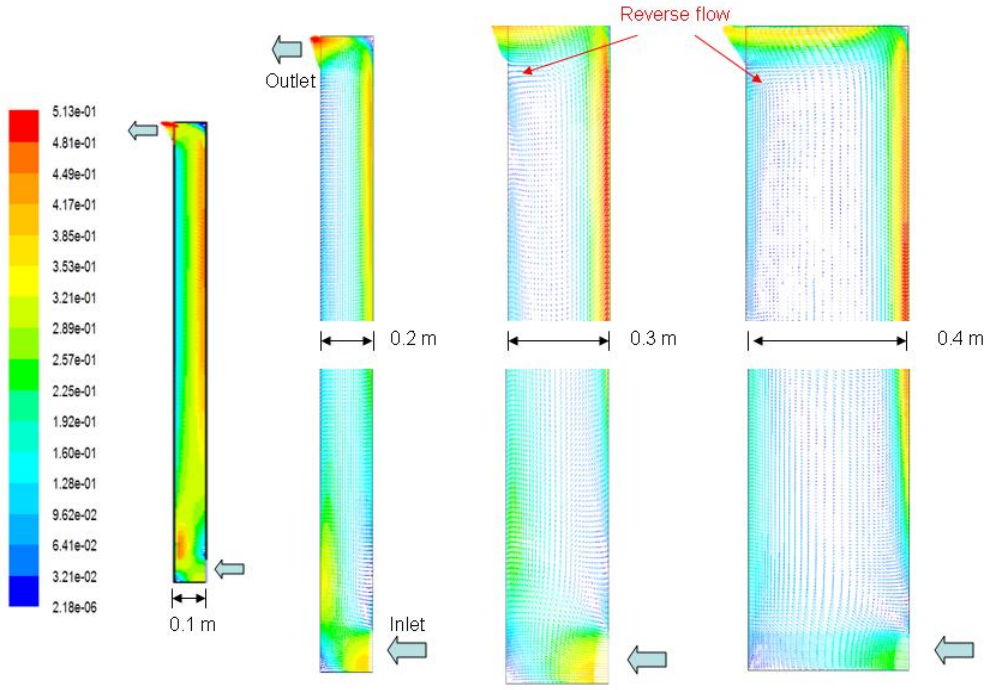

Figure 4- 3 Air flow patterns near the horizontal inlet and outlet of the solar chimney with various cavity depth (H=0.1 m)

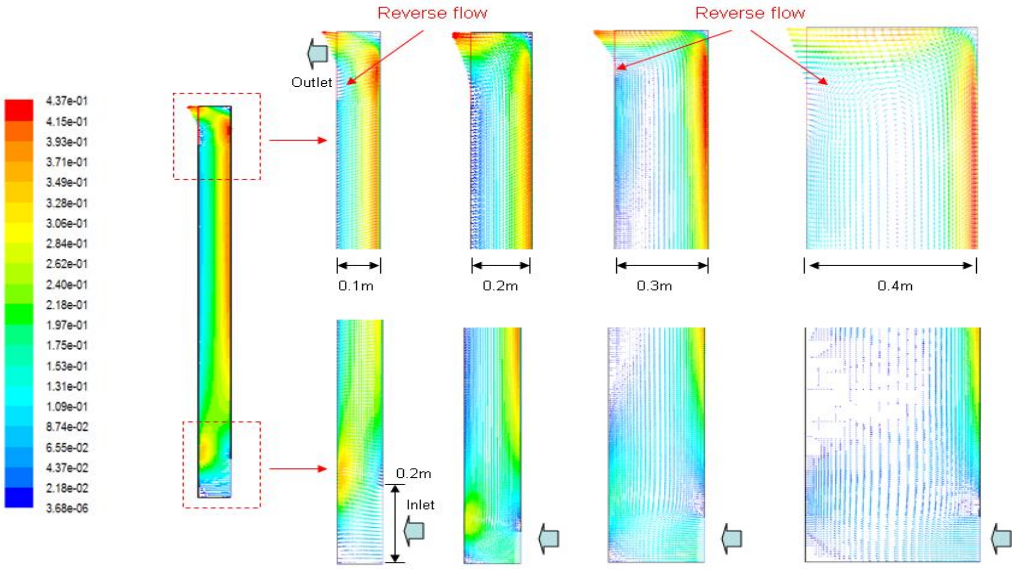

Figure 4- 4 Air flow patterns near the horizontal inlet and outlet of the solar chimney with various air gap depth (H=0.2 m)

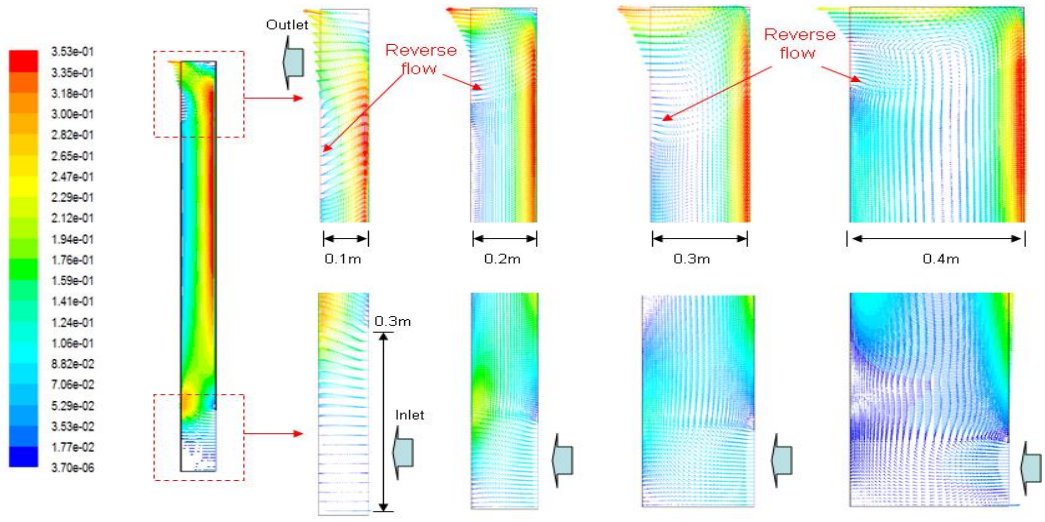

Figure 4- 5 Air flow patterns near the horizontal inlet and outlet of the solar chimney with various air gap depth (H=0.3 m)

It is shown in Figure 4-3 that reverse flow would occur at the outlet for wider air depth (for air gap depth > 0.2 m) when the inlet is set at 0.1 m. The reverse flow would be easier and worse to be found at outlet with the increase of the inlet height (see Figures 4-4 and 4-5). It can be seen that reserve flow is found for cavity depth of 0.3 m when the inlet height is 0.1 m whilst reverse flow occurs at cavity depth of 0.1 m when inlet height increases to 0.2 m except for the depth of 0.2 m. The flow reversal indicates that the buoyancy-induced velocity boundary layer along the top wall near the cavity outlet is less than the outlet height, causing entrainment of fresh air from the exterior of the solar chimney.

4.4.1.2 Mass flow rate

The presence of reverse flow reduces the mass flow rate at the outlet, although the increase of air gap depth and inlet height decreases pressure losses of the chimney. However, meanwhile, the intensity of reverse flow near the outlet increases with the increase of cavity depth and inlet height. The increasing reverse flow of a wide cavity offset the benefit of decreasing pressure loss. Therefore, there must be an optimum air gap depth and an inlet height for specific height of vertical solar chimney to obtain the maximum airflow rate.

Air mass flow rate through the air channel is calculated by following equation:

$$m=\rho \cdot v \cdot A_{out} \tag{4.20}$$

where m is the average mass flow rate at the outlet of the chimney (kg/s), A_{out} is the outlet

area (m^2), *v* is the average air velocity at the cross-section of the outlet (m/s).

The effect of the channel depth on the mass flow rate is shown in Figure 4-6, for channel depths of 0.1, 0.2, 0.3, 0.4 and 0.5 m with different inlet and outlet heights. For the various inlet heights, it can be seen that all the variation curves of the predicted air flow rates are similar, the mass flow rate firstly increases with the increase of air gap depth and then decreases after a certain value of air gap depth, as increasing the depth of the cavity can decrease cavity friction loss, whilst increasing the occurrence of reverse flow. The negative effect (reverse flow) outstrips the positive effect generated by the fraction loss, resulting in the decrease of mass flow rate at the certain value of channel depth, e.g., the airflow rate increases with the increase in cavity depth up to 0.3 m for the chimney with 0.4 and 0.5 m high inlet, even though the reverse flow occurs at inlet height of 0.1 m. The maximum airflow rate of 0.04 kg/s could be observed at the air gap width of 0.2 m for the inlet height of 0.2 m.

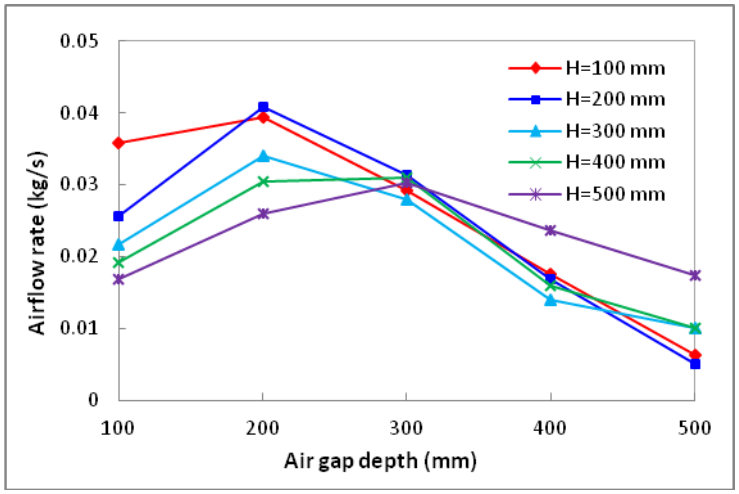

Figure 4- 6 Variations of mass flow rate with air gap depth

4.4.2 Outlet Fixed on Heated Wall

When the solar chimney is in the operation of passive heating mode, the buoyancy force generated by the heated air draws room air to the bottom inlet, and the room air is heated up by the heated wall and then returns to the living space through the top outlet fixed on the heated wall to bring the heat energy into the room. Hence, the air temperature at outlet of the solar chimney is another important factor to evaluate the effect of passive heating.

4.4.2.1 Air flow patterns

Figure 4-7, 4-8 and 4-9 show the predicted air flow patterns near the inlet and outlet of solar chimney with different depths for various inlet heights. Similar to the case of passive cooling mode, the air flows into the horizontal inlet and turns upwards along the unheated wall (left wall), then the air flows toward the heat wall. The recirculation zones are formed in the corner between the unheated wall and bottom wall and in the area above the inlet and the bottom of the heated wall. As mentioned previously, the air flow is asymmetrical in the cavity and the air velocity along the air gap depth is non-uniform.

However, some interesting differences between the air flow patterns of the two cases near the outlet of the cavity are observed. It can be seen that the incoming air flow in the cavity is obstructed by the top wall then separates to outlet direction and the opposite direction of the outlet and forms a recirculation in the corner between unheated wall and top wall. Similarly, the reverse flow occurs at the outlet for certain gap depths and inlet heights. Especially, when inlet height increases up to 0.3 m and above, reverse flows are found at all of the outlets for various gap depths. Consequently the reverse flow bends the air flow near the outlet that quite different from the former case.

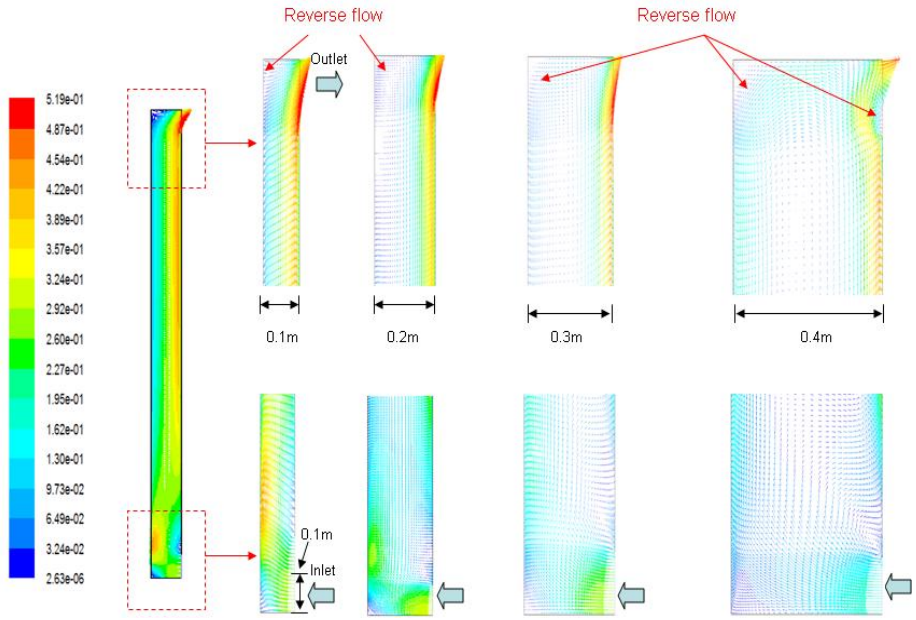

Figure 4- 7 Air flow patterns near the inlet and outlet for various air gap depth (H=0.1 m)

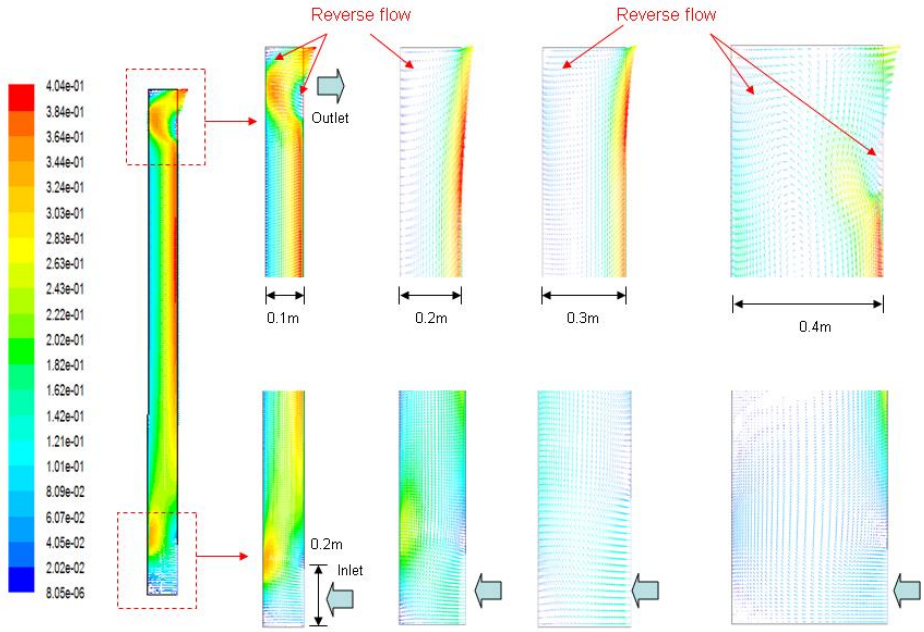

Figure 4- 8 Air flow patterns near the inlet and outlet for various air gap depth (H=0.2 m)

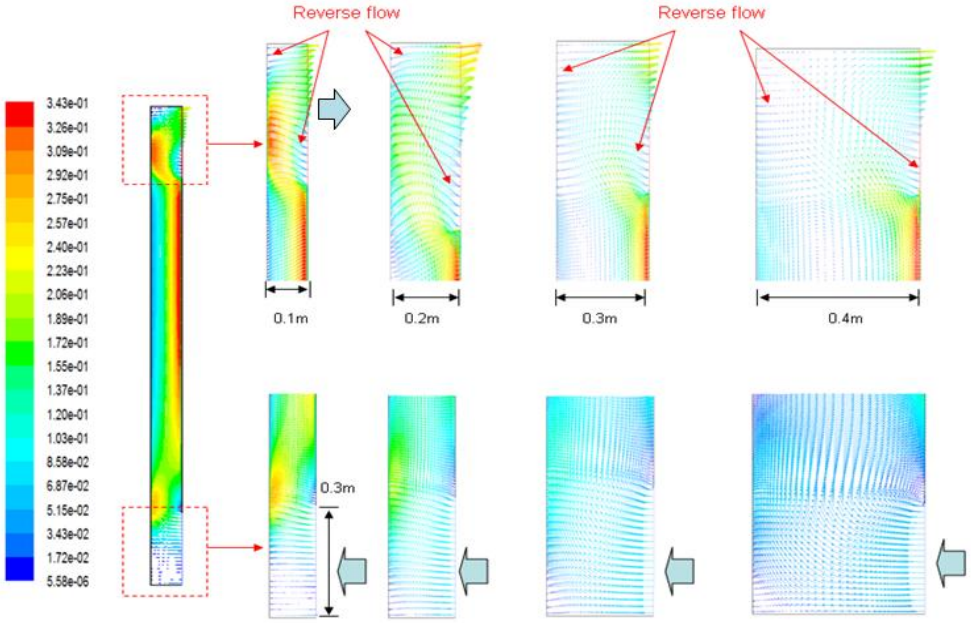

Figure 4- 9 Air flow patterns near the inlet and outlet for various air gap depth (H=0.3 m)

4.4.2.2 Mass flow rate

The variations of the mass flow rate with cavity depth and inlet height are shown in Figure 4-10. Similarly, it is seen obviously that all the trend curves of the predicted air flow rates are similar. In the inlet height range of 0.1- 0.5 m the mass flow rate firstly increases with air gap

depth increases and then decreases after a certain value of air gap width, the maximum airflow rate of 0.037 kg/s could be observed at the air gap width of 0.2 m for the inlet height of 0.2 m. Comparison the maximum mass rate of outlet on heated wall with that of outlet on unheated wall it can be found that the first one is smaller than the latter one. This can be attributed to the flow resistance of the outlet on heated wall would be larger, resulting from airflow turning from vertical to horizontal direction suddenly. Meanwhile as discussed above, a part of air flow turns to the opposite direction of outlet and develops a recirculation in the corner between unheated wall and top wall. The additional flow resistance and the recirculation reduce the flow rate.

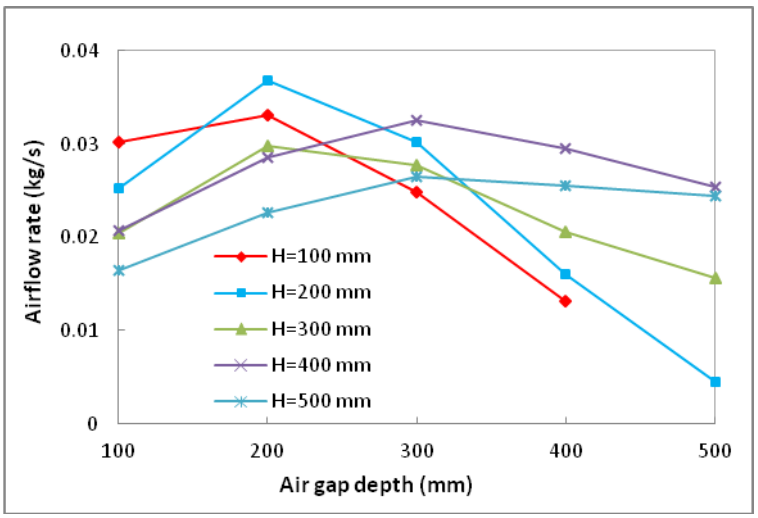

Figure 4- 10 Variations of mass flow rate with air gap depth

4.4.2.3 Air flow temperature distribution at outlet

The temperature distribution patterns within the cavity are displayed in Figure 4-11. The incoming air near the heated wall heated up firstly and expands along the gap depth direction to unheated wall therefore the air temperature distribution in cavity is non-uniform. Air temperature near heated wall is much higher than those in the middle and near the unheated wall. The temperature stratifications along the cavity height are found in all cavities, the temperature stratifications are reduced with the increase of cavity depth. It be clearly seen that the air temperature distribution at outlet where reverse flow occurs disturbed. The reverse flow reduces the average temperature of the mixed air at outlet due to the lower temperature of reverse flow.

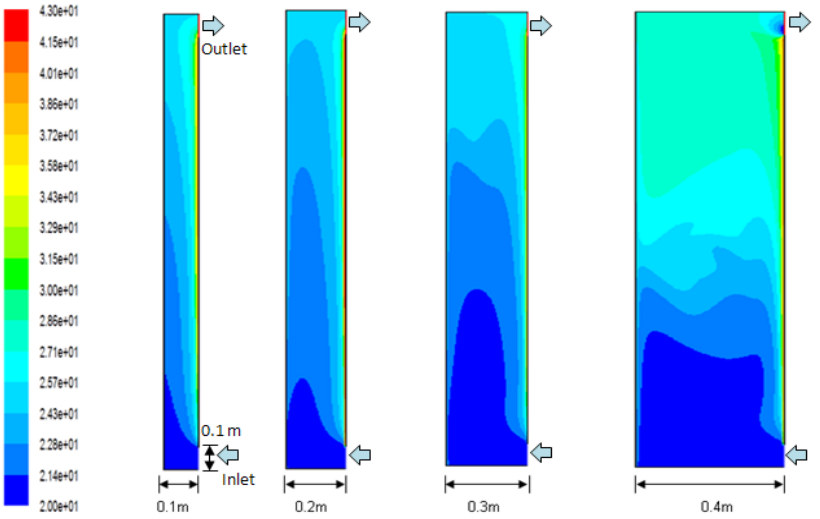
4.30e+01
4.15e+01
4.01e+01
3.86e+01
3.72e+01
3.58e+01
3.43e+01
3.29e+01
3.15e+01
3.00e+01
2.86e+01
2.71e+01
2.57e+01
2.43e+01
2.28e+01
2.14e+01
2.00e+01
Outlet
0.1 m
Inlet
0.1m
0.2m
0.3m
0.4m

(a) (H= 0.1 m)

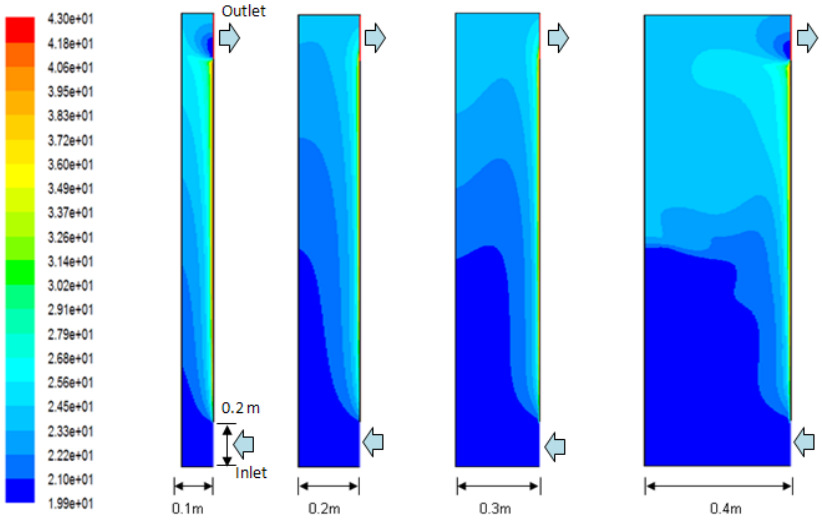
4.30e+01
4.18e+01
4.06e+01
3.95e+01
3.83e+01
3.72e+01
3.60e+01
3.49e+01
3.37e+01
3.26e+01
3.14e+01
3.02e+01
2.91e+01
2.79e+01
2.68e+01
2.56e+01
2.45e+01
2.33e+01
2.22e+01
2.10e+01
1.99e+01
Outlet
0.2 m
Inlet
0.1m
0.2m
0.3m
0.4m

(b) (H= 0.2 m)

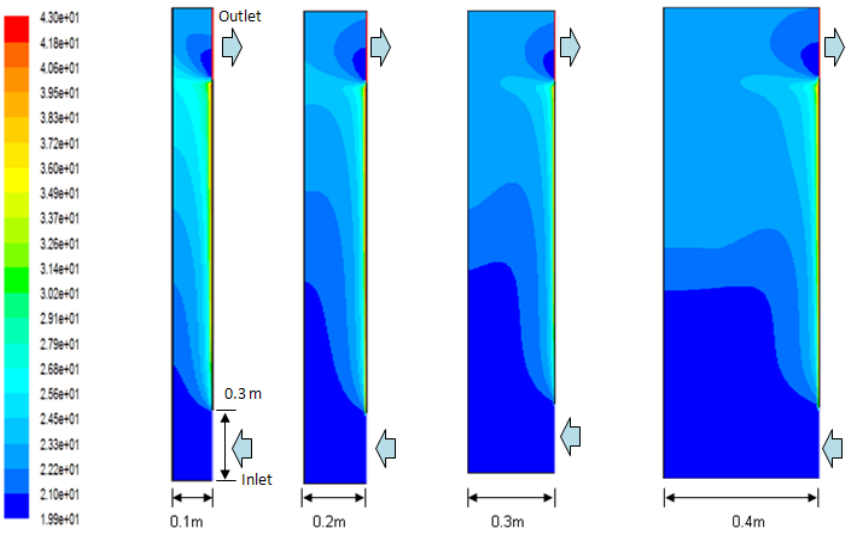

(c) (H= 0.3 m)

Figure 4- 11 Distributions of temperature patterns within air cavities

4.4.2.4 Outlet temperature

Figure 4-12 shows the variations of the air temperature at outlet with cavity depth for various inlet heights. It is seen that for the narrowest cavity (gap depth = 0.1 m) the air temperature at outlet varies only in small range between 27 ℃ and 25.7 ℃ with the gap depth increases up to 0.3 m, and then the temperature drop to 21.5 ℃ sharply due to the reverse flow occurs at outlet, the reverse flow induces fresh air into the outlet that reduces the average air temperature. When the inlet height is 0.2 m, the air temperature increases greatly from only 22 ℃ to around 25.5 ℃ firstly, and then reduces sharply to 21 ℃. The reason for this can be seen from Figure 4-11 (b) that the reverse flow occurs at outlet for the gap depths of 0.1 and 0.4 m but does not for 0.2 and 0.3 m. When the inlet height increases to 0.3 m and above, due to the occurrence of the reverse flow at the outlets, all of the three air temperature curves vary only in a small range between 22 ℃ and 20.5 ℃. The variations depend on the cavity depth. Hence, it could be concluded that the effect of the reverse flow on the air temperature at outlet is more significant than other factors. The air temperature at outlet is as high as 24.5 ℃ when the gap depth and the inlet height are 0.2 m, and it is good enough for thermal comfort of building. The solar chimney with air gap of 0.2 m deep and inlet and outlet of 0.2 m high is chosen for the further study, as maximum mass flow rate and high enough air temperature are obtained at the outlet for the proposed system.

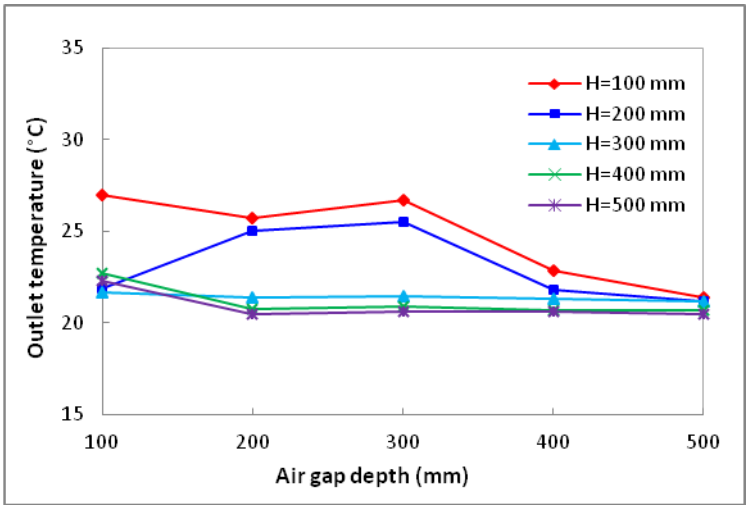

Figure 4- 12 Temperature variations at outlet with cavity depth

4.5 CONCLUSIONS

CFD has been used to study the effects of chimney geometries on buoyancy-driven air flow and temperature distribution in vertical cavity in this chapter. The vertical chimney with a constant height of 2 m and with one horizontal inlet and two horizontal outlets, the inlet fixed on heated wall whilst the two outlets fixed on unheated wall and heated wall respectively to achieve the purpose of winter heating and summer cooling. The reverse flow was observed near the outlet of solar chimney in airflow patterns when air gap depth or inlet height increased to a certain value. Particularly, when the air gap increased to 0.3 m and above, the reverse flows were found near the outlet for various inlet heights.

It is revealed that the total mass flow rate through the solar chimney and air temperature distribution at the outlet with a vertical heated wall is strongly affected by the presence of a reverse flow occurring at the outlet of the channel, the occurrence of the reverse flow results in a reduction of the total mass flow rate through the solar chimney and mean air temperature at outlet, and thus is not desirable for ventilation and heating applications. Hence, in order to maximize the mass flow rate and air temperature to enhance the ventilation and heating performance, it is desirable to minimize the reverse flow entering from the outlet. For this purpose, the solar chimney with air gap of 0.2 m deep and inlet and outlet of 0.2 m high was chosen for the further study, as reverse flow was not found at this geometry consequently obtained the maximum mass flow and high air temperature.

5. DESIGN AND DEVELOPMENT OF A FULL SCALE EXPERIMENTAL RIG AND NUMERICAL MODELS

5.1 INTRODUCTION

In order to undertake experimental assessment of the heating, cooling and ventilation performance of the proposed system, an experimental rig with the predetermined dimensions has been built at the University of Coventry. This solar chimney is set up inside a laboratory to prevent the experimental testing from the influence of variations of weather conditions. This allows the comparison of the performance of the proposed system for various operating procedures under the identical thermal conditions. The experimental rig construction, laboratory testing procedures and instrumentations are provided in this section. Numerical simulation procedure for reproduction of experimental conditions is also described. The numerical models are presented in terms of closed mode and open mode.

5.2 EXPERIMENTAL RIG CONSTRUCTION

An experimental rig is designed for the experimental study purposes and is shown in Figure 5-1. The experimental rig mainly consists of four elements as described below:

1. The rectangular PCM container with an absorber plate to encapsulate the paraffin wax RT 42.
2. The glass cover allows visible light and short-wave infrared to pass through and blocks convective and long – wave radiation heat transfer.
3. The rectangular air channel aims to direct the air flow that creates by buoyancy effect.
4. A large solar simulator to produce the desirable heat fluxes.

The side walls of the air channel are constructed from timber, the channel's internal dimensions are 1 m wide × 2 m high × 200 mm deep. As the experimental rig stands on the laboratory floor, the channel floor is fitted with a rigid polystyrene board in order to minimise radiation and convection heat exchange with the ground. Besides, there are two openings

(outlet) along the top of glass cover and absorber plate façade, respectively. There is also an opening (inlet) along the bottom of the absorber plate façade. Each opening is 1000 mm wide and 200 mm high, and these openings can be closed and opened according to the experimental purposes.

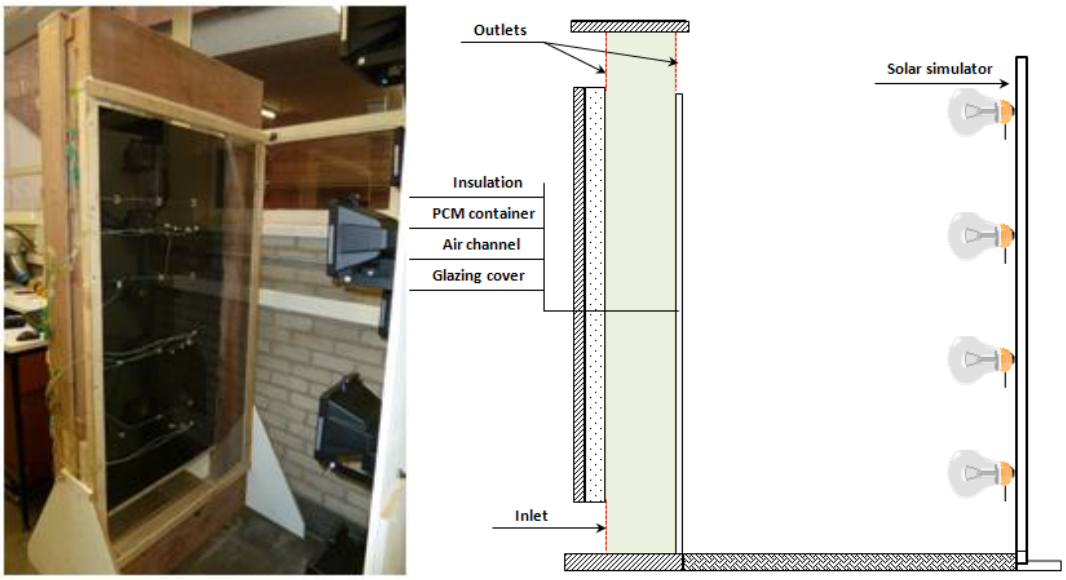

Figure 5- 1 Photo and schematic of the experimental rig

5.2.1 PCM container

The rectangular PCM container is constructed by using stainless steel, and has the dimensions of 1000 mm wide × 1600 mm high × 40 mm deep (as shown in Figure 5-2 (a)). As discussed in Chapter 4, the TCE of HF has the optimum performance among all of the TCEs studied. In order to thus accelerate the charging and discharging processes of the PCM, a total of 30 straight fins made of stainless steel are designed and each fin has the following dimensions: 1 m long, 40 mm wide and 1 mm thick (Figure 5-2 (b)). A tray is first constructed as the main component of the PCM container in where the fins are installed evenly, and each two fins are spaced by 50 mm so that cut the whole PCM into smaller layers. Once the corners of tray were welded carefully, a lid made of the same material with the tray is welded to the tray to form a seal. The lid is painted black as the absorber with high thermal absorption. A hole was drilled into the top lateral side to allow the liquid PCM to pour into inside the container via a funnel. Once the PCM container is completed, the air tightness test is conducted (see Figure 5-2 (c)). The four lateral sides and the back side of the PCM container are well insulated by

applying polystyrene board, in this manner, the heat loss from the side walls and back wall can be negligible.

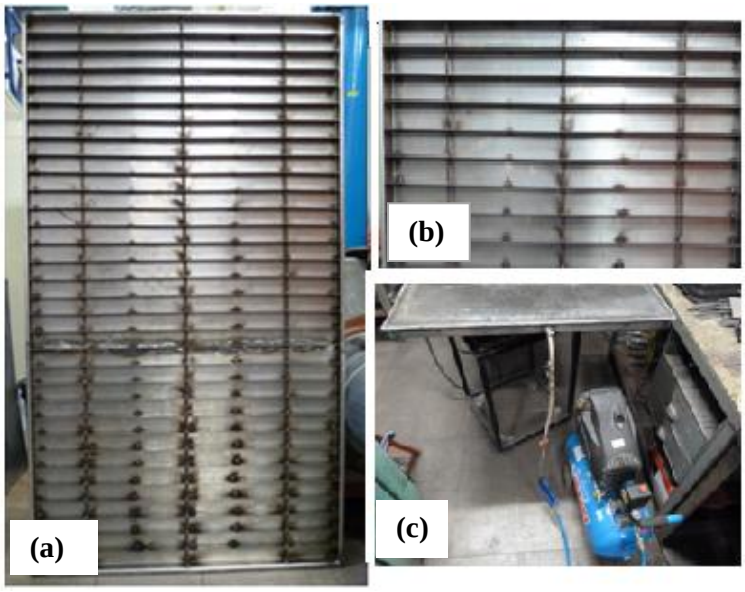

Figure 5- 2 Rectangular PCM container: (a) tray for PCM; (b) straight fins and (c) air tightness

5.2.2 Solar Simulator

A small scale solar simulator has been designed for experimental study in Chapter 3. However its radiation only covers a small area, it is too small to use in the current experiment. Hence, it is necessary to design a large scale solar simulator and use to reproduce the irradiation flux. Same to the small scale solar simulator, the tungsten halogen lamp is used to assemble the large scale solar simulator. The lamps used for the solar simulator are 400W tungsten halogen lamps fixed in fittings with built-in reflectors. Following the design guideline that provided in Chapter 4, the number of lamps and lamp-to-lamp spacing has been determined. The simulator consists of 14 lamps fixed on a light rack. The arrangement of these lamps and the large scale solar simulator designed for the current experiment are shown in Figure 5-3. The technical data provided by the manufacturer are given Table 5-1.

Table 5- 1 Technical data for the tungsten halogen lamp selected

Type of bulb	Tungsten halogen floodlight
Wattage	400 W
Voltage	240 V
Life	1000 hrs
Colour temperature	3000 ℃K
Lamp bulb length	118 mm

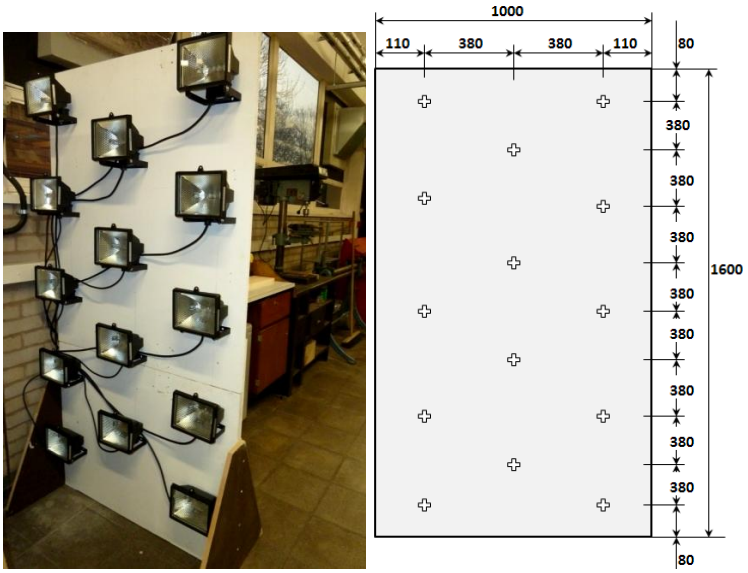

Figure 5- 3 Large scale solar simulator of experimental facility (all units are in mm)

5.3 TEST PROCEDURES

The current experiment is developed to evaluate the thermal performance of the solar chimney incorporating PCM. The following procedures are carried out to achieve these purposes.

5.3.1 Charging Process

Three different heat fluxes of 700 W/m^2, 600 W/m^2 and 500 W/m^2 (received by the absorber surface) are studied in the experiments. Each of charging-discharging cycle runs for 24 hrs.

(i). Heat flux of 700 W/m^2 is applied to the heated surface firstly
(ii). The three openings are closed
(iii). The solar simulator is turned on to start the charging process of PCM
(iv). The temperature variations inside air channel, within the PCM at different positions, and outside the solar chimney are recorded

(v). Surface temperature variations of glass cover, and absorber plate are measured

(vi). The time of the charging process is determined as all thermocouple readings within the PCM reaches the steady state condition, this can prevent the presence of solid PCM in the lower region of the PCM container. Once the thermocouple readings reach steady state condition, this indicates the charging process is finished.

(vii). Charging tests are repeated at different heat flux of 600 W/m^2, 500 W/m^2.

5.3.2 Discharging process

After the charging tests the subsequent discharging experiments are conducted immediately. The discharging test has double purposes of

1) Evaluating the heating performance of the solar chimney

(i). The solar simulator is turned off.

(ii). The inlet and the outlet along the top of absorber plate facade are opened.

(iii). The temperature variations inside air channel, within the PCM, and outside the solar chimney are recorded.

(iv). Surface temperature variations of glass cover and absorber plate are measured.

(v). Inlet air temperature, outlet air temperature and air velocity inside channel are measured.

2) Evaluating the cooling/ventilation performance

(i). The solar simulator is turn off.

(ii). The inlet and the outlet along the top of glass cover facade are opened.

(iii). Repeat the steps (iii) to (v) mentioned above.

All data are automatically recorded in a PC through data logger at interval of 60 s for the further data processing. The main aim of the current testing was to investigate how the solar chimney behaves when changing the operating procedures i.e. changing the heat flux and the outlets. To measure the temperatures of different components of the solar chimney, a number of K-type thermocouples are distributed on the glass cover, absorber plate, inside the PCM, at the openings and inside the air channel. The air velocity is measured by using an anemometer. The quality of the solar simulator in terms of distribution of flux intensity, and flux stability,

and the amount of light reflected by the glass cover are tested by using a pyranometer. The technical specifications of the instruments and their arrangements in the experiment are described below.

5.4 INSTRUMENTATION

Air velocities and air temperature inside cavity, surface temperature of heated surface and glass cover and ambient temperature are measured. Besides, the reflectance of the glass cover is also measured in the experimental analysis. The instruments are used to measure these parameters and their technical specifications are provided in Table 5-2.

Table 5- 2 Instruments for experimental study and their technical information

Instrument	Manufacture	Measurement parameter	Parameter Unit	Measurement range	Accuracy
K-type thermocouple	RS Components Ltd.	Air temperature	℃	-50~250	±0.3 ℃
Solar meter	Iso-Tech	Solar flux	W/m^2	0~2000	within ±10 W/m^2
Airflow meter	TSI Incorporated	Air velocity	m/s	0~50	±3% of reading

5.4.1 Air Velocity Measurements

As shown in Figure 5-4 and Table 5-2, air velocities inside air channel are measured by using a TSI8455 airflow probe. This velocity meter can measure very low air velocity, which is suitable for the present experiment, where air velocity is supposed to be low. The response time of the sensor is 0.2 s, the fast response time is essential for accurate estimation of turbulence air flow. It should be noted that the influence of disturbances from the chimney inlet and outlet would result in overestimating or underestimating the real air velocity value. To minimize the error, during the testing thus the airflow probe is fixed at the location of 1.2 m above the chimney bottom where the error caused by the influence of inlet and outlets is believed to be small, so that the local air velocity is much more representative. The velocities measured at the three points along the depth of air channel at cross plane are therefore considered to represent the average air velocity at height of 1.2 m. The positions of three points are 50,100 and 150 mm away from heat absorber. When using the probe, make sure

the sensor window is fully exposed and the orientation dimple is facing upstream. Due to the turbulent nature of the airflow, the average velocity is measured with 20 measurements per 20 s to represent the velocity of the airflow for each point.

Figure 5- 4 Airflow probe for measuring air velocity inside solar chimney

5.4.2 Temperature Measurements

5.4.2.1 Air temperature measurements

Air temperatures inside chimney are measured at inlet, outlet, inside the chimney and outside the chimney by using eighteen calibrated K-type thermocouples. Three thermocouples are evenly distributed at the vertical centreline of the inlet as shown in Figure 5-5. The mean temperature from the three measurements is taken as the inlet temperature. At each outlet, the air temperature is measured by three thermocouples equally distributed across the opening. The distributions of the thermocouples at outlets are the same as that at inlet. The outlet temperature is the mean of the three thermocouples readings.

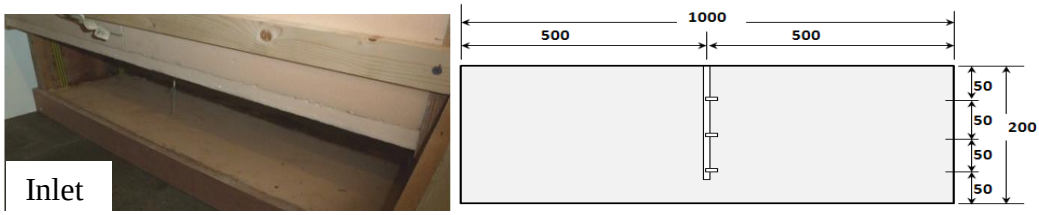

Figure 5- 5 Thermocouple distribution at inlet

Nine thermocouples are placed into the channel – typically at three positions of 600 mm, 1000 mm and 1400 mm along the height of the channel from ground level to measure air

temperature at the vertical centre-line of the channel. Three thermocouples are equally placed at each position. Figure 5-6 illustrates the distribution of nine thermocouples used for measuring air temperature inside the channel.

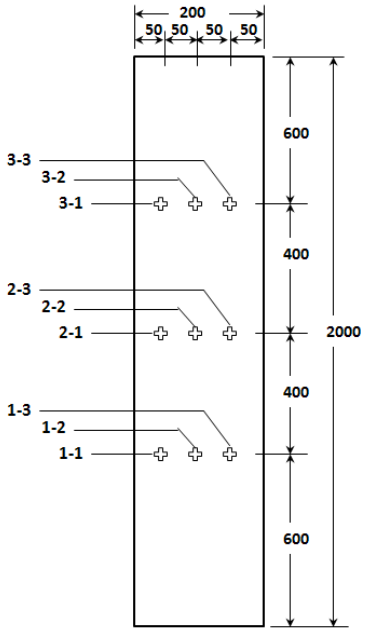

Figure 5- 6 Distribution of nine thermocouples in air channel

The thermocouples inside the channel are inserted inside reflective aluminium shields. The shields are designed specifically to avoid the thermocouples being directly heated by the thermal radiation to reduce as far as possible the measurement error. The ambient temperature is measured by a thermocouple at the height of 1000 mm from ground level. The thermocouple location is out of the coverage of the solar simulator and shielded by one side of the experimental rig. Figure 5-7 illustrates two of shielded k-type thermocouples used to measure heated surface temperature and air temperature inside cavity.

Figure 5- 7 Shielded thermocouples on heated surface and inside cavity

5.4.2.2 Surface temperature measurements

The surface temperatures of the absorber plate and glass cover are measured with fifteen thermocouples. To measure the temperatures of absorber surface, 12 thermocouples are fixed to the absorber surface with clear tape and screened from light source by using tiny strips of aluminium foil tape. The external surface temperature of glass cover is measured with 3 screened thermocouples. The distributions of the thermocouples were shown in Figure 5-8.

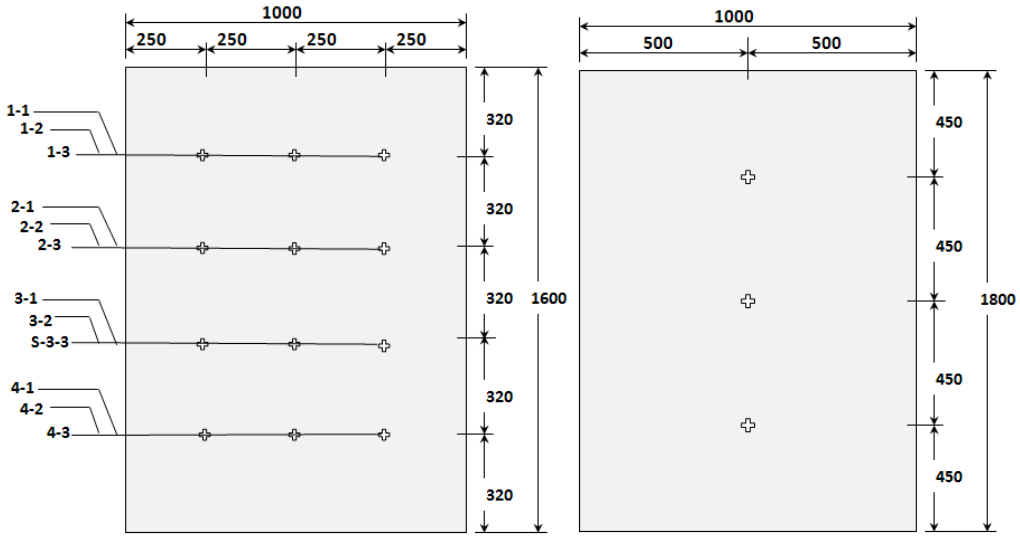

(a) absorber plate (b) glass cover

Figure 5- 8 Illustration of locations of thermocouples on heated surface and glass cover

5.4.2.3 PCM temperature measurements

To measure the temperature profiles inside PCM and determination of the charging time and discharging time, nine thermocouples are inserted into the PCM along the height at the vertical centre-line of container. The thermocouples are equally placed along the height of the container at 30, 800 and 1300 mm, which are measured from the container base. Every three thermocouples are distributed at 5, 20 and 35 mm away from the absorber plate at each location, respectively. Each thermocouple set is encased in a thin plastic tube, and the total volume of the three thermocouple sets can be ignored compared with the volume of container, they therefore have little effects on the heat transfer process during charging and discharging processes. The positions of the thermocouples are as shown in Figure 5-9.

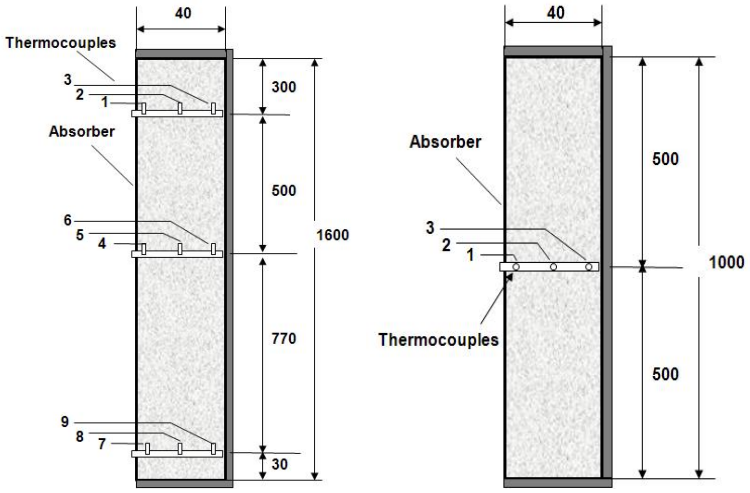

Figure 5- 9 Dimensions of PCM container and locations of the thermocouples: (a) lateral section; (b) cross section

5.4.2.4 Data Acquisition System

A DT85 is used as the data acquisition system, which is a general purpose data logger that allows it to be used across a wide variety of applications. Some of technical information for DT85 is provided in Table 5-3. DT85 is capable of storing up to 5 million data points in user defined memory, and also the stored data can be transferred and stored on a PC. The users can view real-time data in mimics, trend charts or tables and retrieve your historical data for analysis. The data-logging system is shown in Figure 5-10.

Figure 5- 10 DT85 used for data-logging and storage

Table 5- 3 Technical specifications for DT 85

Manufacturer	Thermo Fisher Scientific Ltd
Weight (kg)	2.5
Temperature range (℃)	-45~70
Humidity	85% RH, non-condensing
Data storage capacity	5 million
Thermocouple compatibility	B, C, D, E, G, J, K, N, R, S, T
Power Supply	External voltage range: 10 to 30Vdc Internal battery: 6Vdc 4Ahr lead acid

5.5 SIMULATION MODELS

A mathematical model is developed to study the performance of the proposed system, and the model will be validated by the data previously obtained from experimental measurements. The verified numerical model will be then used for the parametric analysis of the full-scale solar chimney.

5.5.1 Charging Model

As described above, the numerical simulations are based on the experimental conditions. During the charging process, all of the openings are closed. Therefore, no airflow occurs inside the air channel over this period. The theoretical analysis of heat transfer exchange for each component of the solar chimney for charging model has been expressed in Chapter 3. However, the HF as the TCE is used to enhance the thermal conductivity of the PCM. Hence the calculating equations for PCM need to be modified. Moreover, it is worth noting that heat transfer inside PCM/TCEs mixture is a very complicated phenomenon because of the existence of different phases, the solid phase of the TCEs and the PCM, which could be in solid, mushy or liquid phase during charging or discharging process. As a result, it requires writing separate energy equations for different components and phases. This numerical study concerns the performance of the whole solar chimney system and not just the PCM. Therefore, the entire domain of PCM/ TCE component could be treated as a single phase with modified properties governed by one set of conservation equations (Whitaker, 1999). Approximating the thermo-physical properties of the mixture will simplify the simulation process, and average properties of the mixture based on the volume of the PCM/TCE unit are

used in this numerical simulation. This approximate thermo-physical property method is proposed by Chow et al. (Chow et al., 1996). They examined the validity of the method by comparing the numerical results with the experimental results. It was found that the numerical results can agree with the experimental results strongly. The calculating equations for the average thermo-physical properties are expressed as

$$k_{eff} = \frac{k_f V_f + k_p V_p}{V} \tag{5.1}$$

$$\rho_{eff} = \frac{\rho_f V_f + \rho_p V_p}{V} \tag{5.2}$$

$$C_{eff} = \begin{cases} \frac{C_f V_f + C_{p,s} V_p}{V} & \text{solid PCM} \\ \frac{C_f V_f + (L/\Delta t) V_p}{V} & mushy\ PCM \\ \frac{C_f V_f + C_{p,l} V_p}{V} & liquid\ PCM \end{cases} \tag{5.3}$$

where k_{eff} is average thermal conductivity of mixture, W/m ℃; ρ_{eff} is average density of mixture, kg/m^3; V is volume of latent heat storage system, m^3; while the subscripts f, p , s, and l stand for the fins, PCM, solid state of PCM, liquid state of PCM, respectively.

5.5.2 Discharging Model

For the problem under consideration, the working fluid is air. At any time when the vents are open, fresh air at ambient conditions enters the inlet. The air passes through the air cavity, where it exchanges heat with the absorber plate. The heated air then flows back to the surroundings through the exit. Heat transfer characteristics between various components have been discussed in detail previously. Only some changes are made for description of energy balance for various components of the solar chimney during discharging process and are presented below.

The glass cover

Energy transfer through the glass cover can be written as follows:

$$\frac{dT_g}{\Delta t} \rho_g C_g \delta_g A = q_{p-g} A + q_{air-g} - q_{g-sky} A \tag{5.4}$$

where q_{air-g} is heat transfer rate convected from air inside channel to glass cover, W/m^2 .

The absorber plate

Heat transfer analysis of the plate considering the air flow is provided.

$$\frac{dT_p}{\Delta t}\rho_p C_p \delta_p A = q_{l-p}A - q_{p-g}A - q_{p-air}A \quad (5.5)$$

where q_{l-p} is heat transfer transferred from PCM to absorber surface, W/m^2.

The working fluid-air

To simplify the analysis of the air, we make the following assumptions:

1) The air flow through the system is steady at any given time step, and the accumulation of air in the system is negligible. Therefore, the air inlet and outlet mass flow rates are equal.
2) The buoyancy forces generated due to density differences are counterbalanced by flow resistances through the system.
3) The temperature of the air is uniform at any cross-section of the air channel, but may vary along the flow direction.
4) The air is treated as a perfect gas with the density linearly dependent on the temperature over the working temperature range.

The heat gained by the air in the channel between the glass cover and absorber plate suggests that this amount of energy must be equal to heat convection from absorber to the air –heat convection from air to the glass – useful heat brought by the air. The energy balance equation for the working fluid can be written as:

$$\frac{dT_{air}}{\Delta t}\rho_{air} C_{air} V_{air} = q_{p-air}A - q_{air-g}A - mC_{air}(T_i - T_o) \quad (5.6)$$

Where T_i and T_o are the air temperature at inlet and outlet; T_{air} is the mean air temperature inside cavity; *m* = air mass flow rate, kg/s.

The mean air temperature can be described as below:

$$T_{air} = \gamma\, T_i + (1-\gamma) T_o \qquad (5.7)$$

In the above equation, γ is the mean temperature approximation coefficient, the value of 0.74 has been suggested by Ong and Chow (Ong and Chow, 2003).

Airflow rates

As discussed previously, the buoyancy force is balanced by the friction force throughout the system. Hence, the air flow rate can be calculated by using the following equation (Bassiouny and Koura, 2008).

$$m = C_d \rho_{air} A_o \cdot \sqrt{1 + A_r^2} \cdot \sqrt{2 g H_c (\Delta T / T_i)} \qquad (5.8)$$

Where C_d is a discharge coefficient, which would be experimentally determined; ρ_{air} is the density of the air; $\triangle T$ is temperature difference between the outlet air and inlet air; T_i is the inlet air temperature; A_o is the chimney outlet area; H_c is the height along the chimney, and $A_r = A_i / A_o$ is an aspect ratio.

5.5.3 Initial and boundary conditions

For the charging period, the PCM is initially solid and its temperature and the temperatures of various components of the system are assumed at room temperature, T_0. This situation can be expressed as follows

$$T_{m,s} = T_0\,, \qquad t = 0 \qquad (5.9)$$

$$T_g = T_0\,, \qquad t = 0 \qquad (5.10)$$

$$T_p = T_0\,, \qquad t = 0 \qquad (5.11)$$

Boundary conditions

$$-k_l \frac{\partial T_l}{\partial x} = q_{w-m}\,, \qquad x = 0,\ t > 0 \qquad (5.12)$$

$$\frac{\partial T_m}{\partial x} = 0, \qquad x = \delta_m, t > 0 \qquad (5.13)$$

where δ_m = thickness of PCM, m; x = direction from absorber to PCM.

For discharging period, the PCM's temperature and the temperatures of various components depends on the final condition of melting during the charging period. The air inlet temperature equals to the room temperature, T_0. A computer program written in 'Matlab' is used for calculation the temperatures of T_w, T_g, T_l and T_{air}. These temperatures along with equation 5.8 can be used to obtain the air mass flow rate.

As expected, if the total amount of heat stored during charging period completely released to the air flowed through the channel and to the outside environment of the system within the discharging time, i.e. $Q_p = Q_{air} + Q_{am}$, the program procedure is ended. Otherwise, the program procedure would be stopped at the end of discharging time. The air flow rate is expressed in terms of mass flow rate instead of volumetric flow rate since mass flow rate remains constant in all parts of the system, regardless of changes in temperature.

5.6 SIMULATION DATA / SPECIFICATION

The data used for the numerical simulation is given in Table 5-4.

Table 5- 4 Numerical simulation data

Quantity	Units	Value
Height between inlet and outlet	m	1.8
Chimney depth	m	0.2
Chimney width	m	1
Insulation material thickness	m	5×10^{-2}
Outlet area	m^2	0.2
Inlet area	m^2	0.2
Height of the PCM container	m	1.6
Depth of the PCM container	m	4×10^{-2}
Width of the PCM container	m	1
Thermal conductivity of stainless steel	W/m K	16
PCM mass	kg	50
Initial PCM temperature	℃	varying
Heat flux	W/m^2	700, 600 and 500
Solar chimney tilt angle	°	90
Ambient temperature	℃	varying
Inlet air temperature	℃	varying
Thermal conductivity of insulation material	W/m K	0.0361
Dynamic viscosity of air	m^2/s	19.5×10^{-6}
Absorber plate emittance	-	0.94
Absorber plate absorptivity	-	0.94
Effective emissivity of glass cover	-	0.94
Transmissivity of glass cover	-	0.88
Glass cover thickness	m	5×10^{-3}

5.7 CONCLUSIONS

A full scale solar chimney rig with optimum geometries was set up for investigation of its thermal performance when the pre-selected PCM was applied to it. Meanwhile, one of aims of experimental test is to obtain a data set, and then the data would be validating the accuracy of a numerical model, which is developed based on the experimental conditions. The numerical models will be further used to predict the thermal performance of a solar chimney by changing various parameters.

6. ANALYSIS OF EXPERIMENTAL AND NUMERICAL RESULTS

6.1 INTRODUCTION

In Chapter 5, the experimental procedure for study of the performance of the solar chimney under laboratory conditions was provided. In this chapter, the influence of heat flux on the thermal performance of the PCM-based solar chimney is studied. One of main purposes for undertaking an experimental study is to obtain a data set that could be used to verify the ability of a mathematical model to predict the air flow rate, air temperature at outlet, glass cover temperature and absorber plate temperature.

6.2 STABILITY OF LAMPS AND TRANSMITTANCE OF GLASS COVER

Before starting the experimental test, it is necessary to ensure that the heat flux from the solar simulator is stable. Consequently, the heat flux applied to the experiment does not vary significantly. The transmittance of glass cover is also required for the numerical simulation. Figure 6-1 shows the flux from a single halogen lamp over a period of 10 min and the flux passed through the glass cover. It can be seen that the heat flux of 800 W/m^2 obtained from a single halogen lamp is nearly stable over this period of 10 min. It hence can be concluded that a stable flux intensity obtained by using this kind of halogen tungsten lamp. The transmitted heat flux of about 700 W/m^2 is obtained and is nearly stable also. Therefore the transmittance of the glass cover is 87.5 % would be used to numerical simulation later.

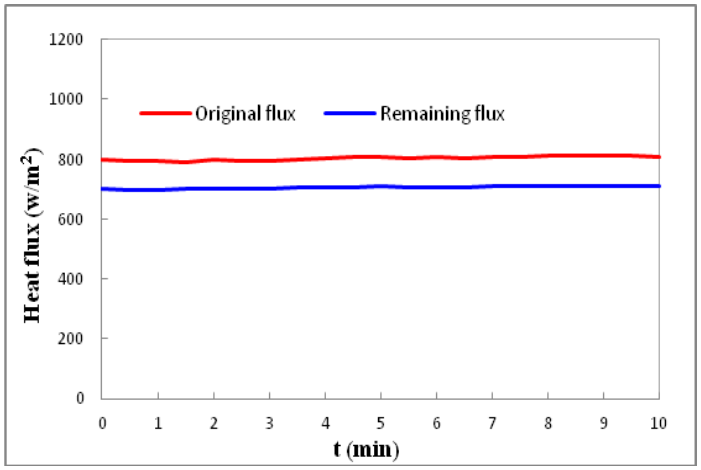

Figure 6- 1 A 10-min period of heat flux obtained from a single lamp

6.3 DISCHARGE COEFFICIENT CALCULATION

Prior to conducting the simulation study, a number of experimental works were carried out to measure a characteristic parameter, namely the discharge coefficient (C_d). Discharge coefficient is an important parameter to determine the mass flow rate through the system in theoretical models. The discharge coefficient takes into account the non-uniform distribution of inlet velocities, contraction of fluid stream, surface roughness, etc. The discharge coefficient has been experimentally investigated on different full scale systems. Flourentzou et al. (Flourentzou et al., 1998) defined the discharge coefficient as the product of the velocity coefficient and the contraction coefficient. Ong (Ong, 2003) used a value of 0.6 as it was suggested in the literature (Flourentzou et al., 1998). Similarly, in the present work the coefficient is experimentally determined by measuring the air flow rate, the air inlet and air outlet temperatures, the inlet and outlet areas and the height of the chimney, by using the equation derived by Bansal et al., (Bansal et al., 1993), which is:

$$Q_{in} = C_d \cdot A_o \sqrt{[2 \cdot (\Delta T/T_i) \cdot g \cdot H]} / \sqrt{1 + A_r^2} \quad (6.1)$$

The discharge coefficient can be calculated as follows:

$$C_d = Q_{in} \cdot \sqrt{1 + A_r^2} / A_o \sqrt{[2 \cdot (\Delta T/T_i) \cdot g \cdot H]} \quad (6.2)$$

Where Q_{in} is the volumetric air flow rate in the chimney *kg/s*, C_d is the discharge coefficient, A_o is the outlet area m^2, H is the height along the chimney m, g is the gravitational

acceleration, $A_r = A_i/A_o$ is an aspect ratio, $\triangle T$ is the air temperature difference between outlet and inlet K and T_i is the inlet temperature K. The average discharge coefficients of 0.47 and 0.44 are experimentally determined for cooling mode and heating mode to model the mass flow rate on numerical model of the proposed system.

6.4 RESULTS AND DISCUSSIONS

In this section the results from the experimental testing and numerical simulation of the thermal performance of the solar chimney are presented. Three different heat fluxes of 700, 600, and 500 W/m^2 are studied in experiments. The following analysis is carried out:

- Temperature distributions of the PCM
- Temperature distributions of the absorber plate
- Temperature variation inside chimney
- Comparison of experimental and numerical results

6.4.1 Temperature Distributions inside PCM

Each experiment is performed for 24 h. To eliminate any unexpected errors during testing, each test is repeated twice and so for each heat flux two separate sets of data are obtained (1st test and 2nd test). The measured temperatures with time for the 1st test are shown here. Figure 6-2 shows the temperature profiles of the PCM with 700 W/m^2 during the whole charging and discharging processes. As shown, during the initial melting period of 1h 40 min, there is almost a linear increase in all temperatures. The conduction heat transfer dominates this period and the absorbed heat is stored as sensible heat and raises the PCM temperature, until the temperature reaches 38 ℃, at which point the melting starts. Abrupt rises are found from thermocouples T-1 to T-6, which are located in the upper region of the PCM, whilst the temperatures of T-7 to T-9 still climb slowly due to the occurrence of convection. The temperature in the upper region of the PCM is higher than the lower region.

T-9 is the last point at which melting starts, when the temperature reaches around 43 ℃ and keeps stable, indicating that the whole PCM inside the container has fully melted. The total melting time is 7 hr 10 min. After the melting period the discharge period starts. As shown in Figure 6-2, the temperature of the upper region drops dramatically, while the temperature of

the lower region keeps almost steady. This is attributed to the fact that the stored thermal energy in the upper region is mainly sensible heat (higher than 43 ℃), whilst that in the lower PCM is latent heat. At the initial 3h 50min, the temperature difference between the upper and lower region descends sharply till the upper region temperature reduces to around 43 ℃. T-6 is the last point to solidify, when its temperature reduces to around 38 ℃ the whole PCM is solidified completely. The whole freezing process including the initial sensible heat discharging period is 13h 50min, and afterwards the second sensible heat discharging period starts.

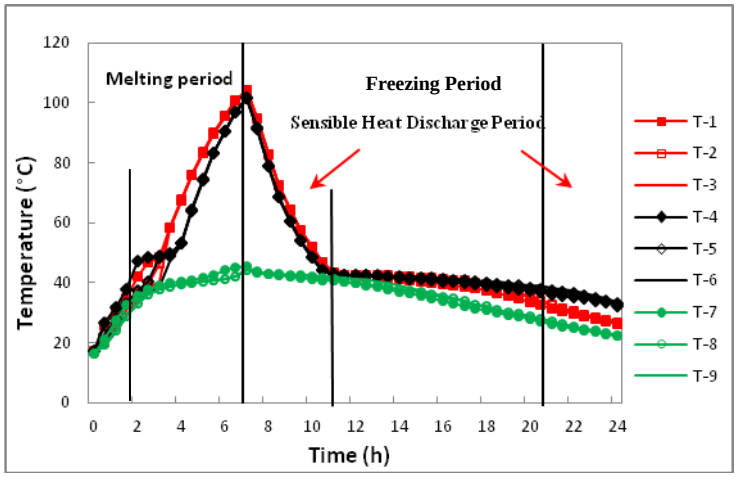

Figure 6- 2 Temperature variations of the PCM during charge and discharge periods (700 W)

Figures 6-3 (a) and 6-3 (b) illustrate the temperature variations of the PCM during charging and discharging periods under heat fluxes of 600 and 500 W/m^2, respectively. The charging processes of the two cases last for 7h which are the same as that of the case of 700 W/m^2. Within the same charging period, comparing the figures in the case of 700 W/m^2, though the applied heat fluxes are different, the trends of temperature inside the PCM vary similarly. For 600 W/m^2, it can be seen that only thermocouples T-1~T-7 reach or exceed the melting temperature of the PCM. While the temperatures for thermocouples T-8 and T-9 are still lower than the melting temperature, the temperature for last point T-9 is 41.1 ℃. For 500 W/m^2 the temperatures of thermocouples T-7~T-9 are below the melting temperature of 42 ℃, The temperature of T-9 is 40.5 ℃. This means that the PCM in the container is partially melted at the end of the charging process in these two cases. The whole freezing process, including the initial sensible heat discharging period, is 13h 50min for the case of 600 W/m^2, while that for the case of 500 W/m^2 is 13h 20 min. It is seen that, although the heat fluxes are

different, the freezing times are almost the same in each case.

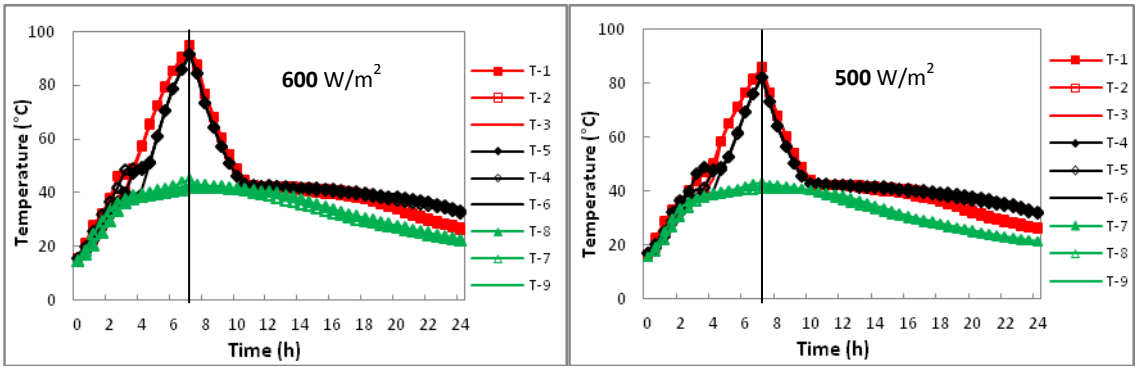

(a) b)

Figure 6- 3 Temperature variations of the PCM during charge and discharge periods: a) 600 W; b) 500 W

6.4.2 Temperature Distributions of the Absorber Plate

Absorber surface temperature profiles at four different heights in the case of 700 W are shown in Figure 6-4, Figures 6-5 (a) and 6-5 (b) illustrate the temperature variations of the absorber plate under heat fluxes of 600 and 500 W/m^2. As shown, similar to PCM temperatures, the temperatures of the absorber demonstrate the similar variation trends. It is seen that the surface temperature begins to increase over time during the charging period. Similar to the PCM, the absorber surface temperatures are nearly identical at the early stage of the charging process. As around 43 ℃, the surface temperatures begin to differ, increasing from top to bottom, indicating the PCM begins to melt. The further heat transfer in the PCM is convection controlled. An interesting phenomenon between the surface temperatures is observed. The upper surface temperatures (heights 1-3) ascend to a higher level, then reduce steeply to around 55 ℃ and then keep almost stable. This is because the input heat is slowly transferred to the solid PCM by conduction, due to the low thermal conductivity of the PCM, and consequently most of the input heat is used to raise the temperature of the absorber surface. The heat transfer by conduction almost becomes negligible as the melting process continues. The further melting is mostly by natural convection, which accelerates the heat transfer process, resulting in temperature reduction of surface. When the phase change transition process starts, the PCM stores the input heat as latent heat with little rise in temperature. Once the local PCM fully melts the surface temperatures rises sharply till the

whole PCM is in a liquid state. When the discharging process starts, the surface temperatures reduce quickly to a plateau, about 41 ℃, and then continue to drop slowly. Unlike the PCM temperatures, the surface temperatures at different heights are nearly the same over the discharging period.

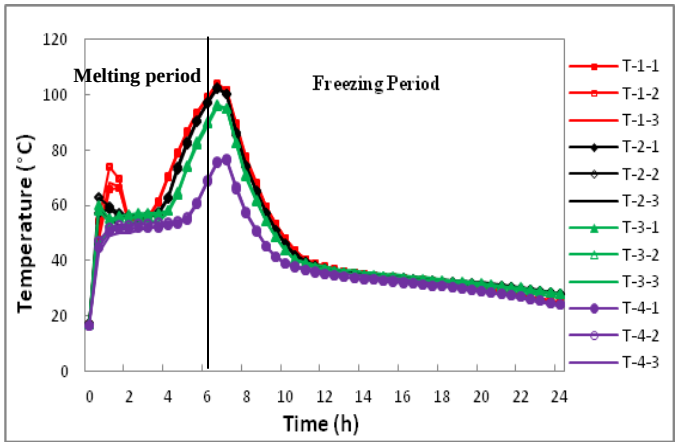

Figure 6- 4 Temperature profiles of the heat absorber at four heights (700 W/m^2)

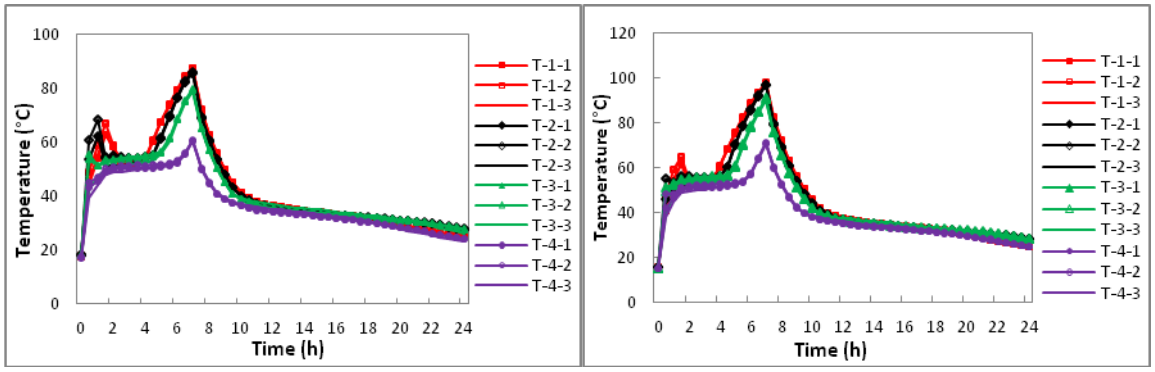

(a) (b)

Figure 6- 5 Temperature profiles of the heat absorber at four heights: (a) 600 W/m^2; (b) 500 W/m^2

6.4.3 Temperature Variation inside Chimney

The variation trends of temperature inside the chimney in all cases are similar. Figure 6-6 shows the temperature profiles along the chimney gap at a height of 600 mm above the chimney bottom for heat flux of 500 W/m^2. It is seen that the temperature distribution along the chimney gap is very uniform, and the temperature variation trend is similar to that for the absorber surface during the charging period. Once the ventilation starts, the air temperature drops sharply until the inlet air is heated by the absorber surface. During the discharging period, the temperature distribution stops being uniform, with higher air temperature near the

absorber and lower temperature near the glass cover. As the absorber temperature descends, the air temperatures are uniform again at the late discharging period. Figure 6-7 shows the temperature variation along the channel height at the three different heights of centre-line. It can be seen that during the charging period, the air temperatures vary, corresponding to the absorber surface temperature at the same heights. When the ventilation begins the air temperature inside the chimney increases gradually along its height. It is also observed that the air temperature at upper zone of the channel is higher than those at the middle zone and lower zone during the whole charging and discharging periods.

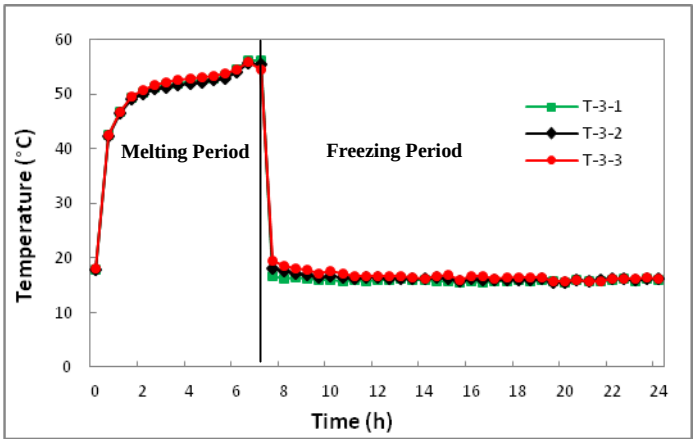

Figure 6- 6 Temperature distribution along channel gap at 600 mm above the channel floor (500 W/m^2)

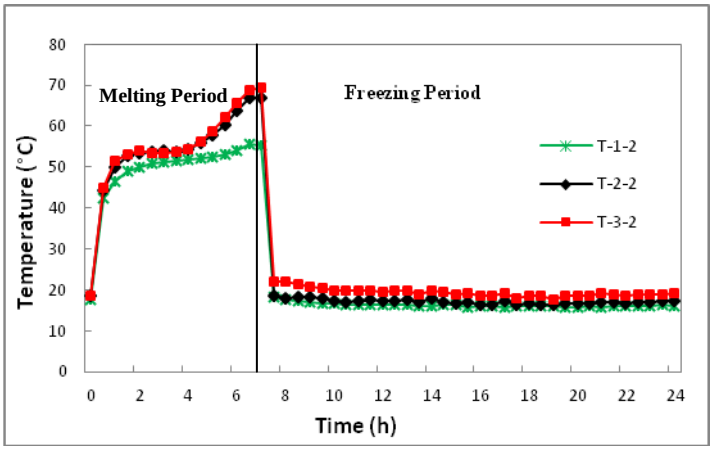

Figure 6- 7 Temperature distribution along channel height at centre-line of channel floor (500 W/m^2)

6.4.4 Comparison of Experimental and Numerical Results

In order to simulate accurately the experimental process, the corresponding experimental conditions are employed to mathematical model. The total simulation period is 24 h and the

charging time in simulation is 7h 10min. The mean ambient air temperature measured during the tests is used in the simulation and the experimental heat flux on the absorber surface is taken as the heat input to the simulation model. The simulations are performed for heating and cooling operations.

6.4.4.1 Charging and discharging behaviours of the PCM

A detailed numerical model based on the experimental conditions is developed and simulations are carried out. A comparison of numerical and experimental melting and solidification processes of the innermost layer PCM under the radiations of 700, 600 and 500 W/m^2 are shown in Figures 6-8 (a) to 6-8 (c), respectively. The numeral and experimental results show the similar variation trend with time in the case of 700 W/m^2. With the same charging time, the model gives a good prediction of the PCM temperature for 600 and 500 W/m^2. At the end of the charging process, the simulated temperature of the PCM is 40.5 ℃, which is only 0.6 ℃ different from that of the actual temperature for 600 W/m^2, whilst the simulated PCM temperature is 40 ℃, which is 0.5 ℃ lower than that of the actual temperature for 500 W/m^2. Regarding the freezing times for 500 and 600 W/m^2, except for the very initial solidification periods, the numerical predictions achieve good agreement with the experiments. Thus, the present model has the capability of predicting the melting and freezing time for different operating conditions.

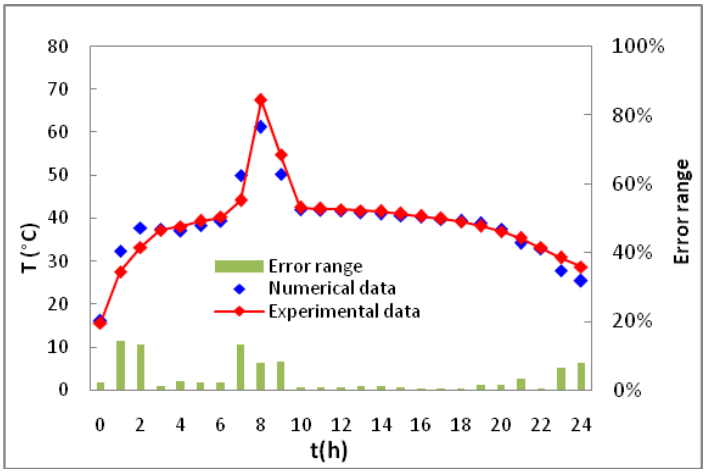

(a) 700 W/m^2

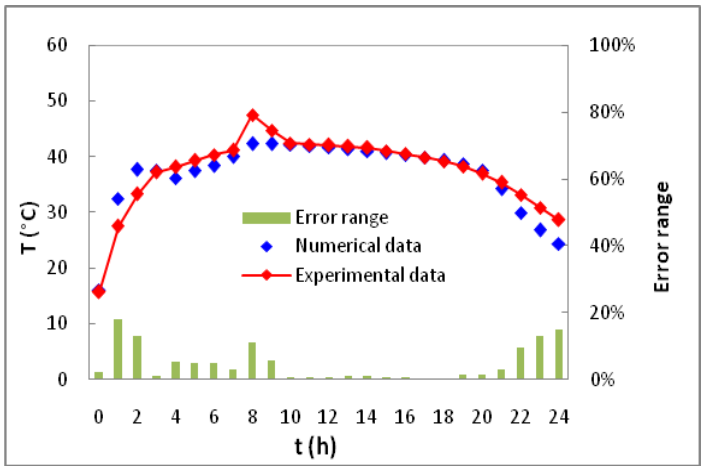

(b) 600 W/m^2

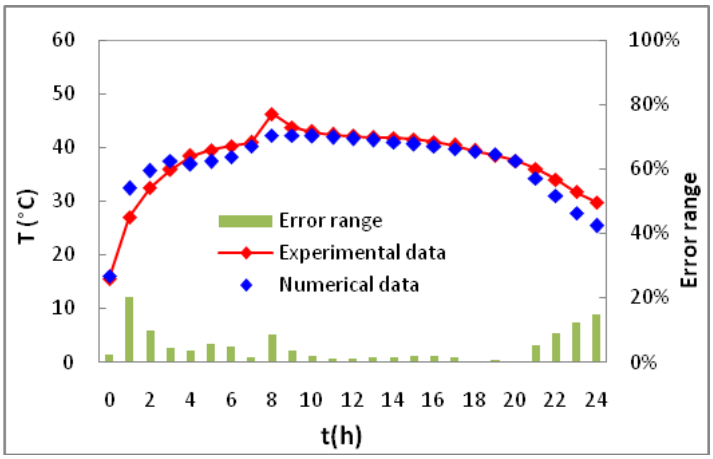

(c) 500 W/m^2

Figure 6- 8 A comparison of the numerical result and experimental result during charging and discharging periods: (a) 700 W/m^2; (b) 600 W/m^2; (c) 500 W/m^2

6.4.4.2 Absorber surface temperature

Figures 6-9 (a) to 6-9 (c) show the numerical and actual absorber surface temperatures during the charging and discharging processes for heat fluxes of 700, 600 and 500 W/m^2. The absorber surface temperature is the mean value of 12 individual temperature readings taken over the plate. For all of the cases studied, the figures show that the trends of the simulated temperature and the experimental result for the absorber surface are essentially the same. There is, however, a marked difference in the temperature during the charging process. This difference is caused by the natural convection occurring in the PCM that was not considered in numerical simulation. It is this mechanism that causes the non-uniformity of the surface temperature.

As seen, the model predicts a more accurate absorber surface temperature during the

discharging process. The predicted surface temperature is lower than experimental temperature during the initial period and late period of freezing process. The reason for this is that PCM absorbed more sensible heat during the charging process compared with the numerical simulation, due to the natural convection and the average thermo-physical properties method applied to this present model. However, the actual temperature closes to the predicted temperature very quickly. Hence, the present model and the experimental results are in reasonable agreement. As seen, comparing the results in the cases of 600 and 500 W/m^2 with those in the case of 700 W/m^2, similar agreement is found for absorber surface temperature. The model can predict the absorber surface temperature accurately for different heat fluxes.

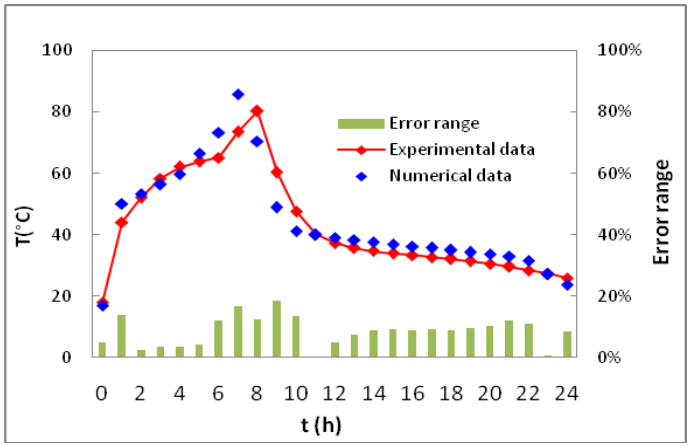

(a) 700 W/m^2

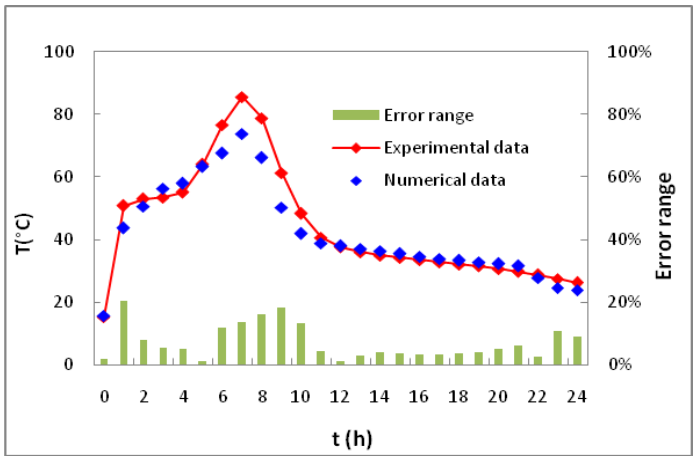

(b) 600 W/m^2

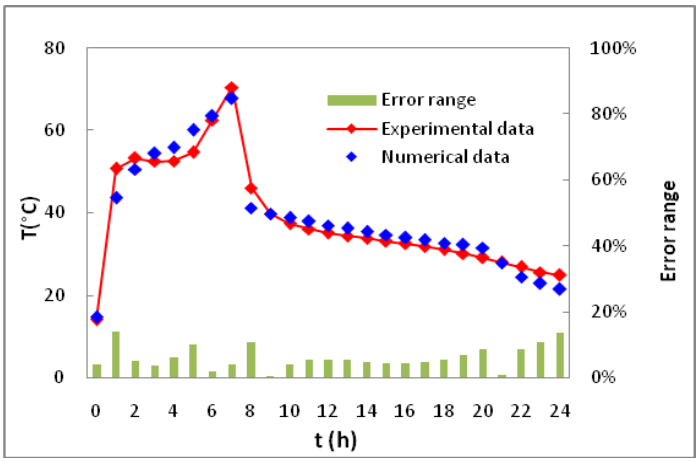

(c) 500 W/m^2

Figure 6- 9 A comparison of the numerical result and experimental result for absorber surface during charging and discharging periods: a) 700 W/m^2; b) 600 W/m^2; c) 500 W/m^2

6.4.4.3 Glass temperature

Figures 6-10 (a) to 6-10 (c) illustrate the temperature profile of glass predicted by the present model and experimental result under heat fluxes of 700, 600 and 500 W/m^2 for the discharging process, respectively. For all of the cases studied, as seen, the numerical result shows a very good agreement with the actual glass temperature. However, the numerical results are slightly lower than experimental results. This may be attributed to the differences between the actual thermo-properties of the glass and the theoretical values assumed in the numerical simulation. Comparison of the temperature profile of the glass to that of the heated surface, it can be seen that they have a similar variation trend, which means that the glass temperature does have an influence from the absorber plate.

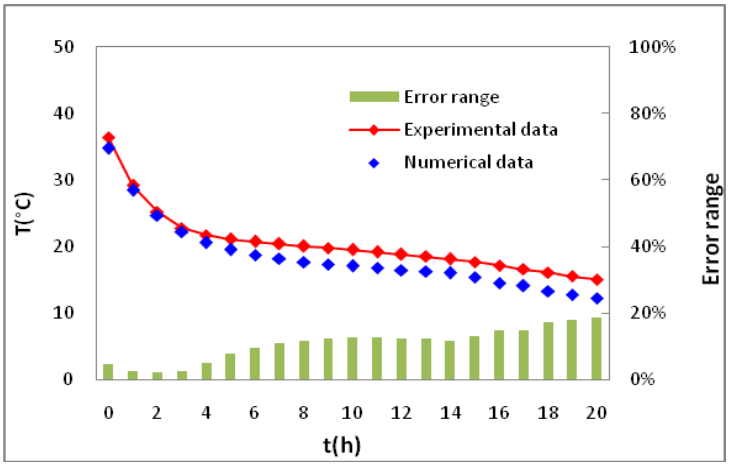

(a) 700 W/m^2

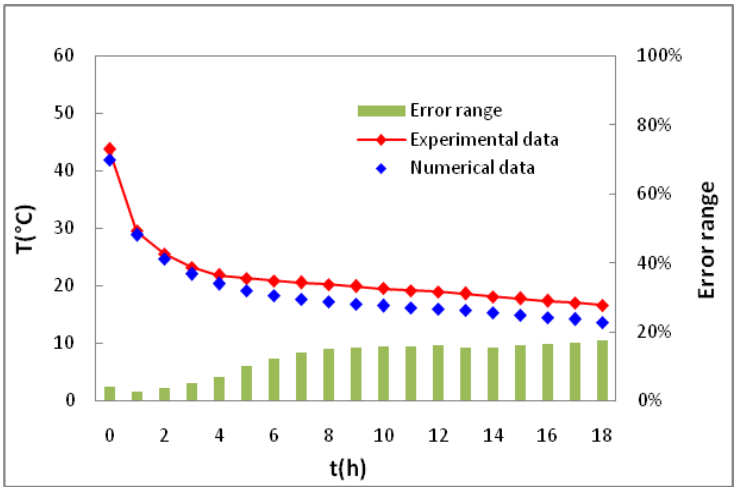

(b) 600 W/m^2

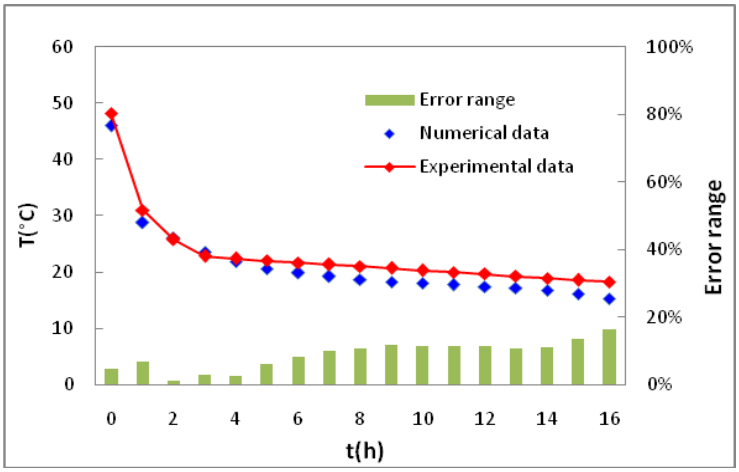

(c) 500 W/m^2

Figure 6- 10 A comparison of the numerical result and experimental result for glass temperature: (a) 700 W/m^2; (b) 600 W/m^2; and (c) 500 W/m^2

6.4.4.4 Mass flow rate

For heating purposes, the most important quantity of a solar chimney is the outlet temperature, which should be warm enough to provide thermal comfort to a living space. However, for cooling and ventilation purposes, the useful commodity is the mass flow rate, which should be high enough to provide fresh air to a living space. The two quantities predicted by numerical simulation and experiment are presented below.

Figures 6-11 (a) to 6-11 (c) present the mass air flow rates for numerical simulation and experimental tests for a complete freezing process under heat fluxes of 700, 600 and 500 W/m^2. The experimental mass flow rate is the mean of the three simultaneous readings at the height of 1.2 m from ground. In comparing numerical results to experimental results, as seen, the numerical model has the ability to predict the mass flow rate accurately. The mass flow rate is high initially, due to the high heat transfer rate between the air and the heated surface. The maximum experimental mass flow rates are 0.092 kg/s, 0.08 kg/s and 0.79 kg/s for heat fluxes of 700, 600 and 500 W/m^2, respectively. However, there is a sharp drop in the mass flow rate found for all of the cases during the initial 2h. This is the period where sensible heat exchange is predominant. Although it lasts for a short time compared to the total discharging period, its effect on mass flow rate is significant. After the temperature of the PCM reaches the melting point, heat transfer between the air and the PCM occurs at a relatively constant rate and lasts for 11h. The mass flow rate decreases very slowly and varies around 0.038 kg/s, followed by 0.037 kg/s and 0.36 kg/s for the cases of 700,600 and 500 W/m^2.

This is the period where the latent heat exchange is predominant. This period is followed by a sharp drop in mass rate. The heat exchange between the air and the PCM decreases quickly due to sensible heat dominating this period again.

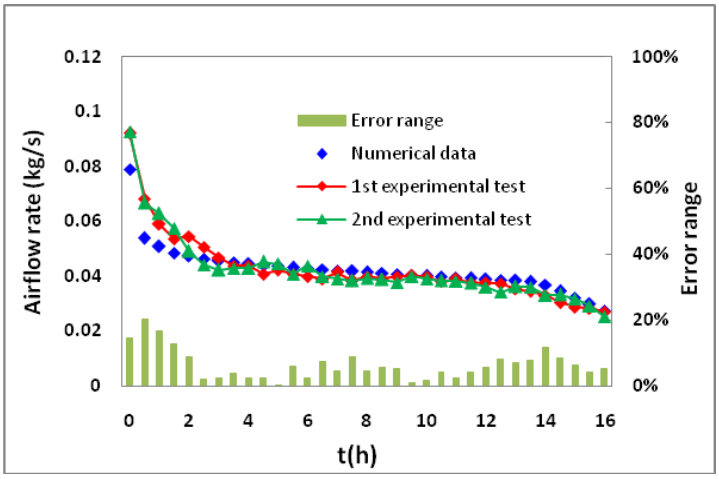

(a) 700 W/m^2

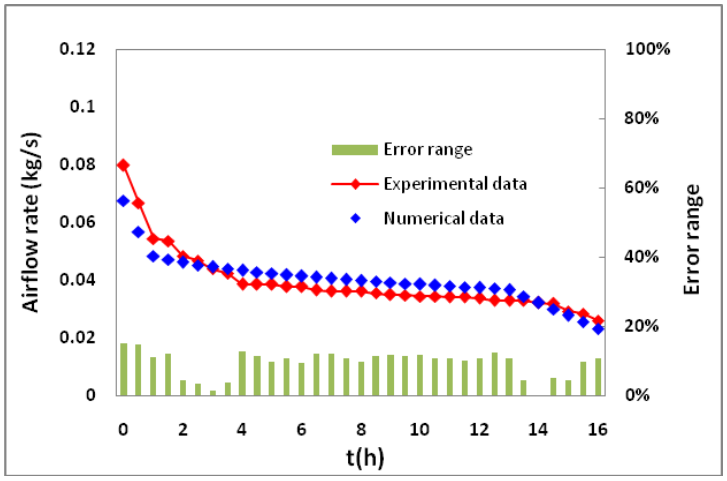

(b) 600 W/m^2

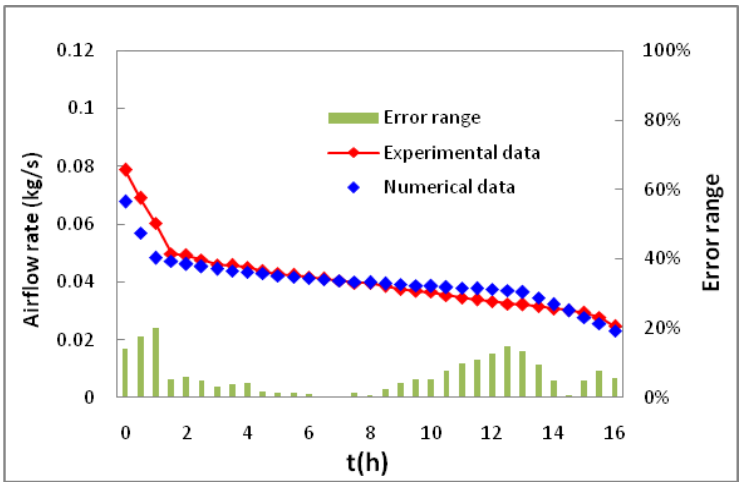

(c) 500 W/m^2

Figure 6- 11 A comparison of the numerical result and experimental result for mass flow rate: (a) 700 W/m^2; (b) 600 W/m^2; and (c) 500 W/m^2

Figures 6-12 (a) to 6-12 (c) illustrate the mass flow rate for numerical simulation's prediction and experimental tests for cooling and ventilation operation under heat fluxes of 700, 600 and 500 W/m^2. It is seen that the mass flow rates of the cooling mode show a similar variation trend to those of heating mode. That is, the mass flow rate is high and drops quickly initially. The maximum experimental mass flow rates are 0.101 kg/s, 0.095 kg/s and 0.84 kg/s for heat fluxes of 700, 600 and 500 W/m^2, respectively. After the initial 2h, the mass flow rate decreases very slowly during the latent heat discharging period, which lasts for 11h. The mass flow rate varies around 0.04 kg/s, followed by 0.039 kg/s and 0.38 kg/s for the cases of 700,600 and 500 W/m^2 during this period. After the latent heat discharging period, the mass flow rate drops sharply again. It can be seen that the mass flow rates are slightly higher than those in the heating mode through the whole discharging period. This is due to the discharge coefficient of the solar chimney for cooling mode being smaller than that for the heating mode.

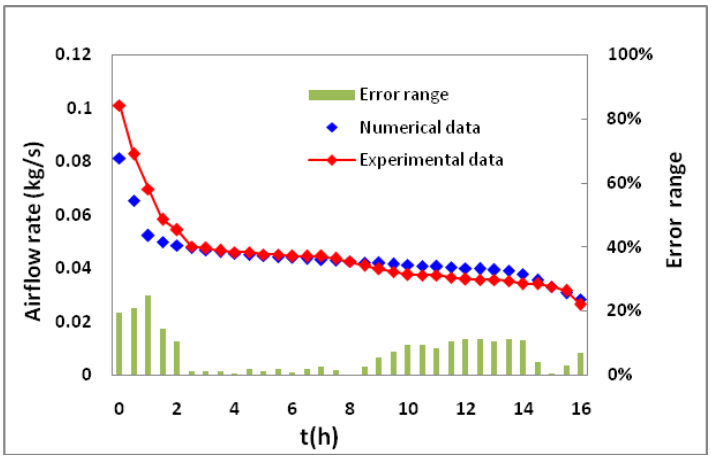

(a) 700 W/m^2

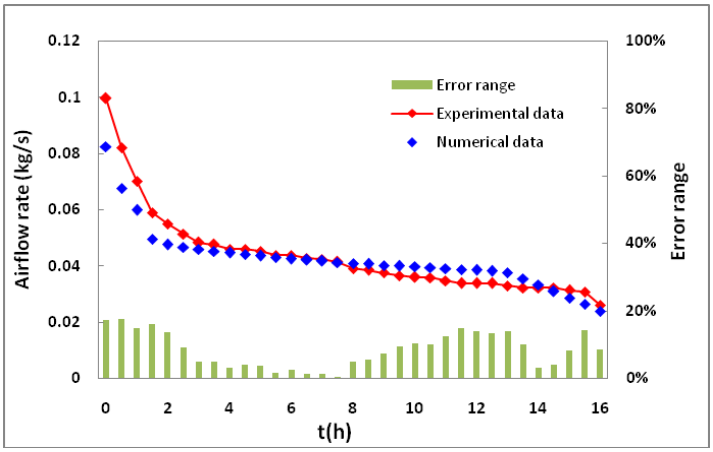

(b) 600 W/m^2

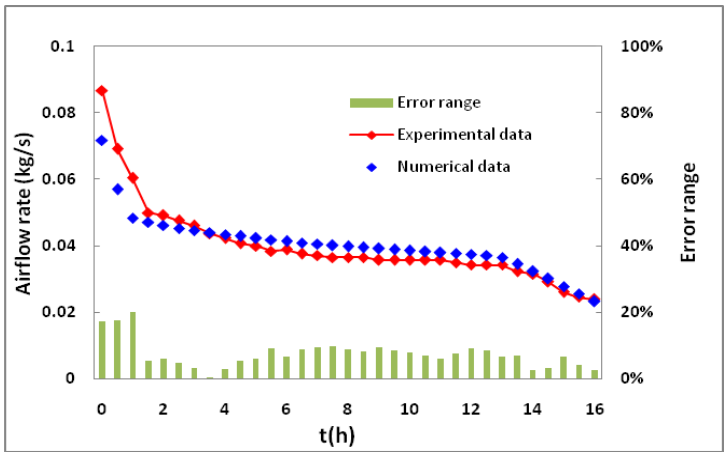

(c) 500 W/m2

Figure 6- 12 Mass flow rates of numerical simulation and experimental test for cooling and ventilation operation: (a) 700 W/m^2; (b) 600 W/m^2; and (c) 500 W/m^2

As mentioned previously, the mass flow rate is calculated by the present model based on the predicted total heat energy stored in the PCM. Therefore, the present model predicts accurately the total heat stored in the PCM during the melting period and the amount of the energy for each component of the system during freezing.

6.4.4.5 Outlet air temperature

Figures 6-13 (a) to 6-13 (c) show the simulated and experimental results for outlet air temperature during the discharging process in the cases of 700, 600 and 500 W/m^2. The measured inlet air temperatures are almost same, which are around 15 ℃, and this value is applied to the numerical model as inlet air temperature. For the cases studied, as shown, a

close agreement between numerical results and experimental results is found. Similar to the figure of mass flow rate, there is a quick drop of air outlet temperature in both numerical simulation and experimental test initially. When the temperature of the PCM decreases to its solidification temperature, and afterwards, the variation curves of air temperatures become stable with time. However, a marked difference between the numerical results and the experimental results during the initial phase of the discharging period is found. That is, lower temperature is predicted by the numerical model. This may not be due to the inability of the numerical model to predict accurately the outlet temperature at the initial period. This might be that the heat absorbed by the chimney wall and also by the top of the PCM container affects the readings of thermocouples that distributed at outlet. During the initial period of melting, the temperatures of the inner chimney wall and top PCM container surface are high as they are not insulated, therefore, it is reasonable to assume that the radiation heat exchange between thermocouples and the chimney wall and top container surface, to some extent have an influence on the actual outlet air temperature, though the thermocouples are shielded by reflective aluminium shields. With the heat stored in the chimney wall and top container surface diminishing, the error between numerical results and experimental results becomes small.

One of the advantages of using a PCM as a heat storage medium which is often mentioned is that the heat release process occurs within a relatively constant temperature range, namely, solidification temperature. It can be seen that when the temperature of the PCM closes to the solidification temperature, the outlet air temperature varies across a small range during this period which is dominated by latent heat. The little variations in mass flow rate and outlet temperature, as well as the outlet air being warm enough, are important for the design of such a solar air heating system, because the heated air delivered from the solar chimney is directed to a living space to keep it warm during the discharging period. The average increases in outlet temperatures are 5 ℃, 5.4 ℃ and 6.5 ℃ for the heat fluxes of 700, 600 and 500 W/m^2, respectively.

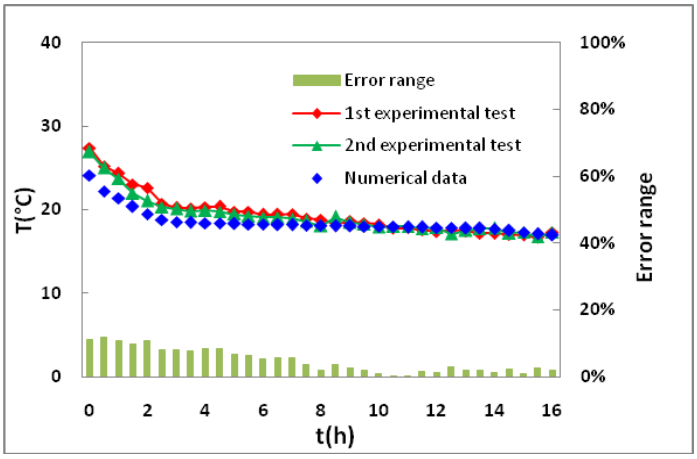

(a) 700 W/m^2

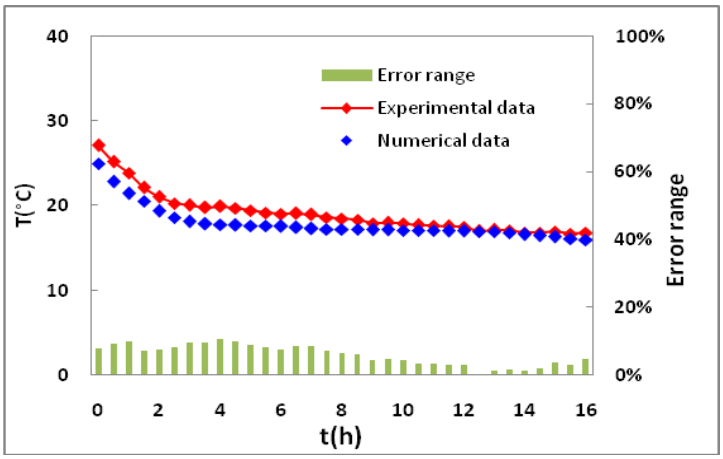

(b) 600 W/m^2

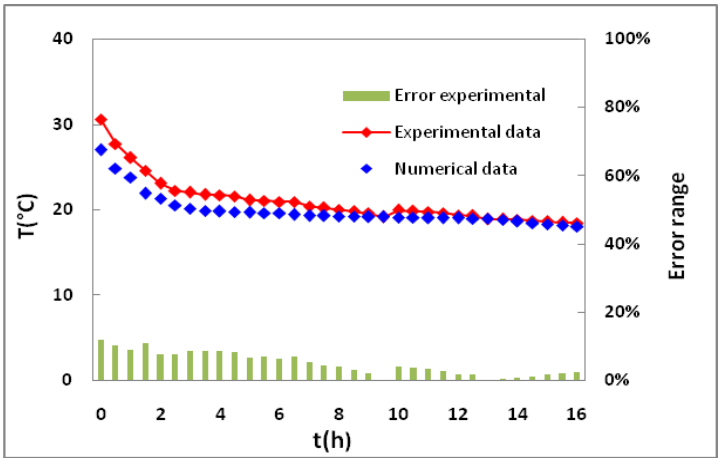

(c) 500 W

Figure 6- 13 A comparison of the numerical result and experimental result for outlet air temperature: (a) 700 W/m^2; (b) 600 W/m^2; and (c) 500 W/m^2

6.5 INVESTIGATIONS ON THE SYSTEM'S THERMAL PERFORMANCE

As shown, the model developed was validated using three sets of experimental data and showed a very close agreement with the experimental results. As discussed previously, with the heat fluxes studied, the thermal performances of the proposed system were slightly changed. Thus, the system should be studied further with lower heat fluxes to complement of the thermal performance characteristics. A further prediction of the thermal performance of the system is carried out by using the verified numerical model.

6.5.1 Simulation Specification

The configurations and specifications of the proposed system under this numerical investigation are the same as those that have been presented in Table 5-4 in Chapter 5, and the thermophysical properties of the PCM are the same as those that have been listed in Table 3-1 in Chapter 3. The initial PCM temperature and inlet air temperature are kept at 20 ℃ and the applied heat fluxes under investigation are 100, 200, 300, 400, 500, 600, 700 and 800 W/m^2. As the charge period of the PCM is limited by the period of solar irradiation availability, a same charge period of 7 h is fixed in each case in this study.

6.5.2 Simulation Results and Discussion

In this section, eight heat fluxes range from 100 – 800 W/m^2 are considered in analysis of the thermal performance of the proposed system. The purposes of this investigation are to explore how the system performs under the various possible conditions encountered by the system, and to identify conditions by which a satisfactory performance of the system can be attained.

6.5.2.1PCM temperature

Figure 6-14 shows the temperatures of the innermost layer of the PCM for heat fluxes of 100 – 800 W/m^2. As seen, the PCM temperatures for heat flux 700 and 800 W/m^2 present a typical fully charging and discharging processes, respectively. The melting times in these two cases are 5.6 and 6.6 h, respectively, whilst the freezing times are almost the same accordingly. However, in the case of 600 W/m^2, the PCM temperature is 41.6 ℃ at the end of the charging

process. That is, the PCM is not fully melting. The time during which the PCM maintains a nearly stable temperature is 14.5h, which is slightly shorter than those in the cases of 700 and 800 W/m^2. With further decreases in heat flux, the stable PCM discharge times are dramatically shortened to7h, 6h, 4h, 3h and 1h for heat fluxes of 500, 400, 300, 200 and 100 W/m^2. The results reveal that for the full melting processes of 800 and 700 W/m^2, there are no clear differences between their performances. This is probably because after the PCM is fully melted the heat stored is predominantly sensible heat, which slightly affects the freezing time. Once the heat flux falls to or below 500 W/m^2, the performance of the system deteriorates sharply. To explain why the performances are so distinctly different when the heat flux reduces to 500 W/m^2, the temperature distributions in the PCM for the cases of 800, 600, 500 and 100 W/m^2 are shown in Figure 6-15. As shown, for the heat flux of 800 W/m^2, the whole volume of the PCM changes its phase completely at the end of 7 h. However, for 600 W/m^2, around 30 % of the whole PCM is still in the phase change state at the end of charging. When the heat flux reduces to 500 W/m^2, the volume of the PCM that does not fully melt increases to around 40%, 10% of the whole PCM even being in a solid state, not having reached the melting temperature 38 ℃. This would reduce the thermal storage capacity of the system greatly, and this is the reason why the system's performance sharply deteriorates at 500 W/m^2. When the heat flux is 100 W/m^2, as shown in Figure 6-15(c) the temperature of the PCM at each thickness is well below 38 ℃. Thus, the stable discharge time can be negligible.

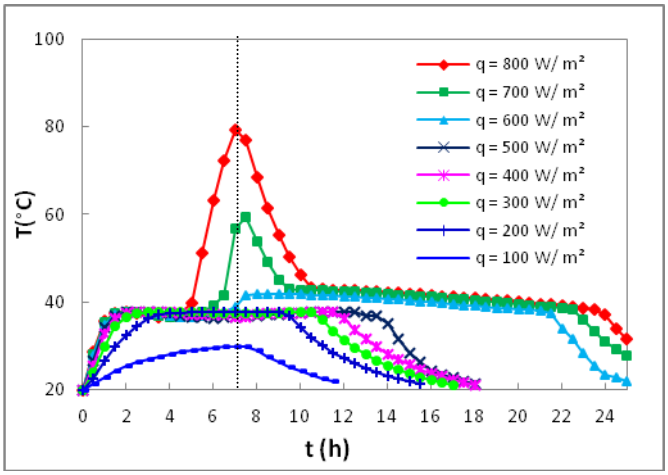

Figure 6- 14 PCM temperatures of the innermost layer for various heat fluxes during charge and discharge periods

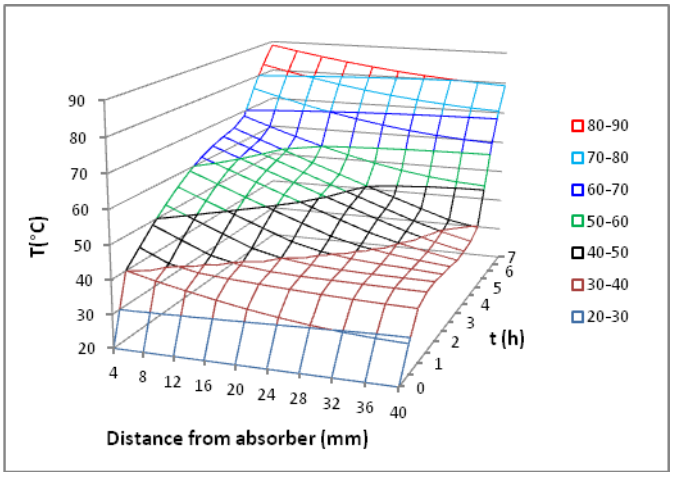

(a) 800 W/m^2

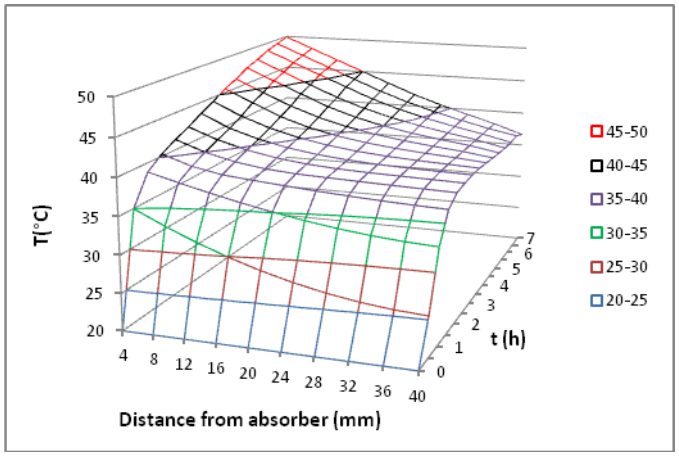

(b) 600 W/m^2

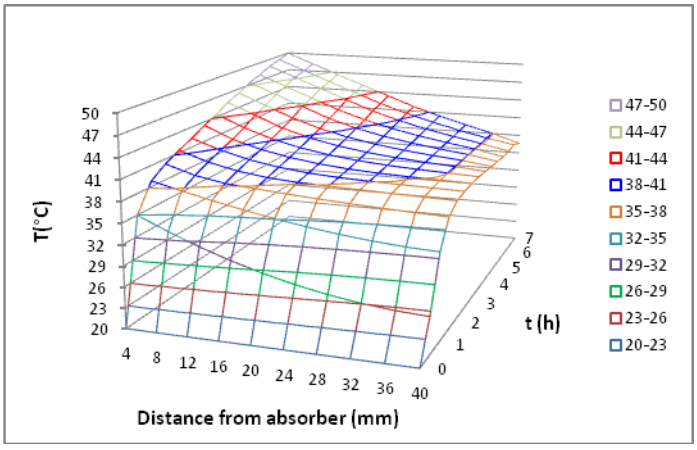

(c) 500 W/m^2

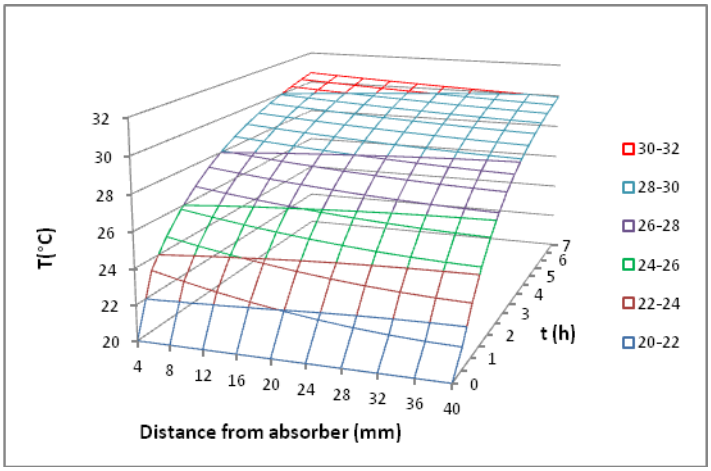

(d) 100 W/m^2

Figure 6- 15 Temperature distributions inside the PCM for (a) 800 W/m^2; (b) 600 W/m^2; (c) 500 W/m^2; and (d) 100 W/m^2

6.5.2.2 Absorber surface temperature

Figure 6-16 presents the absorber plate temperature for heat fluxes 100-800 W/m^2 during charging and discharging periods. As shown, during the charging period, the surface temperature depends on the applied heat flux, the higher the heat flux the higher the absorber temperature. There are abrupt transitions shown in the cases of 700 and 800 W/m^2, indicating that the PCM is completely melting. However, the transitions are not found from other heat fluxes, meaning the PCM does not melt. Among these applied heat fluxes, the surface temperatures for the cases of 100 – 300 W/m^2 slightly exceed or are below the upper melting temperature of 43 ℃. When the discharge starts, in the cases of 400 – 800 W/m^2, the surface temperatures drop sharply at the initial discharge period. After the surface temperatures reach 43 ℃, the temperature curves vary slowly and are nearly coincident. The temperature curves for 400 and 500 W/m^2 are steeper and separate from others quickly. However, for 100 – 300 W/m^2, the temperature curves drop continuously and quickly until the surface temperature reaches 20 ℃.

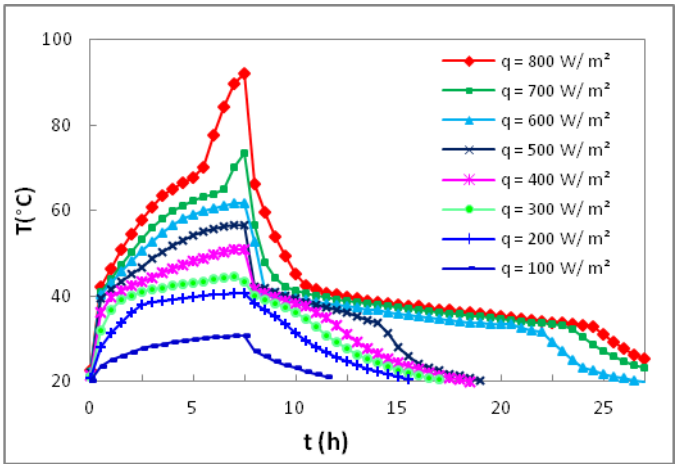

Figure 6- 16 Absorber surface temperatures for various heat fluxes

6.5.2.3 Mass flow rate and air temperature difference

Mass flow rates and air temperature differences for heat fluxes 100 – 800 W/m^2 are shown in Figures 6-17 and 6-18, respectively. As expected, the mass flow rate and air outlet temperature delivered by the system depends on their respective surface temperature: the higher the surface temperature the higher the mass flow rate and air outlet temperature. Similar to the surface temperatures, the mass flow rate and air temperature profiles for 400 – 800 W/m^2 drop quickly at the initial discharge period. When the mass flow rate and temperature difference reduce to 0.44 kg/s and 2.5 ℃, the mass flow rate and temperature curves for 600 – 800 W/m^2 vary slowly. However, in the remaining cases, the mass flow rate and temperature curves still drop quickly until the ventilation process ends.

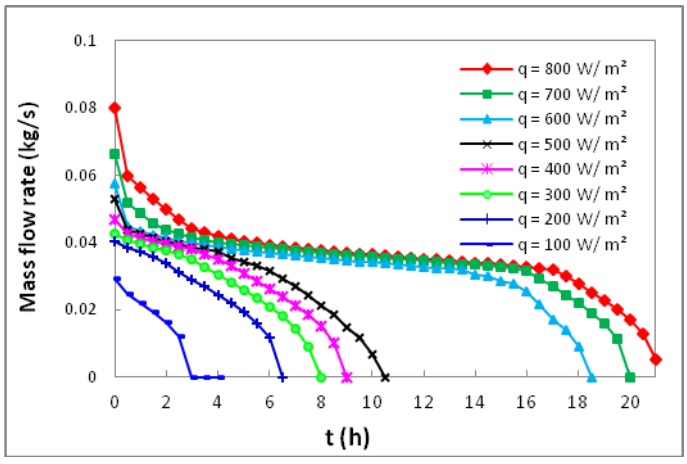

Figure 6- 17 Mass flow rates for various heat fluxes

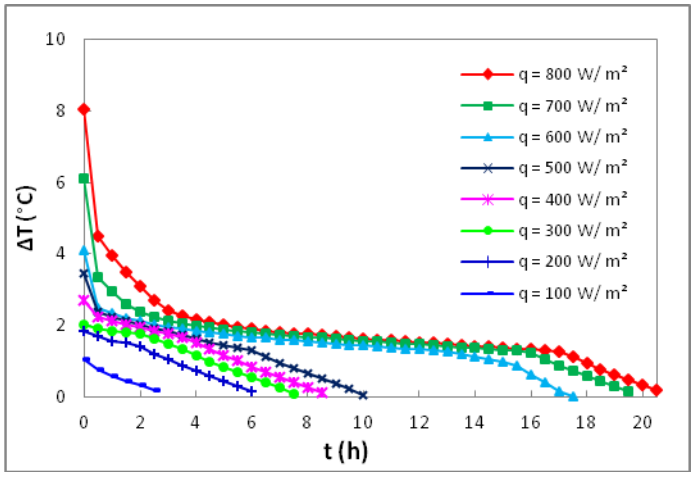

Figure 6- 18 Air temperature differences for various heat fluxes

6.5.2.4 Energy charged and discharged by the system

Figure 6-19 shows the energy stored, and the energy discharged to the glass and air for various heat fluxes. Percentages of the energy stored by the system discharges to the air are 18.9%, 19.5%, 20.2 %, 22.5%, 22.9 %, 25%, 28.2% and 31% for the heat fluxes of 100 – 800 W/m^2, respectively. The percentage increases with heat flux- the higher the heat flux, the higher energy contribution percentage. It is also seen that around 50% of the total energy stored by the system is discharged to the glass by radiant heat transfer. This is due to that the glass temperature being much lower than the absorber surface temperature during the discharge period, resulting in a high heat transfer rate between the glass and absorber plate. Therefore, some measures (for instance, using solar transparent insulation materials to replace the ordinary glass) are required to decrease the heat loss from the glass and so improve the thermal efficiency of the proposed system.

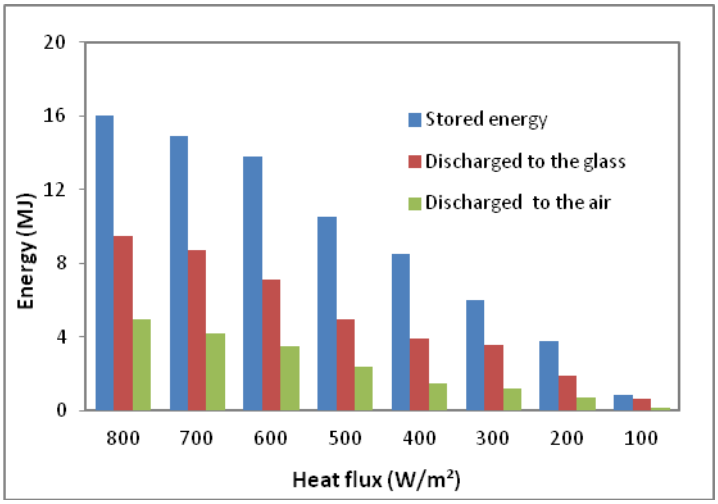

Figure 6- 19 Energy stored and the energy discharged to the air for various heat fluxes

6.6 CONCLUSIONS

In this chapter, the heating and cooling performances of a solar chimney incorporating latent heat storage using RT 42 as the PCM were investigated. The rig was built and tested in a laboratory under heat fluxes of 500 W/m^2, 600 W/m^2 and 700 W/m^2. The results obtained from experimental tests then are used to validate the numerical model, which are developed based on the experimental conditions. This model can be further used to study the thermal performance of the solar chimney under other conditions.

1) Results indicated that for the three heat fluxes studied, with the same charging period the whole freezing process including the initial sensible heat discharging periods were 13h 50 min, 13h 50 min and 13 h 20 min for the cases of 700, 600 and 500 W/m^2. It was seen that, although the PCMs were partially melting at the end of the charging process in last two cases, the freezing times were almost the same.

2) An interesting phenomenon concerning the absorber surface temperatures during the discharging period was observed. That is, although clear temperature stratifications between different heights along the container were found during the charging period, the surface temperatures at different heights were nearly the same over the discharging period. When the discharging process started, the surface temperatures reduced quickly to a plateau, about 40 ℃, and then the temperatures dropped slowly.

3) The variation trends of temperature inside the chimney were found to be similar for all cases studied. The temperature of the absorber plate had a significant effect on the temperature profiles of the channel air. For channel depth direction, the temperature distribution along the chimney gap was very uniform during the charging period. During the discharging period, the temperature distribution was not uniform, with higher air temperature near the absorber and lower temperature near the glass. For channel height direction, temperature stratifications were found, with higher temperature at higher positions during charging and discharging periods.

4) Numerical simulations based on the experimental conditions were carried out and validated by using the experimental results. The numerical results showed a very close agreement with the experimental results. The following are the main findings:

i) The predicted absorber surface temperature for the discharging process was more accurate compared with that for charging process. As natural convection occurred in the PCM during the charging process, that was not considered in the numerical simulation.

ii) The model predicted a slightly lower glass temperature than the experimental one. This may be attributed to the differences between the actual thermo-properties of the glass and the theoretical values assumed in the numerical simulation. Comparison the temperature profile of glass to that of heated surface, it can be concluded that the glass temperature did have an influence from the absorber plate.

iii) The numerical model had the ability to predict the mass flow rate accurately. Results indicated that although the initial sensible heat discharging period lasted for a short time compared to the total discharging period, its effect on mass flow rate is significant. The latent heat discharging period lasted for 11h, and the mass flow rate descended very slowly and varied around 0.038 kg/s, followed by 0.037 kg/s and 0.36 kg/s for heating operation under the heat fluxes of 700,600 and 500 W/m^2. However, the mass flow rates were around 0.04 kg/s, 0.039 kg/s and 0.38 kg/s for cooling ventilation operation during this period. This period was followed by a sharp drop in mass rate due to sensible heat dominating this period again.

iv) The outlet air temperature varied within a small range during the latent heat discharging period. The small variations in mass flow rate and outlet temperature as well as the outlet air being warm enough are important for a solar air heating system. The average temperature increases in outlet temperatures are 5 ℃, 5.4 ℃ and 6.5 ℃ for the heat fluxes of 700, 600 and 500 W/m^2, respectively under the experimental conditions.

5) Using the verified model, a thermal performance study has been carried out for various heat fluxes. The main findings are that when the heat flux drops to or below 600 W/m^2, the PCM could not be fully melting. However, the performances for heat fluxes of 800, 700 and 600 W/m^2 are comparable. It can be concluded that overcharge or slightly undercharge of the system has a slight effect on the system. With the heat flux further decreasing, the performance of the system deteriorates sharply. The reason for this is the volume of the PCM in which the temperature is lower than the initial melting temperature of 38 ℃. Therefore, more effective techniques are necessary for the system when the heat flux is below 500 W/m^2.

Though the experimental test and numerical simulation indicated that the PCM-based solar chimney can provide a relatively constant mass flow rate and outlet air temperature during phase change transition, the thermal performance characteristics of the PCM based solar chimney should be studied further, due to the complicated heat transfer characteristics of the PCM. Using the current verified model, a parametric study will be carried out on the parameters affecting the performance of the proposed system in next Chapter.

7. PARAMETRIC STUDY AND THERMAL PERFORMANCE ANALYSIS OF THE PROPOSED SYSTEM

7.1 INTRODUCTION

The thermal performance of the proposed system was experimentally and numerically investigated in Chapter 6. The purpose of this chapter is to carry out a parametric study on the proposed system to identify significant parameters that affect the system performance by using the verified numerical model. Consequently, this study may provide the criteria for optimising the thermal performance of the proposed system. The numerical results analysed are quantified in terms of (1) charging/discharging time of the PCM, (2) temperature difference between outlet air and inlet air of the solar chimney, and (3) mass flow rate of the chimney, which are the three most important quantities of the proposed system.

Extensive parametric studies on solar chimneys have been carried out to enhance their performance. Some of the design parameters, including the chimney width, ventilation height (height between inlet and outlet), inlet and outlet areas and chimney tilt angle are found to have a predominant effect on chimney performance. Bassiouny and Koura (Bassiouny and Koura, 2008) analytically and numerically investigated the effect of chimney inlet size and width on ventilation performance to optimise design parameters. They found that with a three times increase of the inlet size, 11% increase in the air changes per hour (ACH) was attained, whereas with a factor of 3 increase in the chimney width and with the inlet size fixed, an increased ACH of about 25% was achieved. It was concluded that the chimney width has more significant influence on ACH than the inlet size.

The influence of the chimney depth on the natural ventilation was experimentally studied by Ong and Chow (Ong and Chow, 2003). The experimental chimney consisted of a rectangular box of 1.875m height, 0.45m width and the air gap depth could vary at 0.1m, 0.2m and 0.3m. The gap at the bottom of the heated wall through which the air entered the channel was kept at 0.1m. The experimental results were verified by the numerical results obtained from a

simplified mathematical model which is similar to the one developed by Ong (Ong, 2003). It was seen that the air velocity increased from 0.25m/s to 0.39m/s, when air gap depth increased from 0.1m to 0.3m for radiation intensity up to 650W/m^2. The results indicated that the air velocity for 0.3m air gap width was 56% higher than that for 0.1m air gap width.

Lee and Strand (Lee and Strand, 2009) recently carried out a parametric study on the performance of a solar chimney. In their study, the effect of chimney height, air gap width and other parameters were evaluated. Their results showed that the effect of air gap width on the ventilation performance is least amongst the parameters. However, as discussed previously, Bassiouny and Koura (Bassiouny and Koura, 2008) believed that the chimney width was a significant parameter on ventilation performance in terms of ACH in their study.

It is also important to highlight that the PCM does have a great influence on the LHS system, and a number of experimental and/or numerical studies on the effects of various parameters of PCM on the thermal performance of various applications have been carried out. Neeper (Neeper, 2000) theoretically investigated the effects of various parameters of the PCM on the thermal storage of the wallboard. It was concluded that the energy stored during a daily cycle depends on the melting temperature, the melting temperature range over which melt occurs, and the latent capacity per unit area of wallboard. Zhang et al. (Zhang et al., 2008) presented a modified model based on Neeper's findings by considering the finite latent heat of the PCM. The examination of the effects of the latent heat, melting temperature, and thermal conductivity on the thermal storage in the PCM wallboards was performed. Koo et al. (Koo et al., 2011) performed a numerical simulation to investigate the effects of various parameters of PCM including the nominal average melting temperature, melting temperature range, the convective heat transfer coefficients and the wallboard thickness on the thermal storage performance of the wallboard such as the thermal energy storage and the time shift. They concluded that when the average phase change temperature was close to the average room temperature, the maximum thermal heat storage in the wallboards could be achieved. The melting temperature range should be narrow to maximise the thermal heat storage. It was also found that the thermal heat storage increased with the convective heat transfer coefficient, and the time shift decreased with the convective heat transfer coefficient and the phase change temperature range.

The packed bed latent heat thermal energy storage systems with the advantage of a large surface to volume ratio, higher storage density and simplicity of configuration have been used for applications such as, solar thermal energy storage, low temperature storage systems for central air conditioning, energy efficient buildings and waste heat recovery systems (Regin et al., 2008). The effects of the inlet heat transfer fluid temperature (Stefan number), mass flow rate and melting temperature range on the thermal performance of the capsules of various radii have been investigated by Regin et al. (Regin et al., 2009). The results showed that the temperature range of the PCM must be accurately known, and should be taken into account for proper modelling of the performance of a packed bed system,

Solar air heater with LHS is the solar energy collection for it's off sunshine hours use (Tyagi et al., 2012). Jurinak and Abdel-Khalik (Jurinak and Abdel-Khalik, 1978) presented a parametric study to determine the optimum physical properties of the PCM for solar air-heating systems in terms of the system performance over the entire heating season for different space heating load. A solar air heater with a built-in LHS system was studied for different PCM melting temperatures of 61, 51, 43 and 32 ℃. The results indicated that for this solar heater system, the PCMs with melting temperatures of 51 and 43 ℃ gave the best performance (Fath, 1995). The sensible heat term of a PCM is also a significant factor which may affect the system performance, when this term cannot be neglected. For example, Bruno and Saman (Bruno and Saman, 2001) have shown that for PCM fibre boards used as heat storage, the sensible heat is significant in the overall heat transfer, whereas the model involving only the latent heat is not valid. Saman et al. carried out a numerical analysis to examine the effects of sensible heat which existed when the initial temperature of the PCM was well below or above the melting point during melting or freezing. The results are compared with a previous analysis based on a one dimensional model which neglected the effect of sensible heat. The effect of the sensible heat was reflected in a sharp increase in the outlet air temperature at the initial period of melting and a sharp decrease in the initial period of freezing.

As mentioned above, all the solar chimney parametric studies focused on the influence of its own geometry on the performance of the system. However, it has been indicated that introducing LHS to a system would affect its performance greatly. Thus a parametric study on the PCM based solar chimney could be a new area of further research. To gain further insight into the proposed system, a comprehensive sensitivity analysis is performed to

examine how a number of parameters affect the thermal performance of the system. The results of the numerical simulation in terms of the effect of a number of parameters on the overall thermal performance of the proposed system are presented in this chapter.

7.2 PARAMETRIC STUDY

The numerical study of the effects of various parameters on the system performance has been carried out by using the numerical model which was developed and validated in Chapter 6. The results from the simulation of the thermal performance of the solar chimney are presented in this section.

Three quantities as the measures of thermal performance of the system by changing the parameters are chosen. They are: the melting/freezing time, the air flow rate and the outlet air temperature. For a LHS system design, the time taken for the whole PCM to melt or solidify is a crucial factor. That is, the charging and discharging times must be considered for any LHS system for improving its efficiency. The air flow rate which is a direct measure of how much fresh air or warm air is delivered into a living space depends on the system operation. For heating mode, during the discharging period, the outlet air is directed to a living space to supply thermal comfort. Temperature difference between outlet air and inlet air ($\triangle T = T_o - T_i$) tells us how much the inlet air temperature is elevated after it was heated by the heated surface. Lastly the surface temperature of the absorber is also presented in this study.

7.2.1 Simulation Set-up

Unless specifically stated, the specifications of the proposed system in this parametric investigation used are the same as those that have been presented in Table 5-4 in Chapter 5, and the thermophysical properties of the PCM have been listed in Table 3-1 in Chapter 3. The initial PCM temperature and inlet air temperature are kept at 20 ℃ as reference temperature and the reference heat flux in this study is 700 W/m^2. A number of quantities such as some of the specifications of the system and thermophysical properties of the PCM are set as variables whilst the remaining parameters are set as inputs.

7.2.2 Simulation Results and Discussion

7.2.2.1 Effect of latent heat of fusion

Figure 7-1 shows the effect of latent heat of fusion on the melting and freezing times of the proposed system. Three values of latent heat of fusions under investigation are: 70, 120 and 170 kJ/kg, respectively. As seen, the latent heat of fusion has a great effect on the melting and freezing times. The larger the latent heat, the longer melting and freezing times. The melting times are 3.2 h, 4.6 h and 6.5 h accordingly, while the freezing times are 10 h, 13.5 h and 16 h, respectively. It is seen that the effect of the latent heat of fusion on melting time is more significant than that on freezing time due to the extra sensible heat stored in the PCM prolongs the freezing to some degree.

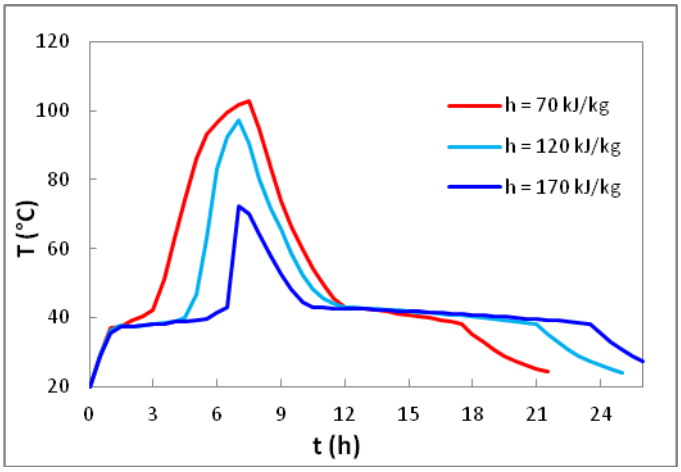

Figure 7- 1 Effect of latent heat of fusion on melting and freezing times. Simulation conditions: PCM initial temperature = 20 ℃, air inlet temperature = 20 ℃, heat flux = 700 W/m^2

Figure 7-2 presents the absorber surface temperatures for various latent heat of fusion. The latent heat of fusion greatly affects the absorber surface temperature during the melting and freezing processes. The variations trends of the absorber surface temperature are similar to those of the PCM. That is, the higher the latent heat of fusion, the lower the surface temperature during the whole melting period and at the initial freezing period. And then the absorber surface temperature for lower latent heat of fusion drops faster than higher ones.

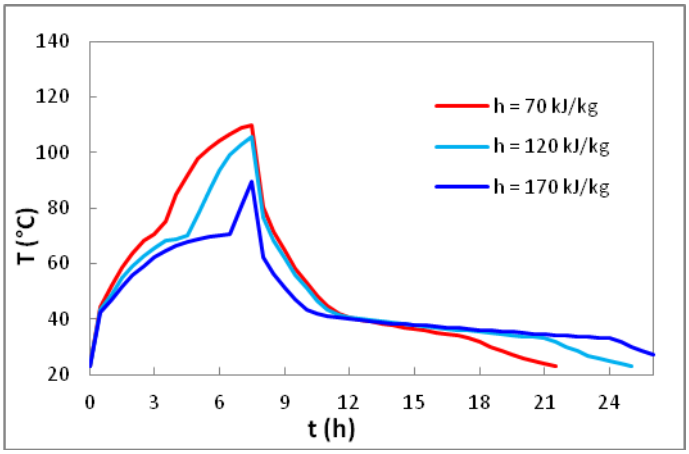

Figure 7- 2 Effect of latent heat of fusion on absorber surface temperature. Simulation conditions: PCM initial temperature = 20 ℃, air inlet temperature = 20 ℃, heat flux = 700 W/m^2

Figures 7-3 and 7-4 show the effect of latent heat of fusion on mass flow rate and air temperature difference during the freezing period. As expected, the mass flow rate and temperature difference are higher with lower latent heat of fusion at initial freezing period but are lower at late freezing period. The ventilation period is, however, longer with higher latent heat of fusion. Air enters into the chimney through the inlet at a constant temperature of 20 ℃ and is then heated as it passes the absorber plate. Initially, due to the high temperature difference between the air and the absorber surface, the mass flow rate and outlet air temperature approach their maximum values and drop linearly and sharply during the initial period. When the PCM reaches the solidification temperature, the mass flow rate and outlet temperature drop gradually. The mass flow rate and temperature follows the same pattern: a drastic drop at the initial period of freezing, a relatively constant value for a long period, and a sharp drop at the late period of freezing.

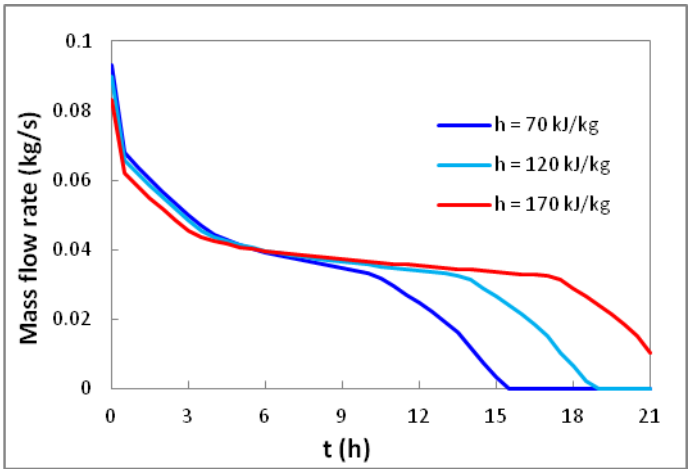

Figure 7- 3 Effect of latent heat of fusion on mass flow rate. Simulation conditions: PCM initial temperature = 20 ℃, air inlet temperature = 20 ℃, heat flux = 700 W/m^2

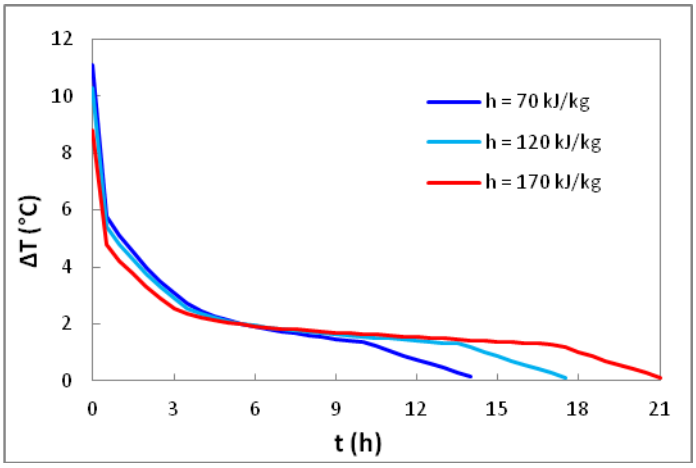

Figure 7- 4 Effect of latent heat of fusion on air outlet temperature difference. Simulation conditions: PCM initial temperature = 20 ℃, air inlet temperature = 20 ℃, heat flux = 700 W/m^2

7.2.2.2 Effect of specific heat

Although the PCM predominantly stores thermal energy in latent heat, it also stores a certain amount of sensible heat. The contribution of the sensible heat would be significant if the melting temperature of the PCM is high or there is a large temperature rise above the PCMs melting point. Hence, it is necessary to include the sensible heat term in a model to describe the heat transfer between PCM and air, where it cannot be neglected. Moreover, the effect of the sensible heat is also important for thermal comfort consideration, since the proposed system is aimed to deliver air with heating capacity to a living space to maintain the thermal comfort, any factors that affect the thermal comfort need to be considered carefully.

Figure 7-5 presents the effect of specific heat on the melting time and freezing time of the proposed system. Three values of specific heat of 1200, 1800 and 2400 J/kg ·K are given as parameters, and 1200 and 2400 J/kg ·K are hypothetical values whilst 1800 J/kg ·K is the true value of PCM.

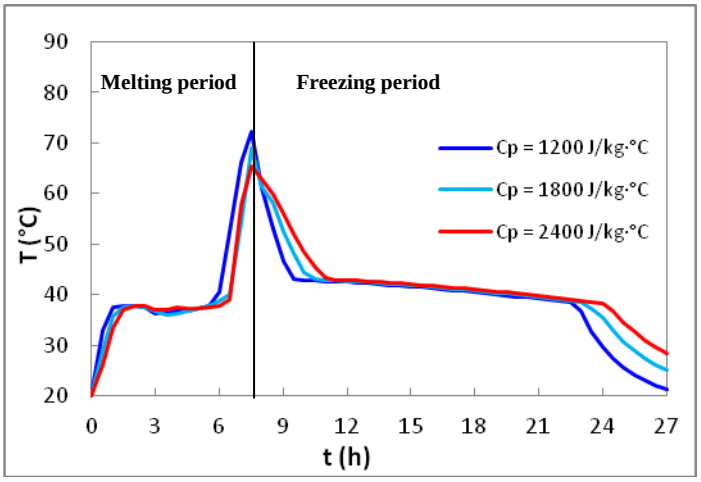

Figure 7- 5 Effect of specific heat on melting and freezing times. Simulation conditions: PCM initial temperature = 20 ℃, air inlet temperature = 20 ℃, heat flux = 700 W/m^2

As can be seen, the specific heats slightly affect the melting time. At the initial period of melting, only sensible heat exchange takes place in the PCM and the time required for the PCM to reach the melting temperature is shorter for lower specific heat than that for higher specific heat. The melting time is also affected in the same manner. Accordingly, the melting times are 6h, 6.5h and 6.8h for specific heats of 1200, 1800 and 2400 J/kg ·K, respectively. The simulated results indicate that the melting time is increased by half an hour when the specific heat is doubled. Similar to the melting process, the specific heat effect at the initial period of freezing is shorter for lower specific heat than that for higher specific heat, and the freezing time is affected accordingly. However, the role of the sensible heat effect on the freezing process is more important than that for the melting period. The freezing times are 15 h, 16 h and 16.5 h, respectively, which means that the freezing time is prolonged by 1.5 h when the specific heat is doubled. The reason for this is that of the relatively low heat transfer rate between the air and the absorber plate, resulting in a longer time for the PCM to reach the freezing temperature.

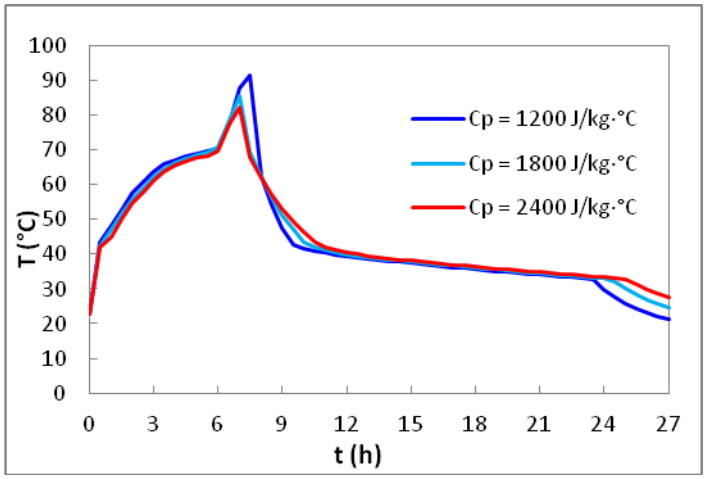

Figure 7- 6 Effect of specific heat on the absorber surface temperature during melting and freezing process. Simulation conditions: PCM initial temperature = 20 ℃, air inlet temperature = 20 ℃, heat flux = 700 W/m^2

As shown in Figure 7-6, the effect of specific heat on absorber surface temperature could be neglected during the melting period. The absorber surface temperatures for the three specific heats are nearly consistent during this period. The specific heat slightly affects the surface temperature at the initial and late periods of freezing.

The mass flow rates and temperature differences for specific heats – 1200, 1800 and 2400 J/kg ·℃ are shown in Figures 7-7 and 7-8. One of the attractive advantages of using a LHS system is that the heat absorbed/released process is at a relatively constant temperature, namely the melting/solidification temperature of the PCM. However, due to the presence of the sensible heat during freezing process, the temperature of PCM varies in a broader range. Consequently, there is a sharp rise in the outlet temperature at the initial period of freezing that would cause thermal discomfort in a living space. As can be seen from Figure 7-8, the initial period is marked by the high temperature difference (ΔT) between inlet air temperature and outlet air temperature resulting from the high heat transfer rate between the air and the PCM. The initial temperature differences are 7.9, 6.8 and 6 ℃ for 1200, 1800 and 2400 J/kg ·℃, and the times required for the air temperature difference to drop to a relative value around 2.5 ℃ are 2 h, 3 h and 3.5 h for the three specific heats, respectively. Though sensible heat discharge lasts for a short time compared to the total melting time, its effect on the air outlet air temperature is significant. Therefore, high specific heat capacity is required for the candidate PCM to avoid overheating of the PCM and to provide rapid warming effect during the initial freezing period.

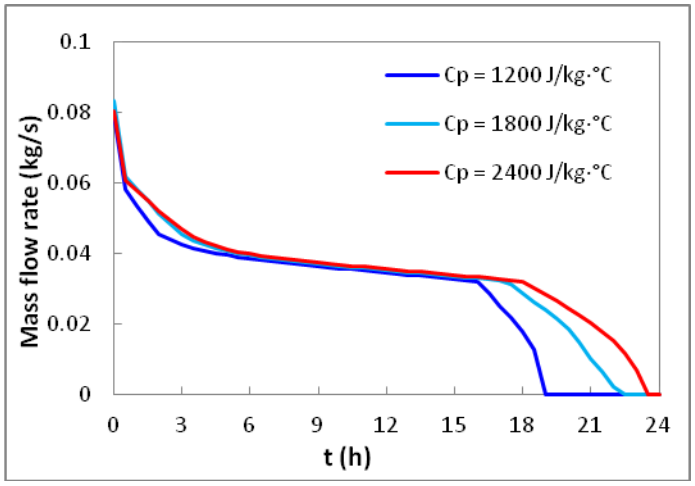

Figure 7- 7 Effect of specific heat on the air mass flow rate during freezing process. Simulation conditions: PCM initial temperature = 20 ℃, air inlet temperature = 20 ℃, heat flux = 700 W/m^2

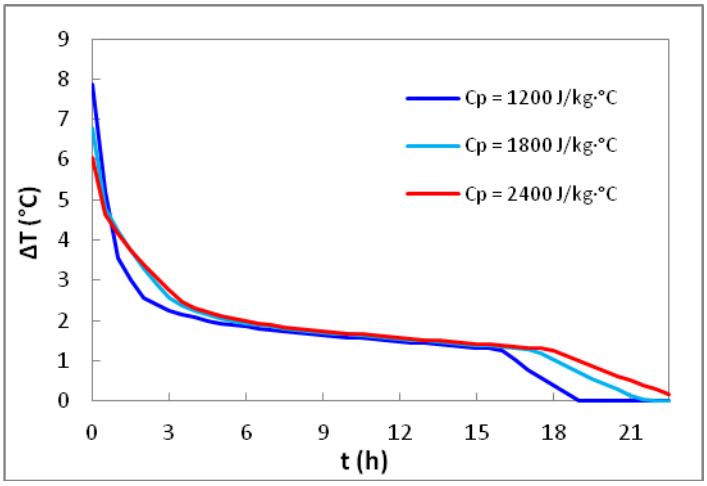

Figure 7- 8 Effect of specific heat on air outlet temperature difference. Simulation conditions: PCM initial temperature = 20 ℃, air inlet temperature = 20 ℃, heat flux = 700 W/m^2

7.2.2.3 Effect of thermal conductivity of PCM

Figure 7-9 shows the effect of the thermal conductivity of the PCM on the melting and freezing time profiles. The thermal conductivities used in this study are 0.2, 0.4 and 0.6 W/m ℃, respectively. As seen, the higher the thermal conductivity, the shorter the melting and freezing times. This is expected as higher thermal conductivity leads to a higher heat transfer rate in the PCM. Consequently, The PCM starts to melt and completes melting and solidification quicker. The melting times are 8.5 h, 6.7 h and 5 h, and the freezing times are 20 h, 18 h and 17 h, respectively. This indicates that the melting time is reduced by nearly half when the thermal conductivity is tripled.

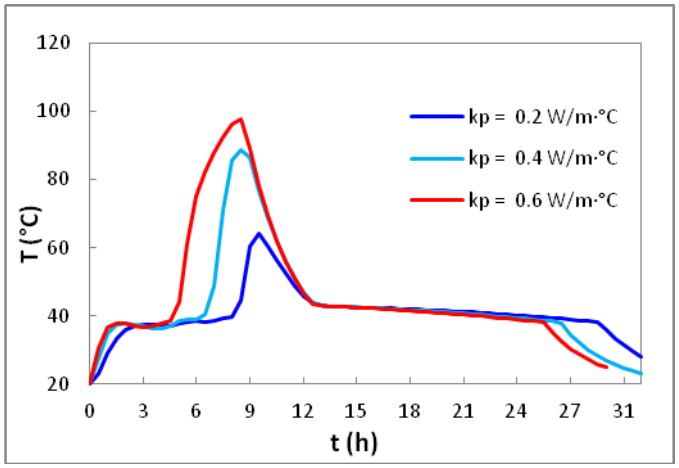

Figure 7- 9 Effect of thermal conductivity of the PCM on the melting and freezing times. Simulation conditions: PCM initial temperature = 20 ℃, air inlet temperature = 20 ℃, heat flux = 700 W/m^2

Figure 7-10 shows the effect of the thermal conductivity of the PCM on absorber surface temperature during melting and freezing periods. As shown, the higher the thermal conductivity, the lower the absorber surface temperature during the melting process and the higher the surface temperature during the freezing process. This is reasonable as the PCM with higher thermal conductivity can extract the heat applied to the absorber surface more quickly than that with lower thermal conductivity, thus, the surface temperature of the absorber for higher thermal conductivity is reduced during the melting period. Conversely, during the freezing period the heat stored in the PCM transfers to the absorber plate faster for higher thermal conductivity than that for lower thermal conductivity, resulting in higher absorber temperature.

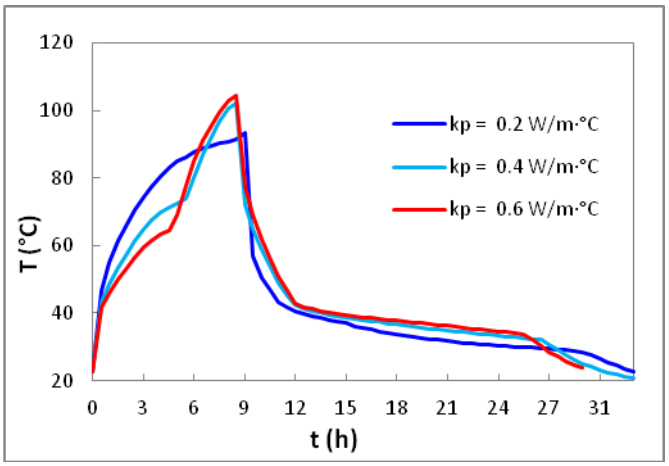

Figure 7- 10 Effect of thermal conductivity of the PCM during melting and freezing process. Simulation conditions: PCM initial temperature = 20 ℃, air inlet temperature = 20 ℃, heat flux = 700 W/m^2

Figures 7-11 and 7-12 present the mass flow rates and air outlet temperature differences for various thermal conductivities of the PCM. As the thermal conductivity of the PCM significantly influences the absorber surface temperature, the mass flow rate and outlet temperature are also affected accordingly, where during the freezing period the mass flow rate and outlet air temperature are higher with higher thermal conductivity. The PCM with higher thermal conductivity discharges at a higher heat transfer rate, resulting in a faster and higher increase in the outlet temperature. The average mass flow rates for thermal conductivities of 0.2, 0.4 and 0.6 W/m ℃ are 0.033 kg/s, 0.037 kg/s and 0.038 kg/s during the phase change transition period, whilst the air temperature differences are 1.5 ℃, 1.8 ℃ and 2 ℃ accordingly. The results show that the thermal conductivity of the PCM not only impacts the melting and freezing time, but also impacts the mass flow rate and outlet temperature during the phase change period.

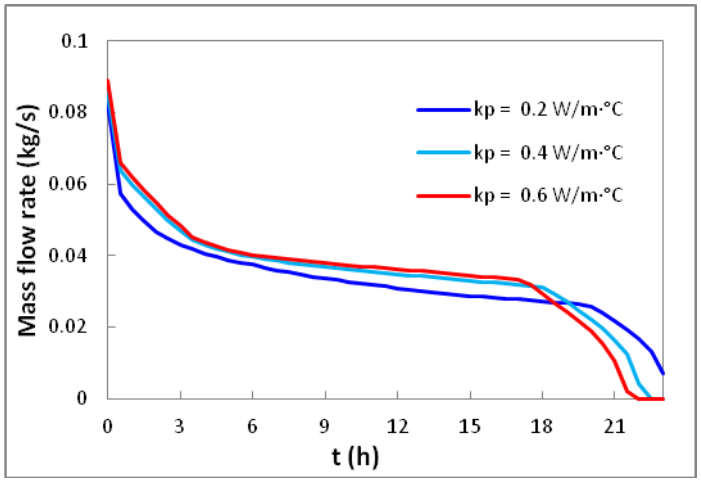

Figure 7- 11 Effect of thermal conductivity of the PCM on air mass flow rate. Simulation conditions: PCM initial temperature = 20 ℃, air inlet temperature = 20 ℃, heat flux = 700 W/m^2

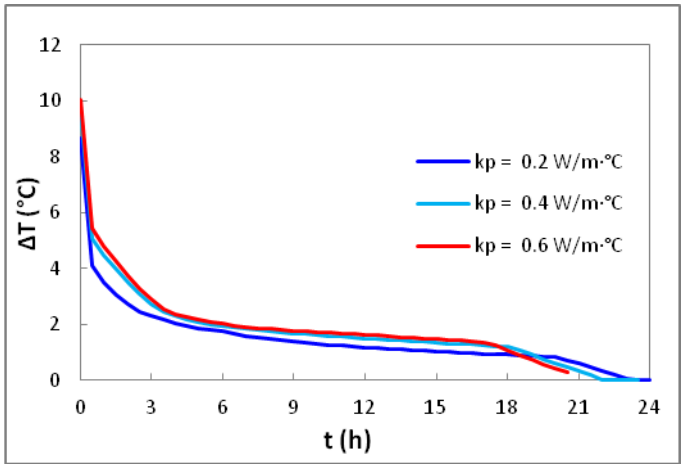

Figure 7- 12 Effect of thermal conductivity of the PCM on air outlet temperature difference. Simulation conditions: PCM initial temperature = 20 ℃, air inlet temperature = 20 ℃, heat flux = 700 W/m^2

7.2.2.4 Effect of phase change temperature range difference

Figure 7-13 shows the effect of phase change temperature range on the melting and freezing times. The phase change temperature range differences considered are: 3 ℃, 5 ℃ and 7 ℃, respectively. The phase change temperature range are assumed as 38 – 41 ℃, 38 – 43 ℃ and 38 – 45 ℃, respectively. The melting times are 7.8 h, 6.6 h and 5.3 h, respectively, whilst the freezing times are almost the same, which is around 16.5 h. The results reveal that the wider the phase change temperature range, the shorter the melting time though the latent heat of fusion is kept constant in this study. This is due to the fact that the surface temperature of the absorber increases significantly with the increase of phase change temperature range (see Figure 7-14), resulting in a higher heat transfer rate between the absorber and PCM. As a result, the PCM having wider phase change temperature reaches the complete melting earlier than the PCM with narrower phase change temperature.

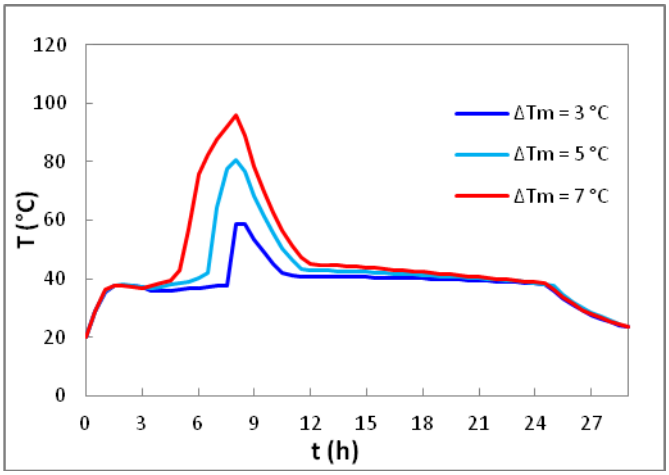

Figure 7- 13 Effect of phase change temperature range difference on melting and freezing times. Simulation conditions: PCM initial temperature = 20 ℃, air inlet temperature = 20 ℃, heat flux = 700 W/m^2

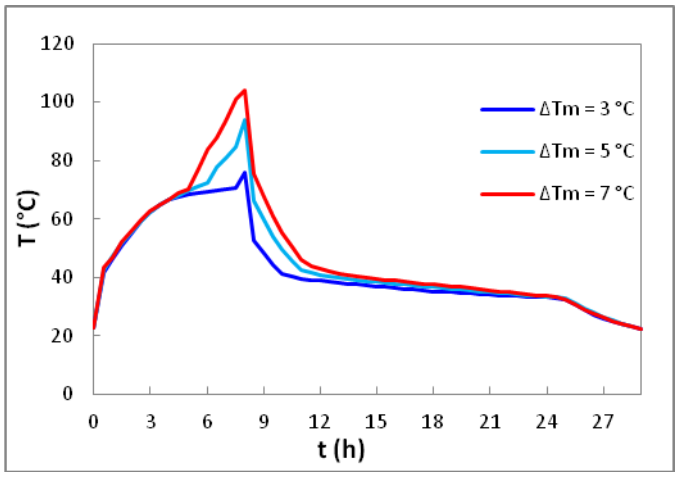

Figure 7- 14 Effect of phase change temperature range difference on air mass flow rate. Simulation conditions: PCM initial temperature = 20 ℃, air inlet temperature = 20 ℃, heat flux = 700 W/m^2

As shown in Figures 7-15 and 7-16, the wider the phase change temperature range the higher mass flow rate and outlet air temperature at the initial freezing period and at the phase change transition period. When the freezing approaches the late period of freezing, the mass flow rate and outlet temperature become close. It could be concluded that the thermal storage performance of the system could be optimised by selecting the phase changing temperature range.

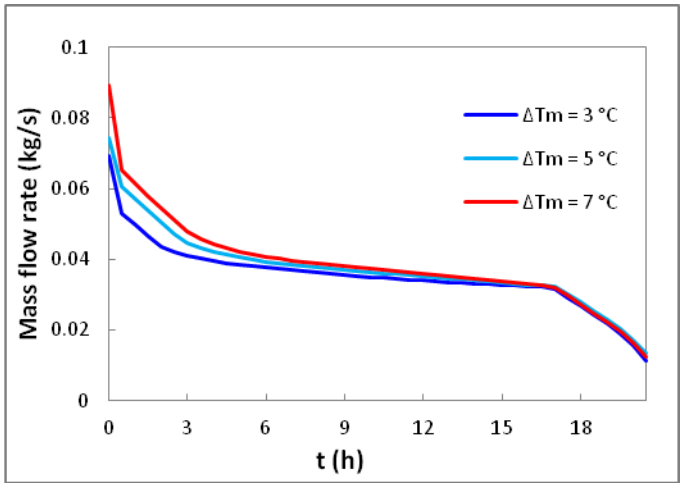

Figure 7- 15 Effect of phase change temperature range difference on air mass flow rate. Simulation conditions: PCM initial temperature = 20 ℃, air inlet temperature = 20 ℃, heat flux = 700 W/m^2

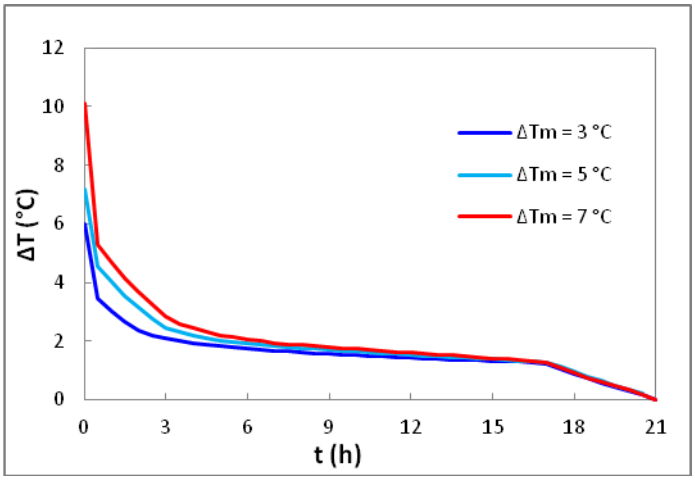

Figure 7- 16 Effect of phase change temperature range difference on air outlet temperature difference. Simulation conditions: PCM initial temperature = 20 ℃, air inlet temperature = 20 ℃, heat flux = 700 W/m^2

7.2.2.5 Effect of air inlet temperature

The predicted melting and freezing times for various air inlet temperatures 15, 20 and 25 ℃ under identical conditions are presented in Figure 7-17. It is seen that the effect of air inlet temperature on the melting time can be ignored, since there is no air flow rate occurs during charging period. The melting times are around 6.6 h for the air inlet temperatures studied, respectively. However, it is found that the air inlet temperature has a great effect on freezing time during the freezing period. The lower inlet air temperature induces the shorter freezing time due to the increased heat transfer rate between the air and the absorber surface.

Changing the inlet air temperature from 15 ℃, 20 ℃ to 25 ℃, the freezing times are 12.5 h, 16 h and 20.5 h, respectively.

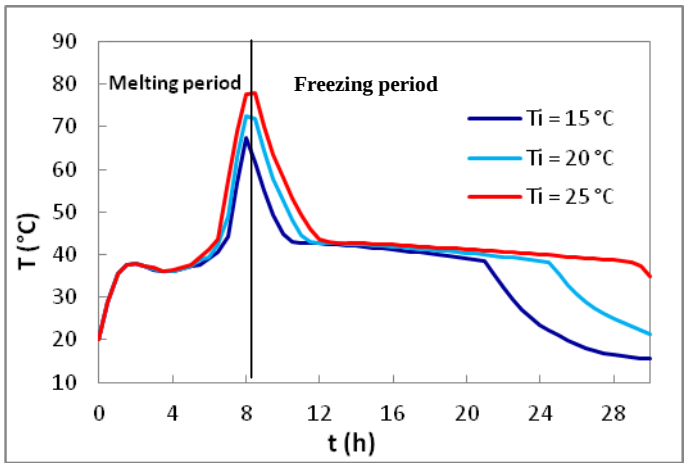

Figure 7- 17 Melting and freezing times for various air inlet temperatures. Simulation conditions: PCM initial temperature = 20 ℃, heat flux = 700 W/m^2

Figure 7-18 shows how air inlet temperature affects the absorber surface temperature during melting and freezing process. It is seen clearly that the inlet air temperature affects the surface temperature more greatly especially during the freezing period. The lower inlet temperature has a lower surface temperature due to the high temperature difference between inlet air and absorber surface leading to high heat transfer rate. As a result, further reduction in the absorber surface temperature is found.

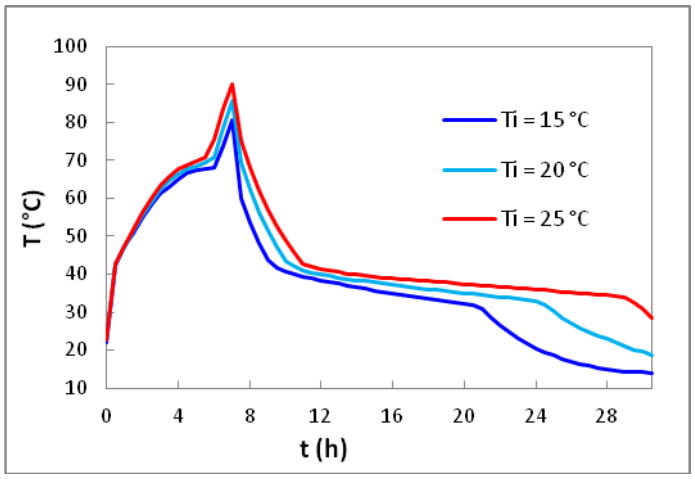

Figure 7- 18 Absorber surface temperature for various air inlet temperatures during melting and freezing of the PCM. Simulation conditions: PCM initial temperature = 20 ℃, heat flux = 700 W/m^2

Figs 7-19 and 7-20 present the mass flow rate and air temperature difference for various inlet temperatures during freezing period. Converse to the surface temperature the lower inlet air temperature results in higher mass flow rate and temperature difference. As the higher inlet air temperature will reduce the temperature difference between the air and the absorber surface, and then subdued the thermal buoyancy effect leading lower mass flow. The average mass flow rate and temperature difference are 0.041, 0.039 and 0.37 kg/s and 2.3, 2 and 1.8 ℃ for the inlet air temperatures of 15, 20 and 25 ℃, respectively.

Although the lower inlet temperature increases the mass flow rate and temperature difference, the desired working time, namely that within the initial sensible and latent heat discharge periods of freezing, is also reduced greatly. After this relative steady period, the heat transfer rate between the air and surface plate drops quickly resulting in too low mass flow rate and temperature difference to meet the heating purposes.

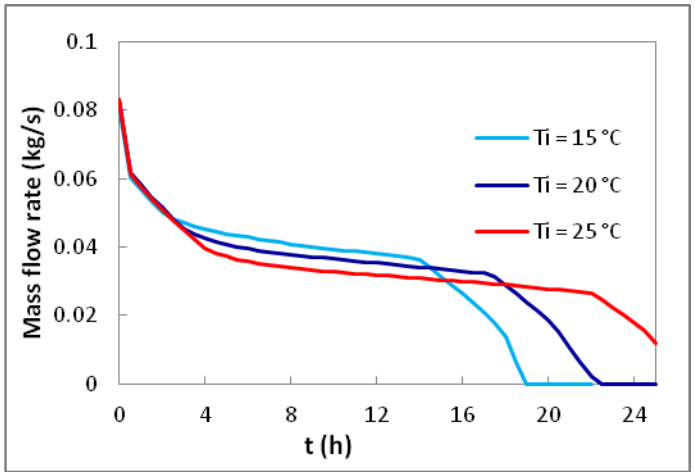

Figure 7- 19 Effect of air inlet temperature on mass flow rate during freezing period. Simulation conditions: PCM initial temperature = 20 ℃, heat flux = 700 W/m^2

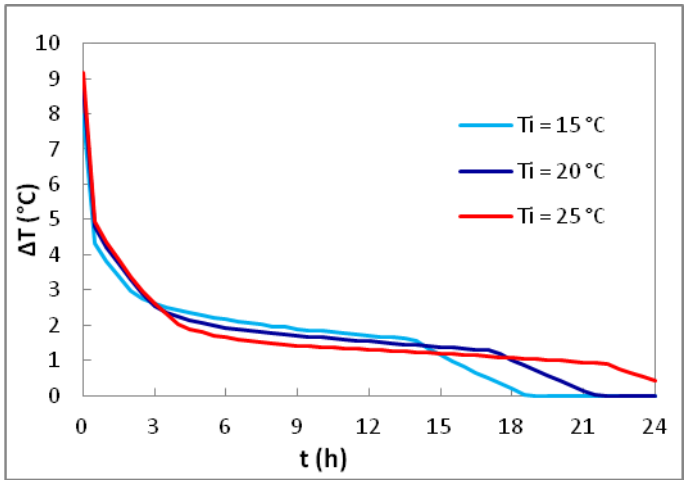

Figure 7- 20 Effect of air inlet temperature on temperature difference during freezing period. Simulation conditions: PCM initial temperature = 20 ℃, heat flux = 700 W/m^2

7.2.2.6 Effect of initial PCM temperature

Figures 7-21 and 7-22 show the effect of initial PCM temperature on the melting and freezing times and on surface temperature. The initial PCM temperature used in this study are 15, 20 and 25 ℃. As can be seen, the PCM initial temperature only affects the initial melting period of the first 1.5 h. During this period, the PCM temperature rises quickly from the initial temperature to the melting temperature for higher initial PCM temperature. The PCM initial temperature has very little influence on the melting process after the first half an hour. This is to be expected as it only relates to the sensible heat terms. The melting times for various initial PCM temperatures are 6.7, 6.5, 6.3 h, respectively. Nevertheless, the investigation of this parameter will determine how soon the PCM to fully melt will take place at different temperatures. While the initial PCM temperature hardly influences the freezing time during the freezing period, the effect of the initial PCM temperature on the surface temperature is further reduced. Very little effect in changing the initial temperature of the PCM on the surface temperature during melting and freezing periods is found. The surface temperatures are almost the same for all three initial PCM temperatures during melting and freezing processes.

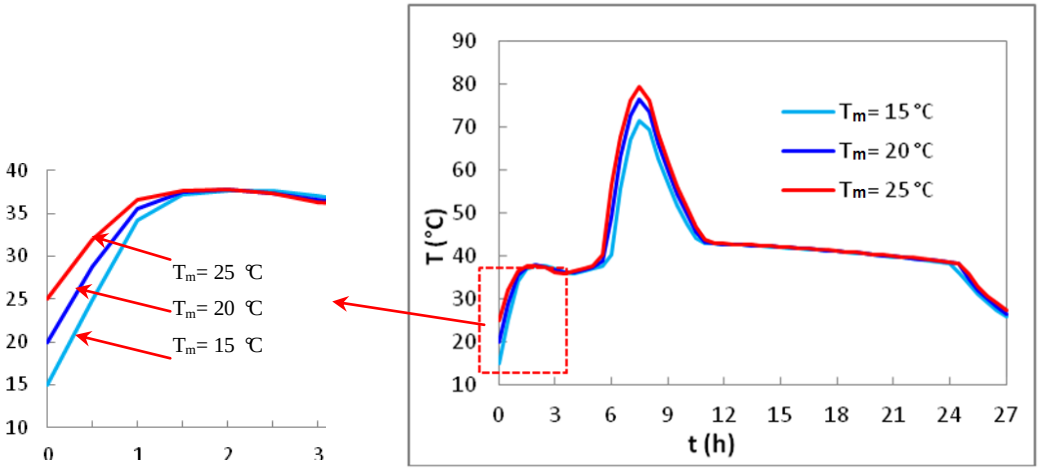

Figure 7- 21 Melting and freezing times for various initial PCM temperatures. Simulation conditions: initial air inlet temperature = 20 ℃, heat flux = 700 W/m^2

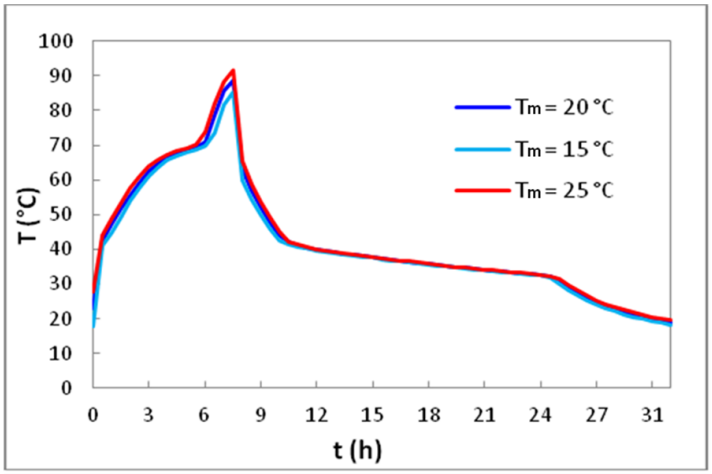

Figure 7- 22 Absorber surface temperatures for various initial PCM temperatures. Simulation conditions: initial air inlet temperature = 20 ℃, heat flux = 700 W/m^2

Effects of initial PCM temperatures on mass flow rate and air temperature difference are shown in Figures 7-23 and 7-24, respectively. As shown, no clear influences in changing the initial PCM temperatures on the mass flow rate and temperature difference are observed. This can be expected since the initial PCM temperature only affects the sensible heat storage during the melting period, which can be neglected compared to the amount of the latent heat component. The results reveal that the mass flow rate and the outlet temperature are hardly affected by change in the initial PCM temperature while other parameters are kept constant.

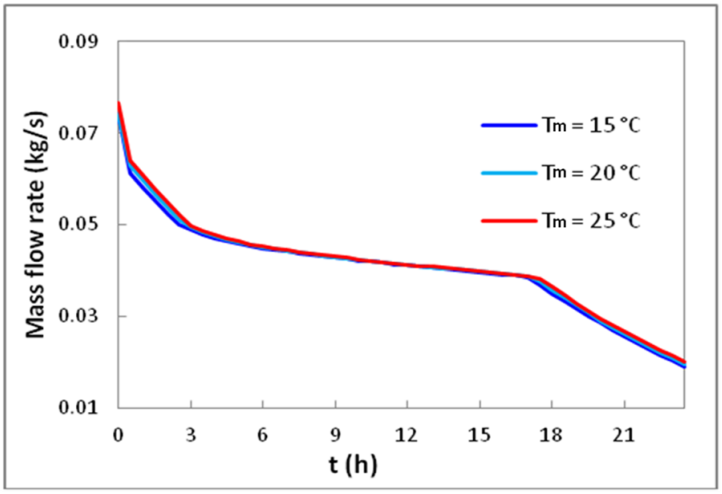

Figure 7- 23 Air mass flow rates for various initial PCM temperatures. Simulation conditions: initial air inlet temperature = 20 ℃, heat flux = 700 W/m^2

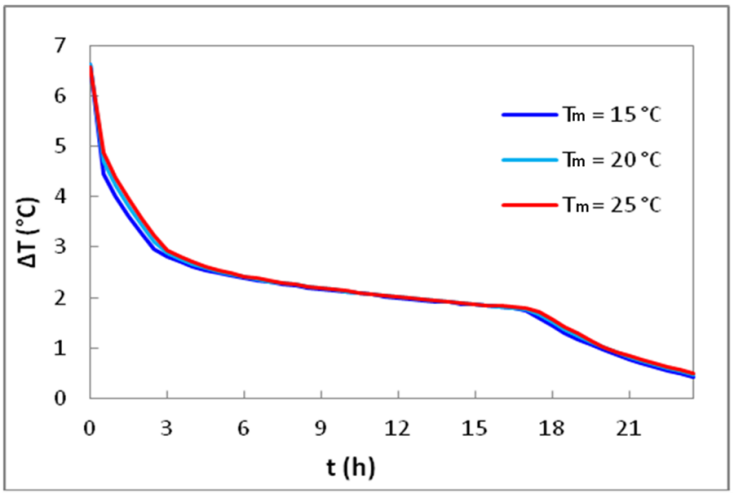

Figure 7- 24 Temperature differences for various initial PCM temperatures. Simulation conditions: initial air inlet temperature = 20 ℃, heat flux = 700 W/m^2

7.2.2.7 Effect of thermal conductivity of the insulator

Figures 7-25 and 7-26 show the effect of the thermal conductivity of the insulator on the melting and freezing times and on absorber surface temperature. The three values of thermal conductivity of the insulator considered are 0.02 W/m ℃, 0.04 W/m ℃ and 0.06 W/m ℃. As seen in Figure 7-25, the melting times are 5.3 h, 6.6 h and 7.8 h, and the freezing times are 18.5 h, 16.5 h and 14 h, respectively. This indicates that the surrounding insulation situation can impact the energy storage and releasing heavily.

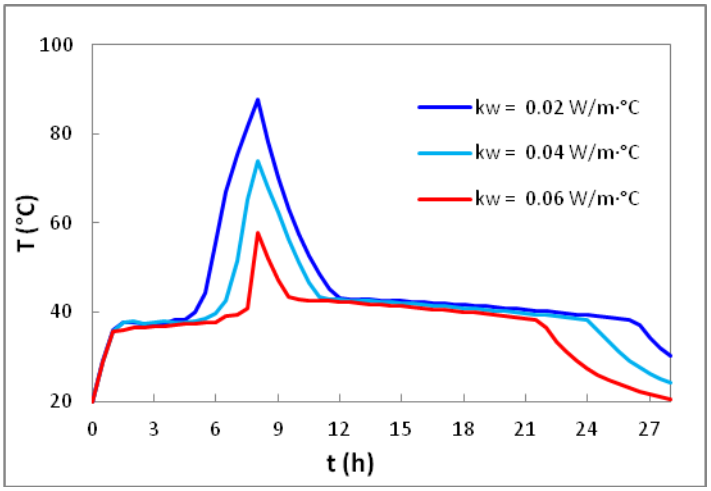

Figure 7- 25 Effect of thermal conductivity of the insulator on the melting and freezing times. Simulation conditions: PCM initial temperature = 20 ℃, air inlet temperature = 20 ℃, heat flux = 700 W/m^2

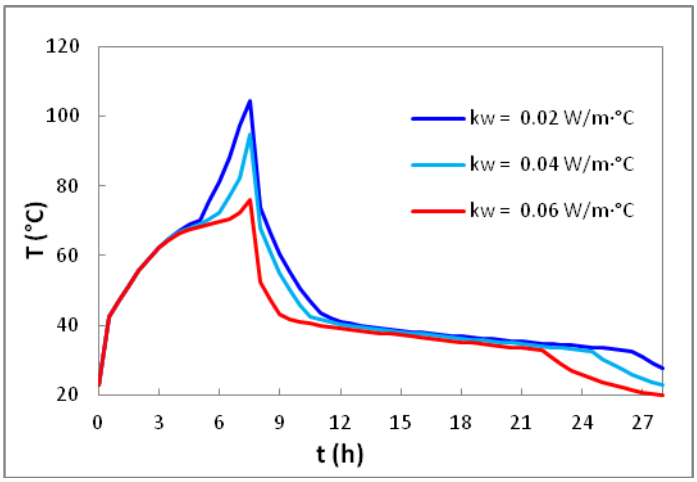

Figure 7- 26 Effect of thermal conductivity of the insulator on the absorber surface temperature. Simulation conditions: PCM initial temperature = 20 ℃, air inlet temperature = 20 ℃, heat flux = 700 W/m^2

Effects of thermal conductivity of the insulator on mass flow rate and temperature difference are shown in Figure 7-27 and 7-28, respectively. It is seen that the mass flow rate and air temperature difference are clearly affected by the insulator accordingly. The higher the thermal conductivity causes the lower the mass flow rate and air temperature difference especially at initial and late period of freezing. In the practical application, the decrease in the heat loss through the system is a very important part to be considered.

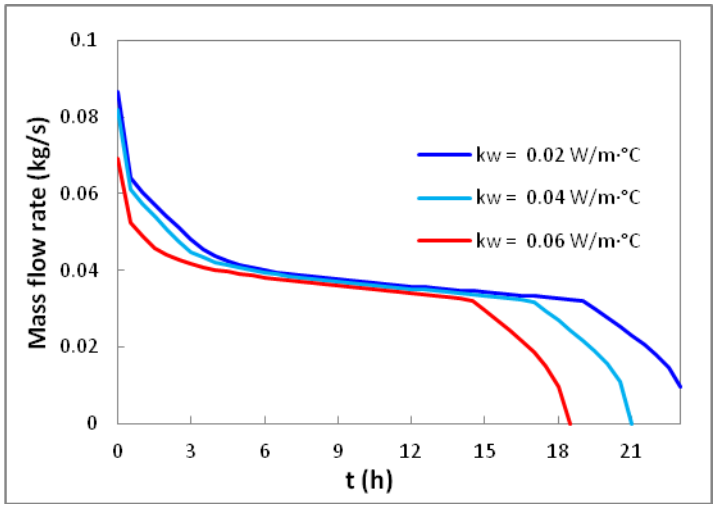

Figure 7- 27 Effect of thermal conductivity of the insulator on air mass flow rate. Simulation conditions: PCM initial temperature = 20 ℃, air inlet temperature = 20 ℃, heat flux = 700 W/m^2

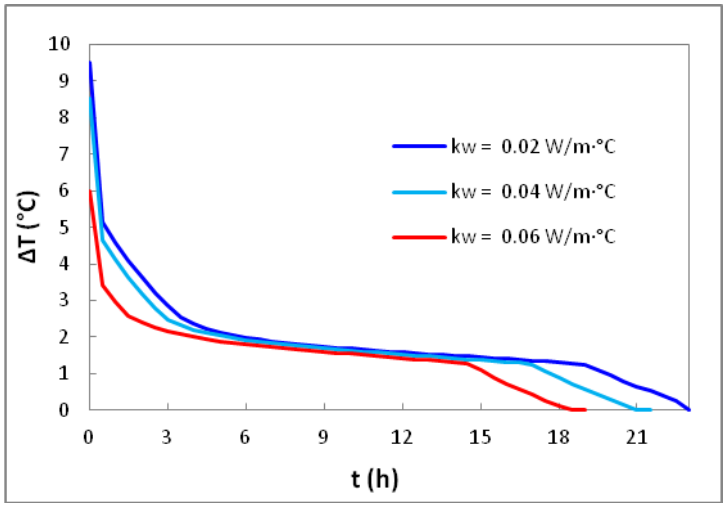

Figure 7- 28 Effect of thermal conductivity of the insulator on air temperature difference. Simulation conditions: PCM initial temperature = 20 ℃, air inlet temperature = 20 ℃, heat flux = 700 W/m^2

7.2.2.8 Effect of the heat flux

Figure 7-29 and 7-30 show the simulation results of melting and freezing times and surface temperature for three different heat fluxes, respectively. The heat fluxes under consideration are 600 W/m^2, 700 W/m^2 and 800 W/m^2, respectively. The melting times are 8.8 h, 6.5 h and 5.6 h, respectively, while the freezing times are 15 h, 17 h and 18 h accordingly. That is, a higher heat flux increases the heat transfer rate during the melting period and therefore, shortens the melting time, and a higher heat flux induces more sensible heat stored which

prolongs the freezing time. As the charge period is limited by the period of solar energy availability, this parameter of heat flux is an important factor to determine the efficiency of the system in terms of melting and freezing time. Higher heat flux means that the system is more chargeable. Similarly, the higher the heat flux results in the higher absorber surface temperature during the melting period but not remarkable for freezing period.

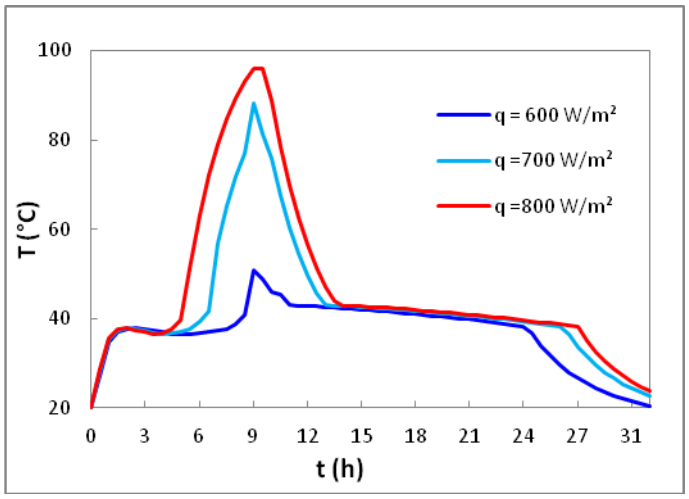

Figure 7- 29 Effect of heat flux on the melting and freezing times. Simulation conditions: PCM initial temperature = 20 ℃, air inlet temperature = 20 ℃

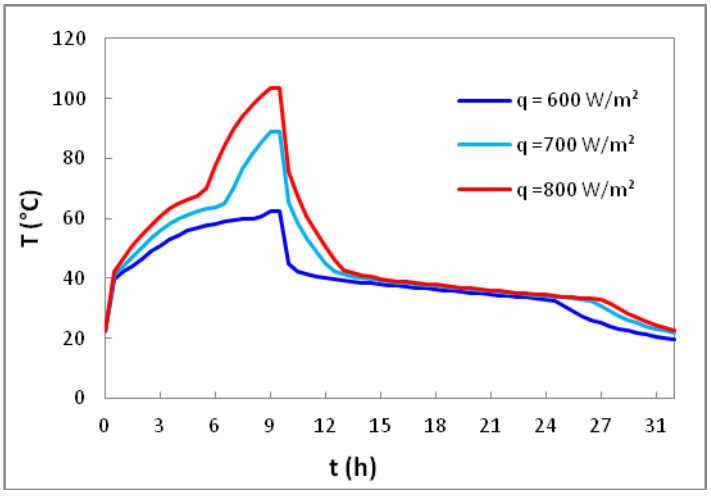

Figure 7- 30 Effect of heat flux on the absorber surface temperature. Simulation conditions: PCM initial temperature = 20 ℃, air inlet temperature = 20 ℃

Figures 7-31 and 7-32 present the simulation results of the mass flow rate and air temperature difference during freezing period, respectively. As seen, the mass flow rate and air temperature difference increase with the applied heat flux raise. However, this increase during the phase transformation period is not outstanding.

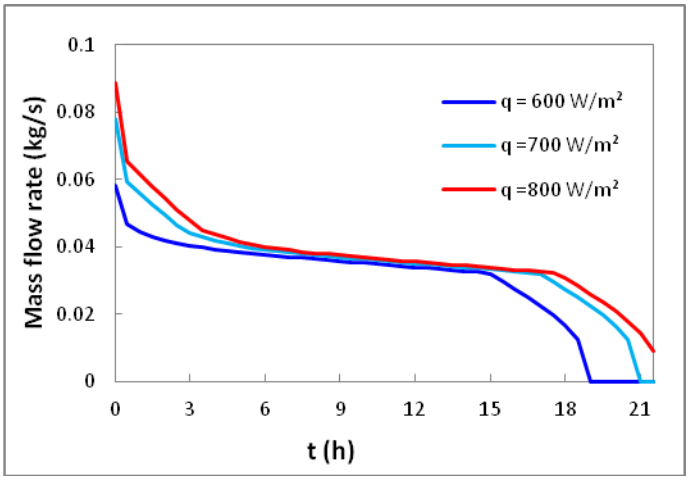

Figure 7- 31 Effect of heat flux on air mass flow rate. Simulation conditions: PCM initial temperature = 20 ℃, air inlet temperature = 20 ℃

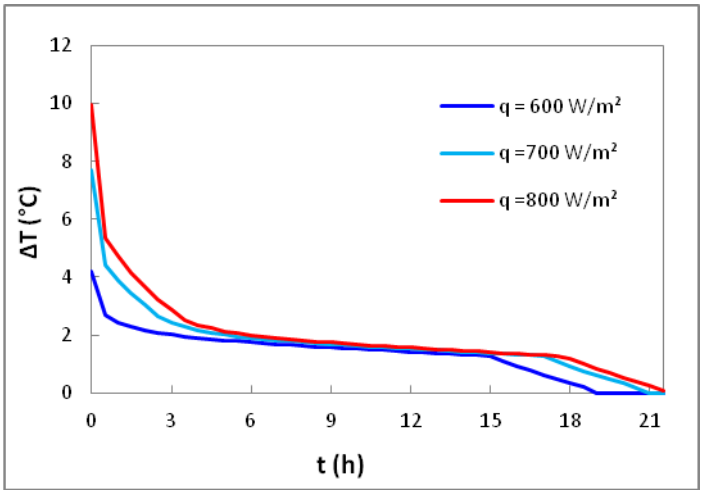

Figure 7- 32 Effect of heat flux on air temperature difference. Simulation conditions: PCM initial temperature = 20 ℃, air inlet temperature = 20 ℃

7.2.2.9 Effect of thermal conductivity of the container

The PCM container is an essential component of a liquid-solid PCM LHS system in order to prevent the PCM from leaving the container. Some researchers claimed that the choice of container material is largely driven by heat transfer efficiency and so the material must possess a high thermal conductivity (Eissenberg and Wyman, 1980; Garcia-Romero et al., 2009).

Three metallic materials, stainless steel, aluminium and copper are investigated in this study. The thermal conductivities of these materials are 16, 226 and 401W/m·℃, respectively. Figures 7-33 and 7-34 show the melting and freezing times for the containers made of copper,

aluminium and stainless steel. The thickness of the container material is kept at 1 mm. The melting times are 6.5 h, 6.3 h, and 6 h respectively. It is seen that the melting time is only reduced by 8 % when the thermal conductivity of the container is increased by 14 times. However the melting time is not further reduced when the thermal conductivity increases from 226 to 401 W /m K, while the thermal conductivity of the container hardly impacts the freezing time during the freezing period. The results indicate that the thermal conductivity of the container slightly affects the melting time, particularly the freezing time. This is because the wall of the container is thin and the overall heat transfer coefficient is mainly dependent on the convective heat transfer components. Similar conclusions were drawn by Liu et al. (Liu et al., 2011), where five materials (Copper, Stainless Steel, Glass, Polyethylene HD and PVC) with different thermal conductivities were numerically studied. They found that the melting time was only reduced by 4 % even the thermal conductivity was increased 2.1×10^3 times. Similarly, the effects of thermal conductivities of a container only affect the surface temperature during the melting period slightly. The surface temperatures during the freezing period are nearly the same.

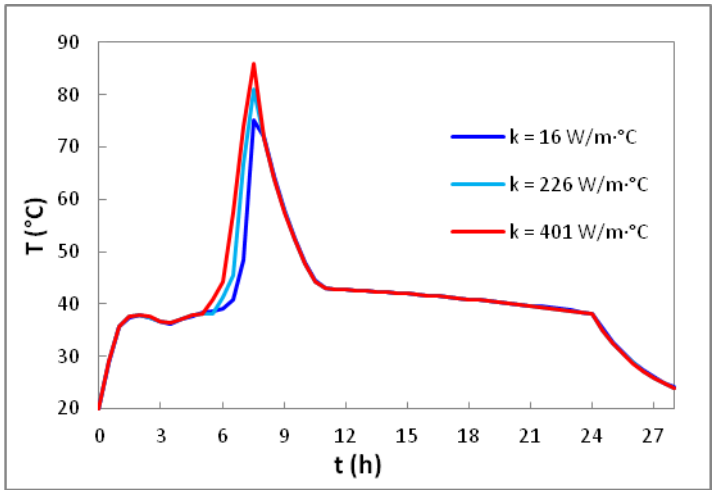

Figure 7- 33 Melting and freezing times for container materials with various thermal conductivities. Simulation conditions: PCM initial temperature = 20 ℃, air inlet temperature = 20 ℃, heat flux = 700 W/m^2

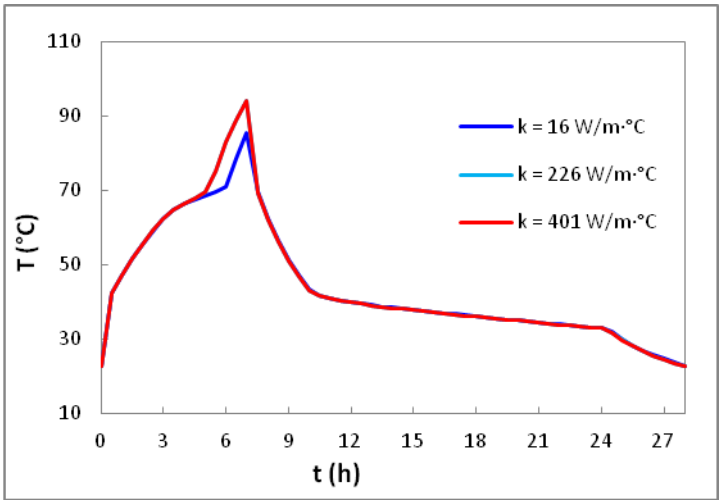

Figure 7- 34 Absorber surface temperatures for container materials with various thermal conductivities. Simulation conditions: PCM initial temperature = 20 ℃, air inlet temperature = 20 ℃, heat flux = 700 W/m^2

Figures 7-35 and 7-36 present the effect of thermal conductivity of the PCM container on air mass flow rate and air outlet temperature, respectively. It can be seen that the mass flow rate and the outlet temperature are hardly affected by the thermal conductivity of the container when other parameters are kept constant.

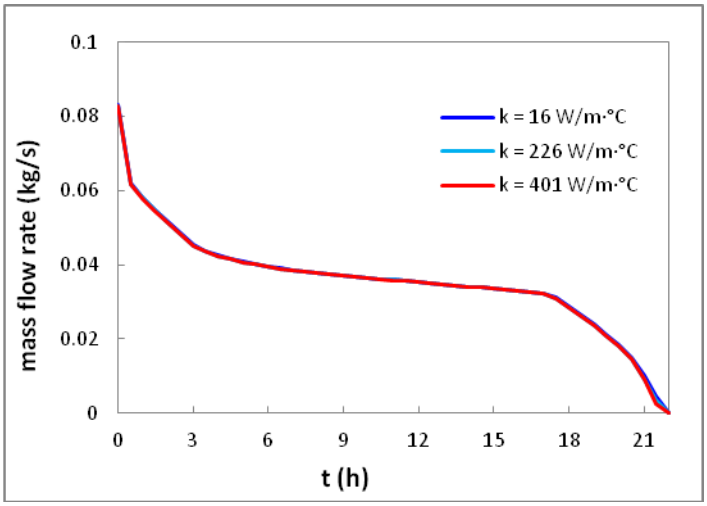

Figure 7- 35 Air mass flow rates for container materials with various thermal conductivities. Simulation conditions: PCM initial temperature = 20 ℃, air inlet temperature = 20 ℃, heat flux = 700 W/m^2

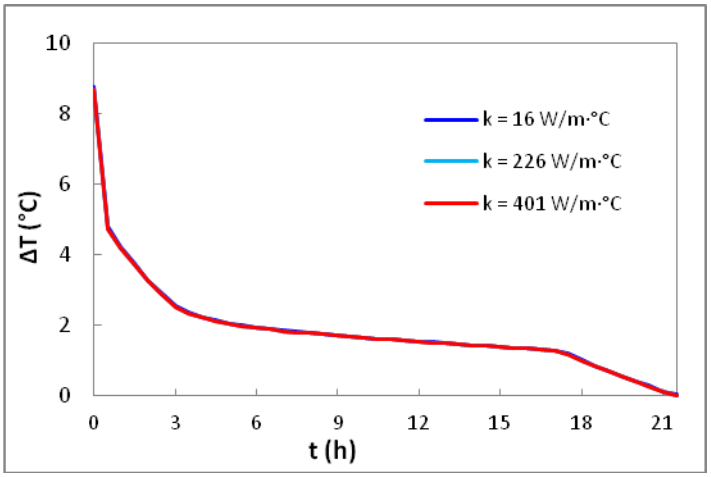

Figure 7- 36 Temperature differences for container materials with various thermal conductivities. Simulation conditions: PCM initial temperature = 20 ℃, air inlet temperature = 20 ℃, heat flux = 700 W/m^2

7.2.2.10 Effect of transmissivity of glass

The transmissivity of glass is also an important factor which would impact the thermal performance of the proposed system, as it directly impacts the incident solar radiation and is basically the fraction of incident solar radiation directly transmitted through the glass.

Figure 7-37 and 7-38 show the effects of the transmissivity of glass on the melting and freezing times and absorber surface temperature, respectively. Three values of transmissivities of glass are given as parameters: 0.8, 0.9, and 1 in this study. The corresponding melting times are 7.5 h, 6.4 h and 5.5 h, respectively. However, the freezing times are 16.5 h, 16.7 h and 16.8 h, respectively. The results indicate that the transmissivity of the glass is an important factor in reducing the melting time, whilst maintaining the freezing time. The charge period is limited by the period of solar energy availability. The effects of the transmissivity of the glass on the absorber surface temperature are similar to those of the glass on melting and freezing times, i.e. the surface temperatures are greatly affected by the transmissivity of the glass during the melting process whilst only slightly affected by it during the freezing period.

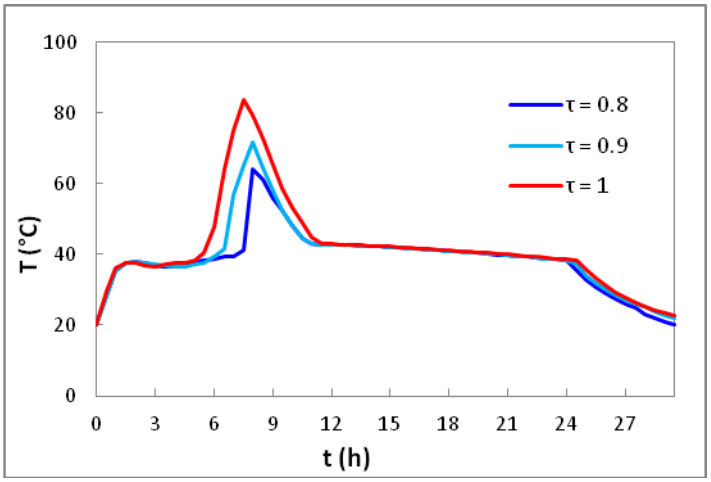

Figure 7- 37 Melting and freezing times for various transmissivities of glass. Simulation condition: initial PCM temperature = 20 ℃, initial air inlet temperature = 20 ℃, heat flux = 700 W/m^2

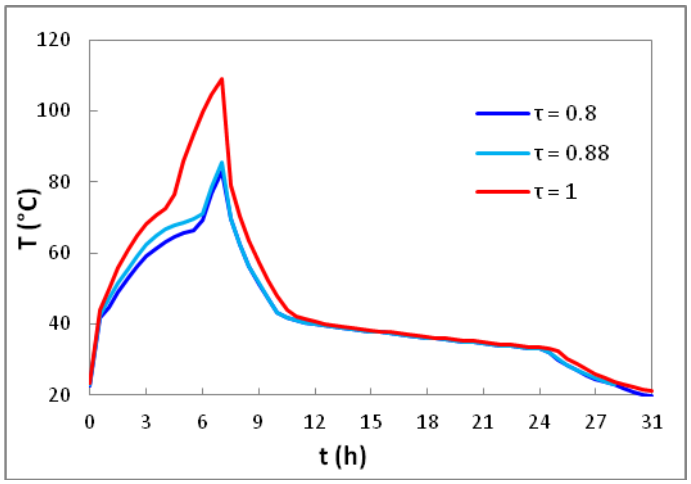

Figure 7- 38 Absorber surface temperatures for various transmissivities of glass. Simulation condition: initial PCM temperature = 20 ℃, initial air inlet temperature = 20 ℃, heat flux = 700 W/m^2

The mass flow rate and temperature difference profiles for various transmissivities of the glass are shown in Figure 7-39 and 7-40, respectively. As shown, there are slight influences in changing the transmissivity of the glass on the mass flow rate and temperature difference at the initial and late freezing periods. The reason is that the higher transmissivity of the glass, the larger amount of the heat stored in PCM during the melting period, which leads the higher mass flow rate and outlet temperature.

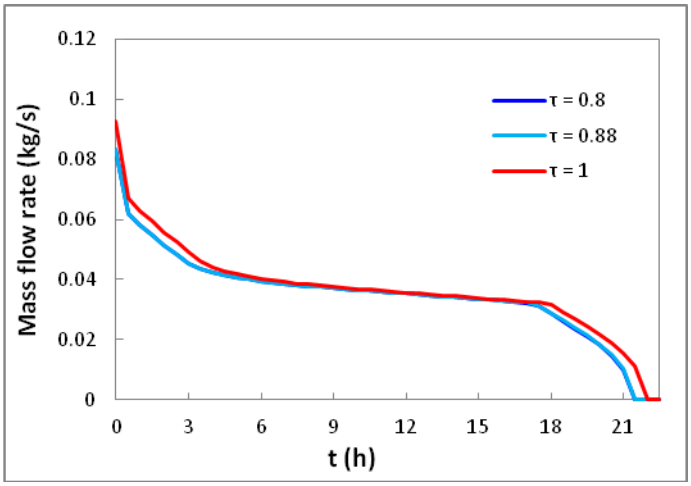

Figure 7- 39 Air mass flow rates for various transmissivities of glass. Simulation condition: initial PCM temperature = 20 ℃, initial air inlet temperature = 20 ℃, heat flux = 700 W/m^2

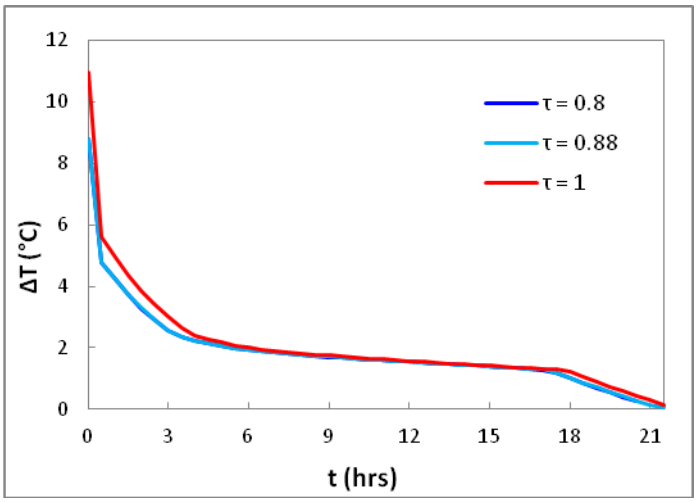

Figure 7- 40 Temperature differences for various transmissivities of glass. Simulation condition: initial PCM temperature = 20 ℃, initial air inlet temperature = 20 ℃, heat flux = 700 W/m^2

7.2.2.11 Effect of the absorptivity of the absorber surface

The absorptivity of the absorber plate strongly influences the thermal performance of the solar chimney, as the absorptivity directly affects the total energy input to the PCM. Leon and Kumar (Leon and Kumar, 2007) have shown that the absorptivity has a stronger effect on the efficiency of the absorber plate than emissivity. Liu et al. (Liu et al., 2007) have been also confirmed that the absorptivity of the absorber surface played an important role on the solar absorber efficiency. However, whilst all these investigations primarily focused on solar dryers or other solar heating applications, very few studies have been conducted on the effect

of absorptivity on the thermal performance of solar chimney. This parameter, thus, will be investigated in this research.

Figures 7-41 and 7-42 show the effects of absorptivities of the absorber plate on melting and freezing times and absorber surface temperature profiles, respectively. The absorptivities of the absorber surface studied are 0.8, 0.9 and 1.0. As shown in Figure 7-41, the absorptivity greatly affects the melting time and freezing time. The melting times are around 7.6 h, 6.6 h and 5.6 h, respectively, whilst the freezing times are 15.2 h, 16.7 h and 20 h accordingly. It is found that increasing the absorptivity of the absorber plate will increase the heat transfer rate between the absorber surface and the PCM, and thus the PCM completes the melting process more quickly. This is due to the fact that the surface temperature increases significantly with the increase of the absorptivity. Consequently, the freezing process is prolonged. The results suggest that the absorber plate with high absorptivity should be used in this proposed system in order to maximize the efficiency of the solar absorber.

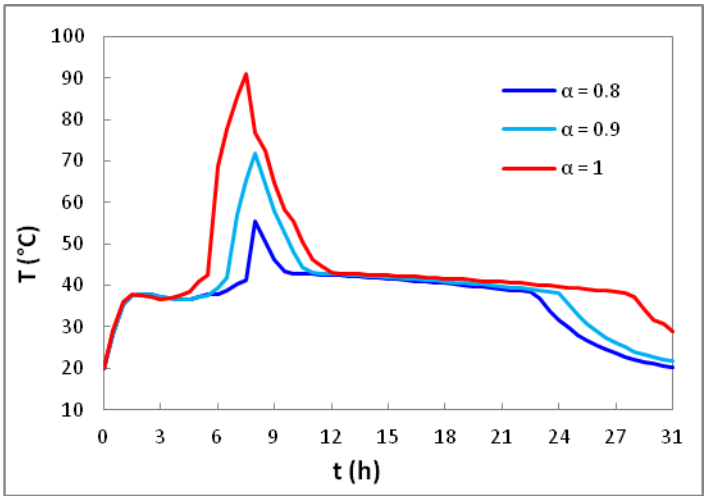

Figure 7- 41 Melting and freezing times for various absorptivities of absorber plate. Simulation condition: initial PCM temperature = 20 ℃, initial air inlet temperature = 20 ℃, heat flux = 700 W/m^2

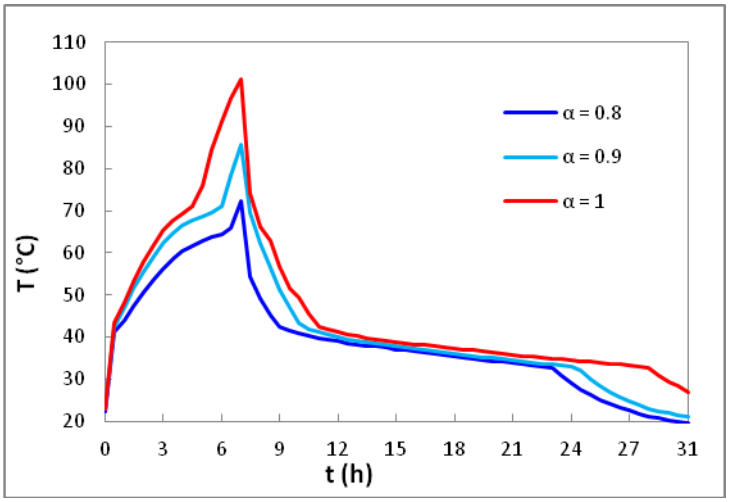

Figure 7- 42 Absorber surface temperatures for various absorptivities of absorber plate. Simulation condition: initial PCM temperature = 20 ℃, initial air inlet temperature = 20 ℃, heat flux = 700 W/m^2

Figures 7-43 and 7-44 present the mass flow rates and outlet air temperature differences for various absorptivities of the absorber plate. It is seen that increasing the absorptivity of the absorber surface will lift up the mass flow rate and the outlet air temperature particularly at the initial and late freezing periods. The mass flow rates are slightly increased by around 0.01 kg/s and 0.02 kg/s, and the temperature differences are increased by 0.7 ℃ and 1.4 ℃ for the absorptivities of 0.94 and 1.0 during the phase change period.

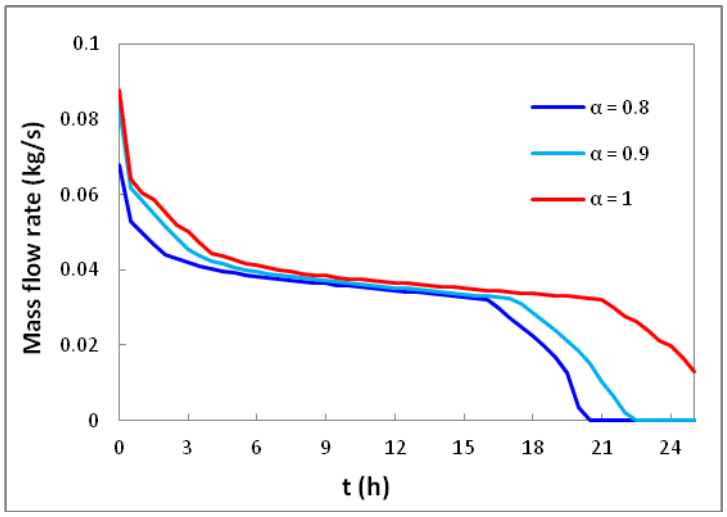

Figure 7- 43 Air mass flow rates for various absorptivities of absorber plate. Simulation condition: initial PCM temperature = 20 ℃, initial air inlet temperature = 20 ℃, heat flux = 700 W/m^2

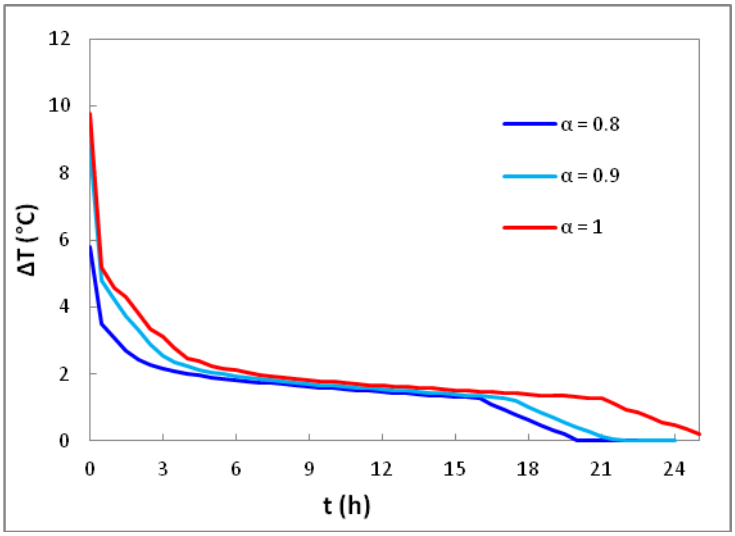

Figure 7- 44 Outlet air temperature differences for various absorptivities of absorber plate. Simulation condition: initial PCM temperature = 20 ℃, initial air inlet temperature = 20 ℃, heat flux = 700 W/m^2

7.3 ECONOMIC AND ENVIRONMENTAL BENEFITS

The study on the thermal performance of the proposed system was previously carried out. A fully charged system can release around 30 % of stored energy to air, being able to heat or cool the living space, since the system is driven by renewable energy – solar energy, no mechanical energy is consumed. Thus, the proposed system has great potential to save energy. An analysis to determine the energy and environmental benefits of utilising the PCM based solar chimney is carried out. The weather data of London is used as the basis for this analysis in this section.

7.3.1 Weather Data

Table 7-1 shows the mean hourly irradiation values on the due south- facing vertical surface in London. To simplify the analysis, the hourly mean solar irradiance intensity is used for all the days in one month. In this analysis, it is assumed that the cooling season is 3 months in total (June, July and August) and the heating season is 9 months from September to May.

Table 7- 1 Mean solar irradiance for a typical day of each month (CIBSE, 2008)

Month	Daily mean irradiance (W/m^2)															
	0430	0530	0630	0730	0830	0930	1030	1130	1230	1330	1430	1530	1630	1730	1830	1930
Jan 29	--	--	--	83	258	483	672	740	738	604	399	215	75	--	--	--
Feb 26	--	--	42	133	310	508	672	759	745	668	538	341	145	45	--	--
Mar 29	--	11	46	178	358	520	639	722	713	649	532	367	183	45	10	--
Apr 28	8	24	57	166	346	485	599	665	667	598	498	340	169	56	23	8
May 29	16	39	72	117	278	424	527	580	578	524	421	275	115	68	37	14
Jun 21	18	41	77	101	266	410	512	566	569	507	405	263	104	77	42	20
Jul 4	16	35	67	101	256	392	491	540	547	489	392	256	100	71	35	14
Aug 4	11	28	59	139	305	444	558	603	597	543	446	295	133	55	28	11
Sep 4	--	12	41	196	375	525	620	669	689	632	517	357	176	41	13	--
Oct 4	--	--	60	193	393	593	701	712	702	644	528	337	168	56	--	--
Nov 4	--	--	--	115	348	592	741	813	752	642	472	281	98	--	--	--
Dec 4	--	--	--	--	183	479	680	752	719	617	434	168	--	--	--	--

As shown in Table 7-2, in the UK for free-running (i.e. non-air conditioned) buildings in the summer, the recommended indoor comfort temperatures for dwellings are from 23 to 25 ℃. As mentioned in the notes, once the indoor temperature rises above 24 ℃, the sleep quality may be affected. Therefore, it is assumed that the air inlet temperature of the proposed system is 24 ℃. The mean outdoor air temperatures are 18.7, 19.6 and 19.8 ℃ in June, July and August, respectively (CIBSE, 2008). Thus the fresh ambient air has the capacity of cooling the living space during summertime. As mentioned in CIBSE previously, the recommended indoor comfort temperature is 21 ℃ during the heating period, and so the air inlet temperature is set at 20 ℃.

Table 7- 2 General summer indoor comfort temperatures for non-air conditioned buildings (CIBSE, 2008)

Building type	Offices	Schools	Dwellings		Retail
			living areas	bedrooms	
Operative temp. for indoor comfort in summer (℃)	25	25	25	23	25
Notes	Assuming warm summer conditions in UK	Assuming warm summer conditions in UK	Assuming warm summer conditions in UK	Sleep may be impaired above 24 ℃	Assuming warm summer conditions in UK

7.3.2 Payback Period

Figure 7-45 shows the total monthly energy output generated by the proposed system except for the cooling months of June – August. The annual heating energy output of the system is 220.7 kWh. As shown, the monthly energy outputs basically correspond to their monthly available solar energy, in which the maximum heating energy of 32 kWh is obtained in October, and the minimum heating energy of 12.5 kWh is provided by the system in May.

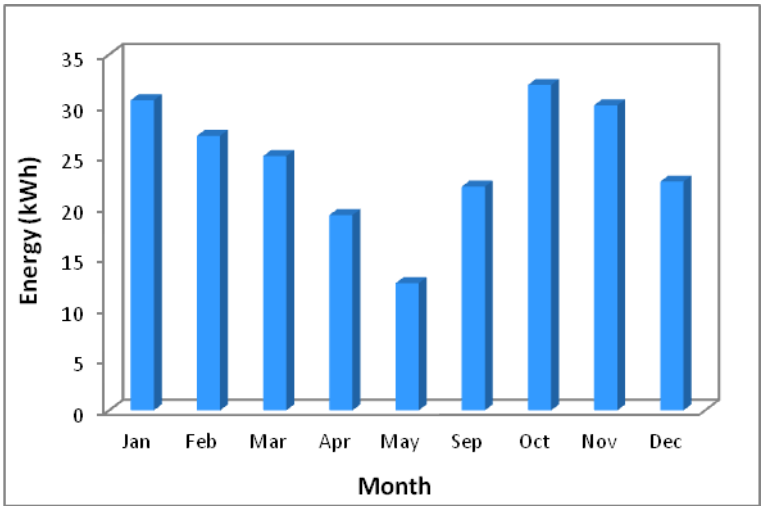

Figure 7- 45 Monthly energy output from the proposed system

The proposed system is designed in a conventional solar chimney configuration, and the increase in the cost of the system is due to the PCM unit. The paraffin wax PCM used in this system is commercially available and very cheap (around £5/ kg). Paraffins are compatible with and can be incorporated into most common building materials, and are compatible with most container materials. Therefore, the cost of the PCM encapsulation would not be a problem. The paraffin wax PCM suffers from negligible supercooling or phase segregation, which means that the long term stability of paraffin wax is not in question and in fact is one of its major advantages. The manufacturer also guarantees RT42 as a long life product, and long term reliability ensures that the PCM performs well after a large number of freeze/melt cycles. Hence, the system would require no maintenance during a long period, resulting in a significant reduction in the cost of the system. As mentioned, the annual energy saving during the heating period (September - May) is 220.7 kWh. The price of electricity in the UK is £0.153 per kWh (http://www.energysavingtrust.org.uk/Energy-Saving-Trust/Our-calculations). Therefore, the payback time of this system is around 7.3 years.

It is seen that the payback time is sensitive to the price of the electricity, as the price of electricity increases the payback period is found to be decreased. Over the last three years (2010 – 2012) the electricity price has been increasing by at least 20% (http://blog.comparemysolar.co.uk/electricity-price-per-kwh-comparison-of-big-six-energy-companies/), and so the evaluated payback time will shorten. Additionally, the system can provide fresh cool air to the living space during the summer time (June – August), there being a total of 2129 kg fresh air driven into the living space, which can reduce the cooling load of the space. As a result, the cost of the proposed system could be further reduced. The ecological impact of the system is estimated in terms of the CO_2 emission. Electricity emits nearly 0.517kg carbon dioxide per kWh (http://www.energysavingtrust.org.uk/Energy-Saving-Trust/Our-calculations). So the annual CO_2 emission saving is 133.9 kg.

7.4 CONCLUSIONS

A comprehensive numerical study has been carried out on the parameters affecting the thermal performance of the proposed system. The main findings are:

1) Parameters affecting the melting and freezing times
   i) The effects of the latent heat of fusion on the melting/freezing processes are quite significant. The higher the latent heat of fusion the slower the melting/freezing process. For lower latent heat, the extra sensible heat stored in the PCM prolongs the freezing to some degree. It can be concluded that the effect of the latent heat of fusion on melting time is more significant than that on freezing time.

   ii) The higher thermal conductivity of the PCM leads to a higher heat transfer rate in the PCM which results in the PCM starting to melt, and completing the melting and solidification more quickly.

   iii) The thermal conductivity of the insulator greatly affects the melting and freezing times. The insulator having a lower thermal conductivity can reduce the heat loss from the system to the environment during the melting and freezing periods. That is, the lower the thermal conductivity, the shorter the melting time and the longer the freezing time.

iv) As expected, higher heat flux shortens the melting time, and brings more sensible heat which prolongs the freezing time.

v) The absorptivity of the absorber surface greatly affects the melting time and freezing time. The increase in the absorptivity of the absorber plate will increase the heat transfer rate between the absorber surface and the PCM, and therefore, the PCM completes the melting process more quickly. Consequently, the freezing process is prolonged.

2) Parameters affecting the melting time

i) Wider phase change temperature range improves the heat transfer rate between the absorber and the PCM. As a result, the PCM having wider phase change temperature reaches the complete melting earlier than that with narrower phase change temperature.

ii) Higher transmissivity of the glass allows more solar energy to pass through the glass, and so reduces the melting time whilst slightly affecting the freezing time.

3) Parameters affecting the freezing time

i) Lower air inlet temperature increases the heat transfer rate between the air and the absorber surface which results in a shorter freezing time and a higher air temperature difference between inlet and outlet.

ii) The specific heat of the PCM affects the way the sensible heat contributes to the melting/freezing process. High specific heat also prolongs the stage I period (sensible energy dominated) of melting/freezing, since only sensible heat exchange take places in the PCM, and the time required for the PCM to reach the melting temperature is longer for higher specific heat than that for lower specific heat at the initial period of melting. However, the role of the sensible heat effect on the freezing process is more important than that for the melting period. The reason for this is that of the relatively low heat transfer rate between the air and the absorber plate, resulting in a longer time for the PCM to reach the freezing temperature.

4) Parameters slightly affecting the melting/freezing time

i) The initial temperature of the PCM has very little influence on the melting process after the early period of melting. This is to be expected as it only relates to the sensible heat terms. The investigation of this parameter which will determine how soon the PCM is to be fully melted will take place at different temperatures.

ii) The thermal conductivity of the container slightly affects the melting and freezing times. This is because the container plate is thin and the overall heat transfer coefficient is mainly dependent on the convective heat transfer components. On this basis, high conductivity materials could not be justified.

5) An analysis of the economic and ecological benefits of the proposed system presents that a total amount of 220.7 kWh heating energy is provided during the heating period. Furthermore, the amount of CO_2 emission savings by this system is 134kg per year. A simple analysis of payback period shows that the payback time of this system is around 7.3 year for London area. It is also shown that the payback time is sensitive to the price of the electricity, as the price of electricity increases the payback time decreases.

8. CONCLUSIONS AND RECOMMENDATIONS

8.1 CONCLUSIONS

The aim of this work is the development of a solar chimney incorporating latent heat storage for space heating and cooling in residential buildings. This aim is successfully achieved by carrying out the objectives presented in Chapter 1. The main findings from the research will be highlighted in this chapter. The following are the main conclusions that can be drawn from the current research.

8.1.1 PCM Selection

The PCM offers a number of advantages over sensible heat material, and has recently received a great deal of interest. The main advantages of the PCM are its high storage capacity and isothermal characteristic during the transition of phase. Consequently, the attractive properties of the PCM lead to large space savings and provide much better thermal comfort in space heating applications. Organic PCM was chosen as the thermal storage medium in this present research. Organic PCMs such as paraffin waxes are a preferred choice to inorganic PCMs as they are more chemically stable, noncorrosive and have low vapour pressure. According to the literature review, a melting temperature range for the proposed system of 25 ℃ - 45 ℃ was determined. The PCMs used in this research are paraffin RT 25 and paraffin RT 42, which are commercial, organic PCM from Rubitherm GmbH Company.

8.1.2 Numerical and Experimental Study on the Selected PCMs

A mathematical model for determination of the thickness of the PCM container for RT 42 has been presented. A long term historic maximum daily solar radiation for the year was used as the basis in this numerical study. The model has been validated by using experimental data which was obtained from a small scale experimental test rig. The experimental results showed high agreement with the assumed melting time. The experimental result indicated

that the numerical model has the ability to determine the mass of the PCM for the proposed system for the given weather conditions.

The charging time and discharging time are two key factors to determine the optimum PCM for the proposed system. In the heating mode, the encapsulated PCM is considered to be capable of being completely charged over a period of 8 hours and have the capacity to discharge heat over a period of up to 16 hours. The small scale experimental rig was developed to investigate the melting and freezing characteristics of RT 42 and RT 25. The experimental results showed that the solidification times of the PCMs decrease with the increase in melting temperature. Hence, the optimum PCM should be selected on the basis of its melting temperature, rather than its other properties such as latent heat. From this point of view, the RT 42 is the optimum PCM for the proposed system, since it has a desirable discharging time among the PCMs within the melting temperature range selected.

Four types of metal finned TCEs were employed to achieve the following three purposes: to reduce the melting time, to facilitate the heat stored discharge before the next charge cycle and to reduce the temperature gradient inside the PCM to increase the absorber surface temperature during the discharging process. The performances of the four TCEs with RT 42 and RT 25 have been investigated. The conclusions from the analysis are shown below:

i) A typical melting or freezing process of a pure PCM or a PCM component consists of three stages: (a) stage I where sensible heat is dominant and characterised by pure conductive heat transfer, (b) stage II where latent heat is dominant with convective and conductive combined heat transfer, and (c) stage III where latent heat dictates the heat exchange with conduction mode.

ii) Introducing TCEs into the PCMs can enhance the heat transfer in the solid region of the PCM but they would suppress the natural convection effect in the liquid zone, resulting in the enhancement performance weakening with the increase in the volume fraction of the TCEs during the melting process.

iv) One of the purposes of using TCEs is to reduce the problem of the PCM being a self-insulating material during the solidification process. However, the experimental results showed that the TCEs do not always have a positive effect on this problem, since the

suppression of the TCEs on natural convection affects the heat transfer in the liquid PCM zone during early discharging period. This phenomenon deteriorates as HCS or SCS insert into the PCM.

For a LHS system with a given volume, the use of metal TCEs to improve the heat transfer performance of the PCM considerably increases the weight and decreases the volumetric heat of fusion of the LHT system at the same time. A new quantity $(\varphi_{ef}/\varepsilon)$ was introduced here to describe the relationship between the heat transfer enhancements of TCEs and the volumes occupied by them. The results showed that the HF is the most effective TCE amongst all the enhancers for RT 42 test samples.

8.1.3 Development of a Solar Chimney

A simple CFD model was developed to optimise the geometry of the proposed solar chimney. The vertical chimney with a constant height of 2 m, with one horizontal inlet and two horizontal outlets, the inlet fixed on the heated wall whilst the two outlets are fixed on the unheated wall and heated wall respectively, to achieve the purpose of winter heating and summer cooling. A fixed wall temperature of 41 ℃ was used to represent the phase change temperature of the PCM.

The simulated results revealed that the total mass flow rate through the solar chimney and air temperature distribution at the outlet with a vertical heated wall was strongly affected by the reverse flow occurring at the outlet, the presence of the reverse flow reducing the total mass flow rate through the solar chimney and mean air temperature at outlet, and thus is not desirable for ventilation and heating applications. In order to maximise the mass flow rate and air temperature to enhance the ventilation and heating performance, it is desirable to minimize the reverse flow entering from the outlet. For this purpose, the solar chimney with an air gap of 0.2 m deep and inlet and outlet of 0.2 m high was chosen for the further study, as reverse flow was not found at this geometry, the maximum mass flow and high air temperature consequently being obtained.

8.1.4 Experimental and Numerical Study on a Full Scale Experimental Rig

A full scale experimental rig with the predetermined dimensions was developed to further

investigate the thermal performance of the proposed system under laboratory conditions. The experiments were carried out for three heat fluxes of 500 W/m^2, 600 W/m^2 and 700 W/m^2. A numerical simulation procedure was also developed to reproduce the experimental conditions. The numerical models were described in terms of closed mode and open mode. One of main purposes for undertaking the experimental study was to verify the ability of a mathematical model to predict the air flow rate, air temperature at outlet, glass temperature and absorber plate temperature.

The following are the main findings:

i) The solar heating and cooling of the dwellings by using a solar chimney with latent heat thermal storage is technically viable.

ii) Results indicated that within the same charging period, the whole freezing process including the initial sensible heat discharging periods were 13h 50 min, 13h 50 min and 13 h 20 min for the cases of 700, 600 and 500 W/m^2. It was seen that though the PCMs were partially melted at the end of the charging process in the last two cases, the freezing times were almost same.

iii) The model results were in close agreement with the experimental results, particularly the simulated results for the discharging process.

iv) Unlike the temperatures of the PCM, the surface temperatures at different heights are nearly the same over the discharging period. Furthermore, the predicted absorber surface temperature for the discharging process was more accurate compared with that for charging process. As natural convection occurred in PCM during the charging process that was not considered in the numerical simulation.

v) The model predicted a slightly lower glass temperature than experimental one. This may be attributed to the differences between the actual thermo-properties of the glass and the theoretical values assumed in the numerical simulation. The results also showed that the glass temperature did have an influence from the absorber plate.

vi) Results indicated that although the initial sensible heat discharging period lasted for a

short time compared to the total discharging period, its effect on mass flow rate is significant. The latent heat discharging period lasted for 11h, and the mass flow rate declined very slowly and varied around 0.038 kg/s, followed by 0.037 kg/s and 0.36 kg/s for the heating operation under the heat fluxes of 700,600 and 500 W/m^2. However, the mass flow rates were around 0.04 kg/s, 0.039 kg/s and 0.38 kg/s for cooling ventilation operation during this period. This period was followed by a sharp drop in mass rate due to sensible heat dominating this period again.

vii) The outlet air temperature varied within a narrow range during the latent heat discharging period. The slight variations in mass flow rate and outlet temperature, as well as the outlet air being warm enough, are important for a solar air heating system. The average temperature increases in outlet temperatures are 5 ℃, 5.4 ℃ and 6.5 ℃ for the heat fluxes of 700, 600 and 500 W/m^2, respectively under the experimental conditions.

viii) Using the verified model, a thermal performance study has been carried out for various heat fluxes. At a same charging period, if the PCM can be fully melted for a certain heat flux, further increasing the heat flux to a higher value could not improve the system's performance significantly, since most extra heat is stored by the PCM as sensible heat. Furthermore, if the temperature of the innermost layer of the PCM is higher than 38 ℃ (initial melting temperature), further decreasing the heat flux to a lower value the performance would also not diminish greatly. Once the temperature of the innermost layer drops below 38 ℃, the performance level decreases dramatically.

8.1.5 Parametric study

Having the verified numerical model, a comprehensive sensitivity analysis is performed to examine how a number of parameters affect the thermal performance of the system. The following conclusions were drawn from this study:

1) Parameters affecting the melting and freezing times

i) The effects of the latent heat of fusion on the melting / freezing process are quite significant. The higher the latent heat of fusion, the slower the melting / freezing process. For lower latent heat, the extra sensible heat stored in the PCM prolongs the

freezing to some degree. It can be concluded that the effect of the latent heat of fusion on melting time is more significant than that on freezing time.

ii) The higher thermal conductivity of the PCM leads to a higher heat transfer rate in the PCM, which results in the PCM starting to melt and completing melting and solidification more quickly.

iii) The thermal conductivity of the insulator greatly affects the melting and freezing times. The insulator having a lower thermal conductivity can reduce the heat loss from the system to the environment during the melting and freezing period. That is, the lower the thermal conductivity, the shorter the melting time and the longer the freezing time.

iv) As expected, higher heat flux shortens the melting time, and brings more sensible heat, which prolongs the freezing time.

v) The absorptivity of the absorber surface greatly affects the melting time and freezing time. The increase in the absorptivity of the absorber plate will increase the heat transfer rate between the absorber surface and the PCM, and therefore the PCM completes melting process quicker. Consequently, the freezing process is prolonged.

2) Parameters affecting the melting time

i) Wider phase change temperature range improves the heat transfer rate between the absorber and the PCM. As a result, the PCM having wider phase change temperature reaches complete melting earlier than that with narrower phase change temperature.

ii) Higher transmissivity of the glass allows more solar energy to pass through the glass, and so reduces the melting time while slightly affecting the freezing time.

3) Parameters affecting the freezing time

i) Lower air inlet temperature increases the heat transfer rate between the air and the absorber surface which results in a shorter freezing time and a higher air temperature difference between inlet and outlet.

ii) Specific heat of the PCM affects the way the sensible heat contributes to the melting / freezing process. High specific heat also prolongs the stage I period (sensible energy dominated) of melting/freezing, since only sensible heat exchange take places in the PCM, and the time required for the PCM to reach the melting temperature is longer for higher specific heat than that for lower specific heat at the initial period of melting. However, the role of sensible heat effect on the freezing process is more important than that for the melting period. The reason is the relatively low heat transfer rate between the air and the absorber plate, resulting in a longer time for the PCM to reach the freezing temperature.

4) Parameters slightly affecting the melting/freezing time

i) The initial temperature of the PCM has very little influence on the melting process after the early period of melting. This is to be expected, as it only relates to the sensible heat terms. The investigation of this parameter will determine how soon the PCM will be full melted will take place at different temperatures.

ii) The thermal conductivity of the container slightly affects the melting and freezing times. This is because the container plate is thin and the overall heat transfer coefficient is mainly dependent on the convective heat transfer components. On this basis, high conductivity materials could not be justified.

8.2 RECOMMENDATIONS FOR FURTHER WORK

A comprehensive numerical and experimental study on the thermal performance of a solar chimney incorporating LHS has been carried out in this research. However, there still remains a number of potential the research tasks to be addressed in order to improve the system performance. This potential work involves experimental and theoretical research and further applied work, and are summarised as following:

8.2.1 Thermal Conductivity Enhancement

One major drawback of LHS systems is the low thermal conductivity of most PCMs. Thus, thermal conductivity enhancement techniques are required in practical LHS application. Four stainless steel TCEs - vertical fin (VF), horizontal fin (HF), honeycomb structure (HCS) and

square cell structure (SCS) have been used to improve the rate of heat transfer in LHS in this research. However, the research shows that once the innermost layer of the PCM fails to reach the melting temperature of 38 ℃, the performance of the current system deteriorates greatly. The literature reveals that some metallic materials such as cooper and aluminium have much higher thermal conductivities than stainless steel. Hence, further development of TCEs in copper or aluminium would allow the use of the proposed system in practical application and may yield good results.

8.2.2 Mathematical Model Modification

The mathematical model developed to investigate the thermal performance of the proposed system has been found to be applicable to various operating conditions. This is important as it may enable the modelling of the system's performance under more complicated operating conditions with more confidence. In the present work, all vents are closed to maximize the thermal storage capacity of LHS during the charging period, that is, no air flow occurs during this period. However, the simulation of the thermal performance of the system with unclosed vents during charging period has not examined in this research. Future simulation work on this is required to complement of the relationships between the thermal performance of the proposed system and the operating conditions.

8.2.3 Proposed System Application

The current research has highlighted that a solar chimney incorporating LHS is highly promising. However, the limitation of the current research is that it provided performance data from experiment testing and numerical simulation only. In order to successfully apply this system to any practical applications, the following issues should be considered:

The system design life is one of the crucial issues to be considered for the successful application of the system. Thus, the main components of the system having long term reliability is reasonably to be expected, as the LHS system is not a cheap form of thermal storage. For the PCM, long term chemical stability over a large number of charge-discharge cycle, the absence of supercooling and corrosion to the encapsulation material are desirable. For the PCM container, reliable/strong encapsulation preventing possible leakages during phase change transition is important in maintaining its thermal performance. For the glass,

the good resistance to extreme weather conditions is required to maintain the high system thermal performance. The above issues require a long term examination.

Since the findings of the present research were summarised under laboratory and simulation conditions, the performance data obtained from field testing is very important prior to widely practical application. The next step in further work is to install and monitor a practical proposed system throughout one year. This would enable a full evaluation of the thermal performance and economical analysis of the system, which is one of the key links in the process of commercialisation.

REFERENCES

Abhat, A., (1983) 'Low Temperature Latent Heat Thermal Energy Storage: Heat Storage Materials.' Solar Energy 30, (4) 313-332

Abhat, A., (1981) Low temperature latent heat thermal energy storage. Holland: D. Reidel Publication Co.

Agyenim, F., Hewitt, N., Eames, P., Smyth, M., (2010) 'A review of materials, heat transfer and phase change problem formulation for latent heat thermal energy storage systems (LHTESS).' Renewable and Sustainable Energy Reviews 14, 615–628

Akhilesh, R., Narasimhan, A., Balaji, C., (2005) 'Method to improve geometry for heat transfer enhancement in PCM composite heat sinks.' Int. J. Heat Mass Transfer 48, (13) 2759-2770

Alkan, C., Sari, A., Karaipekli, A., Uzun, O., (2009) 'Preparation, characterization and thermal properties of microencapsulated phase change material for thermal energy storage.' Sol. Energy Mater Sol. Cells 93, 143-147

Amori, K.E., Mohammed S. W., (2012) Experimental and numerical studies of solar chimney for natural ventilation in Iraq. Energy and Buildings 47,450-457

Arkar, C., (2007) 'Free cooling of a building using PCM heat storage integrated into the ventilation system.' Solar Energy 81, (9) 1078-1087

Athienitis, A.K., Liu, C., Hawes, D., Banu, D., Feldman, D., (1997) 'Investigation of the thermal performance of a passive solar test-room with wall latent heat storage.' Build Environ 2, (5) 3405–3410

Bansal, N., Mathur, R., Bhandari, M., (1993) 'Solar chimney for enhanced stack ventilation.'

Build Environ 28, 373–377

Baran, G., Sari, A., (2003) 'Phase change and heat transfer characteristics of a eutectic mixture of palmitic and stearic acids as PCM in a latent heat storage system.' Energy Convers. Mgmt. 44, 3227-3246

Bassiouny, R., Koura, N.S.A., (2008) 'An analytical and numerical study of solar chimney use for room natural ventilation.' Energy and Buildings 40, (5) 865–873

Belén, Z., José, M. M., Luisa, F. C., Mehling, H., (2003) 'Review on thermal energy storage with phase change: materials, heat transfer analysis and applications.' Applied Thermal Engineering 23, 251–283

Bilgen, E., Richard, M.A., (2002) 'Horizontal concrete slabs as passive solar collectors.' Solar Energy 72, (5) 405–413

Bouchair, A., (1989) Solar induced ventilation in the Algerian and similar climates. PHD thesis, University of Leeds

Bouchair, A., (1994) 'Solar chimney for promoting cooling ventilation in southern Algeria.' Building Services Engineering Research and Technology 15, (2) 81-93

Bourdeau, L.E., (1980) 'Study of two passive solar systems containing phase change materials for thermal storage.' In: Hayes J, Snyder R, editors. Proceedings of fifth national passive solar conference. October 19–26 Amherst, Newark, Delaware: American Solar Energy Society 297–301

Bruno, F., Saman, W., (2001) Utilization of PCM Fibreboards for space heating. In: Proceedings of ISES Solar World Congress, Australia: Adelaide

Buddhi, D., Bansal, N. K., Sawney, R. L., Sodha, M. S., (1988) 'Solar thermal storage systems using phase change materials.' International Journal of Energy Research 12, 547-555

Cabeza, L.F., Castellón, C., Nogués, M., Medrano, M., Leppers, R., Zubillaga, O., (2007) 'Use of microencapsulated PCM in concrete walls for energy savings.' Energy and Buildings 39, 113-119

Chandra, S., Kumar, R., Kaushik, S., Kaul, S., (1985) 'Thermal performance of a non A/C building with PCCM thermal storage wall.' Energy Convers Manage 25, (1) 15–20

Chen, Z.D., Bandopadhayay, P., Halldorsson, J., Byrjalsen, C., Heiselberg, P., Li, Y., (2003) 'An experimental investigation of a solar chimney model with uniform wall heat flux.' Building and Environment 38,893–906

Chow, L., Zhang, J., Beam, J., (1996) 'Thermal conductivity enhancement for phase change materials.' Int. Comm. Heat Mass Transfer 23, (1) 91-100

CIBSE Briefing 6 (2003) Energy performance of buildings. London: The Chartered Institution of Building Services Engineering

CIBSE (2008) CIBSE Concise handbook. London: The Chartered Institution of Building Services Engineers

Comini, G., Guidice, S.D., Lewis, R.W., Zienkiewicz, O. C., (1974) 'Finite element solution of non-linear heat conduction problems with special reference to phase change.' Int. J Numerical Methods in Engineering 8, (3) 613–624

Costa, M., Buddhi, D., Oliva, A., (1998) 'Numerical simulation of a latent heat thermal energy storage system with enhanced heat conduction.' Energy Conversation Management 39, 319-330

Date, A., (1991) 'A strong enthalpy formulation for the Stefan problem.' Int. J Heat Mass Transfer 34, (9) 2231–2235

Dimoudi, A., (1997) Investigation of the flow and heat transfer in a solar chimney. PhD Thesis, University of Bath

Dincer, I., Dost, S., (1996) 'A perspective on thermal energy storage systems for solar energy applications.' International Journal of Energy Research 20, 547-557

Dincer, I., Rosen, M.A., (2002) Thermal energy storage: systems and applications, Chichester: John Wiley and Sons Ltd

DTI (2003) Energy White Paper: Our energy future-creating a low carbon economy. London: Department of Trade and Industry

Eissenberg, D., Wyman, C., (1980) 'What's in store for phase change thermal storage materials for active and passive solar applications.' Solar Age 12-16

Esen, M., Ayhan, T., (1996) 'Development of a model compatible with solar assisted cylindrical energy storage tank and variation of stored energy with time for different phase change materials.' Energy Convers Mgm 37, (12) 1775-1785

Esen, M., Durmus, A., (1998) 'Geometric design of solar-aided latent heat store depending on various parameters and phase change materials.' Solar Energy 62, (1) 19-28

Ettouney, H., El-Dessouky, H., Al-Ali, A., (2005) 'Heat transfer during phase change of paraffin wax stored in spherical shells.' ASME J Sol Energy Eng 127, 357–365

Ettouney H, El-Dessouky H, Al-Kandari E. (2004) 'Heat transfer characteristics during melting and solidification of phase change energy storage process.' Ind. Eng. Chem. Res. 43, 5350–5357

Farid, M. M., Khudhair, A. M., Razack, S. A. K., (2004) 'A review on phase change energy storage: materials and applications.' Energy Convers. Mgmt. 45, 4597-1615

Fath, H. E. S., (1995) 'Transient analysis of thermosyphon solar air heater with built-in latent heat thermal energy storage system.' Renewable Energy 6, (2) 119–124

Feldman, D., Shapiro, M.M., (1989) 'Fatty acids and their mixtures as phase-change materials for thermal energy storage.' Solar Energy Mater 18, 201–216

Feldman, D., Shapiro, M.M., Banu, D., (1986) 'Organic phase change materials for thermal energy storage.' Solar Energy Materals 13, 1-10

Flourentzou, F., Van, der Maas, J., Roulet, C.A., (1998) 'Natural ventilation for passive cooling: measurement of discharge coefficients.' Energy and buildings 27, 283 – 292

Gan, G., (1998) 'A parametric study of Trombe walls for passive cooling of buildings.' Energy and Buildings 27, 37-43

Garcia-Romero, A., Delgado, A., Urresti, A., Martin, K., Sala, J. M., (2009) 'Corrosion behaviour of several aluminium alloys in contact with a thermal storage phase change material based on Glauber's salt.' Corrosion Science 51, (6) 1263-1272

Garg, H.P., Mullick, S.C., Bhargava, A.K., (1985a) Solar thermal energy storage. Holland: D. Reidel Publication Co.

Garg, H.P., Shukla, A.P., Madhuri, I., Agnihotri, R.C., Chakravertty, S., (1985b) 'Development of a simple low-cost solar simulator for indoor collector testing.' Applied Energy 21, 43-54

Ghoneim, A.A., (1989) 'Comparison of theoretical models of phase-change and sensible heat storage for air and water-based solar heating systems.' Solar Energy 42, (3) 209-220

Ghoneim, A. A., Klein, S. A., Duffie, J. A., (1991) 'Analysis of collector storage building walls using phase change materials.' Solar Energy 47, (3) 237-242

Ghoneim, A. A., Klein, S. A. (1989) 'The effect of phase change material properties on the performance of solar air based heating systems.' Solar Energy 42, 441-447

Gracia de, A., Navarro, L., Castell, A., Pardo, A.R., Alvarez, S., Cabeza, L. F., (2013) 'Experimental study of a ventilated facade with PCM during winter period.' Energy and Buildings 58, 324 – 332

Great Britain’s housing energy fact file, available from https://www.gov.uk/government/uploads/system/uploads/attachment_data/file/48195/3224-great-britains-housing-energy-fact-file-2011.pdf

Hasan, A., (1994) 'Phase change material energy storage system employing palmitic acid.' Solar Energy 52,143-154

Hasnain, S.M., (1998) 'Review on sustainable thermal energy storage technologies, part I: heat storage materials and techniques.' Energy Convers 39, (11) 1127-1138

Hawes, D.W., Feldman, D., Banu, D., (1993) 'Latent heat storage in building materials.' Energy Build 20, 77-86

Hawes, D.W., Banu, D., Feldman, D., (1989) 'Latent Heat Storage in Concrete.' Solar Energy Materials 19, 335-348

Hawlader, M.N.A., (2003) Uddin, M.S., Khin, M.M., 'Microencapsulated PCM thermal energy storage system.' Appl Energy 74, 195-202

Heine, D., Abhat, A., (1978) Investigation of physical and chemical properties of phase change materials for space heating/cooling applications. Sun: Mankind’s Future Source of Energy Oxford: Pergamon Press

Herrick, S., Golibersuch, D.C., (1978) Quantitative behavior of a new latent heat storage device for solar heating/cooling systems. In: General International Solar Energy Society Conference

Hirunlabh, J., Kongduang, W., Namprakai, P., Khedari, J., (1999) 'Study of natural ventilation of houses by a metallic solar wall under tropical climate.' Renewable Energy 18, (1) 109–119

Ho, C. J., Chu, C. H., (1996) 'Numerical simulation of heat penetration through a vertical rectangular phase change material/air composite cell.' International Journal of Heat Mass Transfer 39, (9) 1785-1795

Huang, M.J., Eames, P.C., Norton, B., (2004) 'Thermal regulation of building-integrated photovoltaics using phase change materials.' Int. J. Heat Mass Transfer 47, (12-13) 2715-2733

Hunter, L.W., Kuttler, J. R., (1989) 'The enthalpy method for heat conduction problems with moving boundaries.' J Heat Transfer Trans ASME 111, 239–242

IEA (2007) Renewals for heating and cooling: untapped potential. France: OECD/IEA

IP, K. A., Gates, J., (2001) 'Solar thermal storage using phase change materials for space heating of residential buildings.' In: Cobra 2001 RICS Foundation Construction and Building Research Conference. September 3 – September 5, Glasgow Caledonian University, London: RICS Foundation, 118-127

Jegadheeswaran, S., Pohekar, S.D., (2009) 'Performance enhancement in latent heat thermal storage system: A review.' Renewable and Sustainable Energy Reviews 13, 2225–2244

Jegadheeswaran, S., Pohekar, S.D., (2010) 'Energy and exergy analysis of particle dispersed latent heat storage system.' Int. J. Energy Environ. 1, (3) 445-458

Jurinak, J.J., Abdel-khalik, S. I., (1978) 'Properties optimization for phase-change energy storage in air-based solar heating systems.' Solar Energy 21, 377 – 383

Kaassinen, H., (1992) 'The absorption of phase change substances into commonly used building materials.' Solar Energy Materials and Solar Cells 27, 173-179

Kenny, S. P. Davidson, J. H., (1994) 'Design of a multiple- lamp large-scale solar simulator.' J. Solar Energy Eng. 116, 200–205

Khanal, R., Lei, C., (2011) 'Solar chimney—A passive strategy for natural ventilation.' Energy and Buildings 43, 1811–1819

Khedari, J., Boonsri, B., Hirunlabh, J., (2000) 'Ventilation impact of a solar chimney on indoor temperature fluctuation and air change in a school building.' Energy and Buildings

32, 89–93

Khodadadi, J. M., Zhang, Y., (2001) 'Effects of buoyancy-driven convection on melting within spherical containers.' International Journal of Heat and Mass Transfer 44, (8) 1605-1618

Khoukhi, M., Maruyama, S., (2005) 'Theoretical approach of a flat plate solar collector with clear and low-iron glazing covers taking into account the spectral absorption and emission within glazing covers layer.' Renewable energy 30, 1177–1194

Kim, C., Kaviani, M., (1990) 'A numerical method for phase change problems.' Int. J. Heat Mass Transfer 33, (12) 2721-2734

Knowler, T., (1983) 'Proportioning composites for efficient-TSWs.' Solar Energy 31, (3) 319–26

Kondo, T., Iwamoto, T., (2002) Research on using the PCM for ceiling board. IEA ECESIA, Annex 17, 3rd workshop, Japan: Tokyo

Koo, J., So, H., Hong, S.W., Hong, H., (2011) 'Effects of wallboard design parameters on the thermal storage in buildings.' Energy and Buildings 43, 1947‑1951

Kuznik F, Virgone J, Roux JJ. 'Energetic efficiency of room wall containing PCM wallboard: a full-scale experimental investigation.' Energy Build 2008; 40: 148–56

La Pica, A., Rodono, G., Volpes, R., (1993) 'An experimental investigation on natural convection of air in a vertical channel.' International Journal of Heat and Mass Transfer 36, (3) 611–616

Lacroix, M., Duong, T., (1998) 'Experimental improvements of heat transfer in a latent heat thermal energy storage unit with embedded heat sources.' Energy Conversion Management 39, (8) 703-716

Lacroix, M., Benmadda, M., (1997) 'Numerical simulation of natural convection dominated

melting and solidification from a finned vertical wall.' Numer. Heat Transfer Part A-Appl. 31, (1) 71-86

Lacroix, M., Benmadda, M., (1998) 'Analysis of natural convection melting from a heated wall with vertically oriented fins.' Int. J. Numer. Methods Heat Fluid Flow 8, (4) 465-478

Lam, J.C., Yang, L., Liu, J., (2006) 'Development of passive design zones in China using bioclimatic approach.' Energy Convers Manage 47, (6) 746–762

Lamberg, P., (2004) 'Approximate analytical model for two-phase solidification problem in a finned phase-change material storage.' Applied Energy 77, 131–152

Lane, G.A., (1983) Solar heat storage: latent heat materials volume I: Background and Scientific Principles. Florida: CRC Press Inc

Lane G.A. (1986) Solar heat storage: latent heat materials volume II: Technology. Florida: CRC Press Inc

Lane, G.A., (1989) Phase Change Thermal Storage Materials. In: Hand Book of Thermal Design. McGraw Hill Book Co.

Lane, G.A., (1980) 'Low temperature heat storage with phase change materials.' Int J Ambient Energy 1,155-168

Lee, K. H., Strand, R.K., (2009) 'Enhancement of natural ventilation in buildings using a thermal chimney.' Energy and Buildings 41, (6) 615‑621

Leon, M. A., Kumar, S., (2007) 'Mathematical modeling and thermal performance analysis of unglazed transpired solar collectors.' Solar Energy 81, (1) 62 ‑ 75

Li, J., Zhang, G., Wang, J., (1991) 'Investigation of a eutectic mixture of sodium acetate trihydrate and urea as latent heat storage.' Solar Energy 47, (6) 443-445

Lin, K. P., Zhang, Y. P., Xu, X., Di, H. F., Yang, R., Qin, P. H., (2004) 'Modeling and simulation of under-floor electric heating system with shape-stabilized PCM plates.' Build Environ 39, (12) 1427–1434

Liu, M., Bruno F., Saman, W., (2011) 'Thermal performance analysis of a flat slab phase change thermal storage unit with liquid-based heat transfer fluid for cooling applications.' Solar Energy 85, 3017 – 3027

Liu, T., Lin, W., Gao, W., Luo, C., Li, M., Zheng, Q., Xia, C., (2007) 'A parametric study on the thermal performance of a solar air collector with a V-groove absorber.' International Journal of Green Energy 4, (6) 601 – 622

Lv, S., Zhu, N., Feng, G., (2006) ' Eutectic mixtures of capric acid and lauric acid applied in building wallboards for heat energy storage.' Energy and Buildings 38, 708-711

Martlĩ-Herrero, J., Heras-Celemin, M. R., (2007) 'Dynamic physical model for a solar chimney. ' Solar Energy 81, (5) 614–622

Mathur, J., Anupama, Mathur, S., (2006a) 'Experimental investigation on four different types of solar chimneys. ' Advances in Energy Research 151–156

Mathur, J., Bansal, N.K., Mathur, S., Jain, M., Anupma, (2006b) 'Experimental investigations on solar chimney for room ventilation.' Solar Energy 80, (8) 927–935

Mathur, J., Mathur, S., Anupma, (2006c) 'Summer-performance of inclined roof solar chimney for natural ventilation.' Energy and Buildings 38, (10) 1156–1163

Mehling, H., (2004) 'Strategic project ‘‘Innovative PCM-Technology’’— results and future perspectives.' 8th expert meeting and work shop April 18–20 Kizkalesi, Turkey

Meng, Q., Wang, Y., Zhang, L., (2011) 'Irradiance characteristics and optimization design of a large-scale solar simulator.' Solar Energy 85, 1758–1767

Montgomery, R.H., Livingston, J.L., (1986) The Solar Water Heater Handbook A guide to Residential Solar Water Heaters. New York: John Wiley and Sons

Morrison, Abdel-Khalik., (1978) 'Effects of phase-change energy storage on the performance of air-based and liquid-based solar heating systems.' Solar Energy 20, 57-67

Mulligan, J.C., Colvin, D.P., Bryant, Y.G., (1996) 'Microencapsulated phase change material suspensions for heat transfer in spacecraft thermal systems.' J. Spacecraft and Rockets 33, 278-284

NATIONAL STATISTICS (2008) Energy Trends March 2008. London: BERR.

Naumann, R., Emons, H. H., (1989) 'Results of thermal analysis for investigation of slat hydrates as latent heat-storage materials.' J Therm Anal. 35, 1009-1031

Neeper, D. A., (2000) 'Thermal dynamics of wallboard with latent heat storage.' Solar Energy 68, 393‑403

Nguyen, P.H., Yerro, P., Bernard, J.L., Sellitto, P., Dupont, M., (2000) 'Wall temperature experimental investigation in a thermally driven channel.' Renewable Energy 19, 443–456

Ong, K.S., (2003) 'A mathematical model of a solar chimney.' Renewable Energy 28, 1047-1060

Ong, K.S., Chow, C.C., (2003) 'Performance of a solar chimney.' Solar Energy 74, (1) 1–17

Pasupathy, A., Athanasius, L., Velraj, R. Seeniraj, R. V., (2008) 'Experimental investigation and numerical simulation analysis on the thermal performance of a building roof incorporating phase change material (PCM) for thermal management.' Applied Thermal Engineering 28, (28) 556-565

Pasupathy A, Velraj R. (2008) 'Effect of double layer phase change material in building roof for year round thermal management.' Energy Build 40, 193–203

Peippo, K., Kauranen, P., Lund, P., (1991) 'A multicomponent PCM wall optimised for passive solar heating.' Energy Buildings 17, 265

Raj, V.A.A., Velraj, R., (2010) 'Review on free cooling of buildings using phase change materials.' Renewable and Sustainable Energy Reviews 14, 2819–2829

Regin, A. F., Solanki, S. C., Saini, J. S., (2008) 'Heat transfer characteristics of thermal energy storage system using PCM capsules: A review.' Renewable and Sustainable Energy Reviews 12, 2438-2458

Regin, A. F., Solanki, S.C., Saini, J. S., (2009) 'An analysis of a packed bed latent heat thermal energy storage system using PCM capsules: numerical investigation.' Renew. Energy 34, 1765–1773

Ryan, D., Burek, S.A.M., (2010) 'Experimental study of the influence of collector height on the steady state performance of a passive solar air heater.' Solar Energy 84, 1676–1684

Saifi, N., Settou, N., Dokkar, B., Negrou, B., Chennouf, N., (2012) 'Experimental study and simulation of airflow in solar chimneys.' Energy Procedia 18, 1289 – 1298

Saldivar, M.L.P., (2005) Heat and mass transfer behaviours of building materials and structure. PHD thesis, University of Cranfield

Salyer, I. O., Sircar A. K., (1997) 'A review of phase change materials research for thermal energy storage in heating and cooling applications at the University of Dayton from 1982-1996.' Int Journal of Global Energy Issues 9, (3) 183-198

Sari, A., (2003a) 'Thermal reliability test of some fatty acids as PCMs used for solar thermal latent heat storage applications. Energy Convers. Mgmt. 44, 2277-2287

Sari, A., (2003b) 'Thermal characteristics of a eutectic mixture of myristic and palmitic acids as phase change material for heating applications.' Appl. Thermal Eng. 23, 1005 -1017

Sari, A., (2005) 'Eutectic mixtures of some fatty acids for low temperature solar heating applications: thermal properties and thermal reliability.' Appl. Thermal Eng. 25, 2100-2007

Sari, A., Alkan, C., Karaipekli, A., Uzun, O., (2009) 'Microencapsulated n-octacosane as phase change material for thermal energy storage.' Solar Energy 83, (10) 1757-1763

Sari, A., Karaipekli, A., (2007) 'Thermal conductivity and latent heat thermal energy storage characteristics of paraffin/expanded graphite composite as phase change material.' Applied Thermal Engineering 27, 1271–1277

Sari, A., Kaygusuz, K., (2002) 'Thermal and heat transfer characteristics in a latent heat storage system using lauric acid.' Energy Convers. Mgmt. 43, 2493-2507

Scalat, S., Banu, D., Hawes, D., Paris, J., Haghighata, F., Feldman, D., (1996) 'Full scale thermal testing of latent heat storage in wallboard.' Solar Energy Mater Solar Cells 44, 49–61

Liu, Z., Yao, Y., Wu, H., (2013) 'Numerical modeling for solid–liquid phase change phenomena in porous media: Shell-and-tube type latent heat thermal energy storage.' Applied Energy 112, 1222–1232

Shabgard, H., Bergman, T.L., Sharifi, N., Faghri, A., (2010) 'High temperature latent heat thermal energy storage using heat pipes.' Int. J. Heat Mass Transfer 53, (15-16) 2979 – 2988

Sharma, A., Tyagi, V.V., Chen, C.R., (2009) 'Review on thermal energy storage with phase change materials and applications.' Renewable and Sustainable Energy Reviews 13, 318–345

Sharma, A., Wona, L.D., Buddhi, D., Park, J.U., (2005) 'Numerical heat transfer studies of the fatty acids for different heat exchanger materials on the performance of a latent heat storage system.' Renewable Energy 30, 2179-2187

Sharma, S.D., Iwata, T., Kitano, H., Sagara, K., (2005) 'Thermal performance of a solar cooker based on an evacuated tube solar collector with a PCM storage unit.' Solar Energy 78, 416-426

Shatikian, V., Ziskind, G., Letan, R., (2005) 'Numerical investigation of a PCM-based heat sink with internal fins.' Int. J. Heat Mass Transfer 48, (17) 3689-3706

Shukla A, Buddhi D, Sawhney RL. 'Thermal cycling test of few selected inorganic and organic phase change materials.' Renew Energy 2008; 33: 2606–14

Soaresa, N., Costa, J.J., Gaspar, A.R., Santos, P., (2013) 'Review of passive PCM latent heat thermal energy storage systems towards buildings energy efficiency.' Energy and Buildings 59, 82–103

Sparrow, E.M., Patankar, S.V., Ramadhyani, S., (1977) 'Analysis of melting in the presence of natural convection in the melt region.' J. Heat Transfer ASME 99, (4) 520–526

Stark, P., (1990) 'PCM-impregnated polymer microcomposites for thermal energy storage.' SAE (Soc Automotive Eng) Trans 99, 571-88

Stritih, U., (2004) 'An experimental study of enhanced heat transfer in rectangular PCM storage.' Int J Heat Mass Transf 47, 2841–2847

Stritih, U., Medved, S., (1994) 'Use of phase change materials in the wall with TIM.' Journal of Mechanical Engineering 40, (3-4) 155-159

Stritih, U., Novak, P., (1996) 'Solar heat storage wall for building ventilation.' World renewable energy congress (WREC) 268–71

Sukhatme, S.P., (1996) Solar energy principles: Principles of thermal collection and storage. New Delhi: Tata McGraw-Hill Publishing LTD

Swet, J., (1980) 'Phase change storage in passive solar architecture.' In: Proceedings of the 5th national passive solar conference. Massachusetts: Amhearst 282–286

Telkes, M., (1975) Thermal storage for solar heating and cooling. Proceedings of the Workshop on Solar Energy Storage Subsystems for the Heating and Cooling of Buildings Charlottesville (Virginia, USA)

Tihonov, A.N., Samarskii, A.A., (1963) Equations of Mathematical Physics. Pergamon, London

Tuncbilek, K., Sari, A., Tarhan, S., Ergünes, G., Kaygusuz, K., (2005) 'Lauric and palmitic acids eutectic mixture as latent heat storage material for low temperature heating applications.' Energy 30, 677-692

Tyagi, V.V., Buddhi, D., (2007) 'PCM thermal storage in buildings: A state of art.' 11, 1146–1166

Tyagi, V.V., Panwar, N. L., Rahim, N. A., Kothari, R., (2012) 'Review on solar air heating system with and without thermal energy storage system.' Renewable and Sustainable Energy Reviews 16, 2289– 2303

Veerappan M, Kalaiselvam S, Iniyan S, Ranko, G., (2009) 'Phase change characteristic study of spherical PCMs in solar energy storage.' Solar Energy 83, 1245–1252

Velraj, R., Seeniraj, R. V., Hafner, B., Faber, C., Schwarzer, K., (1999) 'Heat transfer enhancement in a latent heat storage system.' Solar Energy 65, (3) 171-180

Venkatasetty, H.V., (1975) 'Corrosion characteristics of phase change materials, Proc. Workshop on Solar Energy Storage Subsystems for the Heating and Cooling of Building.' April 16-18, University of Virginia, Charlottesville 65-67

Voller, V., Cross, M., (1981) 'Accurate solutions of moving boundary problems using the enthalpy method.' Int. J Heat Mass Transfer 24, (3) 545–556

Wada, T., Yokotani, F., Matsuo Y, (1984) 'Equilibria in the aqueous ternary system containing

Na+, $CHCO_2^-$ and $P_2O_7^{4-}$ between 38 and 85 ℃.' Bull. Chem. Soc. Jpn. 57, 1671-1672

Wang, J., Chen, G., Zheng, F., (1999) 'Study on phase change temperature distributions of composite PCMs in thermal energy systems.' International Journal of Energy Research 23, 277-285

Wang, X., Lu, E., Lin, W., Liu, T., Shi, Z., Tang, R., Wang, C., (2000) 'Heat storage performance of the binary systems neopentyl glycol/pentaerythritol and neopentyl glycol/trihydroxy methylaminomethaneas solid-solid phase change materials.' Energy Conversation Management 41, 129-134

Whitaker, S., (1999) The method of volume averaging. USA: Kluwer Academic Publishers

Yao, M., Chait, A., (1993) 'An alternative formulation of the apparent heat capacity method for phase-change problems.' J. Numer. Heat Transfer Part B Fundamentals 24, (3) 279–300

Yener, Y., and Kakac, S., (2008) Heat conduction. fourth ed. London: Taylor & Francis

Zhai, X.Q., Song, Z.P., (2011) Wang, R.Z., 'A review for the applications of solar chimneys in buildings.' Renewable and Sustainable Energy Reviews 15, 3757–3767

Zalba, B., Marin, J.M., Cabeza, L.F., Mehling, H., (2004) 'Free cooling of buildings with phase change materials.' Int. J Refrig 27, 839-849

Zhang, Y., Lin, K., Jiang, Y., Zhou, G., (2008) 'Thermal storage and nonlinear heat-transfer characteristics of PCM wallboard.' Energy and Buildings 40, 1771–1779

Zhang, Y., Yi, J., (1999) 'A simple method, the T-history method of determining the heat of fusion specific heat and thermal conductivity of phase change materials.' Meas. Sci. Technol. 10, 201-205

Zhao, C.Y., Lu, W., Tian, Y., (2010) 'Heat transfer enhancement for thermal energy storage using metal foams embedded within phase change materials (PCMs).' Solar Energy 84,

1402 – 1412

Zhou, D., Zhao, C.Y., Tian, Y., (2012) 'Review on thermal energy storage with phase change materials (PCMs) in building applications.' Applied Energy 92, 593 – 605

Zivkovic, B., Fujii, I., (2001) 'An analysis of isothermal phase change of phase change material within rectangular and cylindrical containers.' Solar Energy 70, (1) 51–61

Websites:

http://gcep.stanford.edu/research/exergycharts.html (10 March 2014)

http://www.rubitherm.de/english/index.htm (15 August 2010)

http://www.metals4u.co.uk/ (21 February 2011)

http://zeisscampus.magnet.fsu.edu/articles/lightsources/tungstenhalogen.html (26 September 2010)

http://www.energysavingtrust.org.uk/Energy-Saving-Trust/Our-calculations (10 April 2013)

http://blog.comparemysolar.co.uk/electricity-price-per-kwh-comparison-of-big-six-energy-companies/ (09 April 2013)

https://www.gov.uk/government/uploads/system/uploads/attachment_data/file/48195/3224-great-britains-housing-energy-fact-file-2011.pdf (25 July 2011)

APPENDIX 1: Hourly direct and diffuse irradiation on vertical surface for London area (Bracknell)

Date and times of sunrise/ sunset	Orientation	Type	Daily mean irradiance (/$W \cdot m^{-2}$) for stated solar time*																
			0330	0430	0530	0630	0730	0830	0930	1030	1130	1230	1330	1430	1530	1630	1730	1830	1930	2030
Jan 29	Normal to beam			--	--	--	104	288	466	593	617	612	507	363	224	81	--	--	--	--
	N	Beam	--	--	--	--	0	0	0	0	0	0	0	0	0	0	--	--	--	--
Sunrise: 07:37		Diffuse	--	--	--	--	9	23	40	53	61	62	57	42	24	10	--	--	--	--
Sunset: 16:23	NE	Beam	--	--	--	--	23	22	0	0	0	0	0	0	0	0	--	--	--	--
		Diffuse	--	--	--	--	25	29	45	53	61	62	57	42	24	10	--	--	--	--
	E	Beam	--	--	--	--	88	217	269	215	77	0	0	0	0	0	--	--	--	--
		Diffuse	--	--	--	--	34	80	99	94	72	71	57	42	24	10	--	--	--	--
	SE	Beam	--	--	--	--	101	285	449	521	460	349	186	53	0	0	--	--	--	--
		Diffuse	--	--	--	--	37	97	135	149	146	128	101	57	27	10	--	--	--	--
	S	Beam	--	--	--	--	55	186	365	522	574	569	447	285	145	43	--	--	--	--
		Diffuse	--	--	--	--	28	72	118	150	166	169	157	114	70	32	--	--	--	--
	SW	Beam	--	--	--	--	0	0	68	217	352	456	446	350	222	79	--	--	--	--
		Diffuse	--	--	--	--	9	26	54	95	126	148	157	129	92	42	--	--	--	--
	W	Beam	--	--	--	--	0	0	0	0	0	76	184	210	169	69	--	--	--	--
		Diffuse	--	--	--	--	9	23	40	53	70	73	101	97	77	39	--	--	--	--
	NW	Beam	--	--	--	--	0	0	0	0	0	0	0	0	17	18	--	--	--	--
		Diffuse	--	--	--	--	9	23	40	53	61	62	57	47	30	29	--	--	--	--
Feb 26	Normal to beam		--	--	--	67	210	375	503	605	647	636	603	552	426	238	77	--	--	--
	N	Beam	--	--	--	0	0	0	0	0	0	0	0	0	0	0	0	--	--	--
Sunrise: 06:46		Diffuse	--	--	--	9	23	40	68	82	92	90	82	66	44	22	9	--	--	--

Sunset: 17:14	NE	Beam	--	--	--	32	77	57	0	0	0	0	0	0	0	0	0	--	--	--
		Diffuse	--	--	--	26	49	59	79	82	92	90	82	66	44	22	8	--	--	--
	E	Beam	--	--	--	64	192	294	302	229	83	0	0	0	0	0	0	--	--	--
		Diffuse	--	--	--	34	81	115	138	130	103	102	82	66	44	22	8	--	--	--
	SE	Beam	--	--	--	59	194	358	466	509	454	330	185	42	0	0	0	--	--	--
		Diffuse	--	--	--	32	81	129	173	184	181	155	121	71	49	22	8	--	--	--
	S	Beam	--	--	--	18	83	213	358	491	558	549	489	392	242	94	21	--	--	--
		Diffuse	--	--	--	24	50	97	150	181	201	196	179	146	99	51	24	--	--	--
	SW	Beam	--	--	--	0	0	0	39	185	336	446	507	512	407	220	67	--	--	--
		Diffuse	--	--	--	8	23	49	74	121	158	177	183	170	133	85	32	--	--	--
	W	Beam	--	--	--	0	0	0	0	0	0	82	228	332	334	217	74	--	--	--
		Diffuse	--	--	--	8	23	44	68	82	104	101	129	135	118	84	34	--	--	--
	NW	Beam	--	--	--	0	0	0	0	0	0	0	0	0	65	87	37	--	--	--
		Diffuse	--	--	--	8	23	44	68	82	92	90	129	77	59	49	26	--	--	--
Mar 29	Normal to beam		--	--	70	221	385	524	610	649	696	683	663	631	552	415	238	76	--	--
	N	Beam	--	--	5	0	0	0	0	0	0	0	0	0	0	0	0	5	--	--
Sunrise: 05:43		Diffuse	--	--	27	30	53	77	96	112	119	120	112	96	75	51	28	24	--	--
Sunset: 18:17	NE	Beam	--	--	53	145	180	131	12	0	0	0	0	0	0	0	0	0	--	--
		Diffuse	--	--	35	72	97	107	90	118	119	120	112	96	75	49	24	9	--	--
	E	Beam	--	--	70	219	355	415	371	248	90	0	0	0	0	0	0	0	--	--
		Diffuse	--	--	41	93	136	167	169	160	128	135	112	96	75	49	24	9	--	--
	SE	Beam	--	--	46	165	322	455	513	489	426	293	141	0	0	0	0	0	--	--
		Diffuse	--	--	33	78	129	176	196	205	194	173	136	117	79	49	24	9	--	--
	S	Beam	--	--	0	14	100	229	354	443	512	503	453	367	241	108	15	0	--	--
		Diffuse	--	--	11	32	78	129	166	196	210	210	196	165	126	75	30	10	--	--

	SW	Beam	--	--	0	0	0	0	0	138	298	418	499	531	480	347	177	50	--	--
		Diffuse	--	--	9	26	51	80	118	137	172	195	204	195	172	126	75	30	--	--
	W	Beam	--	--	0	0	0	0	0	0	0	89	253	384	437	383	236	76	--	--
		Diffuse	--	--	9	26	51	77	96	112	134	129	159	168	164	134	91	37	--	--
	NW	Beam	--	--	0	0	0	0	0	0	0	0	0	12	138	194	156	57	--	--
		Diffuse	--	--	9	26	51	77	96	112	119	120	118	89	104	94	70	32	--	--
Apr 28	Normal to beam		--	74	235	440	555	674	707	744	765	761	740	724	655	568	408	218	69	--
	N	Beam	--	27	59	24	0	0	0	0	0	0	0	0	0	0	22	55	26	--
Sunrise: 04:46		Diffuse	--	25	43	53	87	101	117	130	139	141	131	120	100	88	52	41	25	--
Sunset: 19:14	NE	Beam	--	68	202	316	298	220	71	0	0	0	0	0	0	0	0	0	0	--
		Diffuse	--	33	86	123	142	142	119	145	139	141	131	120	100	77	47	22	8	--
	E	Beam	--	69	226	423	497	519	417	276	96	0	0	0	0	0	0	0	0	--
		Diffuse	--	34	93	146	183	196	185	171	143	155	131	120	100	77	47	22	8	--
	SE	Beam	--	29	118	282	405	513	519	483	392	253	92	0	0	0	0	0	0	--
		Diffuse	--	25	61	115	164	195	202	205	196	179	136	138	100	77	47	22	8	--
	S	Beam	--	0	0	0	76	207	317	407	458	455	404	324	202	78	0	0	0	--
		Diffuse	--	8	24	57	90	139	168	192	207	212	194	174	138	91	56	23	8	--
	SW	Beam	--	0	0	0	0	0	0	92	255	390	480	531	499	415	262	109	27	--
		Diffuse	--	8	23	48	77	101	134	135	175	201	207	210	192	165	110	58	25	--
	W	Beam	--	0	0	0	0	0	0	0	0	97	275	427	504	509	392	210	64	--
		Diffuse	--	8	23	48	77	101	117	130	152	146	173	192	193	184	139	86	34	--
	NW	Beam	--	0	0	0	0	0	0	0	0	0	0	73	214	305	293	187	63	--
		Diffuse	--	8	23	48	77	101	117	130	139	141	146	122	140	143	117	80	33	--
May 29	Normal to beam		--	145	350	482	580	685	753	787	794	793	787	758	693	623	511	371	154	--
	N	Beam	--	73	114	66	0	0	0	0	0	0	0	0	0	0	70	120	78	--

Sunrise: 04:01		Diffuse	--	49	72	77	108	116	126	137	143	142	134	125	113	104	73	68	43	--
Sunset: 19:59	NE	Beam	--	140	308	360	333	255	117	0	0	0	0	0	0	0	0	0	0	--
		Diffuse	--	64	121	144	159	154	136	159	143	142	134	125	108	87	60	36	15	--
	E	Beam	--	125	323	444	498	505	426	280	96	0	0	0	0	0	0	0	0	--
		Diffuse	--	59	124	162	191	197	188	170	145	153	134	125	108	87	60	36	14	--
	SE	Beam	--	36	148	268	372	460	486	443	343	207	47	0	0	0	0	0	0	--
		Diffuse	--	44	81	125	167	189	197	194	184	165	126	134	108	87	60	36	14	--
	S	Beam	--	0	0	0	28	145	261	347	389	388	347	262	147	30	0	0	0	--
		Diffuse	--	16	39	72	89	133	163	180	191	190	177	159	128	85	68	37	14	--
	SW	Beam	--	0	0	0	0	0	0	47	207	343	443	489	465	399	284	157	38	--
		Diffuse	--	16	39	64	90	111	137	128	165	184	190	193	183	160	118	76	39	--
	W	Beam	--	0	0	0	0	0	0	0	0	96	280	429	511	535	471	342	132	--
		Diffuse	--	16	39	64	90	111	126	137	153	145	168	184	191	184	153	117	53	--
	NW	Beam	--	0	0	0	0	0	0	0	0	0	0	118	258	357	382	327	149	--
		Diffuse	--	17	39	64	90	111	126	137	143	142	157	134	149	153	136	114	56	--
Jun 21	Normal to beam		64	191	387	554	683	747	797	826	837	840	809	771	705	639	531	390	192	65
	N	Beam	40	100	132	85	0	0	0	0	0	0	0	0	0	0	82	133	100	40
Sunrise: 03:49		Diffuse	25	55	76	85	111	117	125	134	139	140	135	127	121	114	85	77	58	25
Sunset: 20:11	NE	Beam	64	185	342	417	397	285	134	0	0	0	0	0	0	0	0	0	0	0
		Diffuse	32	72	124	157	158	150	134	158	139	140	135	127	113	94	69	42	21	9
	E	Beam	50	162	352	504	579	544	445	290	100	0	0	0	0	0	0	0	0	0
		Diffuse	27	66	126	175	189	189	180	163	140	149	135	127	113	94	69	42	20	8
	SE	Beam	7	44	155	296	422	484	496	447	345	204	36	0	0	0	0	0	0	0
		Diffuse	21	50	82	133	163	180	187	183	173	157	123	134	113	94	69	42	20	8
	S	Beam	0	0	0	0	18	141	256	342	387	389	335	247	133	17	0	0	0	0

		Diffuse	8	18	41	77	83	125	154	170	179	180	172	158	130	87	77	42	20	8
	SW	Beam	0	0	0	0	0	0	0	37	203	346	438	479	457	395	284	157	44	7
		Diffuse	8	18	41	69	91	110	132	122	156	175	185	193	188	169	133	83	52	21
	W	Beam	0	0	0	0	0	0	0	0	0	101	284	431	513	542	483	355	163	51
		Diffuse	8	18	41	69	91	110	125	134	148	140	165	185	197	196	175	128	69	27
	NW	Beam	0	0	0	0	0	0	0	0	0	0	0	130	269	371	399	345	186	65
		Diffuse	9	19	41	69	91	110	125	134	139	140	159	138	156	164	157	126	75	32
Jul 4	Normal to beam		57	170	362	505	610	687	729	751	753	765	750	717	672	616	502	360	169	57
	N	Beam	35	88	122	75	0	0	0	0	0	0	0	0	0	0	74	121	87	35
Sunrise: 03:53		Diffuse	20	47	64	73	103	110	121	133	140	141	132	123	113	102	78	62	43	18
Sunset: 20:08	NE	Beam	57	165	320	379	353	260	119	0	0	0	0	0	0	0	0	0	0	0
		Diffuse	25	61	103	132	146	143	132	156	140	141	132	123	107	85	64	35	15	6
	E	Beam	45	145	331	461	519	502	409	265	90	0	0	0	0	0	0	0	0	0
		Diffuse	22	57	106	147	174	179	176	166	144	150	132	123	107	85	64	35	14	5
	SE	Beam	7	40	148	273	381	450	459	412	315	190	37	0	0	0	0	0	0	0
		Diffuse	16	43	69	113	151	171	183	186	179	162	124	131	107	85	64	35	14	5
	S	Beam	0	0	0	0	20	135	240	318	355	361	317	236	132	20	0	0	0	0
		Diffuse	6	16	35	67	81	121	152	173	185	186	172	156	124	80	71	35	14	5
	SW	Beam	0	0	0	0	0	0	0	37	187	320	411	451	440	385	272	147	40	7
		Diffuse	6	16	35	60	85	104	129	124	161	180	185	188	176	150	121	67	39	15
	W	Beam	0	0	0	0	0	0	0	0	0	92	264	402	491	524	459	329	144	45
		Diffuse	6	16	35	60	85	104	121	133	149	144	165	181	184	173	157	102	52	20
	NW	Beam	0	0	0	0	0	0	0	0	0	0	0	117	254	357	377	318	164	57
		Diffuse	6	17	35	60	85	104	121	133	140	141	155	135	147	145	141	100	56	23
Aug 4	Normal to beam		--	93	259	411	551	644	698	755	744	727	706	705	609	496	361	227	82	--

	N	Beam	--	40	73	36	0	0	0	0	0	0	0	0	0	0	32	64	35	--
Sunrise: 04:29		Diffuse	--	33	50	58	89	101	116	127	134	135	131	116	100	87	56	47	32	--
Sunset: 19:31	NE	Beam	--	87	225	301	305	222	86	0	0	0	0	0	0	0	0	0	0	--
		Diffuse	--	44	88	118	137	140	122	143	134	135	131	116	100	75	48	27	11	--
	E	Beam	--	84	245	389	486	488	406	276	93	0	0	0	0	0	0	0	0	--
		Diffuse	--	43	93	136	171	186	179	162	138	147	131	116	100	75	48	27	11	--
	SE	Beam	--	31	122	250	383	468	488	465	358	221	70	0	0	0	0	0	0	--
		Diffuse	--	32	62	107	152	182	192	189	182	166	133	130	100	75	48	27	11	--
	S	Beam	--	0	0	0	55	174	284	381	413	404	356	287	164	50	0	0	0	--
		Diffuse	--	11	28	59	84	131	160	177	190	193	187	159	131	83	55	28	11	--
	SW	Beam	--	0	0	0	0	0	0	74	226	350	434	493	442	345	219	107	28	--
		Diffuse	--	11	27	51	77	100	130	126	163	185	200	191	181	146	98	58	31	--
	W	Beam	--	0	0	0	0	0	0	0	0	91	258	410	461	438	342	215	74	--
		Diffuse	--	11	27	51	77	100	116	127	145	141	171	178	184	164	123	85	41	--
	NW	Beam	--	0	0	0	0	0	0	0	0	0	0	87	210	274	264	197	77	--
		Diffuse	--	11	27	51	77	100	116	127	134	135	149	121	140	133	107	80	42	--
Sep 4	Normal to beam		--	--	139	371	551	654	683	678	688	720	716	683	604	452	304	114	--	--
	N	Beam	--	--	19	0	0	0	0	0	0	0	0	0	0	0	0	16	--	--
Sunrise: 05:24		Diffuse	--	--	30	36	58	76	99	115	118	118	109	95	77	59	37	33	--	--
Sunset: 18:36	NE	Beam	--	--	111	252	272	182	32	0	0	0	0	0	0	0	0	0	--	--
		Diffuse	--	--	40	88	105	104	94	123	118	118	109	95	77	55	31	12	--	--
	E	Beam	--	--	137	365	505	515	412	257	89	0	0	0	0	0	0	0	--	--
		Diffuse	--	--	45	112	146	157	165	158	126	131	109	95	77	55	31	12	--	--
	SE	Beam	--	--	84	264	442	546	551	488	399	286	131	0	0	0	0	0	--	--
		Diffuse	--	--	36	90	135	162	188	197	182	159	123	113	79	55	31	12	--	--

	S	Beam	--	--	0	9	120	258	367	433	475	498	457	367	238	99	7	0	--	--
		Diffuse	--	--	12	32	76	117	158	187	194	191	175	150	119	77	34	13	--	--
	SW	Beam	--	--	0	0	0	0	0	124	273	418	515	551	505	363	217	69	--	--
		Diffuse	--	--	11	30	54	78	118	132	162	179	184	178	164	131	88	39	--	--
	W	Beam	--	--	0	0	0	0	0	0	0	93	272	412	475	414	299	113	--	--
		Diffuse	--	--	11	30	54	76	99	115	132	124	148	157	159	141	107	49	--	--
	NW	Beam	--	--	0	0	0	0	0	0	0	0	0	32	168	223	206	91	--	--
		Diffuse	--	--	11	30	54	76	99	115	118	118	116	90	107	104	85	43	--	--
Oct 4	Normal to beam		--	--	--	148	381	551	679	700	644	632	605	568	451	312	121	--	--	--
	N	Beam	--	--	--	0	0	0	0	0	0	0	0	0	0	0	0	--	--	--
Sunrise: 06:22		Diffuse	--	--	--	12	30	52	71	84	94	94	90	76	53	31	13	--	--	--
Sunset: 17:38	NE	Beam	--	--	--	83	155	105	0	0	0	0	0	0	0	0	0	--	--	--
		Diffuse	--	--	--	36	66	71	85	86	94	94	90	76	53	31	12	--	--	--
	E	Beam	--	--	--	145	351	436	412	267	84	0	0	0	0	0	0	--	--	--
		Diffuse	--	--	--	47	107	132	135	124	104	106	90	76	53	31	12	--	--	--
	SE	Beam	--	--	--	122	341	512	611	569	433	308	165	23	0	0	0	--	--	--
		Diffuse	--	--	--	42	105	146	165	169	168	148	123	75	57	31	12	--	--	--
	S	Beam	--	--	--	28	132	287	452	537	528	518	465	378	235	108	23	--	--	--
		Diffuse	--	--	--	32	61	106	141	164	184	184	179	150	102	60	33	--	--	--
	SW	Beam	--	--	--	0	0	0	29	191	314	425	491	511	419	280	100	--	--	--
		Diffuse	--	--	--	12	30	57	69	112	148	168	184	175	137	98	44	--	--	--
	W	Beam	--	--	--	0	0	0	0	0	0	82	231	345	357	287	119	--	--	--
		Diffuse	--	--	--	12	30	52	71	84	106	104	136	144	125	100	49	--	--	--
	NW	Beam	--	--	--	0	0	0	0	0	0	0	0	0	86	127	68	--	--	--
		Diffuse	--	--	--	12	30	52	71	84	94	94	92	90	71	64	38	--	--	--

Nov 4	Normal to beam			--	--	--	173	428	612	693	718	642	569	463	324	130	--	--	--	--
	N	Beam	--	--	--	--	0	0	0	0	0	0	0	0	0	0	--	--	--	--
Sunrise: 07:21		Diffuse	--	--	--	--	10	26	45	56	64	66	60	46	28	12	--	--	--	--
Sunset: 16:39	NE	Beam	--	--	--	--	47	43	0	0	0	0	0	0	0	0	--	--	--	--
		Diffuse	--	--	--	--	29	35	51	56	64	66	60	46	28	12	--	--	--	--
	E	Beam	--	--	--	--	151	327	359	256	90	0	0	0	0	0	--	--	--	--
		Diffuse	--	--	--	--	39	93	106	94	72	76	60	46	28	12	--	--	--	--
	SE	Beam	--	--	--	--	166	420	584	603	527	357	198	57	0	0	--	--	--	--
		Diffuse	--	--	--	--	41	111	143	145	139	128	99	57	32	12	--	--	--	--
	S	Beam	--	--	--	--	84	267	468	597	655	586	490	353	202	63	--	--	--	--
		Diffuse	--	--	--	--	31	81	124	144	158	166	152	119	79	35	--	--	--	--
	SW	Beam	--	--	--	--	0	0	77	241	400	472	495	442	318	125	--	--	--	--
		Diffuse	--	--	--	--	11	30	56	92	121	147	153	136	106	46	--	--	--	--
	W	Beam	--	--	--	--	0	0	0	0	0	81	210	272	248	113	--	--	--	--
		Diffuse	--	--	--	--	10	26	45	56	73	77	102	103	90	44	--	--	--	--
	NW	Beam	--	--	--	--	0	0	0	0	0	0	0	0	32	36	--	--	--	--
		Diffuse	--	--	--	--	10	26	45	56	64	66	60	52	37	32	--	--	--	--
Dec 4	Normal to beam			--	--	--	--	208	456	592	624	591	533	410	187	--	--	--	--	--
	N	Beam	--	--	--	--	--	0	0	0	0	0	0	0	0	--	--	--	--	--
Sunrise: 08:03		Diffuse	--	--	--	--	--	13	29	42	49	50	41	29	13	--	--	--	--	--
Sunset: 15:57	NE	Beam	--	--	--	--	--	7	0	0	0	0	0	0	0	--	--	--	--	--
		Diffuse	--	--	--	--	--	33	32	42	49	50	41	29	13	--	--	--	--	--
	E	Beam	--	--	--	--	--	152	257	210	75	0	0	0	0	--	--	--	--	--
		Diffuse	--	--	--	--	--	42	86	84	60	57	41	29	13	--	--	--	--	--
	SE	Beam	--	--	--	--	--	208	443	527	474	348	207	72	0	--	--	--	--	--

		Diffuse	--	--	--	--	--	50	125	144	136	116	83	45	15	--	--	--	--	--
	S	Beam	--	--	--	--	--	142	369	535	595	563	482	332	127	--	--	--	--	--
		Diffuse	--	--	--	--	--	41	110	145	157	156	135	102	41	--	--	--	--	--
	SW	Beam	--	--	--	--	--	0	80	230	368	449	474	398	187	--	--	--	--	--
		Diffuse	--	--	--	--	--	15	47	88	117	135	134	116	50	--	--	--	--	--
	W	Beam	--	--	--	--	--	0	0	0	0	71	189	231	137	--	--	--	--	--
		Diffuse	--	--	--	--	--	13	29	42	56	61	80	81	42	--	--	--	--	--
	NW	Beam	--	--	--	--	--	0	0	0	0	0	0	0	7	--	--	--	--	--
		Diffuse	--	--	--	--	--	13	29	42	49	50	41	32	33	--	--	--	--	--

APPENDIX 2

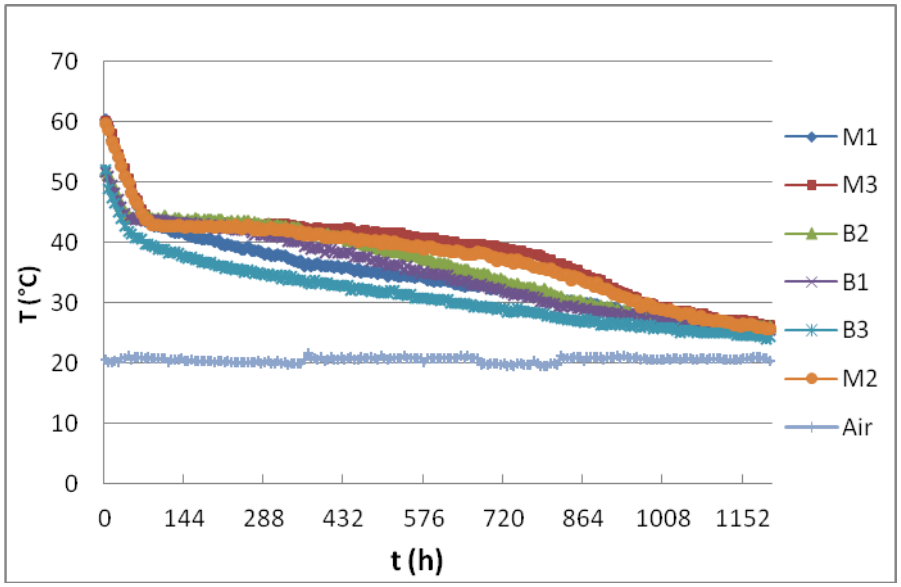

Figure A2.1 Temperature variations of the pure RT 42 during freezing period

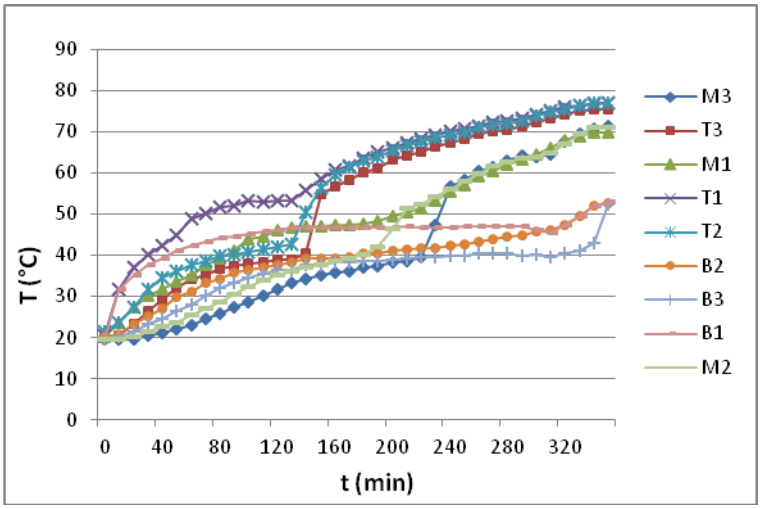

Figure A2.2 Temperature variations inside RT42 during melting process (HF)

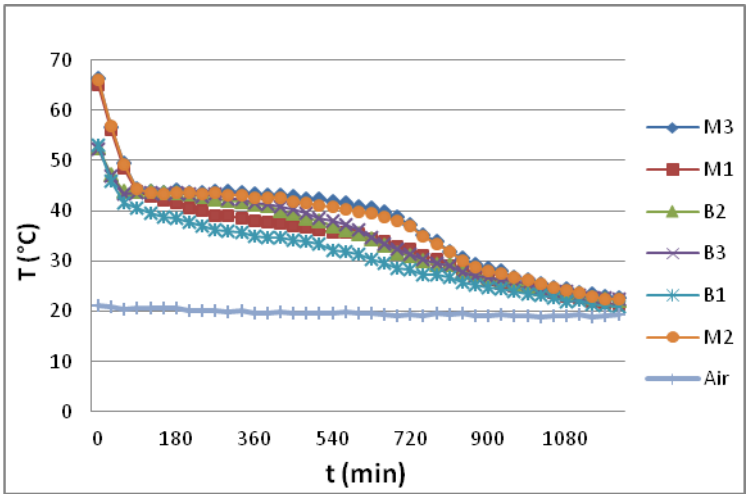

Figure A2.3 Temperature variations inside RT42 during freezing process (HF)

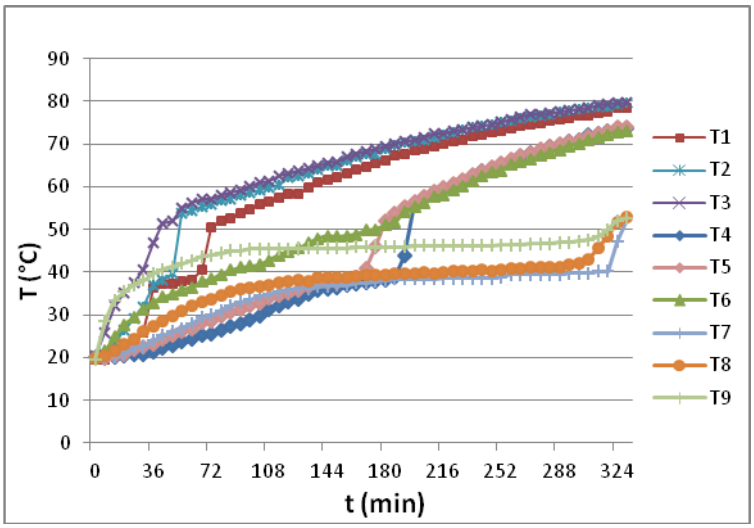

Figure A2.4 Temperature variations inside RT42 during melting process (VF)

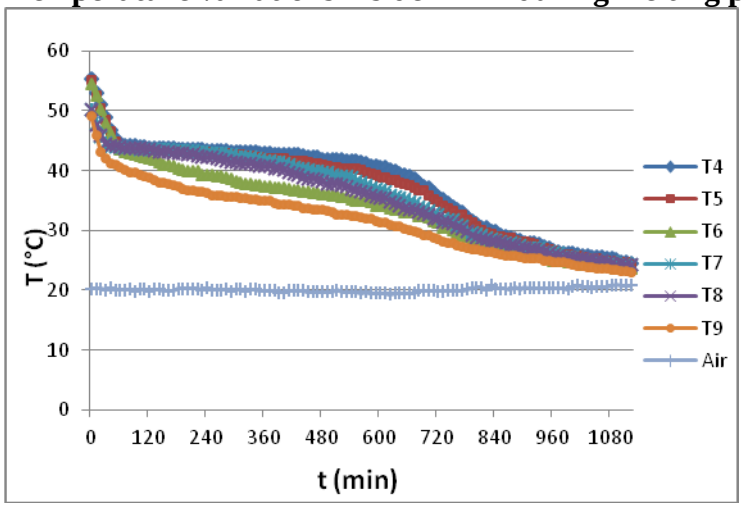

Figure A2.5 Temperature variations inside RT42 during freezing process (VF)

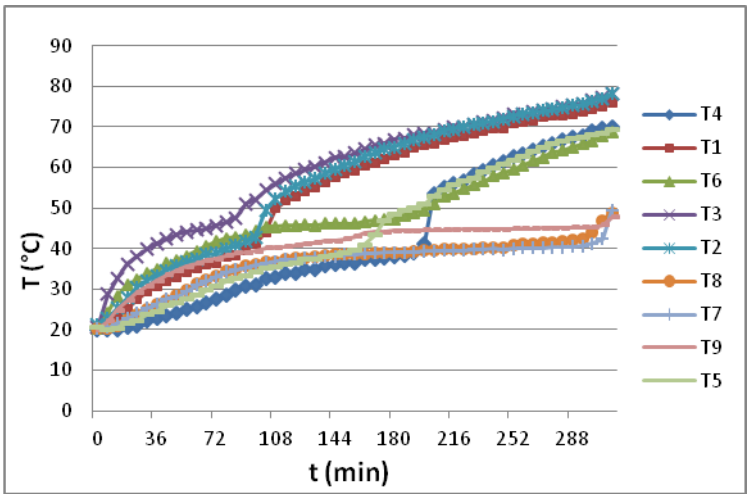

Figure A2.6 Temperature variations inside RT42 during melting process (HCS)

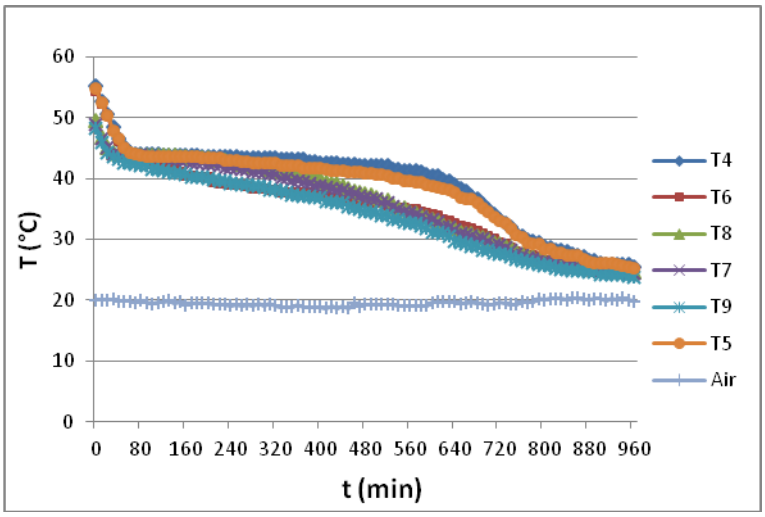

Figure A2.7 Temperature variations inside RT42 during freezing process (HCS)

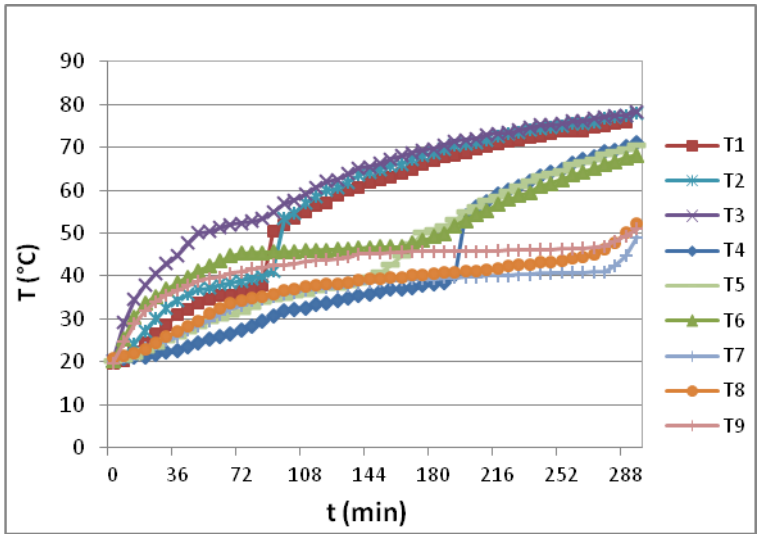

Figure A2.8 Temperature variations inside RT42 during melting process (SCS)

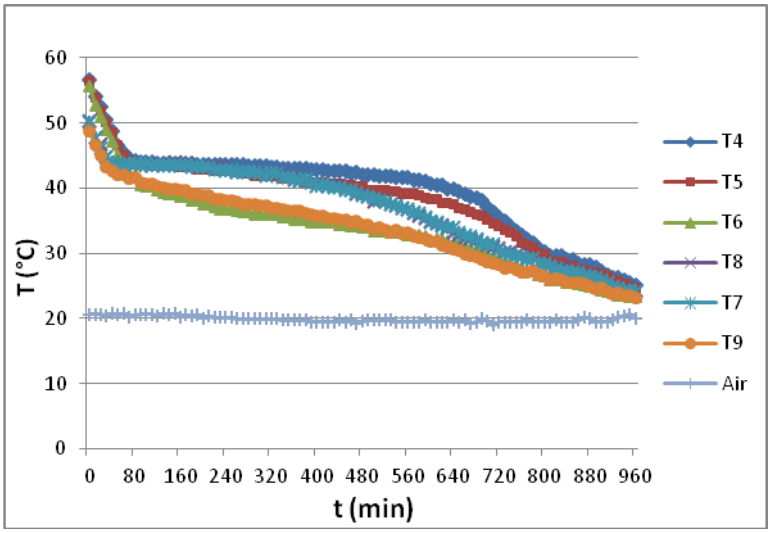

Figure A2.9 Temperature variations inside RT42 during freezing process (SCS)

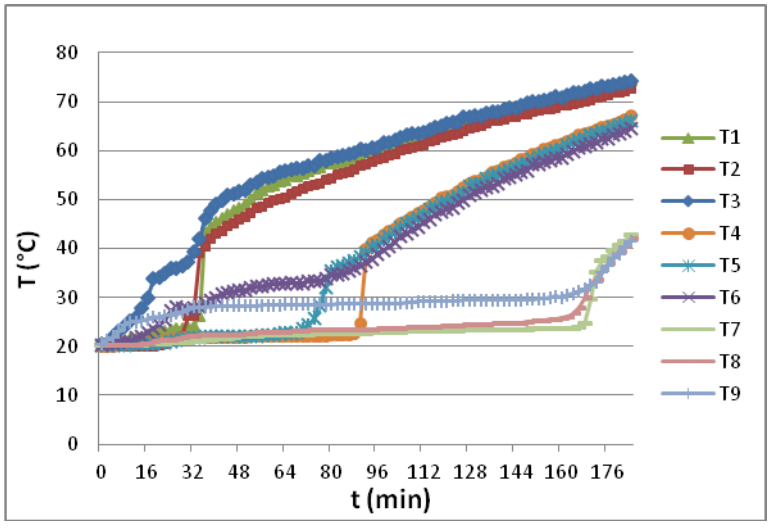

Figure A2.10 Temperature variations inside pure RT25 during melting process

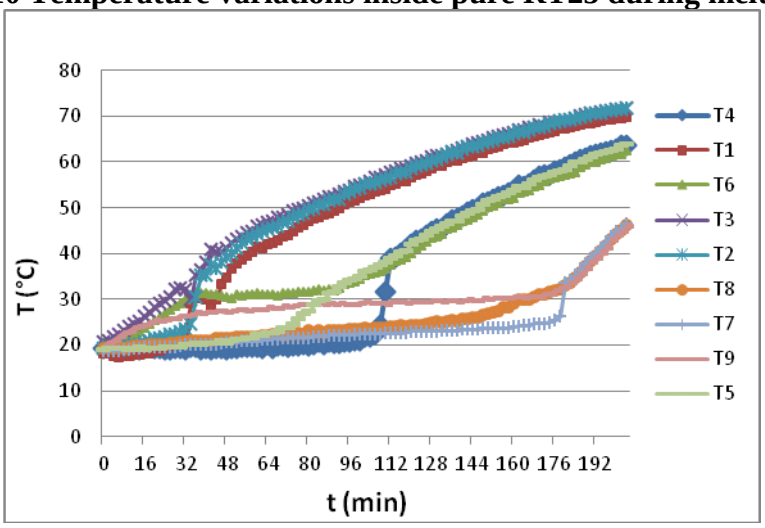

Figure A2.11 Temperature variations inside RT25 during melting process (HF)

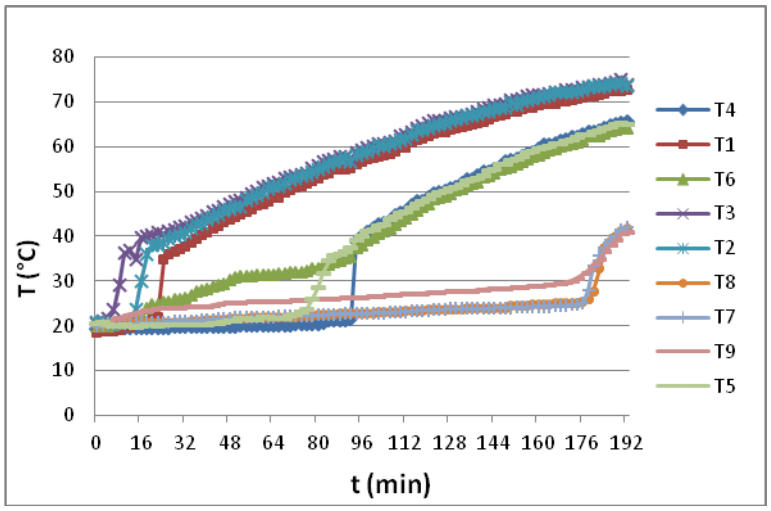

a)

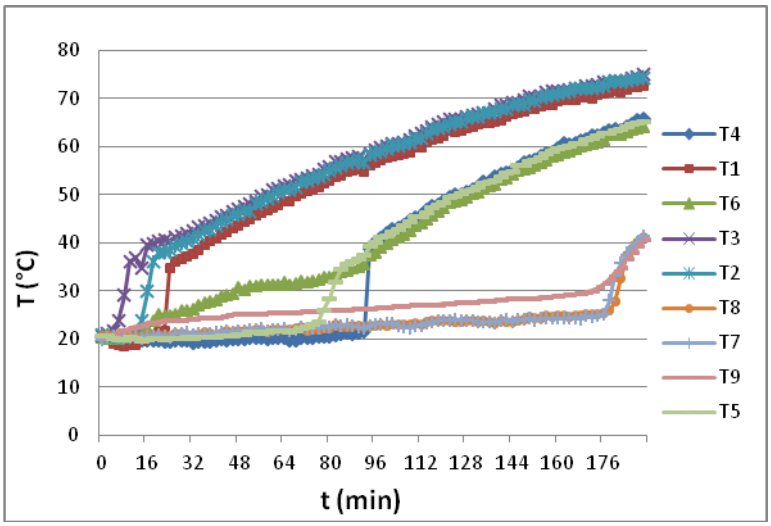

b)

Figure A2.12 Temperature variations inside RT25 during melting process (VF)

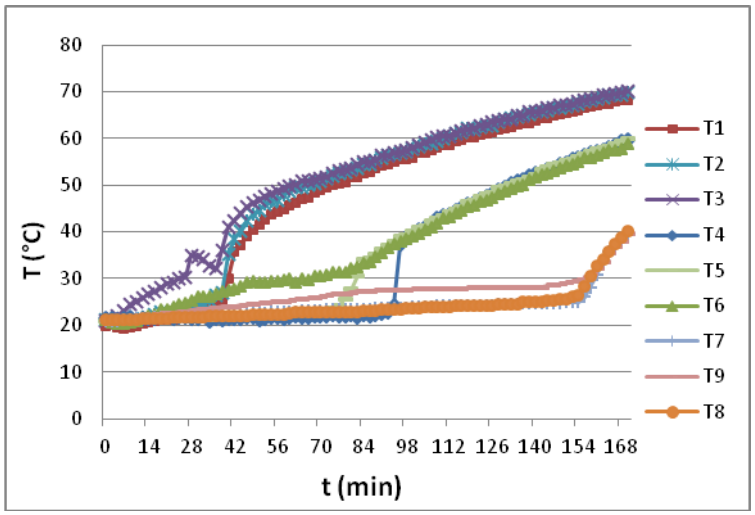

a)

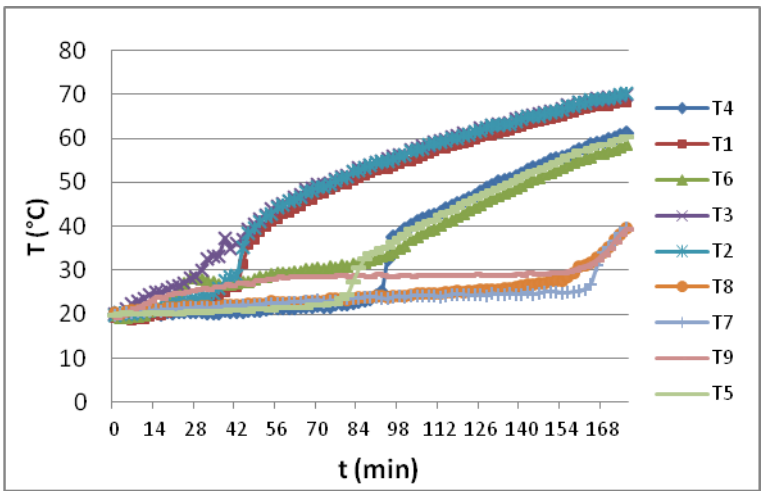

b)

Figure A2.13 Temperature variations inside RT25 during melting process (HCS)

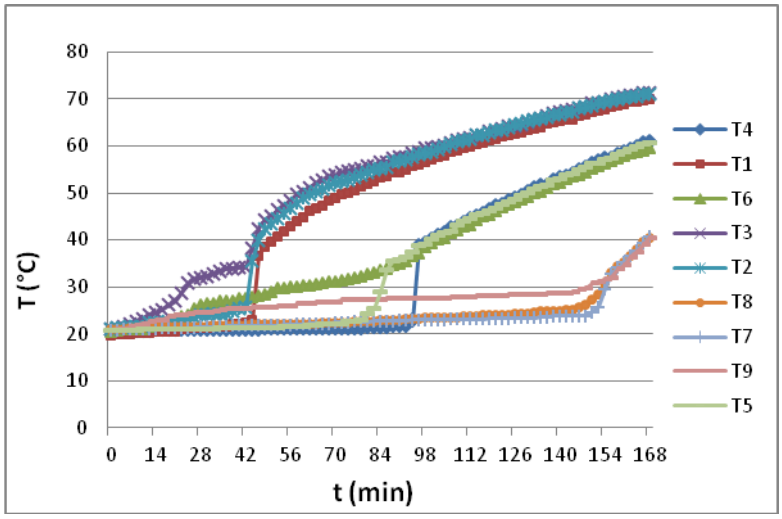

Figure A2.14 Temperature variations inside RT25 during melting process (SCS

APPENDIX 3 Relationship between PCM Mass and Air Channel

The amount of the PCM calculated for the proposed system is based on closed mode in which the inlet and outlets are closed. There is no air flow occurs in the air channel during this period.

Energy balance on the glazing is written as follows:

$$\frac{dT_g}{\Delta t}\rho_g C_g \delta_g A = \alpha_g q_g A + q_{p-g}A - q_{g-sky}A \quad \text{(A3.1)}$$

Since the volume of the glazing is thin, the thermal capacity of the glazing can be ignored, the left hand of the equation A3.1 and the first term of the right hand above are equal to zero.

$$\frac{dT_g}{\Delta t}\rho_g C_g \delta_g A=0 \quad \text{(A3.2)}$$

$$\alpha_g q_g A = 0 \quad \text{(A3.3)}$$

The equation A3.1 can be rewritten as follow:

$$q_{p-g}A - q_{g-sky}A = 0 \quad \text{(A3.4)}$$

Where

$$q_{p-g} = U_{p-g}(T_p - T_g) \quad \text{(A3.5)}$$

$$U_{p-g} = h_{r,p-g} + h_{c,p-g} \quad \text{(A3.6)}$$

$$h_{r,p-g} = \frac{\sigma\left(T_p^2 + T_g^2\right)(T_P + T_g)}{\xi_p^{-1} + \xi_g^{-1} - 1} \quad \text{(A3.7)}$$

$$h_{c,p-g} = \frac{Nu\lambda_{air}}{\delta_{air}} \quad \text{(A3.8)}$$

Where

$h_{r,p-g}$ – Radiative heat transfer coefficient between the absorber and glazing

$h_{c,p-g}$ – Convective heat transfer coefficient between the absorber plate and glazing

ξ_p^{-1}, ξ_g^{-1} – Emittances of the absorber plate and the glazing

λ_{air} – Thermal conductivity of the air between the glazing and the absorber

δ_{air} – Thickness of the air layer between the glazing and the absorber

The Nusselt number is given by the following relation

$$Nu = [0.06 - 0.017(\beta/90)]Gr^{1/3} \quad \text{(A3.9)}$$

β represents the solar collector tilt angle in degrees.

The Grashoff number is given as:

$$Gr = g(T_p - T_g)\delta_{air}^3/v^2 T_{air} \quad \text{(A3.10)}$$

Combining equations A3.8, A3.9 and A3.10, equation A3.8 can be written as:

$$h_{c,p-g} = \lambda_{air}[0.06 - 0.17(\beta/90)]\sqrt[3]{\frac{g(T_p - T_g)}{v^2 T_{air}}} \quad \text{(A3.10)}$$

It can be seen that the equations of energy balance for glazing is independent of the air layer, δ_{air}. Furthermore, the equations for other system's components are also not involved the air layer. Thus, the calculation of the amount of the PCM is just related to the solar radiation data, the thermo-physical properties of the PCM and the assumptions made to the numerical simulation.

APPENDIX 4 Published papers

During the progress of the research many scientific topics were of great interest and were disseminated in various journal papers, conferences. A list of the most relevant contributions is given below.

Papers marked with a "*" are presented in appendix 4.

*Li, Y., Liu, S. (2014) 'Experimental Study on Thermal Performance of a Solar Chimney Combined with PCM'. Applied Energy 114, 172-178

Li, Y., Liu, S. (2016) 'Various TCEs Effects on the Thermal Performance of Two Organic PCMs: RT42 and RT25'. ***Accepted for publication in Journal of Heat Transfer Research - American Society of Mechanical Engineers***

*Liu, S., Li, Y., Zhang, Y. (2014) 'Mathematical solutions and numerical models employed for the investigations of PCMs' phase transformations'. ***Renewable & Sustainable Energy Reviews*** 33, 659-674

Liu, S., Li, Y., Zhang, Y. (2015) 'Review on heat transfer mechanisms and characteristics in encapsulated PCMs'. ***Accepted for publication in Journal of Heat Transfer Engineering*** 36(9)

Li, Y., Liu, S., Zhang, Y. (2012) 'Experimental study of the heat transfer performance of PCMs within metal finned containers'. ***11th International Conference on Sustainable Energy technologies***, September 2-5, Vancouver, Canada

Li, Y., Liu, S., Lu, J. (2010) 'An experimental study of night ventilation performance of a solar roof integrated with PCM'. ***9th International Conference on Sustainable Energy Technologies***, August 24-27, Shanghai, China